UNIVERSITY OF BIRMINGHAM

Polarization Behaviour of On-Body Communication Channels at 2.45 GHz

by

Lida Akhoondzadehasl

A Thesis submitted to

University of Birmingham

for the degree of

DOCTOR OF PHILOSOPHY

School of Electronic, Electrical & Computer Engineering
College of Engineering and Physical Sciences
University of Birmingham

May 2011

Abstract

The advent of body worn devices and the use of them for a wide range of applications, from entertainment to military purposes, indicate the need to investigate to the behaviour of antennas and wave propagation on the body in depth. Knowledge and understanding and of the on-body channel can lead to the design of efficient antennas and systems for wearable devices.

The objective of this work is to identify the propagation mechanism on the body for different polarisation states at 2.45 GHz. In particular, the effect of the body on the antenna performance with normal and parallel polarisation is studied and their capability in launching surface waves is evaluated. It is shown that both vertically and horizontally polarised antennas can launch a transverse magnetic (TM) Norton surface wave mode regardless of their polarisation states. However, horizontally polarised antennas do not launch the wave as strongly as vertically polarised antennas. Also, the change in the far field and near field behaviour of the antennas such as a dipole in proximity to the body is investigated and the observations lead to the design of a novel surface wave parasitic array. This new antenna is directive and can increase the path gain by almost 10 dB compared to other planar antennas. In addition, the effect of the polarization of the antenna on channel path gain is studied and channel cross polarization discrimination is quantified, using both simulation and measurement.

To Ali

ACKNOWLEDGMENTS

I wish to express my immense gratitude to my supervisor, Professor Peter Hall, for his generous support and guidance in every step of my research. This work has not been accomplished without his brilliant supervision, vast knowledge and invaluable comments. He has been a great advisor and role model for me and I have learned so many life lessons from him. His attitude to the life, patience, and persistence has inspired me in many ways.

I had a great opportunity to visit University of Auckland as a part of my PhD. The whole experience was unique and I would like to acknowledge Dr Michael Neve for his great advices.

I would like to thank examiners of my thesis, Dr Costas Constantinous and Dr Robert Edwards, for their time and feedback on my work

I would like to thank Mr. Alan Yates for his assistance with making antennas and using equipments.

I have enjoyed working with all the members of the AAEL group, I would like to say big thank you to Dr Yuri Nechayev and Dr Imdad khan for sharing their knowledge and helping throughout the work. I would like to thank the other members of the group and my wonderful colleagues, Mrs Elham Ebrahimi, Dr Massoud Karbassian, Dr James Kelly, Ms Donya Jasteh, Dr Mohammad Hmaid, Mr Xianuye Wu for their helps and friendship.

The PhD journey has been turning life experience for me. I am grateful to spend time with fabulous friends whose support and affection carried me through difficulties. I heartily thank them all.

Last but not least, I would like to thank my beloved parents and husband, Ali, for their endless support and love and understanding. During my study, half of the burden has been on my husband shoulder. He sincerely listened and discussed many of my research ideas with

me. His encouragement has been my source of inspiration in pursuing and completing PhD. Thank you.

Table of Contents

List of Figures

List of Tables

Chapter 1

Introduction

1.1. MOTIVATION

Wireless communication is an attractive option for connecting various electronic devices carried by a person on their body. Many applications have been suggested, including personal healthcare, the smart home, personal entertainment and the future infantry soldier [1-3]. There are several current on-body wireless links, such as the well known wireless Bluetooth headset for use with mobile phones. Other examples include the wrist watch mobile phone controller, [4], and the Nike/iPod training shoe system, [5]. Currently, there are several evolving standards particularly focused on providing robust and reliable short range links, some of which are being considered for use on the body. The IEEE 802.11 series is developed for wireless local area networks (WLAN) [6], which may be useful as a link from the body to a local base station. The IEEE 802.15 series introduces different standards for various technologies [7], which are already, or in the future may be, used for on-body links, such as 802.15.1 Bluetooth, 802.15.3 high rate wireless personal area networks (WPAN) , 802.15.4 sensor networks, 802.15.4.a ultra wide band (UWB) wireless sensor networks and 802.15.6 body area networks (BANs).

Many investigations have been conducted to estimate the performance of on-body channel, in terms of path gain [8-10] and short and long term fading [11-16]. All these studies highlight the evolving interest in on-body communications and the need to develop guidelines for the design of devices with the most efficient performance for this application. However, in spite of much work in the on-body field, less attention has been paid to the understanding of the propagation mechanism between antennas and the antenna behaviour in launching the various propagation modes.

One of important issues in various wireless applications, such as satellite, outdoor mobile and indoor wireless communication, is the depolarisation of the wave during propagation. Such depolarisation can significantly affect the received signal [17-20]. In general, the polarisation of an electromagnetic wave is elliptical. When one of the orthogonal components of the elliptical polarisation is zero, linear polarisation results. When they are equal circular polarisation results. Usually the polarisation is defined by the transmit antenna polarisation characteristic. However, the wave polarisation may also change during the propagation through a channel by either interaction with a media or by colliding with obstacles in the channel [21]. The media might be, for example, the ionosphere, in the case of a space to earth channel. In indoor propagation, scattering from walls, floor, ceiling and furniture will be the main cause of depolarisation. In on-body channels the presence of the body might be considered either as a propagation medium or a scatterer. The wave depolarisation will cause an extra loss in the channel, due to the polarisation mismatch between the receive antenna and the incident wave [19, 22]. Depolarisation in on-body channels is common due both to body movements and the natural curvature of the body surface, on which the antennas are mounted. Placing antennas in different positions on the body or moving parts of the body may lead to the change in the orientations of antennas at each end of the channel. In addition, the change of the antenna behaviour due to the body proximity may also affect the polarisation of the transmitted wave [14, 23]. In the light of these issues, the characterization of channel

depolarization may give some insight of the underlying propagation processes in on-body channels.

As has already been mentioned, antennas play an important role in determining the quality of the channel. Various practical antennas have been used to perform on-body channel measurements [12, 14-18]. Much research has focused on the use of conventional antennas and attempting to understand and optimise their performance in the proximity of the human body [15, 24-27]. Many of the proposed antennas have been designed for use in free space and the body influence on the antenna characteristics has subsequently been investigated. In other words, the proximity of the body as a dielectric mass close to the antenna is ignored at the antenna design stage. However, as noted above this dielectric may affect the radiation characteristics of the antenna both on and off the body.

1.2. THESIS OBJECTIVES

The aim of this thesis is to better understand the propagation mechanism on the human body and to investigate the capabilities of different antennas in providing reliable on-body communication channels. This knowledge may be useful in allowing optimized wearable antennas to be designed, and also informs the performance of the channel in the case when non-optimum antennas are used due to the higher importance of other factors, such as available space for the antenna or the need to design down to a cost. In addition, an associated issue is that of de-embedding the antenna from the channel, which is desirable to allow simplified prediction of channel behaviour when new antennas are used. In principle, in such a de-embedding process, knowledge of the wave propagation mechanism, polarization and gain pattern of the antenna close to the body is needed to extract the propagation channel characteristics. The objective of the thesis can be summarised as follows:

- Investigation of de-embedding of antenna characteristics from on-body transmission channels by proposing a simple method, and addressing the difficulties and challenges in the de-embedding process

- Investigation of the near and far field behaviour of the antennas with normal and parallel polarisation to the body surface and quantify the path gain of the channel with similar or orthogonal polarisation antennas at each end. Exploring the propagation mechanism on the human body by use of canonical structures such as flat and cylindrical phantom

- Estimating the depolarisation of the wave in different on-body channels

- Development of an antenna that has increased coupling to the surface wave.

- Investigation of millimetre wavelengths for on body applications and addressing the advantageous and disadvantageous of this frequency band

1.3. THESIS OVERVIEW

The thesis includes 8 chapters and is outlined as follows:

Chapter 2: provides general information about on-body area networks, applications and the challenges. Also, it reviews some of the works related to the on-body antenna and propagation.

Chapter 3: Discusses a simple method of de-embedding of the on-body propagation channels. The difficulties in the de-embedding processes are addressed and an experiment which attempts to estimate the errors involved in de-embedding is reported. Some measurements including different polarization and antenna orientations on a stationary posture in the anechoic chamber are presented and the propagation channel values are calculated for each channel.

Chapter 4: describes an investigation into the polarization behaviour of on-body wireless communication channels at 2.45 GHz. The effect of the polarization of the antenna on channel path gain is studied and channel cross polarization discrimination is quantified, using both simulation and measurement. In simulation, short dipoles antennas, which significantly reduce the simulation time, are used to investigate path gain behaviour in different channels for vertically and horizontally polarised antennas. Measurements were taken in an indoor environment using a novel dual polarized antenna, producing normal and parallel polarization to the body surface. The received signals, measured in this way, are also analyzed to extract the Rician K factor which is defined as the ratio of the power in the line of sight (LOS) to the scattered power for various polarization combinations. Furthermore, the polarization diversity for on-body channels is investigated.

Chapter 5: Describes the on-body radio channel from the analytical point of view and investigates the surface wave on the body. The Zenneck wave and Norton wave are explained and their behaviour on the human body is studied. Short dipole behaviours on the human body are explored by analytical and computer simulations, thus providing some insight into the properties of the Norton surface waves on human tissue. Also, the coupling between the antenna and the Norton surface wave polarization modes is calculated for realistic antennas on both flat and curved surfaces. This leads to Norton surface wave launching patterns for these antennas, which can yield significant insight into the operation of wearable antennas.

Chapter 6: Presents the design procedure of a novel planar directive antenna with a capability of exciting the surface wave on the human body. Parametric studies are performed to optimise the antenna directivity on the body phantom surface. The antenna was designed, fabricated and measured. Its performance was tested by the path gain simulation and measurement. The measurements were performed on the muscle liquid phantom inside the anechoic chamber. Also, similar set-up is used to measure and compare the performance of the new antenna to the other antennas.

Chapter 7: Describes use of 60 GHz as a new operation frequency for the on-body communications. The difficulties in use of this frequency for on-body application are addressed and some on-body measurements performed in the chest to belt channel in the laboratory environment are presented and discussed.

Chapter 8: Provides a conclusion to this research work in the on-body antenna and propagation field and summarises the finding in this thesis. Also, suggestions for further work are proposed.

Chapter 2

Literature Review

2.1. INTRODUCTION

In chapter 1, body area networks (BAN) were briefly introduced and the need to explore on-body channels was highlighted. The research scope and summary of the papers were then reported. This chapter provides an overview of previous research relevant to the research scope of this thesis. Recognition of unresolved issues in the literature is the main object of this chapter. In the following sections, research on the following topics is reviewed.

- Antenna de-embedding
- Channel depolarisation
- Propagation modes
- Antennas for surface wave excitation
- On-body channels at 60 GHz application

2.2. DE-EMBEDDING

De-embedding of antenna characteristics from the channel in any wireless communication is essential to provide a generic channel model independent of transmit and receive antenna properties [28]. In free space, where there is no multipath, transmit and receive antennas communicate through line of sight (LOS) as shown in Fig. 2.1. In this case, the Friis formula, given in (2-1), can be used to determine the path loss within the propagation channel [29].

$$T = G_t(\varphi_t, \theta_t) G_r(\varphi_r, \theta_r) P \tag{2-1}$$

which it can be rewritten in dBs as

$$T|_{dB} = G_t(\varphi_t, \theta_t)|_{dB} + G_r(\varphi_r, \theta_r)|_{dB} + P \quad dB \tag{2-2}$$

where T is the transmission channel path loss which is the ratio of the received to the transmitted power, $G_t(\varphi_t, \theta_t)$ is the realised gain of the transmit antenna in the direction of (φ_t, θ_t), $G_r(\varphi_r, \theta_r)$ is the realised gain of the receive antenna in the direction of (φ_r, θ_r) and P is the propagation channel transfer function defined as $\left(\lambda^2/(4\pi R)^2\right)$.

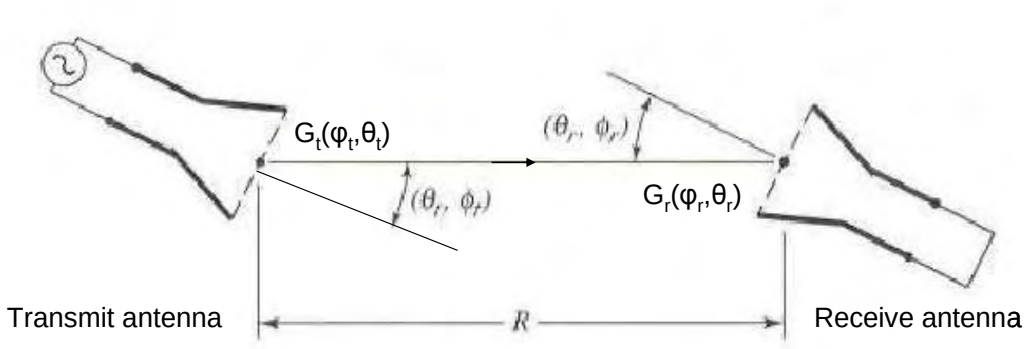

Fig. 2.1 Geometrical orientation of transmitting and receiving antennas in Friss formula [30]

In equation (2.1), the propagation loss term, P, is explicitly separated from the gain of the transmit and receive antennas. The antennas are assumed to be co-polarised. In the more general form of the equation, the polarisation matching factor between transmit and receive antennas is considered in the case where two antennas are polarised differently [30]. In addition to the polarisation matching, other factors including antenna impedance mismatching, and atmospheric absorption can be added. As mentioned, this equation can be used in line of sight, point to point channels, where there is no multipath such as satellite communications or in an anechoic chamber [30]. However, in the most wireless applications, the reflections from the ground and scattering from the surrounding environment are present in the communication channel. In such a scenario, the signal does not attenuate as the Friis formula and modelling of propagation channels requires other extra information [31]. In mobile communications, to modify the Friis formula, both empirical and deterministic models have been developed [32]. One of the most widely used empirical models to predict path loss in urban areas is the Hata model [33]. In this model, the path loss between two isotropic antennas is derived, based on extensive measurements in Tokyo and the formulation includes factors such as transmit and receive antenna heights from the ground plane. Prediction of the path loss by use of Hata's expression provides reasonably good correlation with measurement results, provided that there is not much multipath. One way to take into account the multipath effect in dense areas is to

use the mean effective antenna gain [34]. Mean effective gain is defined as the ratio of the mean signal levels of the test and reference antennas. It is thus a measure of the average of the variations in the antenna gain and removes the radiation pattern data from the channel model. Use of the mean effective gain in the Hata model or the Friis formula allows the inclusion of realistic antennas behaviour whilst operating in the proximity of the scattering objects. In general, to model the propagation channel accurately in indoor or outdoor wireless channels, information relating to multipath rays must be included in the Friis formula [35]. In other words, in the presence of multipath, the transmit and receive antennas communicate through the LOS and multipath rays, which arrive at the receive antenna with various time delays. Array antennas have been exploited at the transmit and receive ends, in order to detect the angle of arrival (AOA) and time of arrival (TOA) of the rays at the receiver and the angle of departure at the transmitter [8]. The number of the antennas determines the resolution [35]. To summarise, in multipath environments, full de-embedding is not performed with mean effective gain being the closest approximation to it.

In on-body channels, antenna de-embedding is as important as in other wireless channels. However, there are no studies reported in the literature. In body area networks, in some channels such as the belt to chest link, the line of sight ray may play a key role. In such channels, it is possible that de-embedding can be done based on some assumptions in order to simplify the model, but in other cases in which the transmission channel is obstructed by the body, de-embedding will be very challenging, due to the existence of the multipath and surface wave. In chapter 3, this hypothesis is tested for the line of sight channels and different issues associated with the on-body de-embedding are investigated.

2.3. POLARIZATION INVESTIGATIONS IN ON-BODY CHANNELS

The depolarisation of the electromagnetic wave is one of the factors considered in describing the channel behaviour of most wireless communication channels [17-20]. To describe the depolarisation, the parameter cross polarization discrimination (XPD) is calculated. XPD is defined as the ratio of the co-polarized to cross-polarized received power, [36]. Higher value of XPD indicates less depolarisation. Hence, the XPD value in a LOS scenario is very high, while obstructed channels experience a lower XPD. Understanding the channel polarisation behaviour is necessary to choose antennas with the proper polarisation characteristics. In addition, the information is valuable to evaluate the performance of either polarisation diversity to decrease the effect of multipath or of multiple input multiple output (MIMO) systems to increase the capacity by employing dual-polarised antennas [37-39]

In spite of much work on the characterisation of the received signal variation for different on-body channels, in terms of slow and fast fading [11-16, 40] and path gain measurement [8-10], few publications are available on the polarisation behaviour of channels in body area networks, including on-body, off-body and in-body. In on-body channels, the depolarisation phenomena can be very significant due to the body movement, as well as the scattering of the wave from the body and surrounding environment. Reference [23] gives energy density, RMS delay spread and frequency response of vertically and horizontally polarised UWB elliptical planar dipoles in a non line of sight (NLOS) channel (chest to back). A time domain electromagnetic method has been used to simulate the antennas on the human phantom. The antenna has been placed as the transmitter in the centre of the chest of the phantom and the probes polarised similar to the transmit antenna have been used to collect the electric field magnitude. It has been shown that the maximum energy density is almost 20 dB larger for the vertically polarized antenna compared to the horizontally polarised one, due to the excitation of the surface wave, but a precise definition of the wave type is not given. The RMS delay has been calculated and it has been shown that it is less than 1 ns for vertical polarisation and less

than 1.2 ns for horizontal polarisation. Reference [14] describes a study on the behaviour of horizontally and vertically polarised UWB antennas on the body, through a measurement campaign performed inside an anechoic chamber. The path loss and RMS delay of these two types of antennas have been presented for various positions of the receive antenna on the body while the transmit antenna has been placed on the left belt. In this study, identical antennas have been used at each end of each channel. It has been shown that the RMS delay of both polarisations of the horizontally polarised antenna is generally higher by 1 or 2 ns compared to the vertically polarized. The attenuation factor of the path loss for vertically polarised antennas on the body was 1.35, while for the horizontally polarised antennas shows much higher attenuation of 2.2. In reference [22], Yazandoost describes the importance of the polarisation for on- and in-body applications and highlights the adverse effect of polarisation mismatch of transmit and receive antennas on the path gain, by calculating the polarisation mismatch factor, but the paper does not provide any experimental evidence. Reference [41] reports on a polarisation investigation of implant antennas in the flat phantom at 480 MHz. Four polarisation combinations of the implant and the base station antennas have been considered and the implant antenna effective radiated power (ERP) is calculated based on the measured data in the anechoic chamber. It has been shown that when both base station and implant are vertically polarised ERP is almost 20 dB higher compared to the scenario in which both of the antennas are polarised horizontally. The mixed polarisation combination, that is, one polarised vertically and the other horizontally, provides values between two co-polarised combinations. The reason for these observations has not been discussed in the paper.

A general full-wave solution of a point source with an arbitrary polarisation has been derived and extended in [42]. Both vertically and horizontally polarised sources have been considered and the azimuthal electric field around a cylinder, which is assumed to model a human trunk, has been simulated at 2.45 GHz. It has been shown that electric field distribution of a horizontally polarised source, oriented along the axis of a cylinder having a radius of 15

cm, shows 1.68 dB/cm loss, while a vertically polarised source results in 0.6 dB/cm loss. The simulation results have been confirmed by measurements in an anechoic chamber. In reference [43], Ali reports on the effect of the human head on the capacity of MIMO systems. In addition to the capacity, which is not considered in this thesis, the paper presents the path gain of the sub channels with and without the presence of the head for 4 different antenna polarisation combinations at the ends of the channels. In the scenario with the head present, two of the antennas (antenna 1 and 3) were mounted on the right side of the temple and the other two (antenna 2 and 4) were placed at a distance of 3 m away from the antenna 1 and 3, as shown in Fig. 2.2. The measurements were conducted at frequencies of 700, 950 1880 MHz, inside a laboratory. It is shown that, in all four polarisation combinations, the user head lowers the received power in the channel 1 (both vertical) by 7 dB and in channel 2 (one vertical and the other one horizontal) by 22 dB.

Fig. 2.2 Dipole arrangements with the user head [43]

In summary, in most work, identical antennas with polarisations either normal or parallel to the body surface have been used in on-body channels and different parameters such as path gain, root mean square (RMS) delay spread, and electric field distribution within the channel, have been investigated both in the narrowband scenario and in UWB channels. However, very few studies of mixed antenna types has been published and, furthermore, no data on the depolarisation in such channels has been reported. On the other hand, the wave depolarisation has been studied in other wireless communication systems such as mobile channels, and in

this work the aim is to test whether the same concept can be applied for on-body channels and provide depolarisation parameters for different channels on a moving body.

2.4. PROPAGATION MECHANISM ON THE HUMAN BODY

In wireless communications, various transmission mechanisms are encountered. For example, in mobile communication systems, line of sight (LOS), plus reflection, diffraction and scattering are the main propagation mechanisms. In on-body channels, sensors and wireless devices located close to the body can communicate in a variety of ways, including LOS, reflection from the body surface or the surrounding environment, such as walls or the ground, scattering from objects located near the user and also through a surface wave on the body. The propagation mechanism in an on-body channel depends on the body size, shape and posture, the antenna radiation pattern at each end of the channel, depending on frequency, the body tissue parameters [40]. In most on-body channels, multipath plays an important role, together with the space wave, including the direct wave and the body reflected wave, and the surface wave. In non line of sight (NLOS) channels, in which the transmitter and receivers are shadowed from each other, the surface wave can be the main propagation mechanism. In reference [44], Vaughan investigates the Zenneck and Norton wave for the vertical source on a flat phantom. These two types of surface wave were initially introduced for the wave propagation over a flat earth which in general consists of a lossy dielectric [45-46]. However, their existence can be presumed on the body surface due to the lossy dielectric property of body tissues. It has been shown that the Norton wave for the layered body model fits measurements around the torso, as shown in Fig. 2.3. The measurements have been conducted at 2.45 GHz, inside the anechoic chamber with two quarter wavelength monopoles with small ground planes. However, Edwards, [47] indicates that despite of the possibility of launching of the surface wave on the body surface, it attenuates very quickly due to the absorption of the energy by body tissues at microwave frequencies including 2.45 GHz.

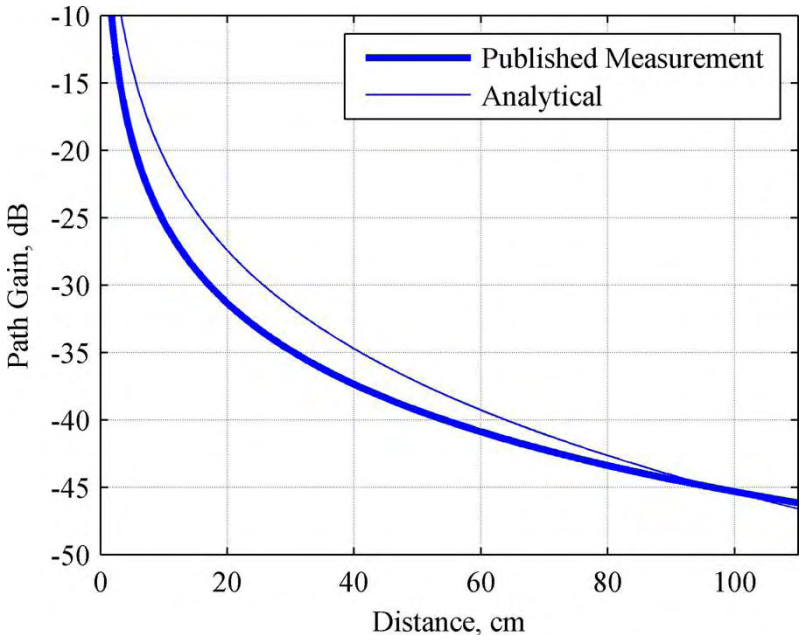

Fig. 2.3 Comparison of the analytical Norton wave with the on-body narrowband path gain measurement, at 2.45 GHz [44]

Rehman, [48], investigates the role of the surface wave in the belt to head channel by simulating the current distribution associated with the surface wave on the human phantom, by placing a metallic barrier between the transmit and receive antennas. It has been shown that when there is no gap between the body and the barrier, there is no current flowing on the body. However, the authors believe that by increasing the gap between the barrier and the body surface to 20 mm, the space wave is blocked while surface wave propagates on the body. They demonstrated this by the depicting the current distribution on the body. The path gain in this scenario is almost 13 dB lower than the one without the barrier.

Reference [49] describes an analytical method to calculate surface wave propagation along a homogenous cylinder, as a model of the arm, in the frequency range of 10-150 MHz and the results are confirmed with FDTD simulations. The behaviour of the electric and magnetic field components along and perpendicular to the cylinder surface have been derived

and discussed. The author of the paper believes the waves propagating along the arm model possesses the features of surface wave transmission.

The simulated electric field distribution of a half wavelength dipole on the surface of a planar and cylindrical phantoms is given in reference [50]. It is concluded that the surface wave is the most likely propagation mechanism in the simulation environment in which multipath is not present. Also, the electric field distribution on a homogeneous muscle and layered phantom have been compared and it is suggested that the use of a layered phantom can disturb the surface wave due to the reduction of the reflections from the phantom surface which is necessary to develop a creeping wave.

Ryckaert, [51], claims that the main mechanism of propagation around the human body is the creeping wave even in the presence of the multipath. It is noted that the path loss level of the wave around the body is of the order of the multipath components for a medium sized room. The delay spread for the creeping wave has been calculated and it was shown that creeping wave reaches the receiver with a much smaller delay than the first multipath component, resulting in an increase of the delay spread.

In the papers discussed above, the majority emphasise that the surface wave is the main propagation mechanism in shadowed channels in the absence of multipath, but few have attempted to characterise the Zenneck and Norton waves on the body. In addition, little work has been conducted to investigated the possibility of the launching the surface wave on the body by the conventional on-body antennas such as monopole, loop, dipole, etc. In this thesis, the Zenneck and Norton wave behaviour will be investigated, while practical antenna capability in launching the surface waves will be examined.

2.5. ANTENNAS FOR SURFACE WAVE EXCITATION

In section 2.4, the propagation mechanism on the body was discussed and research reviewed which suggested that the main propagation mechanism around the torso in the absence of the multipath is the surface wave. It has even been mentioned that in some scenarios, the surface wave contribution can be equal to that from the multipath. Launching of surface waves has been a hot topic for many years and many antennas have been developed to excite them on the earth and sea surface [45, 52-54]. In principle, a surface wave antenna is a type of travelling wave structure whose phase velocity is equal to, or less than, the speed of light in free space, [30]. Most of these antennas are end fire, which couple between 65 and 75% of the input power to the surface wave, [55]. One simple structure of this type of antennas is shown in Fig. 2.4. The antenna consists of a long wire, which is terminated by a load in order to reduce the reflection from its end [30]. As is shown, the radiation pattern of the antenna is tilted down to the ground plane, in order to couple the energy to the surface wave. An array of metallic or dielectric rods can also be used as shown in Fig. 2.5 [55]. Since these antennas radiate much of the power toward the surface, they are possible candidates for on-body applications due to likely enhanced surface wave excitation together with reduced off body radiation.

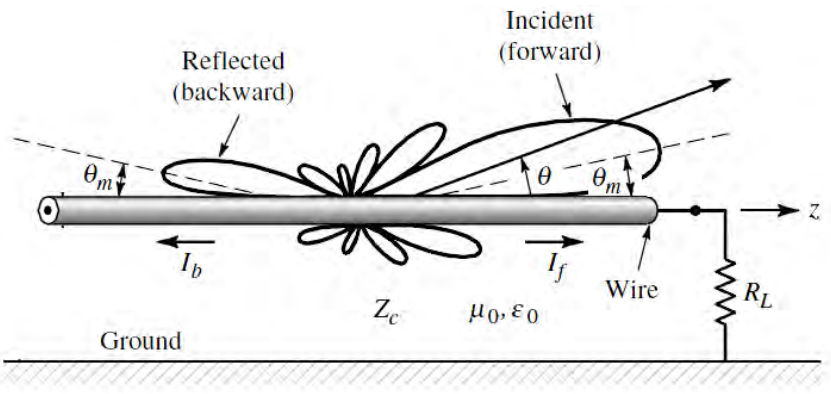

Fig. 2.4 Long wire above ground and radiation pattern [30]

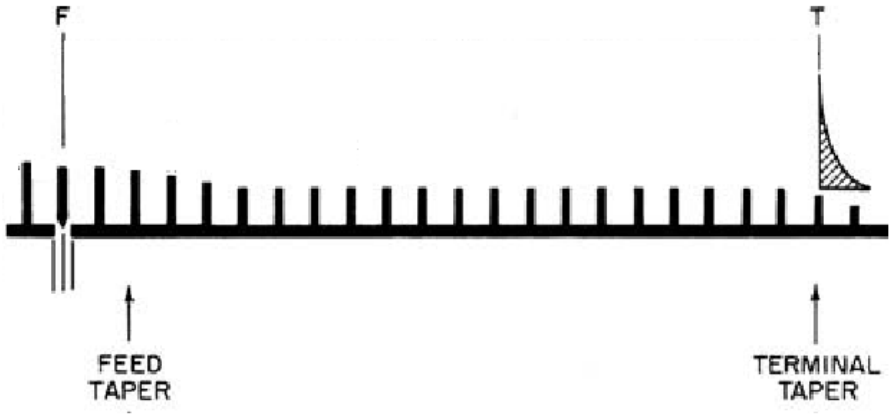

Fig. 2.5 Yagi-Uda monopole array on ground plane [55]

For on-body applications, a few structures have been developed as surface wave antennas [56-57]. In [56] the performance of a higher order mode microstrip patch antenna (Fig. 2.6) in the proximity of the human phantom has been studied at 2.45 GHz. It has been shown that a high path gain in the shadowed channel is achievable by the use of this antenna compared to a conventional microstrip patch antenna operating in the dominant mode. However, the antenna is quite thick (6 mm) which makes it less useful for the on-body devices.

Fig. 2.6 Higher mode microstrip patch structure [56]

Fig. 2.7 shows a cavity backed slot antenna for use on the body, which also operates at 2.45 GHz [57]. This antenna has a low profile and generates a vertically polarised wave on the surface of the body which as reported in the reference can excite a creeping wave around the

human body. However no evidence to support this claim has been provided. This antenna is quite thick for on-body application at 9.6 mm.

Reference [58] describes an artificial magnetic conductor (AMC) above a circular patch antenna to launch a surface wave on the human body (Fig. 2.8). The antenna performance has been evaluated by placing two of them in two opposite sides of the muscle phantom as shown in Fig. 2.9 and simulating the path gain. The path gain of this antenna is almost equal to the antenna reported in [56] and 12 dB higher than a conventional patch antenna. The antenna thickness is 1.9 mm and its width and length are is 136 × 136 mm^2.

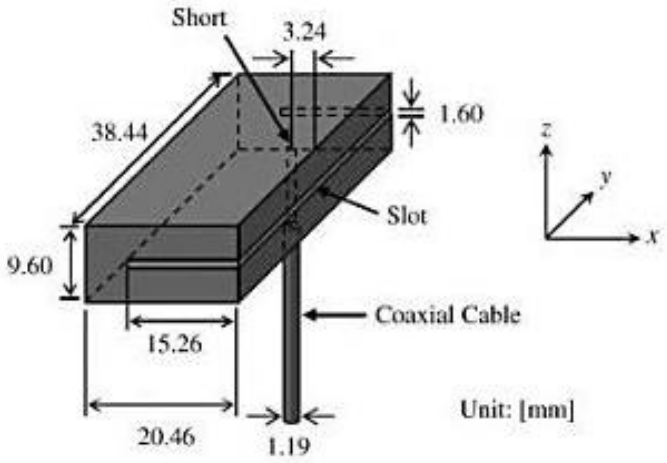

Fig. 2.7 Cavity backed slot antenna [57]

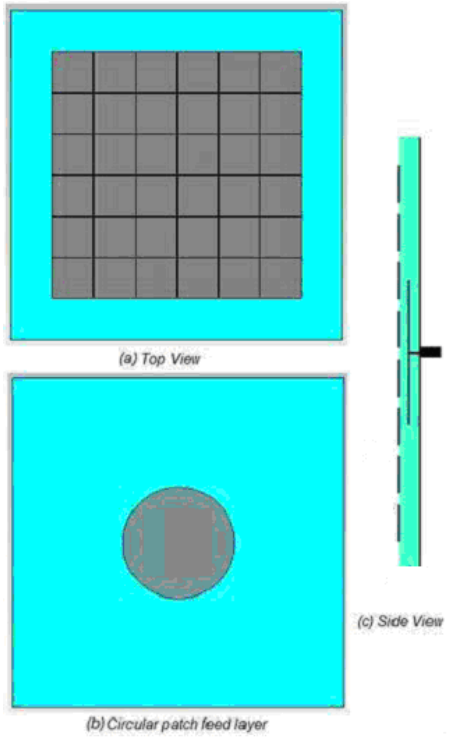

Fig. 2.8 Surface wave AMC patch antenna (SWA) Geometry [58]

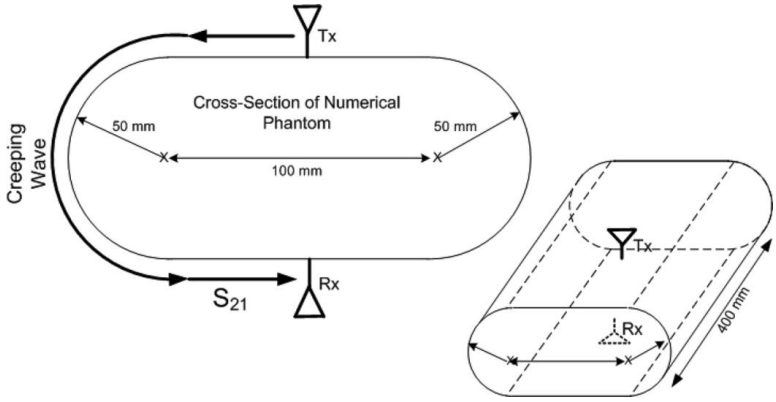

Fig. 2.9 Phantom structure and transmit and receive antenna positions [58]

The antennas discussed above are not very suitable to launch a surface wave on the body due to their significant thicknesses. To integrate antennas into the body worn devices, a much thinner configuration is desired. In this thesis, a design of new thin surface wave antenna for on-body applications is developed and its performance is tested and compared to the conventional on-body antennas.

2.6. MM WAVE FOR ON-BODY APPLICATION

The 5 GHz of unlicensed spectrum around 60 GHz is now being considered for short range wireless communications, opening the door to a new research area for WPAN, WBAN and also Wireless Local Area Networks (WLAN) [59]. At microwave frequencies, control of the energy to the proximity of the body is a serious challenge, due primarily to the limitation in the antenna size for the on-body application. To obtain narrow beamwidths and good radiation control require antennas that are several wavelengths in size. At mm wavelengths, however, antennas with directive beams can have very small size compared to those at microwave frequencies. Such beam control can lower the problem of interference and hence increase the security of WBAN systems. However, on the body channels are shadowed very easily by body movements and, this may be a challenging problem at 60GHz, since at this frequency, diffraction is weak and small movements can prevent communication [60].

Channel characterization in the indoor environment, for example for HD TV distribution, has been performed at 60 GHz [61-69]. In much of this work, indoor line of sight, point to point channels have been investigated. Only in a few of the cases has the temporary obstruction of the channel by human movement been studied. In this shadowed case, the reflected wave from the walls, ceiling and surrounded objectives is considered as the main propagation mechanism. The use of mm-waves for the on-body application is in its preliminary stages and requires considerable investigation to achieve a reliable link. Initial path gain measurements reported in [70] suggests use of many nodes on the body and optimization of their positions is necessary to overcome high attenuation on the body (see Fig. 2.10). In this thesis, application of the 60 GHz is examined on the body and the effect of the shadowing is evaluated.

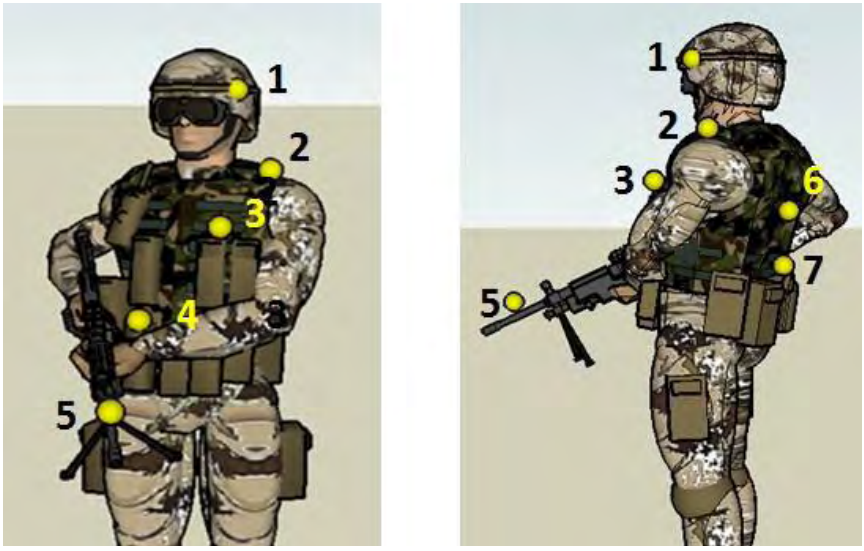

Fig. 2.10 Use of nodes to enable the communication between transmitter and receiver at MM wavelength [70]

2.7. SUMMARY

In this chapter, a summary of research findings in some aspects of on-body antennas and propagation has been presented. It has been found that there are only a limited number of publications available in these topics. Within each section, the discussion has enabled certain hypotheses to be established, which throughout the thesis will be used to guide the work and which are then examined in the concluding chapter.

The hypotheses are as follows:

- Within the on-body transmission channel, the antennas can be de-embedded, to provide the propagation channel description, which then enables designers to establish the transmission channel performance with arbitrary antennas.

- The on-body channel polarisation is significant and behaviour can be investigated by estimating the average power for different polarisation combinations and calculating the XPD values for on-body channels.

- Surface waves are the main propagation mechanism in on-body channels obstructed by the body. The amount of surface wave launched on the body by different practical antennas can be estimated.

- A new planar surface wave antenna for on-body application, which is much thinner than current available designs, can be developed.

- Shadowing is very significant in channels at 60 GHz on the body.

Chapter 3

Antenna De-embedding in On-Body Propagation Channels

3.1. INTRODUCTION

Design of body area network systems would be eased if the antenna could be de-embedded from the channel, thus allowing straightforward prediction of channel performance for novel antennas. However, there are difficulties in de-embedding of the antenna characteristics from the transmission channel. Firstly, it is difficult to know the performance of the antenna on the body, and in particular its radiation pattern. Associated with this is the uncertainty of at which distance to specify the radiation pattern. In conventional mobile communications with the antenna on the body and the base station at a large distance compared to the body dimensions, the radiation pattern of the antenna on the body can be determined at infinity. This is clearly not the case for a body channel. Secondly movement of the body has very large effect on channel characteristics, which are probably more significant than in the mobile channel.

In this chapter, an investigation into antenna de-embedding is discussed. Firstly, the de-embedding procedure is explained and then the propagation channel parameters are estimated from measured data for two on-body channels namely, belt to chest and belt to head.

3.2. DE-EMBEDDING ANALYSIS

The de-embedding can be investigated by examining a simple description of a channel. The transmission channel is considered to be from one antenna port to the other and the propagation channel to be from some interface close to the antennas defined in a way to isolate the antennas from the propagation effects. In such a simple model, the transmission channel path gain, T, is given in terms of the gains, G, of the two antennas and the propagation channel path gain, P, by

$$T = \begin{bmatrix} G_{\theta} & G_{\varphi} \end{bmatrix} . \begin{bmatrix} P_{\theta\theta'} & P_{\theta\phi'} \\ P_{\phi\theta'} & P_{\phi\phi'} \end{bmatrix} . \begin{bmatrix} G_{\theta'} \\ G_{\phi'} \end{bmatrix} \quad (3\text{-}1)$$

where G_{θ} and G_{φ} and $G_{\theta'}$ and G_{φ}' are the gains in the θ and φ directions of antenna 1 and 2 respectively in Fig 3.1. It should be noted that two sets of coordinates are involved, θ and φ, and θ' and φ', at the transmit and receive antennas, which are defined with respect to the body surface normal at the two positions. The selection between these two systems may change during the body movement. $P_{\theta\theta'}$ and $P_{\varphi\varphi'}$ represent the coupling through the propagation channel of the antenna fields in the θ and φ directions respectively, and $P_{\theta\varphi'}$ and $P_{\varphi\theta'}$ represent depolarization within the channel. In principle, knowledge of the antenna performance could be combined with known propagation channel data, to allow the performance of a new transmission channel with new antennas to be determined.

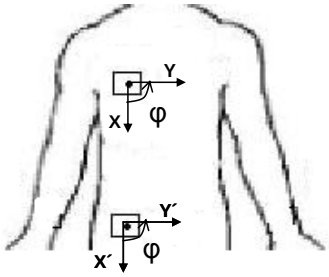

Fig. 3.1 Antenna orientations at belt-chest channel on the human body

In free space one would expect that $P_{\theta\theta'} = P_{\varphi\varphi'}$ and $P_{\theta\varphi'} = P_{\varphi\theta'} = 0$. However for antenna on the human body in a local scattering environment, these approximations are not valid and this formulation thus involves significant problems. For example, the boundary conditions on the body suggest that the propagation coupling coefficients for the two polarizations will have different values. The body curvature and local scattering also suggest that depolarization in the propagation channel will be significant. Multipath propagation also means that the coupling coefficients will involve propagation in a variety of directions, related to the ray bundle directions, and that the antenna gains must include the gains in those various directions. It is also necessary, in general, to characterise the channel for the body in a variety of postures, to obtain fully representative channel models, as is done in the sections above. However in that case, equation (3-1) becomes time variant, leading to the need to solve it statistically. This problem has to some extent been handled in mobile propagation studies by the use of mean effective antenna gain [32], but this is limited because knowledge of the ray statistics is required, thus rendering it difficult to use.

To enable some progress to be made for the on-body channel, some approximations are now made that allow the de-embedding process to be discussed, and a solution to be derived and assessed. Firstly a single body posture is assumed, and equation (3-1) becomes time invariant. Secondly a single ray is assumed, which allows using the single antenna gain value

at the direction of the assumed ray. De-embedding then involves solving equation (3-1) for a known antenna, to obtain the propagation channel coefficients. Antennas that are strongly polarised in the two θ and φ directions would be ideal to separate the coefficients. However, as will be explained in chapter 4, the polarization and the radiation pattern of the antenna may change by placing the antenna in proximity to the body. Indeed, these changes are considered to be part of the antenna to propagation mode coupling mechanism. Because the propagation channel parameters cannot be measured independently, verification of the process can only be made by comparing the coupling coefficients from different antennas or by the same antenna oriented in different directions.

3.3. MEASUREMENTS

Channel measurements were made on a 160 cm height and 54 kg female inside an anechoic chamber. The transmit antenna was fixed on the right side of the belt, 100 mm away from the body centre line and the receiving antenna on the right side of the chest and at the right side of the head. The distance between the body and the antennas placed on the body is around 5-7 mm including the clothing. The coaxial cables are fixed in a way to reduce the coaxial cable effect during the body movement. A vector network analyzer (VNA) set to a time sweep at 2.45 GHz, was used to transmit and receive. The noise floor for the measurement was at -78 dBm. A total of 1601 points were collected for one sweep of 12 s duration for a static posture. It was noticed that, even inside the chamber, there are some reflections from the walls which influence the measurement results when the signal is weak. To minimize the multipath effect and improve the experiment accuracy, some movements such as walking slowly on solid absorber blocks were considered and the collected data averaged out to eliminate the multipath.

3.3.1 Belt to Chest channel

In the belt to chest channel, the antennas are in line of sight (LOS) of the each other and this makes the de-embedding process straightforward. Since choice of the best antennas for de-embedding is crucial, the measurements with different antennas are reported and propagation channel values are compared with each other to draw a conclusion for future measurements.

3.3.1.1 Single Antenna Pair Method

In the measurements described here, changes in antenna orientation were used to change the transmission channel path gain. Two shorted quarter wavelength patches, shown at Fig. 3.2 and operating at 2.45 GHz, were used. These were chosen because they are relatively small and have high co-polarization in the one of the principle planes and high cross in the other, and thus may allow the various components of the propagation channel path gain to be estimated. The two antennas had the dimensions as shown in Fig. 3.2.

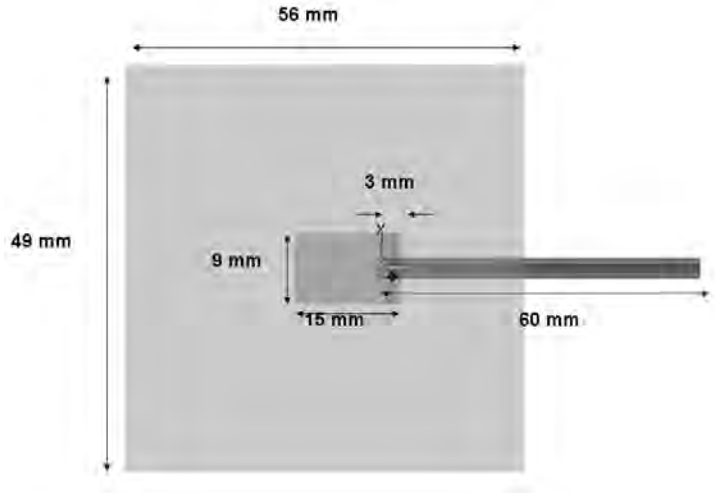

Fig. 3.2 Quarter wavelength patch antenna,
(Top plate located 5 mm away from the ground plane)

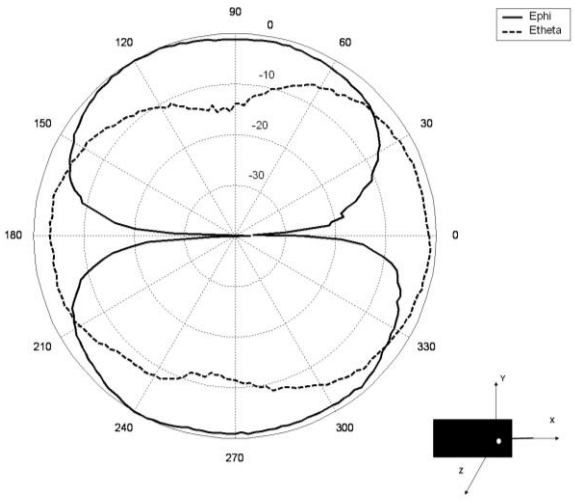

Fig. 3.3 Normalised radiation pattern in free space of the shorted quarter wavelength patch in the XY Plane (solid = E_{φ}, dotted = E_{θ})

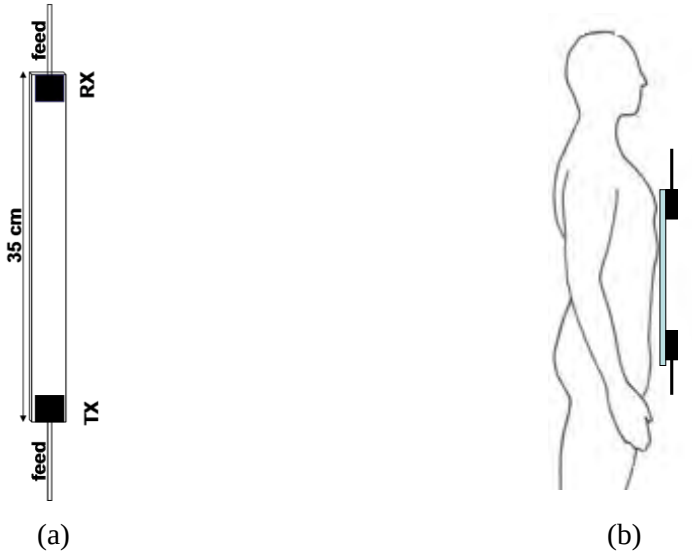

(a) (b)

Fig. 3.4 (a) Antenna mounting frame, (b) Frame on the human body posture

Fig. 3.3 shows the free space radiation patterns in the plane of the ground plane of one of these antennas. The other antenna has similar patterns. There are different directions in which the radiation is either polarised in the θ direction (normal to the body surface) or φ direction (parallel to the body surface), thus enabling extraction of the various propagation coefficients. They also have large differences in gain in various directions, which suggests that they would be useful to estimate the errors in the de-embedding process.

In the de-embedding experiment the antennas were placed close to the body with their ground planes parallel to the surface in the positions shown on Fig 3.1. An external plastic frame shown in Fig. 3.4 was used to locate the antennas in a repeatable way, both in distance apart and orientation. This belt to chest channel was chosen to simplify the processing, as the antennas were in the same plane, and hence $\underline{\hat{\theta}} = \underline{\hat{\theta}}'$ and $\underline{\hat{\phi}} = \underline{\hat{\phi}}'$. Various antenna gains and polarizations were obtained by orienting the antennas at φ = 0º, 90º, 180º and 270º. Measurement of transmission channel path gain, T, with the antennas on the body were taken. From the 4 orientations of each antenna, 16 values of T were obtained. equation (3-1) can be developed to give equation (3-2)

$$T = G_{\theta}G_{\theta'}P_{\theta\theta'} + G_{\theta}G_{\varphi'}P_{\theta\varphi'} + G_{\varphi}G_{\theta'}P_{\varphi\theta'} + G_{\varphi}G_{\varphi'}P_{\varphi\varphi'} \qquad (3\text{-}2)$$

Then it can be rearranged as

$$T = \begin{bmatrix} G_{\theta}G_{\theta'} & G_{\theta}G_{\phi'} & G_{\phi}G_{\theta'} & G_{\phi}G_{\phi'} \end{bmatrix} \begin{bmatrix} P_{\theta\theta'} \\ P_{\theta\phi'} \\ P_{\phi\theta'} \\ P_{\phi\phi'} \end{bmatrix} \qquad (3\text{-}3)$$

Table 3.1 shows the values of T and the gain products for the case where one antenna is fixed in the φ = 0º orientation and the other is rotated through the φ’ = 0º, 90º, 180º and 270º orientations.

The 16 equations with 4 unknowns resulting from (3-3) were solved simultaneously by use of the *lsqnonlin* function in Matlab, which is based on a least square method and the results are shown in Table 3.2.

Table 3.1 Transmission channel path gain and antenna gain products for one fixed and one rotated antenna

φ (deg)	φ' (deg)	T (dB)	$G_{\theta}.G_{\theta'}$ (dB)	$G_{\theta}.G_{\varphi'}$ (dB)	$G_{\varphi}.G_{\theta'}$ (dB)	$G_{\varphi}.G_{\varphi'}$ (dB)
0	0	-48.1	-21.7	-39.6	-44.7	-62.6
0	90	-58.0	-29.8	-24.2	-52.8	-47.2
0	180	-46.9	-21.6	-45.6	-48.4	-68.6
0	270	-56.1	-31.6	-22.3	-54.5	-45.3

Table 3.2 Propagation channel path gain obtained from measurements of transmission channel and free space antenna patterns [free space loss is -31.1 dB]

P matrix component	Least Square Method
$P_{\theta\theta'}$	-24.7
$P_{\theta\varphi'}$	-49
$P_{\varphi\theta'}$	-35
$P_{\varphi\varphi'}$	-39

It can be seen that the value of $P_{\theta\theta'}$ is highest. This might be expected by considering propagation along the human body, as the θ direction is normal to the body surface and is the polarization best supported by the space and surface wave. The free space propagation channel gain for this distance is -31.1 dB. The other P components are all smaller by at least 11 dBs, and the $P_{\varphi\varphi'}$ component is lower than one of the depolarization terms. The two depolarization terms are not similar, and this might be expected from the lack of symmetry of the body surface which affects the antennas at the transmitter and receiver side differently. It is worth adding that, multipath ray effects are not considered in equation (3-1). In general, to extract P values precisely, the multipath rays must be considered in the formulation given in (3-1). However, a large number of measurements with different antenna orientations and

polarisations will be required to achieve this. Furthermore, the free space gain is used in this equation, thus any change in the gain of the antenna is included in the P matrix.

It is expected that the $P_{\theta\theta'}$ component is the most accurate, as it is the strongest, and the effect of the errors induced by non-line of sight multipath propagation and changes in the postures during orientation changes, will have the least effect. The path gain is weak for other P components and can make them prone to the multipath from the environment and radiation from the cables.

The results of one set measurements are given above but the measurements were repeated of the order of 10 times to achieve consistent results. The transmission channel could change from few dBs to 15 dB. The radiation from the cable is one of the major problems. Rotating of the antennas to collect the required data to extract P values requires a change in the position of the coax cable. Varying the orientation of the cable and bending them can change the measurement result. Observation showed that the cable should be kept as far as possible from the channel measurement and they should be kept fixed during the measurement.

3.3.1.2 Well Polarised Antenna Method

As described above, two shorted quarter wavelength patches operating at 2.45 GHz, were used to do the first set of measurements. The free space gain is used to extract P values. These measurements were carried out several times and each time the equations were solved and P values extracted. The results were inconsistent and not repeatable. As explained earlier, rotating the antenna may cause some errors in the measured path gain. To tackle the problem, antennas with different polarizations, oriented with their peak gain toward each other were used in the measurements. This meant that there was no need to change the orientations of the antenna in order to obtain the desired polarization states. To derive P values, described in Section 3.1, small top loaded monopoles, planar inverted F antennas, (PIFAs), loops and

dipoles were used. Path gain was measured with identical antennas, for example, monopole-monopole or loop-loop, to extract co-polarised P values. Also mixture of antennas with orthogonal polarizations for example monopole-loop and loop-monopole, to extract cross-polarized P values. Data was gathered four times for one channel by substituting antennas 4 times at the transmitter and receiver. Fig 3.5 shows these antennas, which had the following dimensions.

Monopole:- *ground plane dia = 40 mm, top loading dia = 26 mm, height = 18 mm, wire dia = 5 mm*

PIFA:- *ground plane (grey) = 40 mm × 20 mm with full metallisation on underside and feed strip (black) of width = 2mm, top plate (black) = 20 mm × 12.2 mm of height = 5mm, short 1mm from lower left hand corner of top plate, feed 2 mm from short.*

Loop:- *substrate of 0.8 mm thick FR4, size = 40 mm × 53 mm, with ground plane metallisation on underside of size (grey) 10 mm x 40 mm, loop dia = 30 mm, loop angle = 350º, strip width = 1 mm, feed and short-circuit length = 10 mm, spacing = 5 mm.*

Dipole:- *substrate of 0.8 mm thick FR4, size = 40 mm × 40 mm, with ground plane metallisation on underside of size (grey) 20 mm x 40 mm, dipole length = 40mm, dipole width = 3mm at centre, = 8 mm at ends, dipole end loading length = 8mm, feed length = 14 mm to dipole lower edge, width = 3 mm.*

As explained earlier, the free space gain of the antennas at the plane in which the antenna is placed parallel to the body surface is used to determine the P values. The gains of the antennas were measured by the three antenna methods. The antennas, monopole, PIFA and

Loop, are placed at the same distance that they were supposed to be mounted on the body and path gain measurements were then done inside the anechoic chamber. Since the P values are known in the free space for a certain distance by use of the Friss formula ($P_{\theta\theta'} = P_{\varphi\varphi'} = -31.5$ dB and $P_{\theta\varphi'} = P_{\varphi\theta'} = -\infty$ dB), 6 nonlinear equations with 6 unknown given in (3-4) were solved and the value of the gains for the theta and phi component were extracted. The dipole gain was easily derived with just one measurement, since the other antenna gains were known.

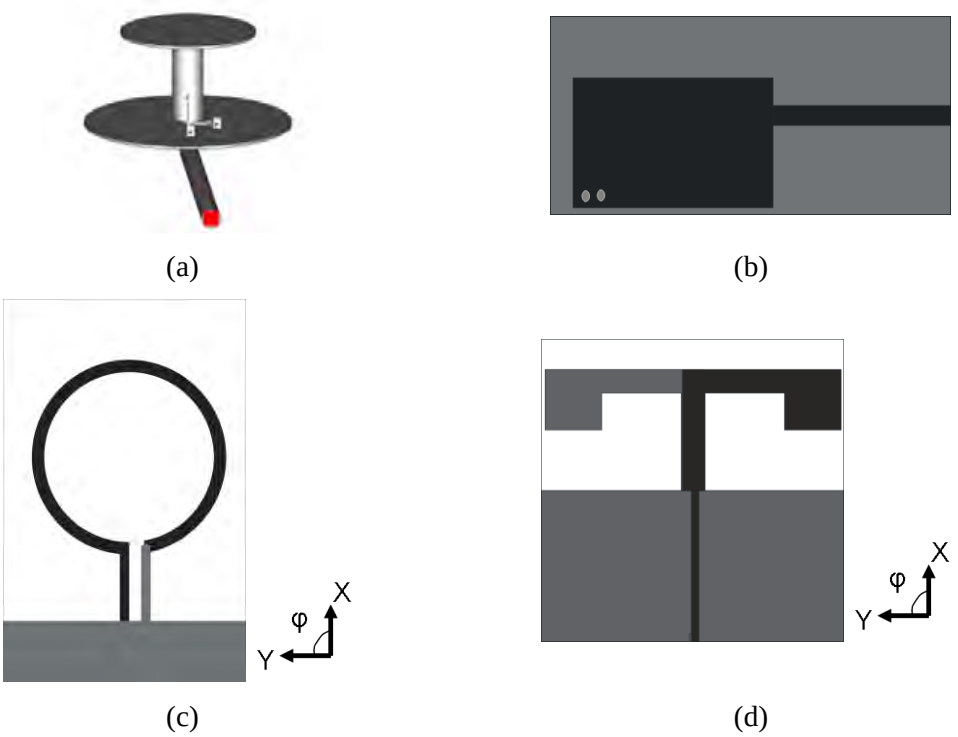

Fig. 3.5 Antennas used for derivation of statistical models
(a) top loaded monopole, (b) planar inverted F antenna, (c) loop, (d) dipole

$$\begin{cases} T_1 = G_M^T \cdot P \cdot G_M^R \\ T_2 = G_M^T \cdot P \cdot G_L^R \\ \quad\vdots \\ T_6 = G_P^T \cdot P \cdot G_P^R \end{cases} \tag{3-4}$$

Table 3.3 Gain of antennas in free space in the XY plane

Antenna	G_θ (dBi)	G_φ (dBi)
Monopole	-0.3	-22.9
Loop	-91.4	-2.8
PIFA	-5.6	-18.1
Planar Dipole	-20.0	0.0

A. Experiment 1

As an initial experiment, 6 combinations of monopole, loop and PIFA antennas including, Loop-PIFA, Monopole-PIFA, Loop-Loop, Monopole-Loop, Monopole-Monopole, Loop-Monopole, were used in the belt to chest link. Each measurement done with one of the combinations can be expressed as equation (3-3). Therefore, 6 different equations with 4 unknowns were available. To calculate the 4 unknowns, it was necessary to have only 4 equations. These four equations can be chosen from the 6, thus 15 sets of equations were solved by a direct elimination method instead of solving them simultaneously by the least square method. The results of some sets of equations were unreasonable, for example, negative values for the propagation channel as a number or they were much weaker or stronger than expected. Investigation of the equations showed that those equations were ill conditioned. An ill-conditioned matrix is one where the solution to **Ax=b** is overly sensitive to perturbations in **A** or **b**. To evaluate the condition of the matrix, a condition number is used. The condition number can be defined as the rate at which the solution, **x**, will change with respect to a change in **A**. Thus, if the condition number is large, even a small error in **A or b** may cause a large error in **x** (ill conditioned). On the other hand, if the condition number is smaller then the error in **x** will not be much bigger than the error in **A or b** (well conditioned).

According to the results and conditions of each matrix, it was concluded that to have proper results, it is necessary to do the measurement with a specific combination of antennas. To determine the condition of each matrix, the *cond* function in Matlab was used. Smaller

value of the condition number implies the well-conditioned property of the matrix. The most well conditioned matrix yields the condition number of 1. For example to extract $P_{\theta\theta}$, both the transmitter and receiver should be polarised strongly in the theta direction. Among the 15 sets of equations with different antenna combinations, just 4 of them gave acceptable results. Table 3.4 shows some antenna combinations which demonstrate the well and ill conditioned results. The condition number of each group is also provided. The well conditioned results combination includes monopole-monopole, monopole-loop, loop-monopole and loop-loop. The condition number of this group is 76. At each combination, the first antenna is the transmitter which is placed at right side of the belt and the second one is the receiver placed at the right side of the chest. In fact, if one notices the orientation of the polarization of each combination, it will be obvious that each of them produces one of the elements of the propagation matrix. For example, Monopole-Monopole produces $P_{\theta\theta}$ or Loop-Loop produces $P_{\varphi\varphi}$, etc. Ill conditioned combinations are Loop-PIFA, Monopole-PIFA, Loop-Monopole, Loop-Loop. Loop-PIFA and Loop-Monopole are supposed to provide the information for the cross polarization values, $P_{\varphi\theta}$ and $P_{\theta\varphi}$, but in spite of using different antennas both combinations produces $P_{\varphi\theta}$. There is no also combination representative of $P_{\theta\varphi}$. The condition number of this group of antennas is 1.24e+17 which is much higher than the well-conditioned group number. Therefore, the ideal methodology for de-embedding is to choose two antennas with well defined orthogonal polarizations and high gains and make four measurements on the body and solve by solution of simultaneous equations, or least squares solution.

Table 3.4 P matrix components for monopole, loop and PIFA combinations in belt to chest channel

P Matrix Component	Well Conditioned Results Monopole & Loop (Condition number = 76)	Ill Conditioned Results Monopole & Loop& PIFA (Condition number = 1.24e+17)
$P_{\theta\theta}$	-37.2	-35.3
$P_{\theta\varphi}$	-45.7	-inf
$P_{\varphi\theta}$	-46.4	-49.4
$P_{\varphi\varphi}$	-53.8	-inf

B. Experiment 2

In this experiment, the loop antenna was replaced with the planar dipole antenna which radiates the same polarization but with higher gain. To extract P values of the belt to chest link, the measurements were carried out on the male and female. Both the transmitter and receiver are mounted on the right side of the body as shown in Fig. 3.1. Four measurements with monopole and dipole combinations were taken. Then, the monopole antenna was substituted by a PIFA and the measurements were repeated. On the female and male, the antenna are separated by 35 cm and 38 cm, respectively. The calculated P values based on the measurements are shown in Table 3.5. $P_{\theta\theta}$ shows smaller variation by the change of posture and the antennas. When the monopole is used as a vertical polarised antenna, the P values on the male and female are almost similar, with only $P_{\theta\varphi}$ on the male being slightly higher than female. On the female, the planar antenna located on the chest is partly shadowed by the breast and thus the path gain is smaller. When the PIFA is used instead of the monopole, the results on the male and female are different. As shown in Table 3.3, the gain of the PIFA is almost 5 dB less than monopole and hence the matrix is not as well-conditioned and more sensitive to errors as when the monopole is used.

Table 3.5 P matrix components for monopole, Dipole and PIFA combinations

P Matrix Components	Dipole and Monopole (Female)	Dipole and Monopole (Male)	Dipole and PIFA (Female)	Dipole and PIFA (Male)
$P_{\theta\theta}$	-32.4	-32.6	-31.1	-29.6
$P_{\theta\varphi}$	-60.7	-57.7	-57.2	-61
$P_{\varphi\theta}$	-52.2	-52.2	-58.8	-58.3
$P_{\varphi\varphi}$	-67.2	-67.3	-67.1	-63.9

3.3.2 Belt to Head Channel

In the previous results, the belt to chest channel was examined and the de-embedding values were extracted by the use of the several antenna combinations and it was shown that the best way to extract P values is the use of the antennas with orthogonal polarization. Dipole and monopole antennas generally provided more consistent results. Therefore, they were also used to extract P values for the belt to head channel. In this channel, the transmitter is placed at the right side of the belt and the receiver is at the right temple, as shown in Fig. 3.6. The dipole is oriented along Y- and Y'- axis parallel to the body surface. Also, the monopole antenna ground plane is parallel to the body surface and the antenna is oriented normal to the body surface at the belt and head. This channel is dynamic in that the head position determines the relative transmitter and receiver antenna orientations. In addition, the antenna located at the head can be shadowed by head movement.

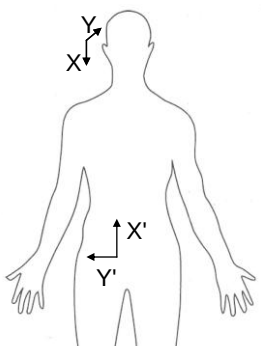

Fig. 3.6 Antenna orientations in belt-head channel on the human body

In this experiment, five different positions of the head are considered and are referred to as looking at left (1), forward left (2), forward (3), forward right (4) and right (5). The experiments were repeated on different days, twice each on the female and male inside the anechoic chamber. P values are calculated for each head position individually by the method that was explained earlier and results are shown in Fig. 3.7. The repeated measured data was very similar to the initial measured data. When the head position is 1, similar antennas in two ends of the channel are co-polarised, $P_{\theta\theta}$ and $P_{\varphi\varphi}$ have their maximum values. By rotating the head to position 3, that is looking forward, the antennas are oriented perpendicular to each other and the P values decrease. By moving the head to the right side, position 4 and 5, the antennas become shadowed and the signal decreases further. The change in $P_{\theta\theta}$ is more than 25 dB. In general, $P_{\varphi\varphi}$ is smaller than $P_{\theta\theta}$ by 15 to 20 dB. The results for the female and male are very close to each other.

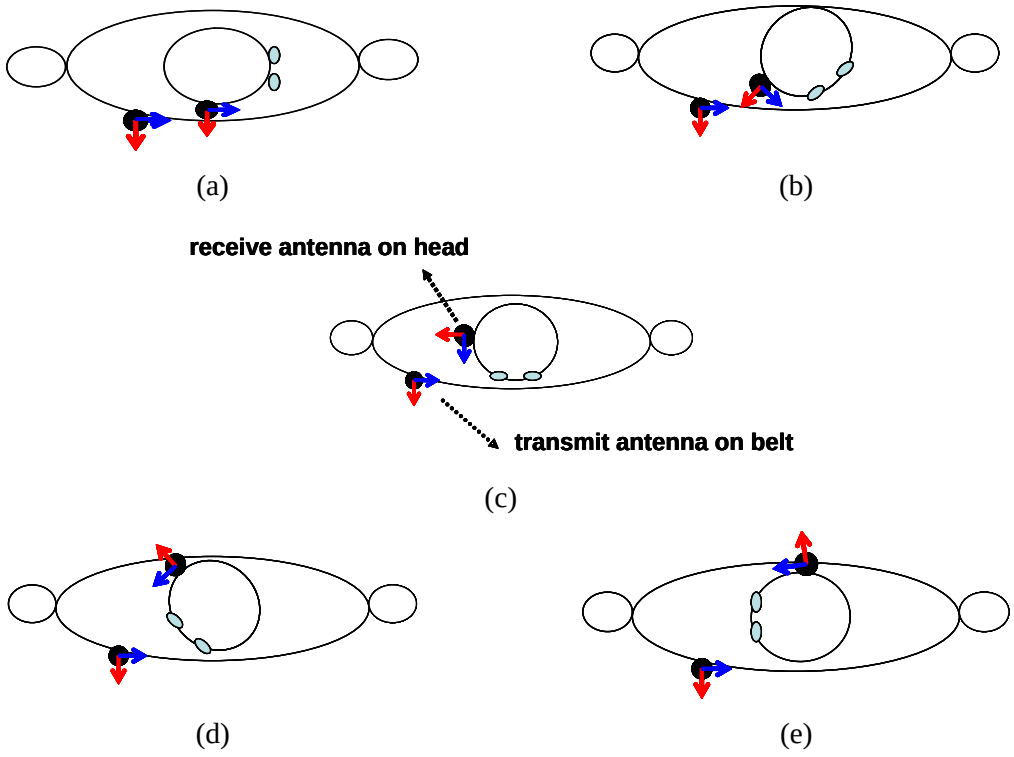

Fig. 3.7 Head positions, (a) looking left, (b) looking left forward, (c) looking forward, (d) looking right forward, (e) looking right

Cross polarization components, $P_{\varphi\theta}$ and $P_{\theta\varphi}$, have a maximum value at position 3, in which antennas with orthogonal polarization are oriented in co-polarised manner. These values on the male and female are different.

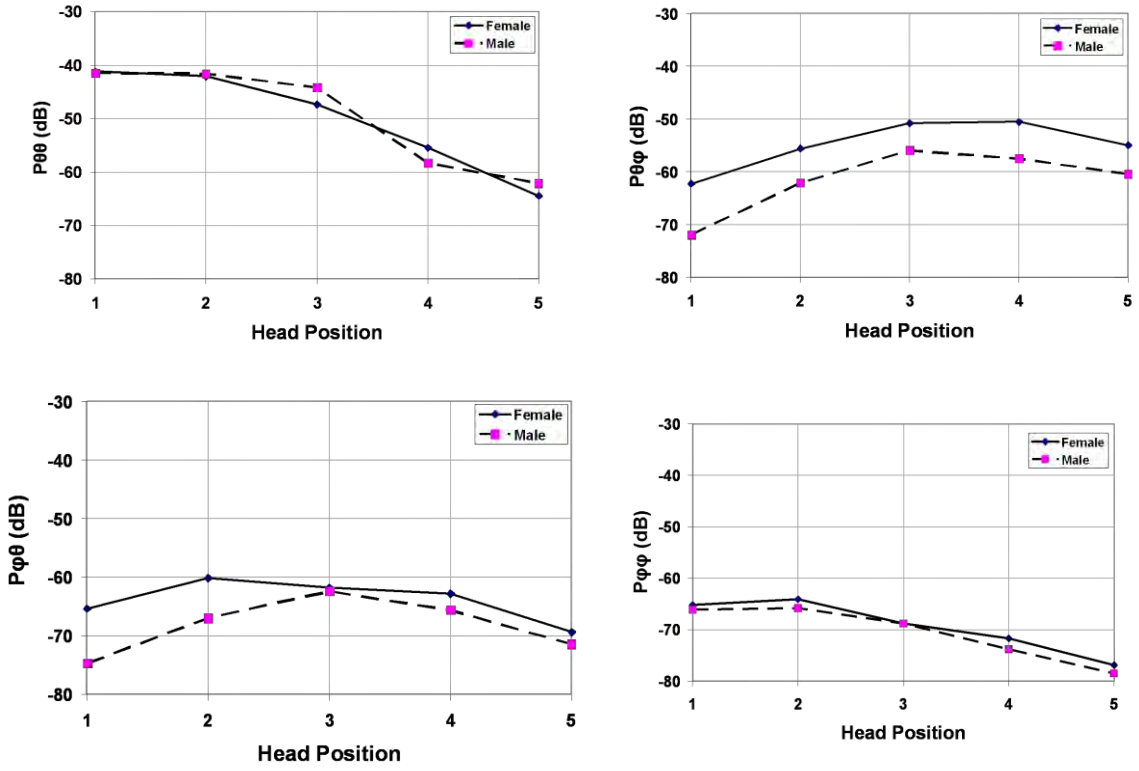

Fig. 3.8 Propagation channel values obtained from measurements of transmission channel on the belt-head,

Looking at (1: left, 2: forward left, 3: forward,4: forward right and 5:right)

3.4. SUMMARY

In this chapter the de-embedding of the antenna from the transmission channel on the human body was examined to determine the propagation channel values. It was shown that if antenna de-embedding is to be performed, determination of the complete set of channel components is needed. This must be done using carefully chosen antennas that allow stable solution of the channel equation. For the channel on the trunk of the body, it is clear that the

effect of antenna gain changes may be predicted from de-embedding using free space patterns, to an accuracy of a few dBs for the dominant $P_{\theta\theta}$ component. For the other components the errors can be much larger. Also, the de-embedding was examined on the belt to head channel. Propagation channel path loss values were provided for different head positions and it was shown the propagation channel changes significantly with the head movements. Furthermore, this method is not reliable when strong multipath rays are present in the channel due to the discounting the spatial antenna radiation pattern in the model. Hence, use of this simple method for the movements is not a proper approach and de-embedding should be done as an ensemble of postures, and a statistical description is needed.

The results presented in this chapter have been largely judged on the stability of the matrix inversion process and their repeatability. On this basis, the component $P_{\theta\theta}$ can be obtained well for static channels or for those with limited movement. As this component is much larger than the others, it is clear that prediction of the transmission with other antennas that are well polarised normal to the surface will be successful, despite this not being done explicitly in this chapter. The results given in chapter 4 show that in this case the transmission channel gain can be well estimated from free space measurements of a given set of antennas knowing their efficiency when placed on the body. This appears to support the conclusion for de-embedding. However, the de-embedding process is difficult in that it requires well polarised antennas and precise placement on the body. It is estimated that a given body posture cannot be duplicated within a few centimetres for some parts of the body. In general, either in free space or on the body, to derive the P matrix, the right antenna combinations must be selected. In particular, matrix instability can occur if antennas having polarisations not close to orthogonal are chosen, whether in free space or on the body. It was found that many of the measurements sets resulted in ill conditioned matrices, and it is therefore concluded that de-embedding of channels on the human body is not likely to be useful in channel design in the foreseeable future.

Chapter 4

On-Body Channel Polarization

4.1. INTRODUCTION

Understanding of depolarization in the channel is useful in allowing optimized wearable antennas to be designed, and also informs the performance of the channel when non-optimum antennas are used due to the higher importance of other factors, such as available space for the antenna or the need to design down to a cost. An associated issue is that of de-embedding the antenna from the channel, which is desirable to allow simplified prediction of channel behaviour when new antennas are used. As it explained in chapter 3, there are major difficulties in doing this. For example, the gain pattern and polarization of the antenna must be known and it is not clear at what distance from the antenna this should be determined. In other words, the far field region condition ($2D^2/\lambda$) may not be applicable on the body. When the antenna is close to the body, it induces some current in the tissue, which will then change the largest dimension, D, of the radiator, or in this case the radiating currents, which is used to define the far field region. Hence, the far field region on the body may be further away than in free space. In addition, body movement has been shown to be very important factor determining channel behaviour, and hence de-embedding should be done as an ensemble of postures, and this further complicates the de-embedding process. Therefore, in the light of

these difficulties, the characterization of channel depolarization may give some insight of the underlying processes at work in on-body channels.

In this chapter, section 4.2 to section 4.5 describes characterization of the transmission channel, for differently polarized transmit and receive antennas, and for different channels. In section 4.3, this is done using simulation with simplified antennas to reveal the underlying mechanisms. In section 4.4 a novel dual polarized antenna is described and the measurement results with this antenna are given in section 4.5. The mean power and cross polarization discrimination are determined, and statistical processing is performed and the ratio of the strongest ray to the scattered ray is presented for different antenna combinations for each channel. Also, the measured polarization diversity performance of on-body communication channels at 2.45 GHz is reported in section 4.6.

4.2. CHANNEL MEASUREMENT FOR STATIC POSTURES

In this section, the path gains are reported for two static postures. Two channels referred to as belt-head and belt-wrist are measured. These channels are of particular interest, as Bluetooth headsets and wristwatch controllers are available for use with cell phones. Top loaded monopoles for vertical polarization, and planar dipoles for horizontal polarization, were used in the methodology described in Chapter 3. These antennas are referred to as monopole-monopole (MM), monopole-dipole (MD), dipole-monopole (DM), and dipole-dipole (DD). To explore a channel from the polarization perspective, four different combinations of the antennas with the orthogonal polarizations are required. The measurements were repeated four times with different antennas at each end of the channel for every channel. The measurements were done on a static body, but because of the dynamic property of these two channels and sensitivity to head and wrist positions in the head and wrist channels, respectively, measurements were repeated for different postures.

Channel measurements were done on a 160 cm height and 54 kg female in an indoor environment, which was a 7.5 m × 9 m sized laboratory containing equipment, tables, chairs, and computers and also repeated in an anechoic chamber. For comparative purposes, the measurements were repeated on a male with 178 height and 72 Kg weight. The transmitter antenna was fixed at the left side of the belt almost 100 mm away from the body centre line and the receiving antenna was placed at the right side of the head and right wrist. The distance between the body and the antennas placed on the body was around 5-8 mm, including the clothing. The coaxial cables were fixed in a way to reduce the cable effect during the body movement. A vector network analyzer (VNA) with operating at 2.45 GHz was used to measure transmission channel gain (S_{21}). The noise floor for the measurement was about -80 dBm and the transmit power was 0 dBm which results in 80 dB dynamic range. During the measurements, slight movements like walking in a small area or stepping forward and backwards were done to reduce the multipath effect both in the laboratory and chamber. The 1601 data points were collected for 60 second and averaged to eliminate the fading from the data.

The measurements reported in the section are of transmission channel path gain, and hence relate not only to the propagation channel but also to the on-body antenna performance. The results thus relate only to the monopole and dipole type antennas, and not to the transmission channel for different antenna types. Section 4.3 contains estimations of the antenna effects, in an attempt to separate antenna from propagation features in the channel.

4.2.1 Belt to Head Channel

The belt to head channel is one the most interesting channels for the on-body communication applications and due to head movement the received signal can vary

significantly. In this section, five different positions for the head were chosen, which were produced by head rotating from left to right in 45° steps and were named as the left, forward left, forward, forward right and right. Such head rotation (see Fig. 4.1), in addition to the changing of the receiver antenna orientation with respect to the transmitter, can cause shadowing effect. Repeatability was the major problem in the measurements which were repeated several times to achieve consistent results. It was observed that cable movement and bending of the cable very close to the antenna had significant effects on the channel behaviour. To tackle the problem, the braided flexible cable was replaced by semi rigid cable, which has a solid copper outer conductor. This cable can be fixed in a way, that moving the body does not cause significant bending or movements near the antenna. For each head position, four antenna configurations namely, monopole-monopole (MM), monopole-dipole (MD), dipole-monopole (DM), and dipole-dipole (DD) were used to take the measurements. One set of the results measured in the laboratory is shown in Fig. 4.2. The numbers on the horizontal axis are representative of the head position. Also, the noise floor is depicted by a horizontal dotted line in the figure .

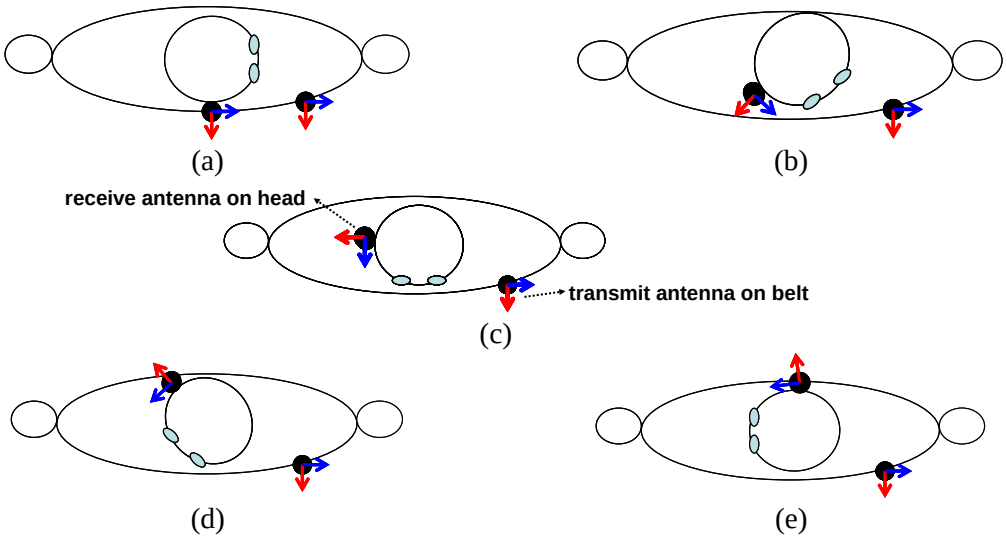

Fig. 4.1 Head positions, (a) looking left, (b) looking left forward, (c) looking forward, (d) looking right forward, (e) looking right

The result shows that the MM combination provides the highest path gain for all the head position except position 5 (looking right) in which the receiver antenna is completely shadowed. When the head is positioned at the forward left and left side, both of the monopole antennas are oriented approximately to the same direction and they are also in the line of sight (LOS) of each other. Looking forward would be expected to yield the lowest path gain for the MM combination, because the antennas are approximately orthogonal. Looking to the right and left side orients the antenna at the transmitter and receiver similarly to each other, but due to the shadowing phenomena at the right side, the path gain falls off significantly. The above reasoning can be also used for the DD combination behaviour at the different head positions which behaves similarly to MM, but lower levels, due to the lower dipole efficiency noted in section 4.3. For MD and DM combinations, the polarizations of the antennas in two ends of the channel are well-matched in the forward position and as shown the maximum mean value is achieved for this position. However, the MD path gain is higher than DM. The reason for this will be explained later. The noise floor which is depicted by a dotted line in the figure reveals that in position 5, the DD path gain falls below the noise and the measured result is not valid.

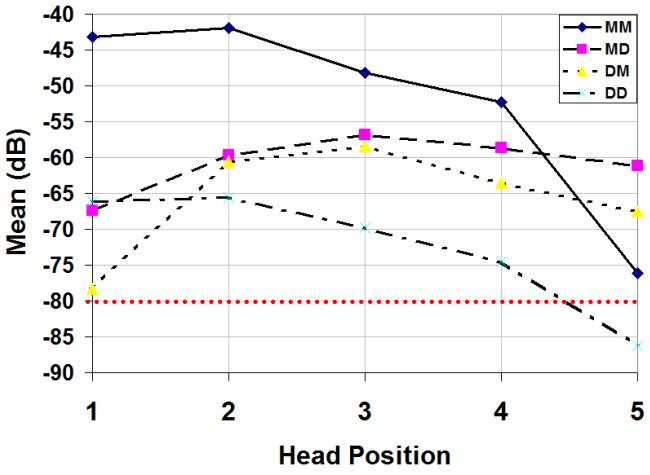

Fig. 4.2 Mean of the measured path gain in belt-head channel in the laboratory for different head positions by use of combination of antennas as monopole-monopole (MM), monopole-dipole (MD), dipole-monopole (DM), and dipole-dipole (DD)
(Head position, X axis: 1: looking left, 2: looking left forward, 3: looking forward, 4: looking right forward, 5: looking right)

To demonstrate the repeatability of the results and also to compare the laboratory and chamber performance, results are shown in Fig. 4.3. For the case of female in the laboratory 1 and 2, average and peak differences are 6 dB and 15, respectively. For the female in chamber they are 5 dB and 13 dB, respectively. One of the problems in repeating measurements is the accurate positioning of the antennas on the body. Fig. 4.3(a) indicates that the repeatability of the monopole antennas was better than the other cases, presumably due to the lower sensitivity of the monopole antenna to it distance from the body surface. In addition, the weaker signal is more likely to show non-repeatable performances because small changes in antenna positioning, and cable position and body posture variation have an increased effect on the signal.

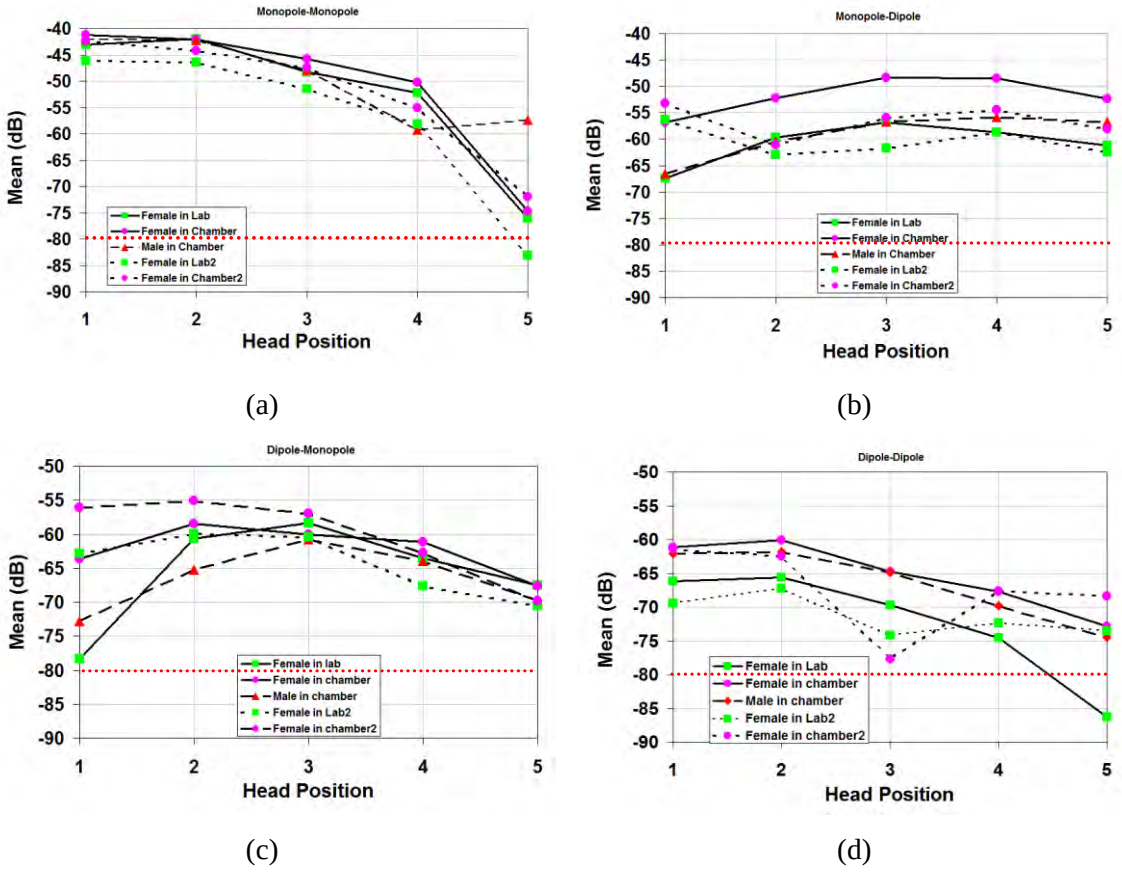

Fig. 4.3 Comparison of the Mean values for the belt-head channel, (a) MM, (b) MD, (c) DM, (d) DD (1: looking left, 2: looking left forward, 3: looking forward, 4: looking right forward, 5: looking right)

4.2.2 Belt to Wrist Channel

In this channel, the transmitter and receiver have been mounted on the right side of the belt and outside of the left wrist, respectively. On the wrist therefore, the back of the antenna faces the transmitter. Because of that, the channel is shadowed more than the belt-head one. Five positions were chosen for the wrists, which represented hand movement during normal walking. Measurements were carried out in the laboratory. The female subject was moving around with the hands kept in one of the positions. Since keeping the hand at the same position during walking is a difficult task, it was necessary to repeat the measurement to attain reasonable results without slow fading. Four different measurements of different combination of the monopole and dipole were done to extract the polarization behaviour for each wrist position.

Fig. 4.4 shows the mean value of S_{21} at each position for different combination of the antennas. The horizontal axis is numbered for the different wrist positions. Number 1 represents the position of hand 20 cm behind of the body, number 2, 10 cm behind of the body, number 3, hanging and number 4 and 5, 10 and 20 cm in front of the body, respectively. The MM combination shows the highest path gain in comparison with the other combinations, except at the 5th location. Hand positions 1 to 3 are shadowed by the body which reduces the received power for all four combinations. By moving the hand to the forward position, the body does not block the path and the received signal improves for all the combinations. When the hand is 10 and 20 cm ahead of the body, the mean value remains constant for all cases except the MM combination, which reduce for the 5th position. As with the belt-head channel, the MM and DD combinations show the best and worst performance, respectively. MD and DM are almost similar and provide higher path gain than DD when the hand is positioned behind the body.

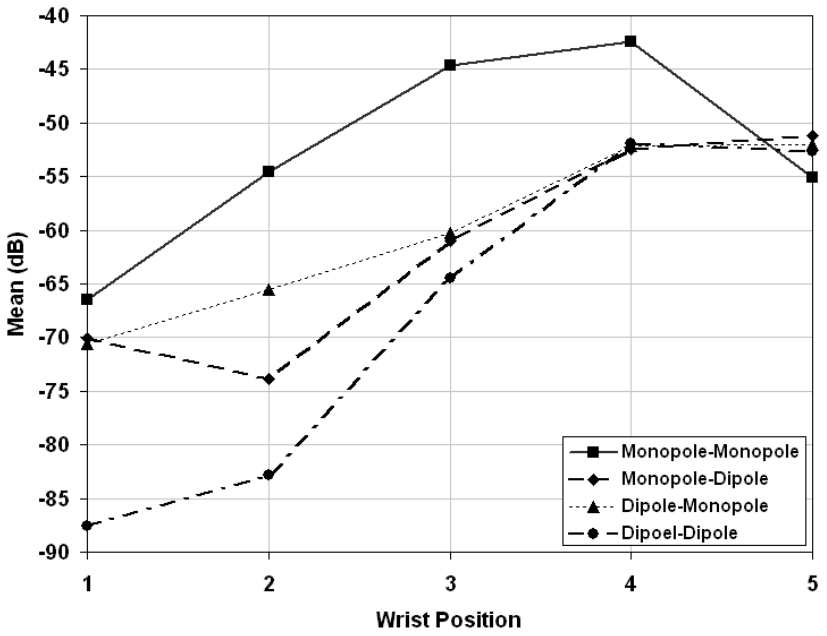

Fig. 4.4 Mean of the measured path gain in belt-wrist channel in the laboratory for different wrist positions by use of combination of antennas as monopole-monopole (MM), monopole-dipole (MD), dipole-monopole (DM), and dipole-dipole (DD)
(1: 20 cm behind the body ,2: 10 cm behind the body, 3: normal, 4: 10 cm ahead of the body, 5: 20 cm ahead of the body)

The results in this section show that the level of the received signal is affected by the antenna choice, and hence polarization and the posture. These results provide useful understanding but it is somewhat difficult to quantify the path gain of each channel based on the static posture as the posture may in general change. To resolve the problem, random movements are considered in a later section. But before this, simulations and analysis were done for small dipoles located very close to the body. The results provide good insight into the problem.

4.3. SIMULATION AND ANALYSIS OF CHANNEL PATH GAIN

4.3.1 Simulation

To explore the polarization behaviour of the transmission channel on the human body, which includes both the antenna and the propagation channel polarization variations, simulations were performed on a static phantom. To reduce the computation time small elementary antennas were used on a homogenous full body phantom in CST Microwave Studio software. Because depolarization is dependent on antenna type, such simplified antennas seemed appropriate for an investigation into underlying mechanisms. Simulations were done with three different tissue types, namely muscle, bone and fat, to resolve tissue type effects on polarization. Whilst, in general, muscle is considered an appropriate approximation for a homogeneous phantom, the others also give useful insights. The electric properties of these tissues are given in Table 4.1. The avatar called James shown in Fig. 4.5 is used as a phantom. James is derived from an animation design software, POSER [71]. The avatar is a male and has a height of 170 cm.

Table 4.1 Electric properties of different tissues at 2.45 GHz

Tissue Name	Conductivity (S/m)	Relative Permittivity
Muscle	1.78	52.67
Fat	0.11	5.27
Bone	0.41	11.352

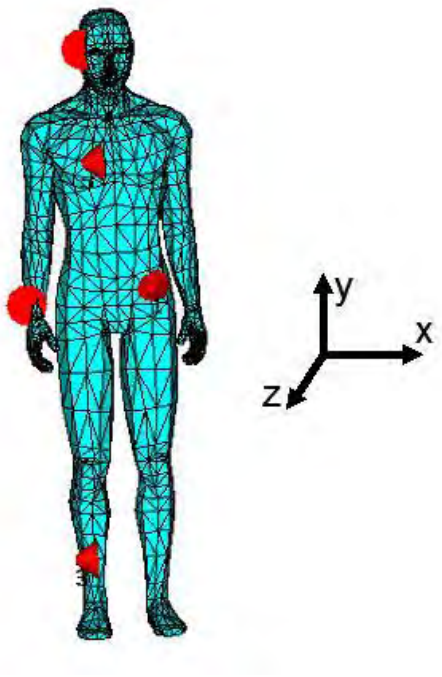

Fig. 4.5 Antenna positions on the body, transmit antenna on the left side of the belt and receive antennas on the right side of the chest, right wrist, right ankle, and right side of the head

The elementary antennas consisted of 2 mm long discrete ports, operating at 2.45 GHz. In CST Microwave Studio software, a discrete port is a current source in the middle of a conducting wire which resembles a dipole antenna. These are mounted 5 mm away from the surface of the phantom which is a typical distance between the antenna and the body surface in the on-body measurements. The transmitter antenna is placed at the left side of the belt and the receivers are put on the right side of the chest, the centre of the back, the right side of the head, the right wrist and the right ankle.

Two different orientations of the short dipoles are used, namely normal and parallel to the body surface, which are referred to as vertical and horizontal in the following. The four different combination results are referred to as vertical-vertical (VV), vertical-horizontal (VH), horizontal-vertical (HV) and horizontal-horizontal (HH), where the first letter is the state of the transmitter antenna, which is located on the belt and the second the receiver state.

The horizontal polarized antenna is oriented along X axis in the all positions on the body except the wrist and the head which is oriented along Z axis.

The simulated path gains (S_{21}) for 5 on-body channels namely, belt-ankle, belt-back, belt-chest, belt-head, belt-wrist, for three different phantom tissues are shown in Fig. 4.6. The values of the transmission channel are low due to the small size of the used antennas and it is the variation amongst the various cases that is of interest here.

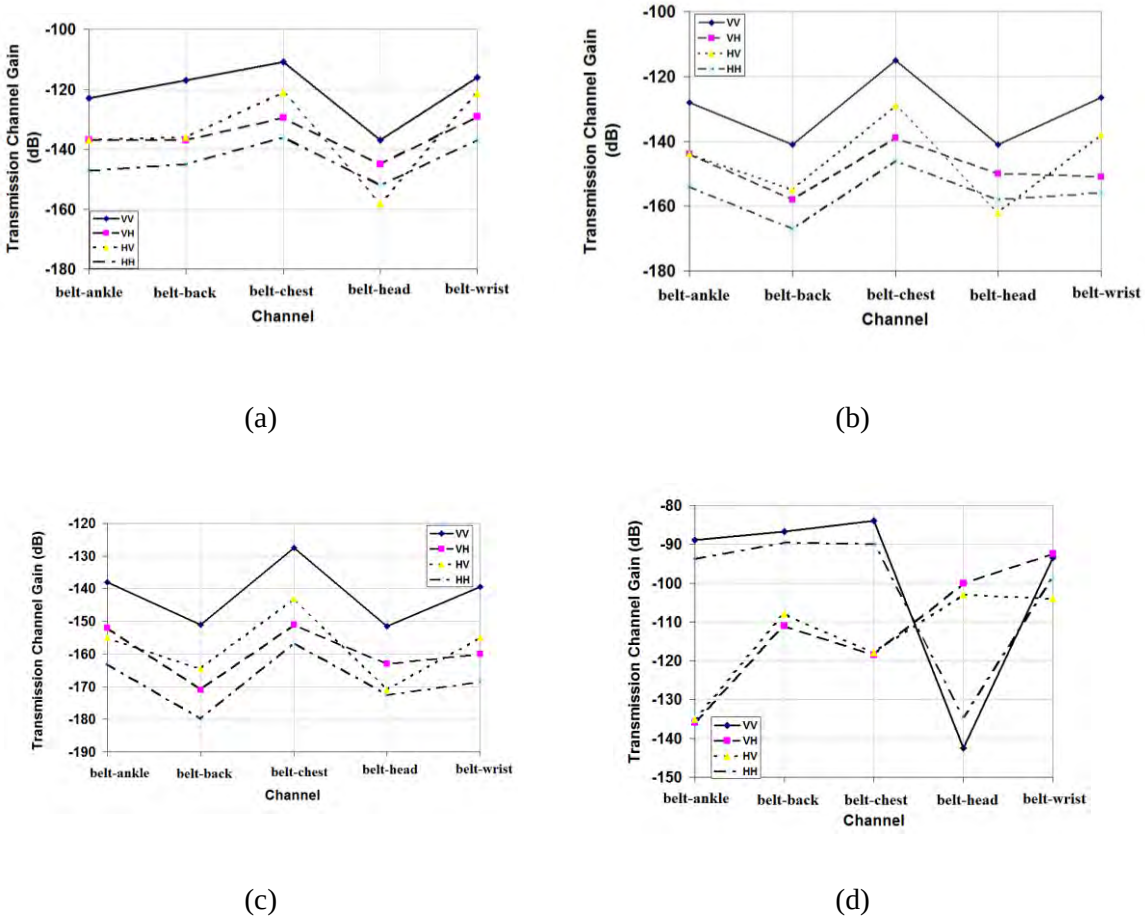

Fig. 4.6 Simulated path gain of different polarization status for different on body channel muscle phantom, (a) fat phantom (b) bone phantom, (c) muscle phantom, (d) free space

From Fig. 4.6, it can be seen that the VV combination provides the strongest link among all the combinations, because the vertically polarized radiator is less affected by the surrounding environment than horizontal one. Also, it benefits from its omni-directional radiation pattern which is very important parameter and reduces the angle dependence of the antenna radiation pattern. Similar to VV, the HH combination uses co-polarized antenna at both end of the channel, but it yields very poor path gain in comparison to three other combinations. In addition to the low efficiency of the horizontally polarized antennas due to presence of the body, which lowers the path gain significantly, the antenna does not radiate equally in different directions. As, both the VH and HV combinations use perpendicular polarizations normal to the surface at one end of each channel, they provide path gain higher than the HH combination. It is worth noting that these two combinations (VH and HV) perform differently from each other, which is an indication of the asymmetrical nature of body channels. The antenna performance is affected by the local environment at each end of the channel which is of course different in all channels. For comparison, Fig. 4.6(d) shows, the transmission channel gain with the phantom removed. As is expected, the co-polarized antenna, VV and HH combination behave almost the same and the difference is due to the radiation pattern effects. The cross-polarized combinations are also similar for all the channels. The slight differences are again just due to radiation pattern differences.

Comparing the results for the three tissue types, Fig. 4.6(a), (b) and (c), shows broad similarities in the variations between the channels. Highest average path gain occurs for fat tissue due to both low ε_r and δ, as noted in Table 4.1, and lowest path gain for the muscle. Comparing the three sets to the free space path gain reveals that there are similarities for the VV and HH cases for the various channels, except for the belt to back when the fat is used. It is assumed the high path gain for VV is due to the possible penetration through the body.

The results shown in Fig. 4.6 only provide a general view on the performance of different polarisation combinations on the body, and they may not be useful to predict path gain in practice, where antennas are relatively large and highly efficient. The small dipole antennas used in these simulations have very low efficiency which lowers the path gain of the order of 100 dB. In addition, these physically small antennas are almost completely obstructed in all the channels by the phantom curvature, while in the measurement on the static body presented in the former section, only the belt to back channel is shadowed and the others are partly or completely in LOS condition.

As a further measure, the standard deviation (STD) of S_{21} for three different tissues at each on-body channel is shown in Fig. 4.7. The higher STD value indicates bigger variation of S_{21} values for different tissue types. As is shown, back and wrist channels for different antenna combinations show high STD in comparison to the other channels. Both of these channels are shadowed and the main propagation mode is through creeping wave which bounds to the surface of the body and possible penetration as noted above. All the combinations except VV which is slightly lower in some channels yield almost the same STD.

It is concluded that antenna type and orthogonal orientation give significant differences in the channel path gain. The following section attempts to quantify the various factors responsible for this.

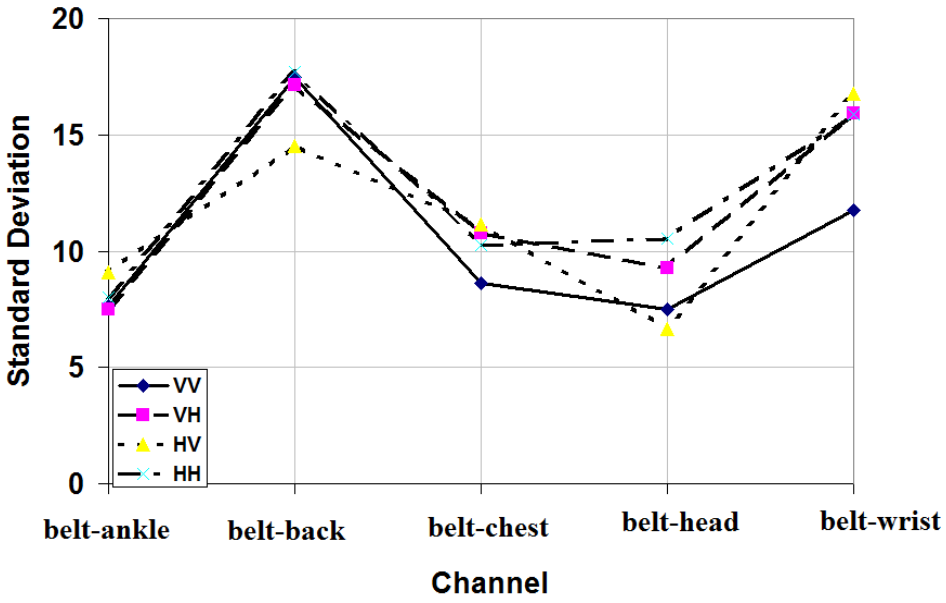

Fig. 4.7 Standard deviation of different on-body path gains for different tissues used in the simulation

4.3.2 Analysis

There are several factors that contribute to channel path gain on the human body. If a single ray model is considered as a first approximation, then the antenna gain in that direction and the propagation channel path length are the main factors. The antenna gain is determined by the efficiency and the directivity which can be derived through simulation or measurement. The path loss in free space, simulated and shown in Fig. 4.6(d) includes contributions due to antenna efficiency and directivity in free space and space path loss. It is further assumed that the directivity on the body is similar to that in free space and that no significant changes in the pattern shape take place when the body is present. An estimate of the transmission channel for the various tissues and antenna orientation can then be made. This is now done, and the approximations used are discussed when conclusions are drawn.

To derive the efficiency and radiation pattern of similar small dipoles to those used in the previous section, they were placed 5 mm away from a phantom box, of size 800 mm × 800

mm made of fat, bone and muscle and simulated in CST Microwave Studio software. The height of the box is varied relative to the tissue type and chosen in such a way that the wave reflection from its bottom side is minimized. For the fat and bone phantom, a height of 200 mm and for the muscle, a height of 50 mm was considered. The simulated total efficiency values for the both horizontal and vertical dipole are given in Table 4.2. Comparing the total efficiency of the vertically and horizontally polarized antenna on the each tissue indicates that changing the polarization can deteriorate the efficiency significantly. For example on the muscle the difference in the efficiency of the two orthogonal polarizations is 13 dB.

Table 4.2 Total efficiency, (η_t), of the horizontally and vertically polarized antenna on different tissues

Material, Dipole direction	Free space	Muscle Vertical	Muscle Horizontal	Bone Vertical	Bone Horizontal	Fat Vertical	Fat Horizontal
Total efficiency (dB)	-28	-47	-60	-41	-50	-38	-45

The radiation patterns of the vertically and horizontally polarized antenna on the muscle phantom and in free space in XY plane are shown in Fig. 4.8. The vertically polarized antenna provides an omni-directional radiation pattern on the body surface with ripple of the order of 1 to 2 dB. The radiation pattern of the horizontally polarized antenna has two deep nulls along the antenna direction as expected and is similar to that of a dipole in free space.

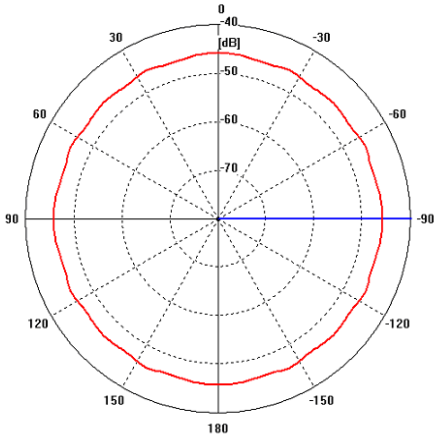

Vertically polarized oriented along Z axis, G_θ

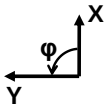

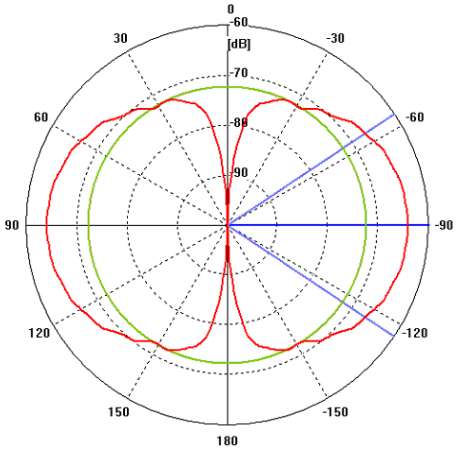

Horizontally polarized oriented along X axis, G_φ

(a)

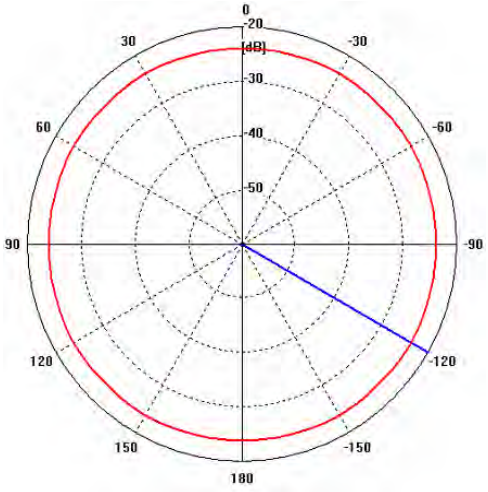

Vertically polarized oriented along Z axis, G_θ

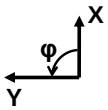

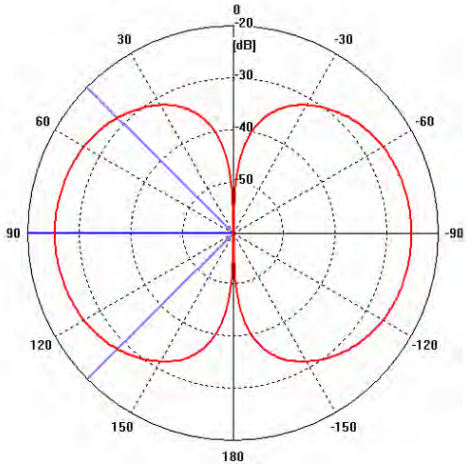

Horizontally polarized oriented along X axis, G_φ

(b)

Fig. 4.8 Far field realized gain pattern of the vertically and horizontally polarized dipole with a length of 2 mm in XY plane($\theta = 90°$),
(a) on muscle phantom with size of 800 × 800 × 50 mm^3, (b) in free space

The transmission path gain can be estimated from those in free space from Fig. 4.6(d) and the antenna efficiency give in Table 4.2. These can then be compared with channels simulated on the human body. The path gain derivation is now given.

The transmission path gain on the body, G_{tb}, is given by

$$G_{tb} = G_{ba1} + G_{ba2} + G_{pb} \quad \text{(dB)} \tag{4.1}$$

where G_{pb} is the propagation channel path gain on the body, G_{ba1} and G_{ba2} are the gains of the transmit and receive antennas on the body and can be expressed as (4.2).

$$G_{ba1,2} = D_{ba1,2} + \eta_{tba1,2} \quad \text{(dB)} \tag{4.2}$$

where $D_{ba1,2}$ and $\eta_{tba1,2}$ are the directivities and efficiencies of transmit (antenna 1) and receive antennas (antenna 2) on the body, respectively and for antennas in free space similar expression is derived as (4.3).

$$G_{fa1,2} = D_{fa1,2} + \eta_{tfa1,2} \quad \text{(dB)} \tag{4.3}$$

The transmission channel path gain in free space is given by

$$G_{tf} = G_{fa1} + G_{fa2} + G_{pf} \quad \text{(dB)} \tag{4.4}$$

where G_{pf} is the propagation channel in path gain free space. Substituting equation (4.3) into (4.4) gives

$$G_{tf} = D_{fa} + \eta_{tfa1} + D_{fa2} + \eta_{tfa2} + G_{pf} \quad \text{(dB)} \tag{4.5}$$

If it is assumed that the antenna directivities do not change between free space and body environments, then G_{tb} can be found in terms of G_{tf} as follows

$$G_{tb} = G_{tf} + (\eta_{tb1} - \eta_{tf1}) + (\eta_{tb2} - \eta_{tf2}) \quad \text{(dB)} \tag{4.6}$$

Now, G_{tf} is given for the various cases in Fig 4.6 (d) and the efficiencies in Table 4.2. The resulting values of the transmission channel path gain on the body can be compared to those shown in Fig. 4.6 (a), (b) and (c). Tables 4.3 to 4.7 show the analytical values for G_{tb} derived from equation (4.6) compared to the simulated for a muscle phantom of Fig. 4.6 (c) for all channels. The muscle was considered to be the closest match to the real tissue of the three given in Fig. 4.6.

Table 4.3 Comparison of analytical and simulation channel path gain for belt-ankle channel

ankle	G_{tf}	η_{tba1}- η_{tf1}	η_{tba2}- η_{tf2}	G_{tb} (eqn (4-6))	G_{tb} (Fig 4.6. (c))	ΔG
VV	-89	-19	-19	-127	-138	11
VH	-136	-19	-32	-187	-152	-35
HV	-135	-32	-19	-186	-155	-31
HH	-93.8	-32	-32	-157.8	-163	5.2

Table 4.4 Comparison of analytical and simulation channel path gain for belt-chest channel

chest	G_{tf}	η_{tba1}- η_{tf1}	η_{tba2}- η_{tf2}	G_{tb} (eqn (4-6))	G_{tb} (Fig 4.6. (c))	ΔG
VV	-84	-19	-19	-122	-127.5	5.5
VH	-118.5	-19	-32	-169.5	-151	-18.5
HV	-118	-32	-19	-169	-143	-26
HH	-90	-32	-32	-154	-156.5	2.5

Table 4.5 Comparison of analytical and simulation channel path gain for belt-head channel

head	G_{tf}	η_{tba1}- η_{tf1}	η_{tba2}- η_{tf2}	G_{tb} (eqn (4-6))	G_{tb} (Fig 4.6. (c))	ΔG
VV	-142.5	-19	-19	-180.5	-151.5	-29
VH	-100	-19	-32	-151	-163	12
HV	-103	-32	-19	-154	-171	17
HH	-134.5	-32	-32	-198.5	-172.5	-26

Table 4.6Comparison of analytical and simulation channel path gain for belt-wrist channel

wrist	G_{tf}	η_{tba1}- η_{tf1}	η_{tba2}- η_{tf2}	G_{tb} (eqn (4-6))	G_{tb} (Fig 4.6. (c))	ΔG
VV	-93.5	-19	-19	-131.5	-139.5	8
VH	-92.5	-19	-32	-143.5	-160	16.5
HV	-104	-32	-19	-155	-155	0
HH	-98.8	-32	-32	-162.8	-168.5	5.7

Table 4.7 Comparison of analytical and simulation channel path gain for belt-back channel

back	G_{tf}	η_{tba1}- η_{tf1}	η_{tba2}- η_{tf2}	G_{tb} (eqn (4-6))	G_{tb} (Fig 4.6. (c))	ΔG
VV	-86.7	-19	-19	-124.7	-151	26.3
VH	-111	-19	-32	-162	-171	9
HV	-108	-32	-19	-159	-164.5	5.5
HH	-89.5	-32	-32	-153.5	-180	26.5

In interpreting the results of Table 4.3 to 4.7, the belt-ankle, Table 4.3, and belt-chest, Table 4.4, are first considered. In both cases, the antennas lie approximately in the same directions at both ends of the channel and there is little shadowing. There is a good agreement between analysis and simulation for the VV and HH cases, where agreement on path gain of 10 dB is assumed acceptable in the face of all the approximations made in analysis. It is concluded that in such cases, knowledge of an equivalent path gain in a free space path and reduction of antenna efficiency due to the body will allow good prediction. For the VH and HV cases, that is cross polarization, there is however a much bigger difference, and its sign is opposite to the same polarization antenna cases. The analysis under predicts the path gain by 20 to 40 dB, compared to the same polarization cases. In later chapters, there is evidence that a horizontally polarized antenna couples much more strongly into the vertical polarizations, that proceeding analysis predicts. Knowledge of this coupling is thus vital to prediction.

For the belt-head case, Table 4.5, there is rotation between the two locations and thus VV and HH become cross polarized cases and VH and HV co-polarized. This can be seen in the prediction differences where the VV and HH comparison gives large negative differences and VH and HV positive, in contrast to the results of the belt to ankle and chest channels.

The belt-wrist case, Table 4.6, is much harder to interpret in the above terms. However, the channel is shadowed and the path lengths on the body and in free space are also significantly different.

The belt-back channel, Table 4.7, is not likely to be well predicted by equation (4.6) as the length of the body channel and the free space channel will be very different. Interpretation of the result is thus hard.

In conclusion, this simple method can be used to predict the path gain of LOS on-body channels where co-polarized antennas used at two ends of the channel. Cross polarization coupling needs further investigation, and when this method is used erroneous results occur. Shadowed channels are also much harder to predict using this simple analysis.

4.4. DUAL POLARIZED ANTENNA

Using individual antennas to quantify the path gain described earlier can increase the errors such as antenna position or body posture repeatability which may lead to unreliable results. In fact, the weak signal which is radiated by a horizontally polarized antenna is more prone the errors created by changing cable direction, the posture movement and multipath propagation, which can all lead to differences of up to 10 dB. In addition, the process is very time consuming as four separate measurements are required to extract the polarization behaviour of each channel. To tackle these problems, the use of a dual polarized antenna with two orthogonal polarizations is essential. The antennas should provide polarizations, normal to and parallel to, the body surface. In the following sections, the antenna design process for such an antenna is explained and simulation and measurement results are presented.

4.4.1 Antenna Design

A monopole and loop which can be arranged for orthogonal polarization with a small configuration were considered. As shown in Fig. 4.9, the monopole is located in the middle of the loop. The monopole uses a small ground plane which is convenient for integration but increases level of cross polarization. However, as shown in Fig. 4.10(a), it is still around -10 dB which was taken as acceptable. Fig. 4.10(b) shows the loop radiation pattern in XY plane. The radiation pattern is slightly tilted due to the unbalanced current in the parallel transmission line feed, which is caused by the connection of an unbalanced coaxial line to the balanced antenna. In addition, the use of the ground plane to feed the antenna through a

microstrip transmission line decreases the level of the gain of the antenna in the ground plane direction. Indeed, the ground plane acts as a reflector and reduces the antenna radiation in that direction.

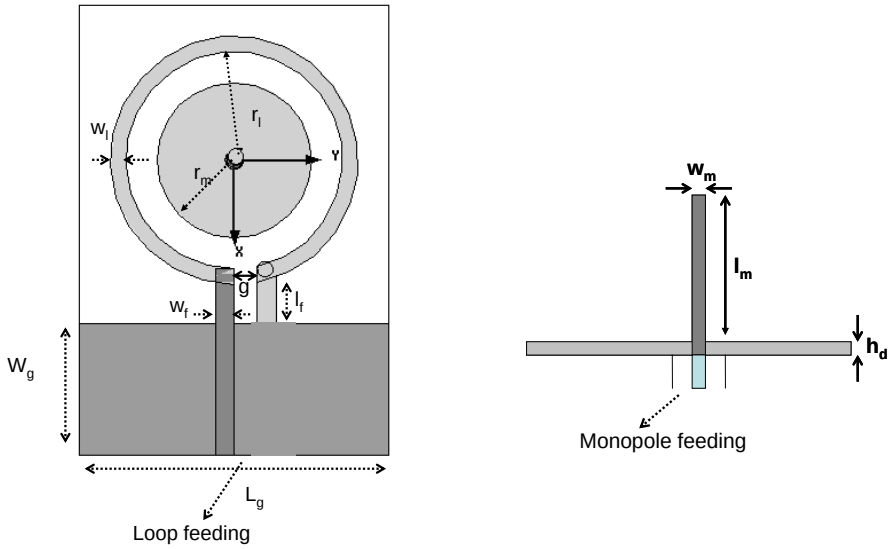

(a) (b)

Fig. 4.9 Combination of monopole and loop antennas printed on FR4 (ε_r = 4.4) (a) Top view, r_l = 14 mm, r_m =10 mm, w_l = 2 mm, w_f = 2.4 mm, l_f = 5 mm, g = 3 mm, W_g = 17 mm, L_g = 40 mm, (b) Side view, w_m = 2mm, l_m = 30 mm, h_d = 1.6 mm

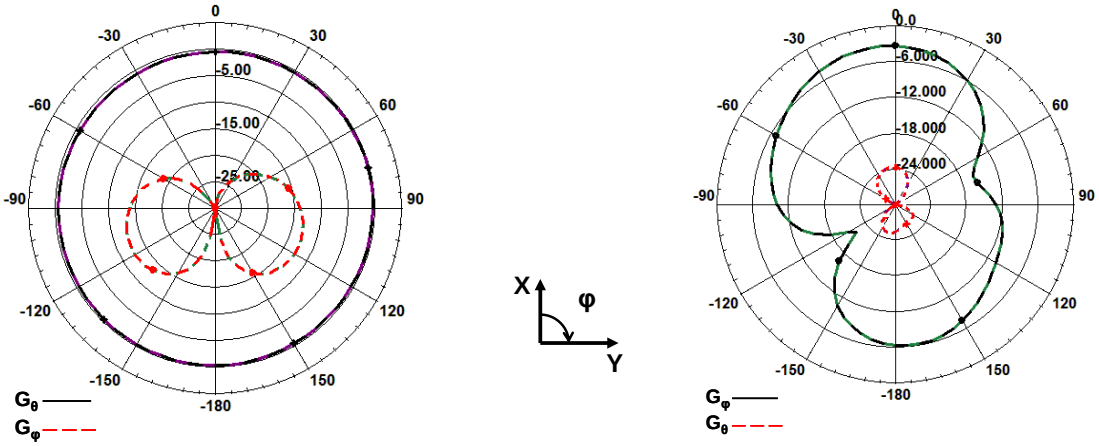

(a) (b)

Fig. 4.10 Simulated far field gain pattern of the antenna shown in Fig. 4.9 in XY plane (a) Monopole antenna (b) Loop antenna

To make it suitable for close mounting on the body surface, a coplanar waveguide (CPW) line is used to move the feed point from the underneath the antenna to the edge of the substrate as shown in Fig. 4.11(a). The ground plane of the monopole is printed on the opposite side of the substrate to the loop. The monopole is connected to the centre conductor line of the CPW through a metallic via. A top loaded monopole is used to reduce the height of the antenna. As is shown, a short parallel strip line is used to feed the loop antenna. The simulated radiation patterns in XY plane of both antennas are shown in Fig. 4.11(b) and (c). The monopole radiation pattern is not affected by changing the feeding method. However, the radiation pattern of loop improves significantly and provides for better symmetry.

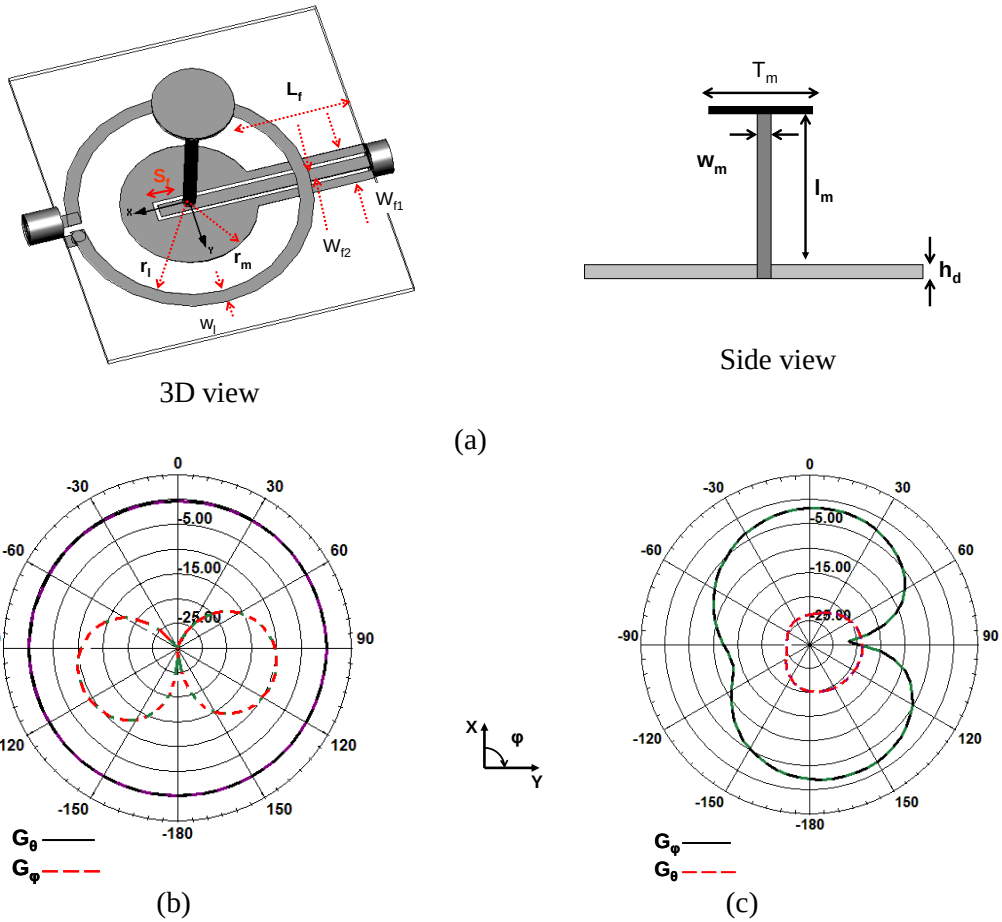

Fig. 4.11 (a) Dual-polarized antenna configuration with the planar feedings: r_1 = 18 mm, w_l = 2 mm, r_m = 10 mm,W_{f2} = 6 mm, W_{f1} = 2 mm, L_f = , S_f = 5 mm, l_m = 25 mm, w_m = 2 mm, T_m = 12 mm, h_d = 1.6 mm, (b) Simulated far field gain pattern of monopole antenna in XY plane, (c) Simulated far field gain pattern of loop antenna printed on FR4 (ε_r =,4.4) in XY plane,

Although the proposed structure in Fig. 4.11 provides reasonable performance, the connection of two coaxial cables to the two feeding of the antennas on the opposite sides of the board can cause problems during measurements.

An improved structure is shown in Fig. 4.12(a), which had planar feed located at one side of the board. The simulation results of this structure show significant increase of the cross polarization component for the monopole antenna, Fig. 4.12(c).

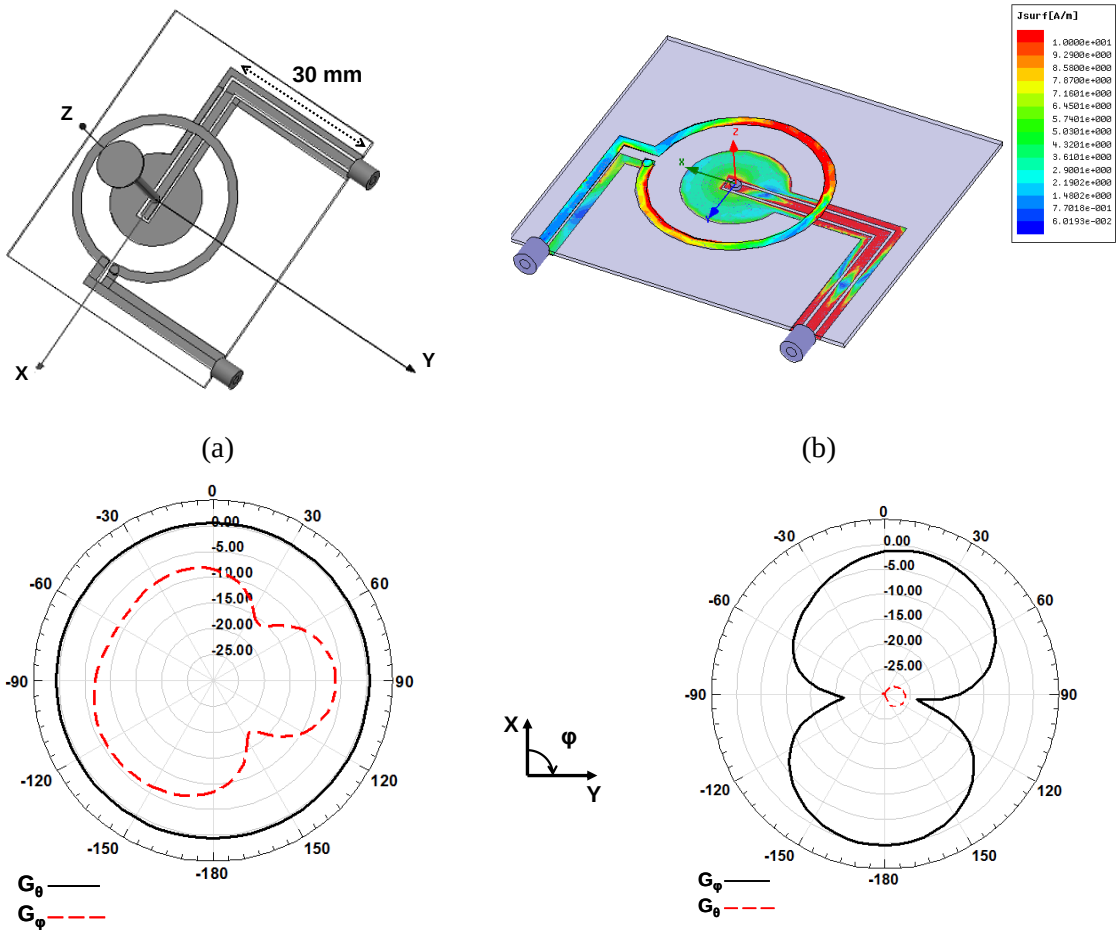

Fig. 4.12 (a) Dual-polarized antenna configuration with the planar feedings at one side of the substrate, (Dimension details as Fig. 4.11 (a)), (b) Current distribution on the loop and monopole ground plane when the monopole port is excited, (c) Simulated far field gain pattern of monopole antenna in XY plane, (d) Simulated far field gain pattern of loop antenna printed on FR4 (ε_r = 4.4) in XY plane,

The current distribution on the loop and monopole ground plane when the monopole is fed is shown in Fig. 4.12(b). The strong coupled current on the loop indicates that the loop radiates while the monopole is excited and this increases the monopole cross polarisation level. Comparing the current distribution in this design and the next design in which the bent in the CPW line is removed (Fig. 4.13), suggests that bending the CPW line is responsible for the increase of the coupling to the loop.

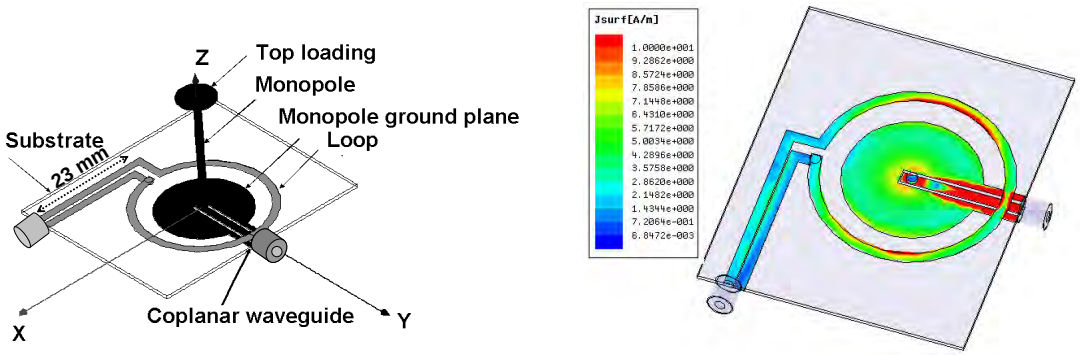

(a) (b)

Fig. 4.13 (a) Dual polarised antenna configuration for reduced monopole cross polarization, (b) Current distribution on the loop and monopole ground plane when the monopole port is excited, (ground plane radius = 13 mm and the other dimension details are as Fig. 4.11 (a))

The ground plane of the monopole and the loop conductor are printed on opposite sides of a 0.8 mm thick, FR4 substrate (ε_r = 4.4). The radius of the monopole ground plane is 13 mm and the inner and outer radii of the loop are 16 and 18 mm, respectively. The monopole is made of a copper cylinder of 30 mm length and 2 mm diameter, and is top-loaded with a circular copper plate of 5 mm radius. The length and the width of CPW line are 23 and 2 mm, respectively. The loop antenna is fed by a parallel strip transmission line of strip width 2 mm and gap size of 2 mm, printed on opposite sides of the substrate. To reduce the effect of the

cables on the channel a 90 degree bend is incorporated in the line, so that both cables are well away from the channel, which is in the -Y direction

The measured and simulated S parameters are shown in Fig. 4.14. In free space, both elements of the antenna resonate around 2.45 GHz. The return loss of both antennas is greater than 10 dB at the resonance frequency. However, the characteristics of the antenna will change in proximity to the human body, and such changes depend on the antenna position relative to the body and its type. Generally, the monopole is not affected by the body due to the presence of the ground plane and the S_{11} of monopole changes slightly in comparison to that in free space. The resonant frequency of the loop shifts from 2.45 GHz to approximately 2.2 GHz when brought close to the body. At the same time, the bandwidth of the return loss is widened. Because of that, return loss in the worst case is above 7 dB at 2.45 GHz.

The measured transmission loss (S_{21}) between the two elements is less than -20 dB at 2.45 GHz, which implies good isolation.

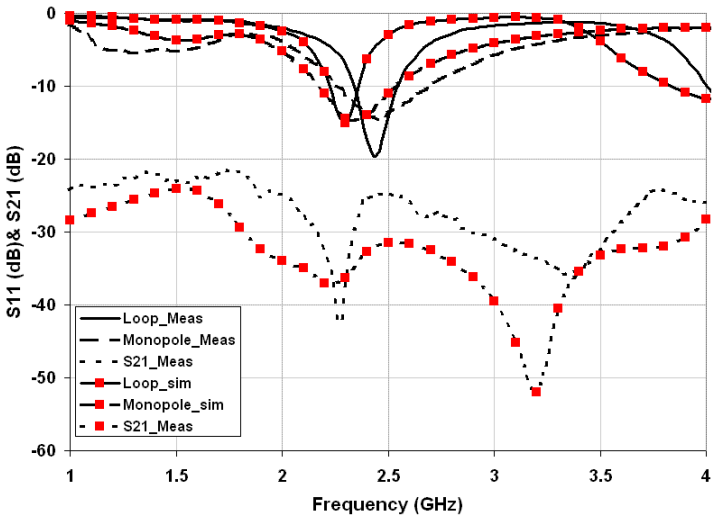

Fig. 4.14 Simulated and measured S parameters of dual-polarized antenna

Fig. 4.15 (a) shows the measured radiation patterns of the monopole antenna in the XY plane, which is the plane parallel to the body surface. In simulation, the co-polar (E_θ) to cross polar (E_φ) ratio is more than 10 dB, but due to the cable effect on the measured results, the difference between the two components is around 6 to 7 dB in some angular directions. Cross polarization in the monopole originates primarily from its feeding line. The radiation pattern of the loop antenna in the same plane is shown in Fig. 4.15(b). The level of the cross-polar is approximately 15 dB lower than the co-polar.

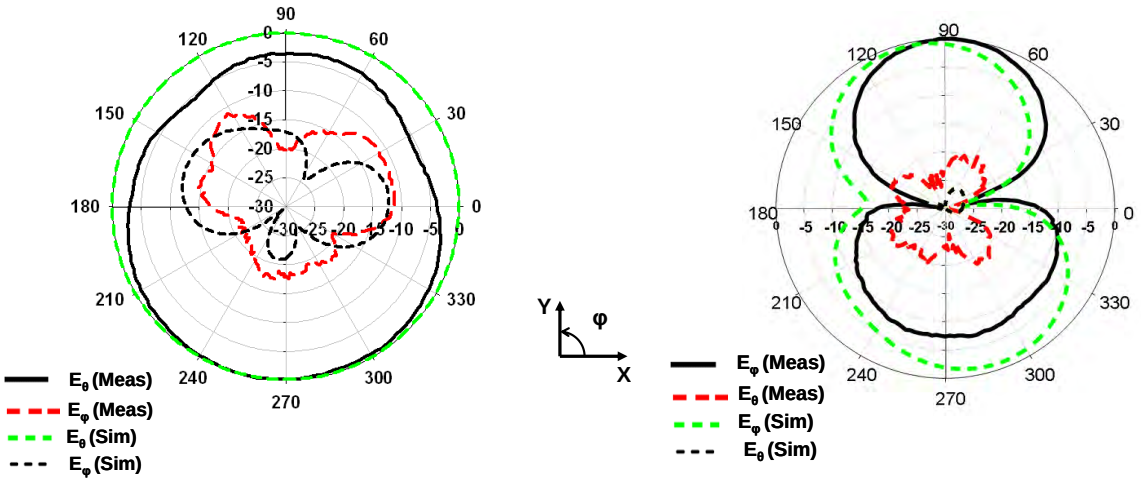

(a) (b)

Fig. 4.15 Normalized measured and simulated radiation pattern of the configuration of Fig. 4.13 in XY plane, (a) Monopole (b) Loop

For comparison, the simulated radiation patterns for both the elements are shown on the same graphs. It can be seen that, the level of the measured cross polarization for both the antennas is higher than simulated. This difference is likely to be due to the short bent coaxial cable, of approximately 5 cm length, which was used to mount the antenna on the stand inside the anechoic chamber. Simulation of the antenna with a cable on it supported this conclusion.

During the measurement, great care was taken to position the cables so that their effect on the antenna radiation patterns was minimized. The effect of the cable was investigated using simulation which showed that if a straight cable of length 15 cm in the plane of the antenna substrate, is used to feed the antenna, the radiation patterns was not affected significantly. However, bends in the feeding cable did give rise to changes in the simulation. Fig. 4.16 shows the radiation pattern of the monopole and loop antennas with bent cable connected to the monopole. As is shown, the monopole radiation pattern is distorted by the presence of the cable. Furthermore, the loop cross-polar increases significantly. Therefore, in the measurement straight cables were used and when it was necessary to bend them, the bend was at least 30 cm from the antenna.

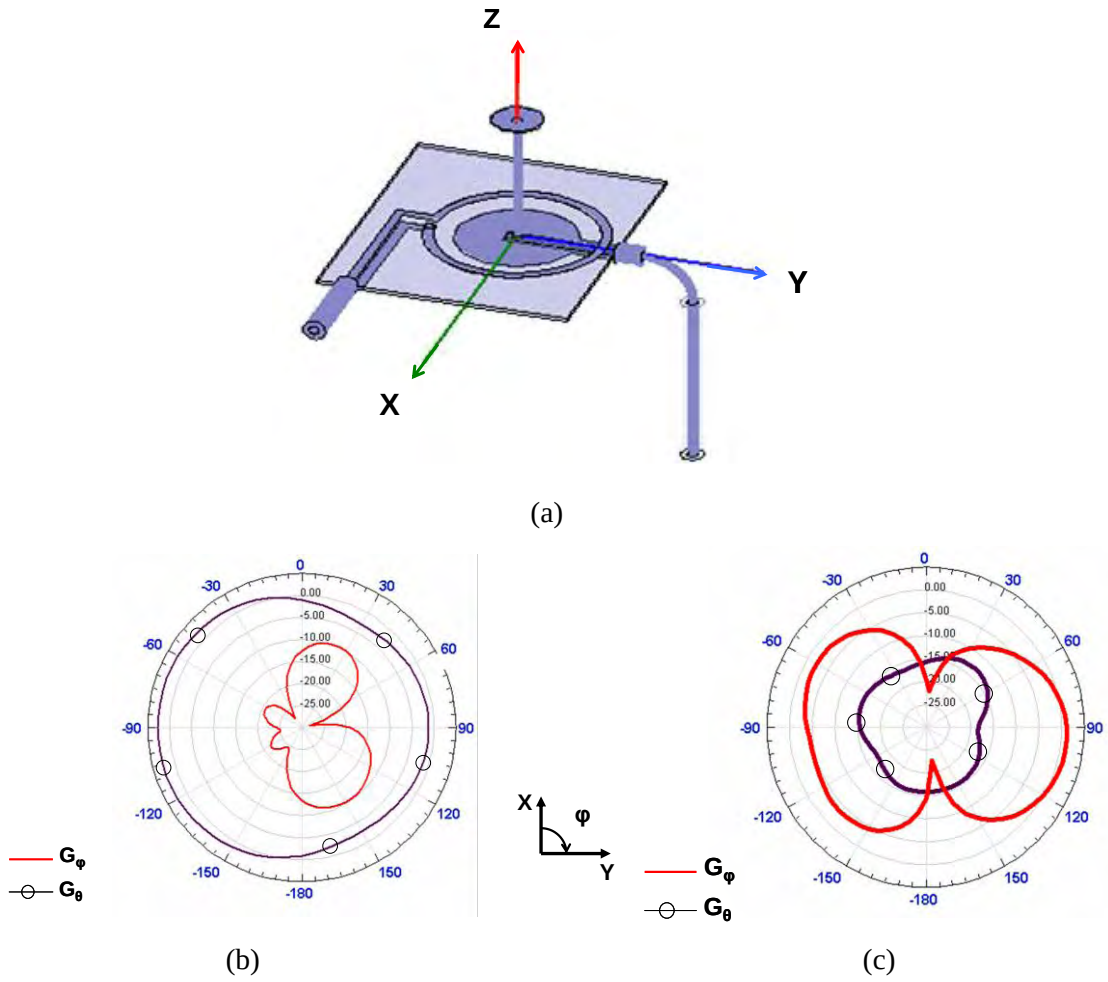

Fig. 4.16 (a) Dual-polarized antenna configuration with a 50 mm bent cable, (b) Simulated far field gain pattern of monopole antenna in XY plane, (c) Simulated far field gain pattern of loop antenna printed in XY plane,

The antenna was mounted 7 mm above a muscle phantom with size of 200 × 200 × 50 mm^3, and simulated. Table 4.8 provides the far field parameters including the efficiency, return loss, directivity and realized gain at 2.45 GHz for both loop and monopole. The simulated loop return loss (S_{11}) in free space and on phantom at 2.45 GHz is relatively high, but as is shown in Fig. 4.14, the antenna is well matched in the measurement at 2.45 GHz.

Table 4.8 Far field parameters of the dual-polarised antenna on the muscle phantom with size of 200 × 200 × 50 mm^3

	S_{11} (dB)	Radiation efficiency (dB)	Directivity (dBi)	Realized gain (dBi)
Monopole-muscle	-15	-2.1	-1	-2
Monopole-free space	-10	0	0	-1
Loop-muscle	-4	-7.4	-11	-20
Loop-free space	-6	0	-1	-3

4.5. CHANNEL MEASUREMENT ON MOVING BODY

As the channel polarization changes with body posture, due to the changes in relative antenna orientation, and changes in the body geometry, it is necessary to perform measurements on a moving body. The antenna shown in Fig. 4.13 was used and random movements performed during the measurements to represent the moving body. In the following sections, the results are presented and discussed.

4.5.1 Measurement set-up

Channel measurements were done on a 160 cm height and 54 kg weight female in an indoor environment consisting of a 7.5 m × 9 m sized laboratory containing equipment, tables, chairs, and computers and also repeated in the anechoic chamber. The experiment was carried out for the on-body channels mentioned in earlier section. The transmit antenna was fixed at

the left side of the belt almost 100 mm away from the body centre line and the receive antenna was placed in different positions including the right side of the head, right side of the chest, centre of the back, right wrist and right ankle positions. The distance between the body and the antennas placed on the body was around 7-10 mm including the clothing. Due to the use of the dual polarized antenna at the both transmitter and receiver, there are two ports at each end. To feed the transmitting antennas, a signal generator operating at 2.45 GHz was connected to them via an RF switch. A vector network analyzer (VNA) in dual channel receive mode with a single frequency sweep at 2.45 GHz was used to receive the two signal from the two receiving antennas simultaneously. The noise floor for the measurement was at -75 dBm. A total of 1601 points were collected for one sweep of 12 s duration whilst subject performs a sequence of pseudo-random activities. Each sample collected contained both amplitude and phase. The 1601 samples collected contained alternate samples from each transmitter. A total of 7 such sweeps were carried out with different random movements of the body for

Table 4.9 Movements done for the channel polarization measurements

sweeps	Belt-Ankle	Belt-Back& Belt-Chest	Belt-Head	Belt-Wrist
1	Walking	Walking	Shaking the head left and right	Walking
2	Moving feet while sitting	Leaning forward and side ways	Shaking the head up and down	Eating and drinking
3	Kicking	Eating and typing while sitting	Eating and drinking and moving the hands	Writing and typing
4	Lifting things from floor while sitting in a chair	Lifting things while sitting on a chair	Lifting the things from the floor	Lifting things and putting up
5	Sit stand	Sit stand	Walking	Waving
6	Running	Exercise	Exercise	Moving hands randomly in front of head
7	Leaning forward and side ways		Leaning forward and side ways	Clapping

each sweep, as tabulated in Table 4.9. In this way a total of 800 × 7 = 5600 instances of the channel matrix were obtained. The measurements were done for the five on-body channels described above by the same procedure but different set of movements in each case.

4.5.2 Mean Amplitude

As is explained in section 4.3.2, the path gain on the body depends on many parameters including path length, transmit and receive antenna efficiencies and propagation channel type in terms of LOS or non-LOS. When the posture is static, prediction of the path gain, for LOS channels with two similarly polarized antennas relative to the body surface at its two ends is relative straightforward. However, using antennas with relative perpendicular polarizations or having a shadowed channel make the prediction of the path gain complicated. Furthermore, this can become even more complex by adding some body movements to the whole scenario. In dynamic channels, in addition to the possible change in the path length by body movements, the polarization state of the antennas may change relative to each other. In this section, the effect of the random movements of the body on the path gain is studied by means of the received signal. Also, to estimate the effect of the antenna characteristics on the path gain, the efficiency of transmit and receive antennas were removed from the mean.

The mean of the signal is shown in Fig. 4.17(a). Monopole-monopole (VV), monopole-loop (VH), loop-monopole (HV), loop-loop (HH) combinations are shown as solid, dashed, dotted and chain lines, respectively. As is shown, the belt-chest and belt-wrist provide higher values in comparison to the other channels. The main reason for the strong received signal at the belt-chest is the shorted path gain and line of sight (LOS) condition. The belt-ankle channel provides lower mean than chest channel due to the longer path length and also the possible shadowing due to the leg movement. The lowest mean is for the head and back channels which are affected by shadowing. In the belt-head channel, in addition, the antennas

at two ends of the channel are aligned perpendicular to each other which cause polarization mismatch (see Fig. 4.1).

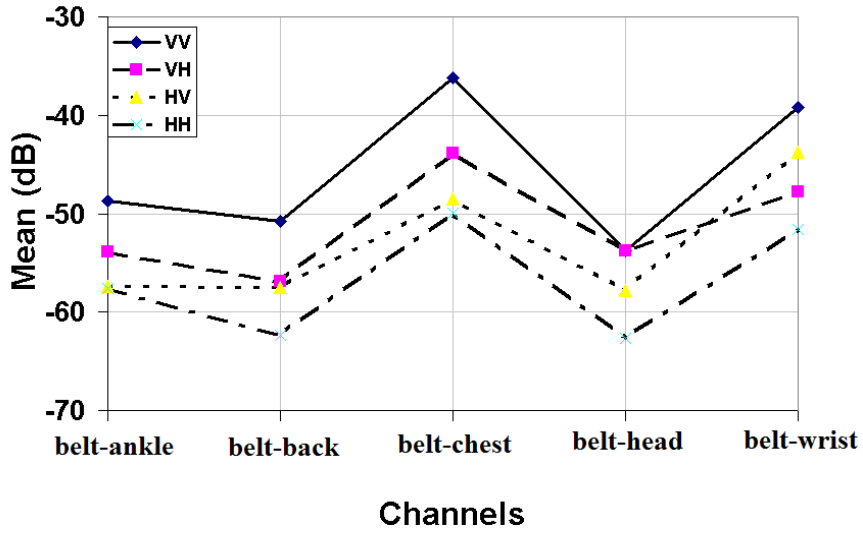

(a)

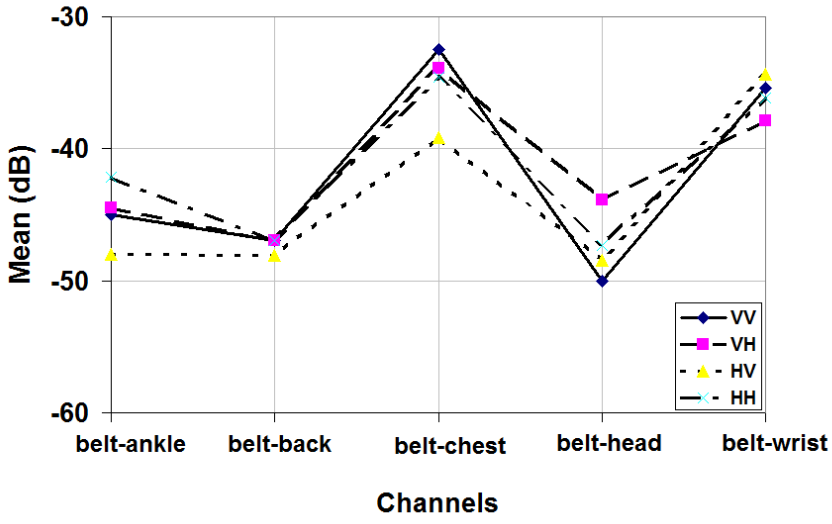

(b)

Fig. 4.17 Mean of the received signal for different antenna combination in different channels , (a) Mean of the raw data ,(b) Mean with removed efficiency of the transmit and receive antennas

Antenna combination type is another important factor, which defines the quality of the channel communication. The VV combination gives the highest mean value for all the channels, and varies between -35 and -54 dB. The combination of loop-loop which is representative of the horizontal to horizontal (HH) polarization gives the lowest level of the power for all the channels changing between -50 dB to -64 dB due to different the path length, and the presence of the shadowing in the channels. Compared to the VV, the level of HH is reduced by almost 10 to 15 dB. The combinations of monopole-loop (VH) and loop-monopole (HV) values are almost the same, with VH slightly higher than HV. In general, as the local environments of the antennas at each end of the channel are different, asymmetrical behaviour results. It is clear that these differences are not very significant here.

The mean of the signal was processed by removing the antenna efficiency of the antennas to yield approximate values for the propagation channel. As is shown in Fig. 4.17(b), the channel provides approximately similar values for VV and HH combination which implies that antenna efficiency is one of the main factors in determining the path gain. The horizontally polarized antenna is more influenced by the body compared to the vertically polarized antenna which reduces the path gain significantly.

The measurement results are similar the simulation results of section 4.3, though the level is much higher due to use of the well matched antennas instead of small short dipoles. The results show that the VV results in higher path gain than other combinations for all the channels. Comparing other combinations show that simulation and measurement results almost follow each other whereas there are some differences which can be explained through differences in the measurement and simulation scenarios. For example, in the belt-chest channel, the VH combination gives higher path gain than the HV combination, whereas in the simulation it is opposite. It is believed that this discrepancy originates from the use of a homogenous phantom. In the measurement, the loop antenna which is located on the chest is

less affected by the body because the antenna is mounted on fat tissue. However, at the belt the tissue is mainly muscle which can lower antenna efficiency more than fat [72]. Hence, VH provides higher value than HV due to the higher efficiency of the loop antenna in the measurement. In the simulation, the phantom is homogeneous and the antennas are primarily affected by their local environment geometry. In other words, the change in the size and shape of the lossy tissue exposed to the antenna affects the antenna radiation characteristics. For example, the antenna radiation pattern and efficiency when located on the chest, which has almost a planar surface, is somewhat different compared to the ankle or wrist which have a cylindrical surface with a relatively small radius.

4.5.3 Cross polarization discrimination

The previous sections described channel behaviour in terms of combination of the antennas. An alternative measure is depolarization, which shows how a given polarization changes in the propagation channel. Cross-polar discrimination (XPD) has been used to represent depolarization in mobile propagation channels, [36]. It is defined in the following way

$$X_{VV-VH} = < P_{VV} > - < P_{VH} > \quad (4\text{-}7)$$

$$X_{VV-HV} = < P_{VV} > - < P_{HV} > \quad (4\text{-}8)$$

$$X_{HH-HV} = < P_{HH} > - < P_{HV} > \quad (4\text{-}9)$$

$$X_{HH-VH} = < P_{HH} > - < P_{VH} > \quad (4\text{-}10)$$

where <P> is the mean value of the received signal and VV, VH, HH, HV subscripts are representative of the source and receiver polarizations. As is depicted in Fig. 4.18, the 1st

equation represents rotation from vertical to horizontal polarization, 2nd is the same but in the opposite direction, the 3rd equation is rotation from horizontal to vertical and finally the 4th is the same but in the opposite direction. Higher depolarization results in the smaller XPD value and vice versa.

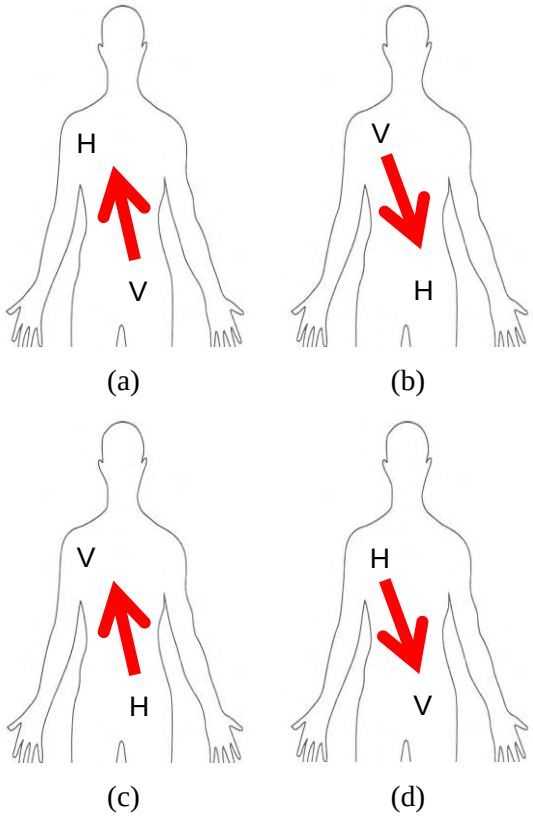

Fig. 4.18 Cross polarization discrimination definition (a) $X_{VV\text{-}VH}$, (b) $X_{VV\text{-}HV}$, (c) $X_{HH\text{-}VH}$, (d) $X_{HH\text{-}HV}$

Fig. 4.19 shows that $X_{VV\text{-}VH} \neq X_{VV\text{-}HV}$ and $X_{HH\text{-}VH} \neq X_{HH\text{-}HV}$ for both the measurement and simulation. This is expected because the local environment at each end of the channel is different and affects each antenna differently. As expected, the XPD extracted from the simulation path gain does not show very high depolarization due to the absence of the body movement and the surrounding environment. The belt-head channel is the only one to show low XPD values because the antennas in this channel are located orthogonally related to each other. It can be also seen that $X_{VV\text{-}VH}$ and $X_{VV\text{-}HV}$ have positive dB values whilst the other two

are very negative for both the measurement and simulation results. The negative values result from the first term in (4-9) and (4-10) being less than the second, that is the mean of HH or VV combination is less than mean of both HV or HV and VH or VH combinations, as can be seen in Fig. 4.17(a). The belt to head channel for a vertically polarized transmitter yields lowest XPD and thus highest depolarization. This is expected, as for vertically polarized antennas, head rotation gives high polarization rotation. However, horizontally polarized antennas do not result in high depolarization and thus XPD values are not closer to 0 dB than for the other channels. The horizontally polarized antenna in the belt to ankle channel shows the lowest XPD and subsequently the highest depolarization, $X_{HH\text{-}HV}$, due to the movement of the ankle in addition to the presence of the shadowing effect in this channel.

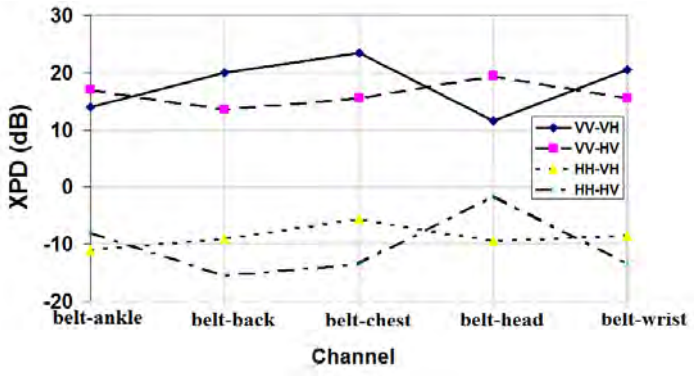

(a)

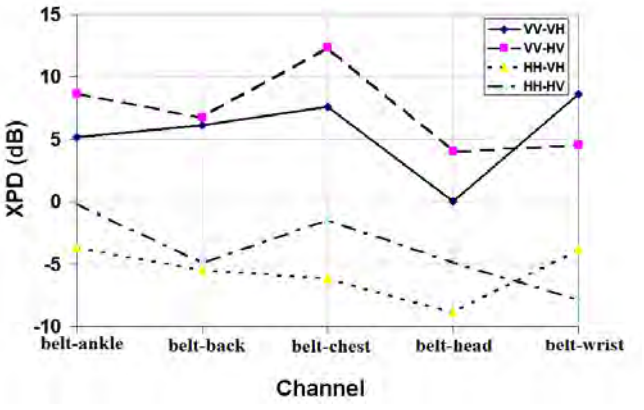

(b)

Fig. 4.19 Calculated vertical and horizontal XPD for different channels (Solid = $X_{VV\text{-}VH,}$ dashed = $X_{VV\text{-}HV}$, dotted =, $X_{HH\text{-}VH}$ chain = $X_{HH\text{-}HV}$,

(a) Simulation, (b) Measurement

4.5.4 Fast Fading Analysis

As an addition to the known statistical models, polarization is an important parameter that should be considered in the models. According to the previously published works, the fast fading variations for on-body channels follow Rician statistics [73]. Also, the Rician K factor, which is defined as the ratio of the power in the direct ray to the average scattered power, has been derived and shown that the use of vertically polarized antennas, such as monopole, at both end of the channels provide a higher K factor than horizontally polarized antennas at both ends such as the loop or IFA in some specific channels. However, the performance of mixed polarizations at both ends of the channel is not investigated. To extract fast fading statistics, slow fading in the received signal should be eliminated by de-meaning the signal [74]. The received signal can be defined as follows [74]:

$$r(t) = m(t) \times M(t) \tag{4-11}$$

where r(t) is the received signal envelope, m(t) is the short-term fading envelope, and M(t) is the local root mean square envelope, constituting the slow fading which is calculated by use of following equation.

$$M(t) = \sqrt{\frac{1}{2w} \int_{x-w}^{x+w} r^2(t)\, dt} \tag{4-12}$$

and thus

$$m(t) = \frac{r(t)}{M(t)} \tag{4-13}$$

where 2w is the sliding window size.

The demeaning was done by using different size of the window. It was observed that window size of 30 to 40 samples which corresponds to 5 to 7 fast fading oscillations and resampling of each 2nd point provided satisfactory fitting in the Kolmogorov-Smirnov (KS) test [75].

Fig. 4.20 shows the calculated K factor for different combination of the antennas in different channels for both the laboratory and anechoic chamber measurements. As expected, the K factor of all the channels in the chamber is higher than in the laboratory measurements due to lack of the scattering from the environment. It has been noted, that except the VV combination at the belt-chest channel which results in a high K factor due to the presence of a line of sight ray, the rest of the values are almost within the same range. This result suggests that the ratio of the strongest ray to the scattered does not depend significantly on the polarization. Since the scattered ray is mostly due to the environment at this frequency then it is almost independent of the polarization type.

As was mentioned before, each set of measurements includes different random movements. Different movements can affect the channel differently. The data from each movement was processed separately and k factor calculated. It was found that the type of movement can influence the k factor value, significantly. K factors of the belt-wrist channel are presented in Table 4.10 for different movements. The receiver, which is mounted at the back of the wrist, causes partial shadowing, when the hands are in the rest position. Some movements such as writing and typing or clapping, can reduce the shadowing effect which increases the K factor.

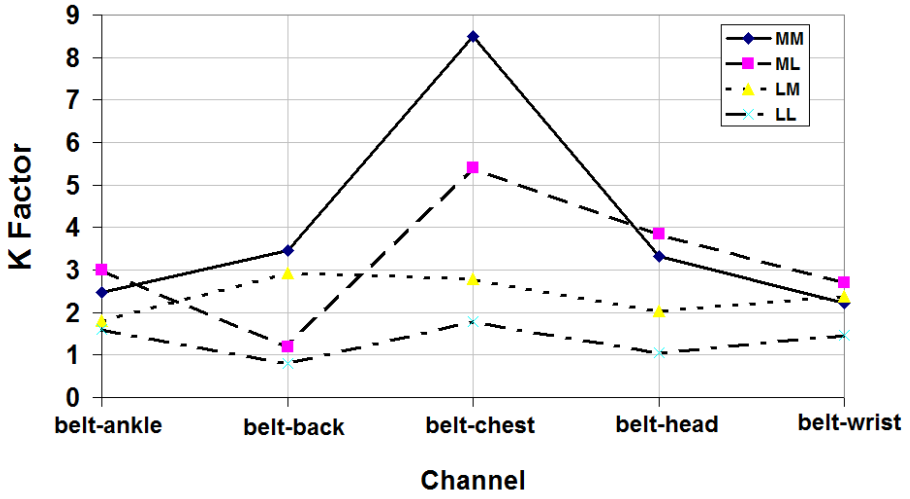

(a)

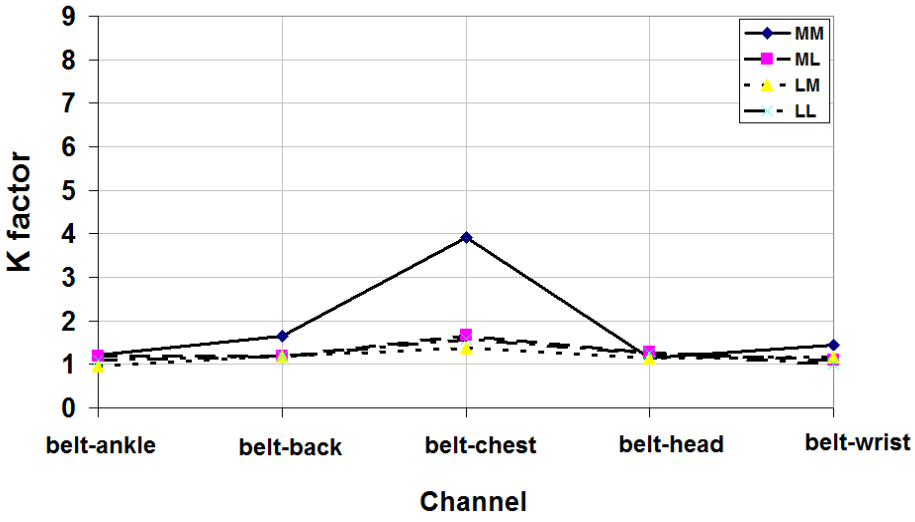

(b)

Fig. 4.20 K factor for different on-body channels

(a) Anechoic Chamber, (b) Laboratory,

(MM= monopole-monopole, ML = monopole-loop, LM = loop-monopole, LL= loop-loop)

The results show that the K factor for the monopole-monopole combination is more sensitive to the type of movement compared to the other combinations. However, the K factor for the loop-loop combination is less likely to be influenced by the type of movements, and because of that, the variation of the K factor is much less. The main reason is that the vertical polarization is not attenuated by the body as much as the horizontal and there is a strong ray on the body so that the shadowing and any other variations are less significant. However, the

horizontal polarization decays rapidly on the body and the scattering plays an important role in the communication for almost all the channels.

Table 4.10 K factor for different movement of the belt-wrist channel at 2.45 GHz

	Walking	Eating and drinking	Writing and typing	Lifting things	Waving	Moving hands	Clapping
monopole-monopole	2.3	3.4	6.9	5.7	1	1.5	4.9
monopole-loop	2.8	1.7	7.9	2.4	2.7	2.8	5.1
loop-monopole	2.2	0.3	3.9	1.7	1.4	1.1	8.1
loop-loop	1.1	1.3	4	1.7	1.6	1.7	1.7

4.6. POLARIZATION DIVERSITY

On-body channels are prone to multipath fading due to the scattering from the moving body parts as well as the surrounding environment. Diversity is a well known technique to mitigate fading and improve the output signal to noise ratio (SNR). The increasing demand of wireless devices and the future high data rate in application areas like entertainment, security and personal identification, fashion, and personalized communications drives the research to establish more reliable and efficient links between the devices mounted on the body and demands the use of multiple antennas and diversity reception for the on-body and off-body channels. Radiation pattern and space diversity have shown significant improvement in the output SNR for on-body channels [76-78]. However, these types of diversity usually require multiple antennas which are physically separated and this makes the overall size larger. The use of a single antenna with dual-polarization can help to reduce the antenna size.

In on-body communications, the presence of the human body makes the propagation environment very different to that in the mobile communication areas. Apart from

depolarization due to the surrounding environment, depolarization of the transmitted wave due to body effects may also occur. The presence of a line of sight (LOS) in static on-body channels, like the belt to chest, can result in less depolarization than that in highly dynamic channels, such as the belt to wrist or ankle and in channels with non LOS or partial LOS. In the dynamic channels, polarization mismatch is caused by body and limb movements which change the orientation of the antennas. Diversity can compensate for such polarization mismatch.

This section investigates the significance of two-branch polarization diversity, by analyzing the maximum achievable diversity gain (DG) and the correlation between the branch signals for the various on-body channels. Measurements were carried out in an indoor laboratory environment at 2.45 GHz by mounting antennas on a real human subject performing random movements. A dual-polarized loop-monopole pair antenna was used at the receive end. When the antenna is mounted with the loop parallel to the body, the loop element has its polarization tangential to the surface of the body and the monopole produces polarization normal to the surface. Two single element transmitting antennas were used alternately, one, a monopole antenna, generating normal polarization and the other, a printed loop antenna, generating polarization parallel to the body surface. Five on-body channels were investigated, namely, belt-chest, belt-ankle, belt-back, belt-wrist, and belt-head.

4.6.1 Measurement set-up

The measurement set-up is exactly the same as channel measurement on moving body (see section 4.2.1). The only difference is instead of having two transmitter, there is just one transmitting antenna was connected to a 2.45 GHz signal generator and there is no need to switch between two transmit antennas.

4.6.2 Analysis and Results

The collected data for each channel was demeaned, to remove the long-term fading and to extract the short-term fading envelopes, by the same procedure used in [78-80]. The gauge for diversity improvement is the diversity gain (DG), which is the improvement in received signal power or SNR at a certain outage level. The DG can be calculated by plotting the cumulative distribution function (CDF) of the branch and diversity combined signals, and calculating the difference between the combined signal and the averaged strongest branch signal at a certain probability level [74], which was selected to be 1% in this study. The diversity signals can be combined using three methods namely selection diversity (SC), equal gain combining (EGC), and maximal ratio combining (MRC), [78-79, 81-82].

The performance of a diversity receiver greatly depends upon the correlation and the power imbalance between the received signals at the diversity branches. Low correlation is desirable, as it indicates that the branch signals fade differently. An envelope correlation coefficient of 0.7 is considered suitable for most of the mobile communication scenarios [74, 79]. Similarly, high power imbalance significantly reduces the DG. The envelope correlation coefficient (ρ_e) between the two branch signals was calculated by [79]:

$$\rho_e = \frac{\sum_{k=1}^{N}(r_1(k)-\bar{r}_1)(r_2(k)-\bar{r}_2)}{\sqrt{\sum_{k=1}^{N}(r_1(k)-\bar{r}_1)^2}\sqrt{\sum_{i=1}^{N}(r_2(k)-\bar{r}_2)^2}} \qquad (4\text{-}14)$$

where N is the total number of samples, $r_i(k)$ is the short-term fading envelope of the received signal at the i^{th} branch, and $\bar{r}_i$ is the mean value of the received signal at the i^{th} branch.

The CDFs of the branch and combined signals were plotted and the DG was calculated at a 1% probability for each on-body channel. Fig. 4.21 shows the CDF of the two branch signals and the three diversity combined signals for the belt-head channel with the monopole as the transmitter as an example. The calculated DG values, along with ρ_e, and power imbalance are given in Tables 4.11 and 4.12 for the two different transmit antennas, respectively. The transmitted signal from the printed-loop antenna, by the virtue of its polarization, is attenuated much more rapidly on the surface of the body compared to that with the monopole transmit antenna. This is confirmed by the comparison of the mean signal values in the Tables. For the same reason, there is a high power imbalance due to the strong direct ray with the monopole transmit antenna which reduces the diversity gain. This is particularly true in the belt to chest channel, where the two antennas have the same orientation, which does not change with body movement, and thus the channel has very low depolarization. However for some channels, such as the belt to head, the specific geometry and strong movement will give rise to large depolarization.

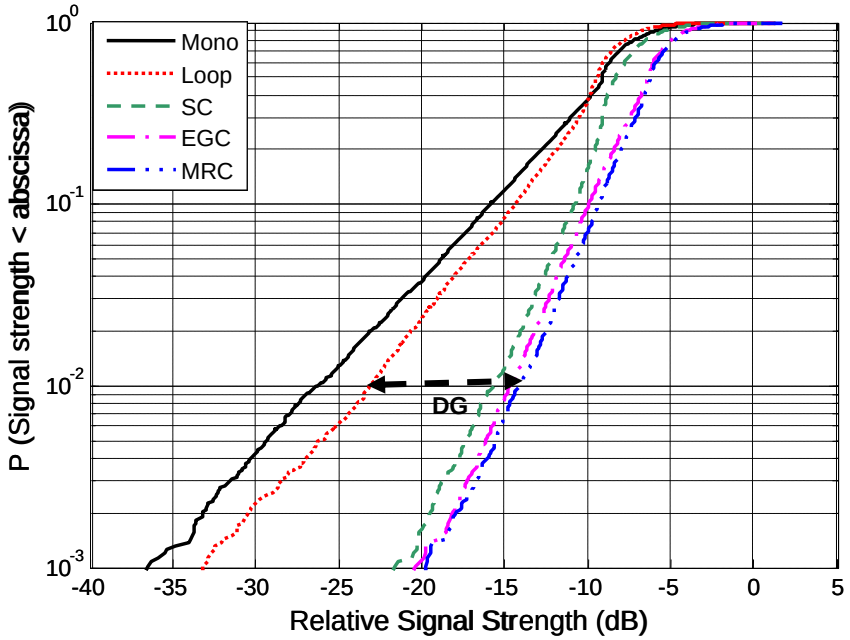

Fig. 4.21 CDF plots and diversity gain calculation for belt-head channel with monopole Tx

Table 4.11 Results with monopole Tx

		Ankle	Chest	Back	Head	Wrist
DG(dB)	SC	5.2	0.1	2.9	7.6	2.9
	EGC	6.0	0.4	3.8	8.7	3.6
	MRC	6.6	0.7	4.3	9.2	4.2
ρ_e		0.3	0.2	0.3	0.1	0.3
Mean power monopole branch (dB)		-46.5	-39.6	-49.4	-49.4	-44.1
Mean power loop branch (dB)		-55.6	-54.4	-60.9	-49.8	-58.1
Power diff (dB)		9.1	14.8	11.5	0.4	13.9

Table 4.12 Results with loop Tx

		Ankle	Chest	Back	Head	Wrist
DG (dB)	SC	6.8	0.1	3.4	3.7	3.2
	EGC	7.3	0.3	4.3	5.0	4.2
	MRC	7.9	1.1	4.9	5.4	4.7
ρ_e		0.4	0.2	0.2	0.1	0.2
Mean power monopole branch (dB)		-55.1	-50.3	-58.9	-58.3	-52.8
Mean power loop branch (dB)		-59.5	-64.3	-68.8	-68.7	-64.8
Power diff (dB)		4.4	14.0	9.9	10.4	12.0

For the belt-chest channel, both cases give very low DG values due to strong correlation and high power imbalance. It has been shown in [77-78] that the static channels, which do not involve movement of the antennas with respect to each other, show low diversity gain values. Being a static channel, the belt-back channel also shows low DG values and high power imbalance. The other three channels have reasonable diversity gains. The belt-ankle channel involves strong reflections from the floor and thus have significant multipath. The reflections

cause significant depolarization and hence this channel has high diversity gain with relatively low power imbalance. The belt-wrist channel involves LOS most of the time and hence has high power imbalance despite the random orientation of antennas. Indeed, the belt-wrist channel with random movements represents a case where pure polarization diversity cannot be achieved with this antenna and it is a combination of polarization and pattern diversity. However, for most of the activities performed, the side of the antenna giving similar radiation patterns, for both the elements, was facing the transmitter and polarization diversity may be considered as a dominant factor. The belt-head channel shows considerably higher diversity gain in comparison to the other on-body channels. In this channel, due to the body curvature, the transmitter and receiver are aligned perpendicularly to each other, in the other words, the normal polarization to the surface of the body at the belt will be received by a parallel polarization antenna located on the right side of the head and vice versa. This leads to a better power balance between the two channels, and as there is some degree of decorrelation in all channels, the belt to head one has better diversity gain.

The diversity gains of the monopole and printed-loop, are not very different but the DG values are slightly lower for the printed-loop transmitting antenna. The diversity gains, for all cases, are about 3-4 dB less than those reported in [78] for the same channels with different antennas, which suggests that polarization diversity is not as effective as space or pattern diversity for the on-body applications. However, the improvement due to the polarization improvement in some channels is reasonable, and for example the gain for belt-ankle and belt-head channels is of the order of 8 dB. The belt-head channel shows about 1-2 dB difference in DG compared to those achieved in [78]. It is expected that if polarization diversity is used in combination with some other type of diversity, it will provide a better diversity performance by increasing the DG to the order of 10 dB.

4.7. SUMMARY

The on-body transmission channels were investigated for different antenna combination with orthogonal polarizations in each on-body channel. The path gain and XPD values of each combination were presented for five on-body channels. In spite of differences in the simulation and measurement scenarios, both of them suggest that VV provides higher path gain, 10-15 dB in the measurement and around 20 dB in the simulation, compared to HH combination for different channels. For all the antenna combinations, belt-chest channel provides highest path gain while belt-head and belt-back channels yield lowest path gain. In addition to quantifying the path gain for different antenna combinations, XPD parameter which is a representative of the depolarization rate originating from the surrounding environment and also the human body was calculated for both vertical and horizontal polarizations. The calculated XPD for the measured results suggests that belt–chest which can be assumed as a static channel shows the highest XPD (lowest depolarization) and belt-head shows the lowest XPD (highest depolarization) because two co-polarized antennas are aligned orthogonally with respect to each other. However, XPD for the simulated channels does not show significant depolarization except the belt-head channel. Since the horizontal polarized launches weaker signal than the vertical one, the scattered signal play important role and because of that the level of the XPD for the horizontal polarized transmitter is generally lower than the vertical polarized one. Also, the fast fading analysis was performed for the measured data. The results reveal that all the antenna combinations provide almost similar K factor at different channels in the lab environment except belt-chest due to the presence of strong LOS for VV combination.

The polarization diversity technique has been investigated for on-body communication channels. The results suggest that polarization diversity can yield good diversity gain for dynamic channels, such as belt-ankle and belt-head. Channels such as belt-chest and belt-wrist do not provide significant gain due to the presence of strong LOS. The main advantage of this

method is the smaller size of the diversity antennas compared to the space and pattern diversity types, which makes it a more practical proposition for on-body applications. Further work, however, is still required to reduce the height of the antenna and thus make it more conformal.

Chapter 5

Wave Excitation on a Human Body by a Short Dipole

5.1. INTRODUCTION

In on-body communication channels, the propagation mechanism on the body is a combination of line of sight (LOS), multi-path and surface wave. Surface waves around the body have been referred to as creeping waves [51]. Shadowing can be significant and may repeatedly occur due to the body movement, which thus reduces the LOS contribution to the received signal. In addition, some channels such as belt to back are completely shadowed simply because of the transmitter and receiver positions. In this case, the trapped wave on the body surface will play an important role, particularly when the multi-path contribution is small due to the body being in a low scattering environment. Apart from a general knowledge of on-body channels, some of the fundamental mechanisms involved are not yet well understood. This leads to difficulties in optimised antenna design, and through imperfect channel understanding, shortfalls in optimum transceiver design results. Both of these issues have an impact on power consumption, and as power is at a premium in body area networks, this is of great importance.

This chapter presents an analytic description of waves on the body, which provides a good insight to on-body channel behaviour. In section 5.2 and 5.3, Zeneck and Norton surface waves on human tissues are described and the conditions to support them are derived. In Section 5.4, these two surface waves are compared and the possibility of launching each of them is discussed. Section 5.5 presents short dipole characteristics on body phantoms through simulations. Section 5.6 investigates the path gain between two short dipoles on the human torso. The wave behaviour launched by small dipole around a cylinder made of muscle tissue is studied by use of an analytical method in section 5.7. Finally, the coupling between the antenna and the Norton surface wave modes is calculated for realistic antennas on both flat and curved surfaces.

5.2. ZENNECK SURFACE WAVE ON HUMAN TISSUE

The possibility of plane wave guiding with low attenuation on the interface of between two different dielectric media, specifically the air-earth interface was initially investigated by Ulter in 1903 and later by Zenneck in 1907 [83]. Zenneck's model is a lossy dielectric half-space, for Z < 0, a complex permittivity, ε_2, as shown in Fig. 5.1. Zenneck's analysis assumes a field distribution on the surface, which is infinite in the Y plane. This is not a practical case, as there is no source considered, and later sections show how important the source is. Nevertheless, the analysis gives good insight into the conditions necessary to support the surface wave and at the end of the section consideration is given to whether human tissue can support a wave of this type.

A surface wave can be either of transverse magnetic (TM) wave, that is, there is no magnetic field in the propagation direction, or in transverse electric (TE) wave form, that is, there is no electric field in the propagation direction. The electric property of the material on

both sides of the interface determines the surface wave mode. Dielectric interfaces which are inductive can support only TM wave. However, to support TE mode, capacitive surfaces are required which occurs on the interface of two materials with different permeabilities which is out of scope of the current work. In the following analysis, a TM solution is derived and the condition to support the wave is extracted. TE mode solution can be simply derived in a similar way to TM mode by applying the duality theorem to TM solution [83].

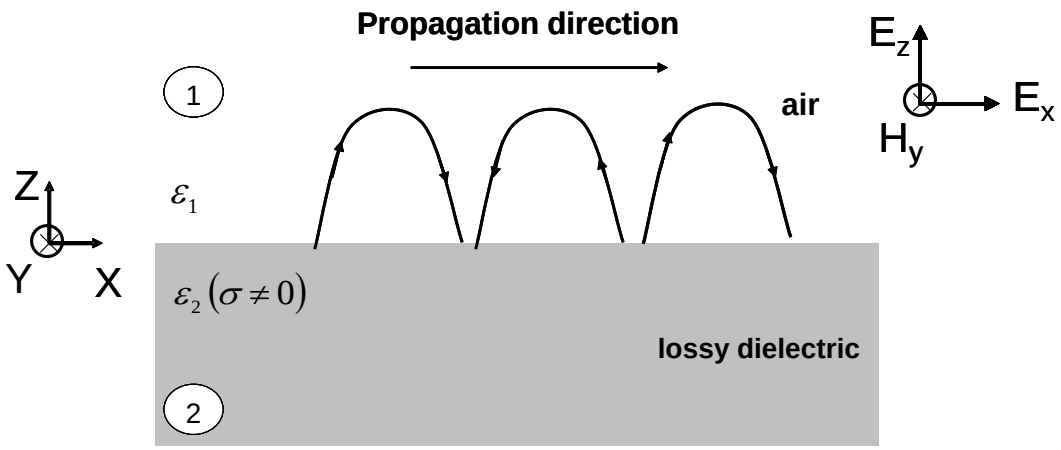

Fig. 5.1 Composite electric field lines in Zenneck wave propagation in an air-dielectric interface [84]

A TM wave with respect to X axis, for which $E_y = 0$ is considered. In the general form of Zenneck model there are two materials with different properties, and the magnetic field in two materials has the following form, in which the factor $e^{j\omega t}$ is implicit [83]:

$$H_y = A\exp(jk_{z1}z - jk_x x) \qquad z > 0 \qquad (5\text{-}1)$$

$$H_y = A\exp(jk_{z2}z - jk_x x) \qquad z < 0 \qquad (5\text{-}2)$$

where $k_{z1}^2 + k_x^2 = k_1^2$ and $k_{z2}^2 + k_x^2 = k_2^2$. The wave impedances in material 1 and 2 are given by

$$Z_1 = \frac{k_{z1}}{k_1} Z_{0,1} \tag{5-3}$$

$$Z_2 = \frac{k_{z2}}{k_2} Z_{0,2} \tag{5-4}$$

where $Z_{0,1}$ and $Z_{0,2}$ are intrinsic impedance of material 1 and 2 , respectively and k_1 and k_2 are the wave number inside material 1 and 2, respectively. The condition for the existence of a surface wave is that the reflection coefficient at the interface boundary vanishes. This implies that, $Z_1 = Z_2$.

The solution for the wavenumbers, k_{z1} and k_{z2}, and also the propagation constant k_x can be obtained by solving the two following equations:

$$k_{z1}^2 - k_1^2 = k_{z2}^2 - k_2^2 \tag{5-5}$$

$$\frac{k_{z1}}{k_1} Z_{0,1} = \frac{k_{z2}}{k_2} Z_{0,2} \tag{5-6}$$

Solving the equations result in:

$$k_{z1} = \sqrt{\frac{\varepsilon_1^2}{\varepsilon_1 + \varepsilon_2}} k_0 \tag{5-7}$$

$$k_{z2} = \sqrt{\frac{\varepsilon_2^{\,2}}{\varepsilon_1 + \varepsilon_2}} k_0 \tag{5-8}$$

$$k_x = \sqrt{\frac{\varepsilon_1 \varepsilon_2}{\varepsilon_1 + \varepsilon_2}} k_0 \tag{5-9}$$

where k_0 is the wavenumber in free space. For simplicity, if material 1 can be considered free space, $\varepsilon_1 = 1$, then equations (5-7) to (5-9) will be as follows:

$$k_{z1} = \sqrt{\frac{1}{1 + \varepsilon_2}} k_0 \tag{5-10}$$

$$k_{z2} = \sqrt{\frac{\varepsilon_2^{\,2}}{1 + \varepsilon_2}} k_0 \tag{5-11}$$

$$k_x = \sqrt{\frac{\varepsilon_2}{1 + \varepsilon_2}} k_0 \tag{5-12}$$

From these equations, it is clear that TM surface waves do not exist on nonconductive dielectric materials. If ε_2 is positive, then and k_{z1} and k_{z2} are real, and the waves do not decay with distance from the surface; they are simply plane waves propagating through the dielectric interface. On the other hand, if ε_2 is less than –1, or if it is imaginary, the solution describes a wave that is bound to the surface. These TM surface waves can occur on metals, lossy dielectrics or materials with negative dielectric constant. The properties of surface waves from a surface impedance point of view will be explored in the following sections.

5.2.1 Surface Impedance

To obtain further insight into the surface wave and how a dielectric surface supports it, it is useful to investigate the surface impedance Z_s which is defined as the ratio of the tangential electric and magnetic field on the surface. The magnetic field H_y of the assumed TM surface wave is given in equation (5-1), and the electric field components can be driven from Maxwell equation:

$$E_z = \frac{1}{j\omega\varepsilon_0}\frac{\partial H_y}{\partial x} \tag{5-13}$$

$$E_x = -\frac{1}{j\omega\varepsilon_0}\frac{\partial H_y}{\partial z} \tag{5-14}$$

Then, Z_s is

$$Z_s = -\frac{E_x}{H_y}\bigg|_{z=o^+} = \frac{k_z}{\omega\varepsilon_0} = \frac{k_z}{k_0}Z_0 \tag{5-15}$$

on the other hand, if Z_s is a complex number with resistive and reactive parts,

$$Z_s = R_s + jX_s \tag{5-16}$$

The solution for k_z in free space is

$$k_z = k_z' + jk_z'' = k_0 \frac{Z_s}{Z_0} = k_0 \frac{R_s + jX_s}{Z_0} \quad (5\text{-}17)$$

and the solution for k_x is [83]

$$k_x = k_x' - jk_x'' = \left(k_0^2 - k_z^2\right)^{1/2} = k_0 \left(1 + \left(\frac{X_s}{Z_0}\right)^2 - \left(\frac{R_s}{Z_0}\right)^2 - 2j\left(\frac{X_s}{Z_0}\right)\left(\frac{R_s}{Z_0}\right)\right)^{1/2} \quad (5\text{-}18)$$

A surface wave is usually characterised by fields that decay normal to the surface. To support the surface wave, its attenuation normal to the surface should be increased. According to equation (5-17), this condition can be satisfied if the reactive part of the surface is inductive. Obviously, the more inductance the tighter the wave will be bound to the surface. However, the attenuation increase requires the tilt of the Poynting vector of the wave into the material as shown in Fig. 5.2.

To reduce the attenuation rate of the surface wave along the surface, the imaginary part of k_x should be as low as possible, which means X_sR_s should be small. In order to support surface wave with low attenuation, the material should provide small R_s and large X_s. For example, on a good conductor, such as metal R_s is larger than X_s and the wave is only loosely attached to the surface. The surface wave trapping can in this case be improved by use of a dielectric coating on top of the metal.

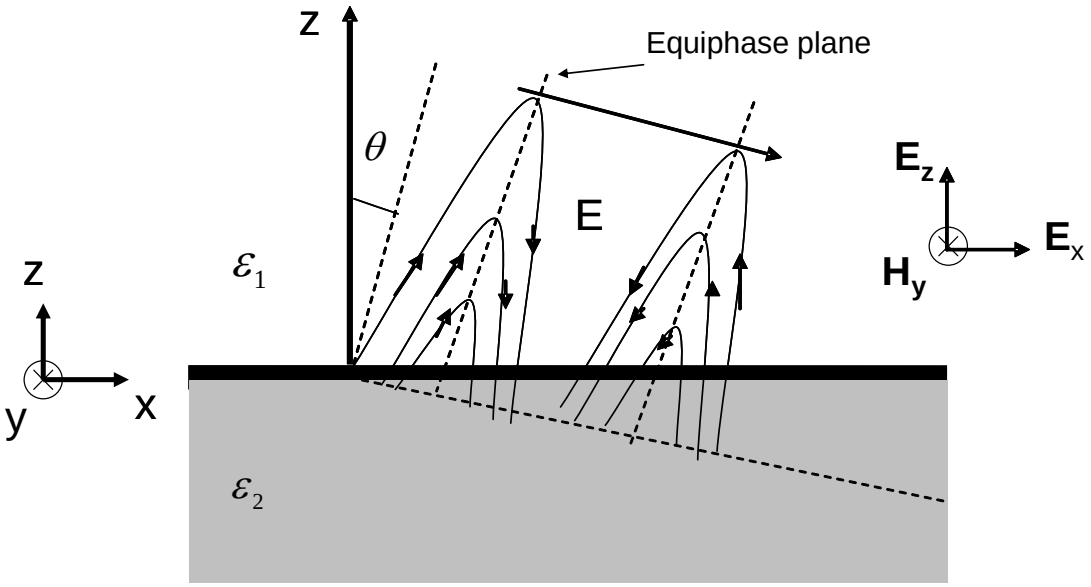

Fig. 5.2 Zenneck wave inclining toward to a lossy dielectric [84]

The constant phase plane (equiphase plane) which shows the tilt of the wave toward the surface can be obtained by:

$$k_z' z - k_x' x = C \tag{5-19}$$

where C is a constant number. The angle θ relative to Z axis, which is the wave tilt toward the surface is [83]

$$\tan\theta = \frac{k_z'}{k_x'} \tag{5-20}$$

The phase velocity of the wave along the surface is determined by the real part of k_x and is defined as follows, when $R_s << X_s$ [83]

$$V_p = \frac{\omega}{k_x'} \approx c\left(1+\left(\frac{X_s}{Z_0}\right)^2\right)^{-1/2} \qquad (5\text{-}21)$$

where c is the speed of light in free space. It can be seen that the phase velocity is less than c for a highly conductive surfaces. However, any increase in the resistive part will increase the phase velocity and for the resistive equal or greater than reactive will lead to the phase velocity equal or great than c.

To explore, the likelihood of a Zenneck wave on the human body, the dielectric properties of a few types of human tissues, including skin, fat and muscle, given in Table 5.1 at the frequency of 2.45 GHz are used. They all lie near the surface of the human body and therefore affect propagation of waves near the body surface. Comparing these parameters for the three tissues shows that skin and muscle have very similar properties, while for fat the electric properties are much smaller. The layers of both skin and fat in the human body are usually much thinner than the corresponding penetration depths indicated in Table 5.1. Therefore the currents caused by a propagating surface wave are likely to reach the muscle layer and quickly attenuate inside it. In this thesis only uniform models are considered in which only one tissue (either muscle or fat) is present. The one layer model may be sufficient to describe surface wave propagation on relatively flat regions of a human torso (on front or back), when the fat layer is very thin or when it is very thick.

As is shown in Table 5.1, the imaginary part, X_s, of the surface impedances, Z_{TM}, is smaller than the real part, R_s, for all three tissues, indicating that the Zenneck wave is only loosely bound to the surface. The calculated phase velocity is also given in Table 5.1 which implies the Zenneck wave behaves as a fast wave on the human body tissues.

Table 5.1 Dielectric properties and surface wave parameters of human tissues at 2.45 GHz

Tissue	Permittivity ε_r	Conductivity σ (S/m)	Skin depth δ (mm)	Surface Impedance $R_s + jX_s$	R_sX_s	Phase front tilt θ (deg)	Phase velocity related to c V_p/c
Skin (dry)	38.0	1.46	23	58.7 + j7.9	465.9	8.9	1.02
Fat	5.3	0.11	117	150.3 + j9.1	1423.5	23.3	1.09
Muscle	52.7	1.77	22	50.4 + j5.8	292	7.7	1.00

5.3. NORTON SURFACE WAVES ON HUMAN TISSUE

Suppose a short Hertzian dipole of length $l << \lambda$ is placed on the surface of the planar half-space of a lossy dielectric with the complex relative dielectric constant $\varepsilon(\omega) = \varepsilon_r(\omega) - j\sigma(\omega)/\omega\varepsilon_0$ (see Fig. 5.2). Here $\varepsilon_r(\omega)$ and $\sigma(\omega)$ are the relative dielectric constant and the conductivity of the dielectric, $\omega = 2\pi f$ is the cycle frequency and $\varepsilon_0 = 8.85\times10^{-12}$ F/m is the permittivity of free space. The coordinate system is shown in Fig. 5.3 [85]. The half space occupies $Z \le 0$ and the dipole is located at the origin.

The field radiated by the dipole is made up of a space wave and a surface wave. The space wave component of the electric field excited by the dipole is given in equation (5-22) and $\eta I_{in} l \frac{e^{-j(kr-\omega t)}}{4\pi r}$ factor is implicit [85],

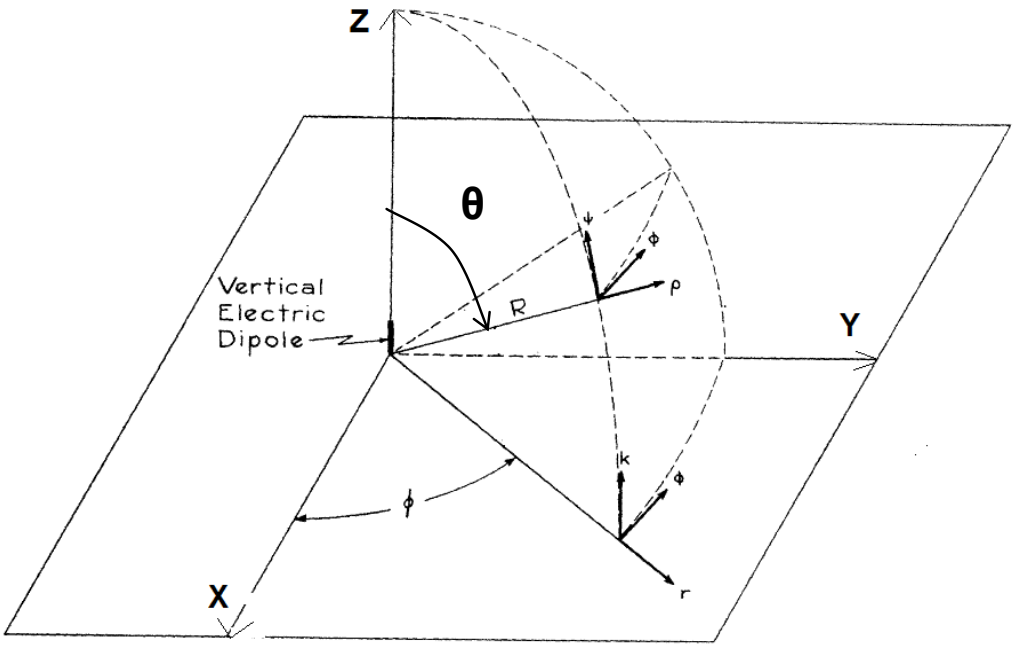

Fig. 5.3 The coordinate system [85]

$$E_{sp}^{v} = jk\sin\theta(1+R_{TM})\hat{\theta} \tag{5-22}$$

when the dipole is perpendicular to the surface (Z direction), and

$$E_{sp}^{h} = jk\{\cos\varphi\cos\theta(1-R_{TM})\hat{\theta} + \sin\varphi(1+R_{TE})\hat{\varphi}\} \tag{5-23}$$

when the dipole is tangential to the surface and oriented along the X axis. In (5-22) and (5-23)

$$R_{TM} = \frac{n_{TM} - 1/\cos\theta}{n_{TM} + 1/\cos\theta} \tag{5-24}$$

$$R_{TE} = -\frac{n_{TE} - \cos\theta}{n_{TE} + \cos\theta} \tag{5-25}$$

are the Fresnel reflection coefficients for TM and TE polarised waves, and n_{TM} and n_{TE} are the corresponding transverse refractive indices:

$$n_{TM} = \sqrt{\varepsilon} / \cos\theta' \tag{5-26}$$

$$n_{TE} = \sqrt{\varepsilon} \cos\theta' \tag{5-27}$$

$$\cos\theta' = \sqrt{1 - \frac{\sin^2\theta}{\varepsilon}}. \tag{5-28}$$

The reflection coefficients in (5-24) and (5-25) are defined so that when both the transmitting and receiving antennas are on the surface (i.e. $\vartheta \approx \pi/2$), $R_{TM} = R_{TE} = -1$. Therefore, from (5-22) and (5-23) it can be seen that the space wave fields disappear on the surface for both the TM and TE polarizations.

The electric field of the surface wave has the following form [85]:

$$E_{su}^{v} = -jk(1 - R_{TM})F(p_{TM})(\hat{z} + \hat{r}\tan\psi_v) \tag{5-29}$$

for the vertical short dipole on the surface, and

$$E_{su}^{h} = -jk\left[\cos\phi(1 - R_{TM})F(p_{TM})\tan\psi_v(\hat{z} + \hat{r}\tan\psi_h) + \sin\phi(1 - R_{TE})F(p_{TE})\hat{\varphi}\right] \tag{5-30}$$

for the horizontal dipole, where

$$F(p) = 1 - j\sqrt{\pi p}e^{-p}\mathrm{erfc}\left(j\sqrt{p}\right) \tag{5-31}$$

is the surface wave attenuation factor, and its argument takes the form

$$p_{TM} = -j\frac{kr}{2}\left(\frac{1}{n_{TM}} + \cos\theta\right)^2 \tag{5-32}$$

or

$$p_{TE} = -j\frac{kr}{2}\left(n_{TE} + \cos\theta\right)^2 \tag{5-33}$$

Coefficients $\tan\psi_v$ and $\tan\psi_h$ equal the ratios of the radial and the vertical components of the surface wave electric field induced by the perpendicular and tangential dipole, respectively. For $\vartheta \approx \pi/2$,

$$\tan\psi_v \approx \frac{1}{n_{TM}} \tag{5-34}$$

$$\tan\psi_h \approx \frac{1}{n_{TE}}\left[1 - \varepsilon\frac{(1-R_{TE})F(p_{TE})}{(1-R_{TM})F(p_{TM})}\right] \tag{5-35}$$

Note that the expressions given above are valid when the distance from the antenna is much greater than the wavelength ($r >> \lambda$). For small antennas, whose size, D, is less than half the wavelength, λ, ($D < \lambda/2$), this also implies that the far-field approximation for antennas in free space also holds, i.e. $r > 2D^2/\lambda$.

Equations (5-29) and (5-30) show that, while the surface wave launched by a vertical dipole is TM polarised (i.e. the electric field exists in the direction of propagation), a horizontal dipole generates both the TM and TE modes of the surface wave, the TE mode being polarised so that the electric field is perpendicular to the propagation direction (ϕ-component). The two modes have orthogonal angular patterns, so that the maxima of the TM pattern at ϕ = 0° and 180° correspond to the minima of the TE pattern, and vice versa, the minima of the TM pattern at ϕ = 90° and 270° correspond to the maxima of the TE mode. At the same separation distance, r, the numerical distance for the TM mode is much smaller than that for the TE mode, $p_{TM} << p_{TM}$, as can be seen from Table 5.2 and equations (5-32), (5-33). Hence, the absolute value of the attenuation factor, $|F(p_{TM})|$, is much greater than $|F(p_{TE})|$, and therefore the TE mode of the surface wave can often be neglected in comparison with the TM polarised surface wave, with the exception for the directions nearly perpendicular to the dipole where the TM mode disappears due to the $\cos\phi$ term.

Table 5.2 Dielectric Properties and Surface Wave Parameters of Human Tissues

Tissue	ε_r	σ (S/m)	δ (mm)	$\lvert p_{TM}\rvert$ (r = 0.1m)	$\lvert p_{TE}\rvert$ (r = 0.1m)	$\lvert\tan\psi_V\rvert$	R_s+jX_s
Skin (dry)	38.0	1.46	23	0.06	103.82	0.16	58.7 + j7.9
Fat	5.3	0.105	117	0.39	16.85	0.39	147 + j8.6
Muscle	52.7	1.77	22	0.05	141.66	0.13	50.3 + j6.0

Variation of the various components of the electric field existing on the dielectric surface with distance is plotted in Fig. 5.4. The dipole and its current are chosen so that the dipole's field in free space at a distance r = 0.1 m is 1 V/m, i.e. $k\eta Il = 0.1$ V. Each component of the field is shown for the direction in which it has a maximum, i.e. E_z is shown for ϕ = 0°, and E_ϕ for ϕ = 90°. Variation of the surface wave field amplitude with the distance is determined by the factor F(p)/r. The TE mode field (E_ϕ component) can be seen to vary as r^{-2} for all the

tissue types, because for large p, $F(p) \sim p^{-1} \sim r^{-1}$. The TM mode ($E_z$ component) attenuates more slowly, following a more complex expression. However, the curves in Fig. 5.3 appear almost linear between 0.1 m and 1 m which covers the range of practical distances between devices mounted on the same side of a human torso. Thus, in this interval the surface wave attenuates approximately according to the power law: $E_{su} \sim r^{-\alpha}$ where α = 1.2 for the TM mode on muscle tissue, and α = 1.6 for the TM mode on fat. Thus, the TM mode surface wave attenuates slower on muscle than fat. Both polarization modes attenuate faster than the space wave in free space, for which α = 1, but slower than the space wave field of the antenna elevated above the surface at large distances, in which case α = 2.

Examining Fig. 5.4(a) reveals that surface wave field of a perpendicular dipole is stronger on muscle than fat by at least 4 dB (for distances over 0.1 m) and attenuates slower with increasing distance. On the other hand, Fig. 5.4(b) shows that a tangential dipole produces stronger fields on fat than muscle at short distances, but since attenuation on fat is faster with distance, the perpendicular component of the electric field on muscle becomes stronger than that on fat at the distances above 0.5 m. The TE mode fields are weaker than the TM mode fields at the same distance by at least 15 dB. Also, the fields on skin and muscle tissue are always very similar. Therefore, in the rest of the work only muscle and fat will be used as tissues representative of the two extreme cases.

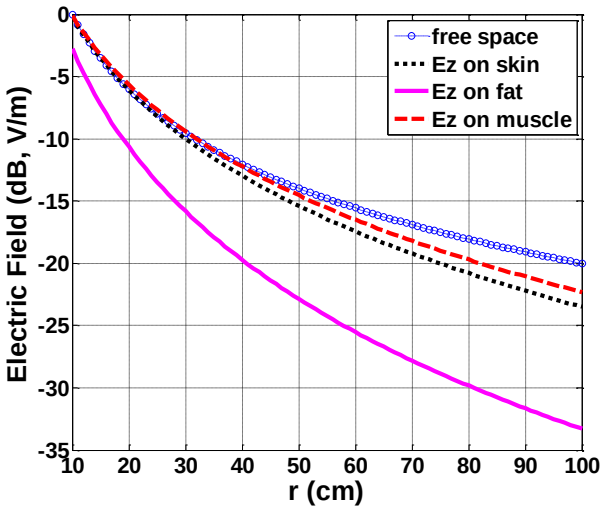

(a)

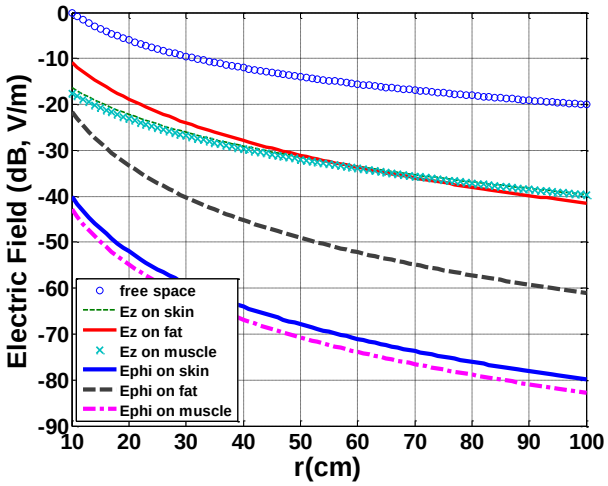

(b)

Fig. 5.4 Electric field amplitude of (a) the perpendicular dipole and (b) tangential dipole (E_z is shown for φ = 0°, and E_ϕ for φ = 90°). The field is normalised so that the field in free space at a distance r = 0.1 m is 1 V/m.

One of the important characters of the surface wave is the phase velocity. The velocity on the surface of the dielectric can be smaller or greater than speed of light which is thus called slow or fast wave, respectively. The phase of the vertical electric component of the total field at a distance r from the transmitting antenna may be expressed as [86]:

$$\psi = \omega t - kr - \varphi(r) \tag{5-36}$$

where ω is the angular frequency of the radiation, d is the distance from the source and $\varphi(t)$ represents the sum of the additional phase variation due to near-field effects and to ground attenuation. Phase velocity can be defined as follows:

$$V_p = \frac{-\partial\psi/\partial t}{\partial\psi/\partial r} \tag{5-37}$$

where

$$\partial\psi/\partial t = \omega \tag{5-38}$$

$$\partial\psi/\partial r = k + \partial\varphi/\partial r \tag{5-39}$$

then

$$V_p = \frac{-\partial\psi/\partial t}{\partial\psi/\partial r} = \frac{\omega}{\omega/c + \partial\varphi/\partial r} \tag{5-40}$$

Rearranging gives:

$$\frac{V_p}{c} = \frac{1}{1 + \frac{\lambda}{2\pi}\frac{\partial\varphi}{\partial r}} \tag{5-41}$$

where λ is the free space wavelength. The result is shown in Fig. 5.5. V_p is slightly smaller than velocity in free space. On muscle and skin the velocity of the wave is almost the same, but on fat at shorter distances (<5λ) distances, it is slightly smaller which indicates wave is slower.

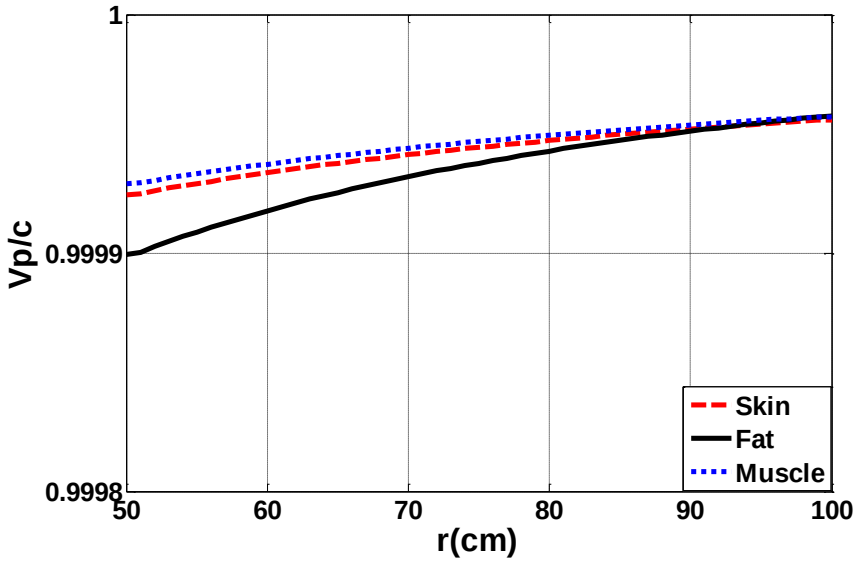

Fig. 5.5 Phase velocity of Norton wave on human tissues, V_p is normalised to speed of wave in free space

5.4. COMPARISON OF NORTON AND ZENNECK WAVES

The previous sections have introduced and explained the Zenneck and Norton surface waves and their properties on the surface of the body. In the case of the Zenneck wave no sources are considered, and the analysis assumes uniformity in the transverse direction along the surface. On the other hand, Norton assumes a small dipole source and developed a space wave, which has the characteristics of a spherically expanding wave with a direct ray and a surface reflected ray, combined with a surface wave, of the form of a cylindrically expanding wave. In this section, these two forms of surface waves are compared.

Fig. 5.6 shows E_z versus distance on the surface of skin, fat and muscle for the Norton and Zennec surface waves. As it can be seen, the Norton wave behaviour is totally different from Zenneck wave and in particular, the attenuation of the Norton wave is much faster than Zenneck. Both the Norton and Zenneck wave experience higher attenuation on fat than muscle and skin which can be explained by the surface impedance of these materials. Comparison of these two waves on the human body tissue reveals that a Zenneck wave is more desirable, since it can provide a stronger communication link. However, in practice launching of a Zenneck wave is not easy. To be able to excite a Zenneck wave without exciting other wave modes, an infinite source should be used [45, 52]. Detection of the Zenneck wave has been reported a few times, but many researchers believe that Zenneck wave excitation is not possible and they question the validity of other researcher observations [53-54]. In this work, which is concerned with surface wave excitation for on-body communication, very small antennas are used and based on the explanation given above, the Norton wave is more likely to be excited on the body than any other surface wave modes.

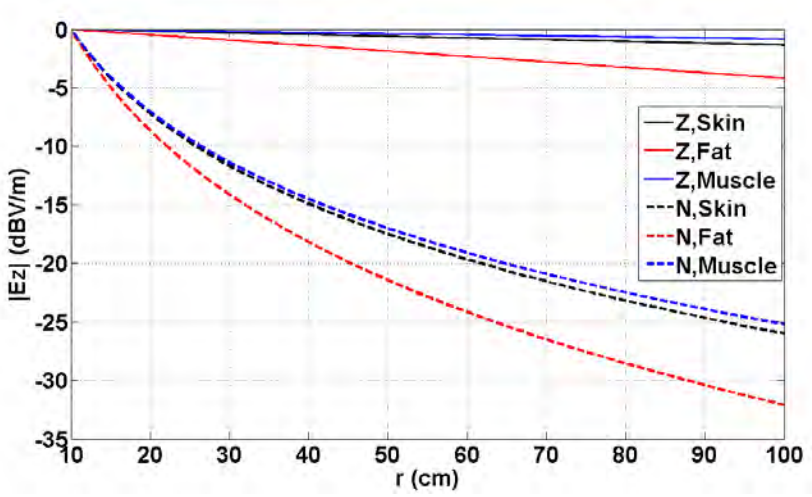

Fig. 5.6 Electric field amplitude of TM mode for Zenneck and Norton wave, (The field is normalised to their values at distance r = 0.1 m is 1 V/m)

5.5. SIMULATIONS OF SHORT DIPOLES ON HUMAN PHANTOMS

The Norton wave analysis provides valuable insight into the field distribution of a short dipole on the surface of human body. In this section, numerical methods will be used to investigate these fields. The near and far field behaviour of vertical and horizontal dipoles will be studied in detail.

5.5.1 Vertical Dipole

To investigate the vertical polarization behaviour on the body, simulations were done at 2.45 GHz with a 2 mm long dipole placed 5 mm vertically away from a rectangular phantom made of fat and muscle tissue, as is shown in Fig. 5.7. The phantom surface size is 600×600 mm^2 and the depth is 200 and 50 mm for fat and muscle, respectively. To overcome diffraction from the box edges, a perfect matched layer (PML) boundary condition is used. PML is placed as close as possible to the phantom edge. The antenna radiation pattern on the box surface (XY plane) is omni-directional. Fig. 5.8 shows the three electric field components on the surface of a muscle phantom (ε_r=52.7, σ=1.77 S/m). As it can be seen, all three components exist on the surface. Detailed examination showed that the E_x and E_y components form the radial components on the box surface, which is in the direction of wave propagation. This confirms that the main propagation mechanism is a TM surface wave.

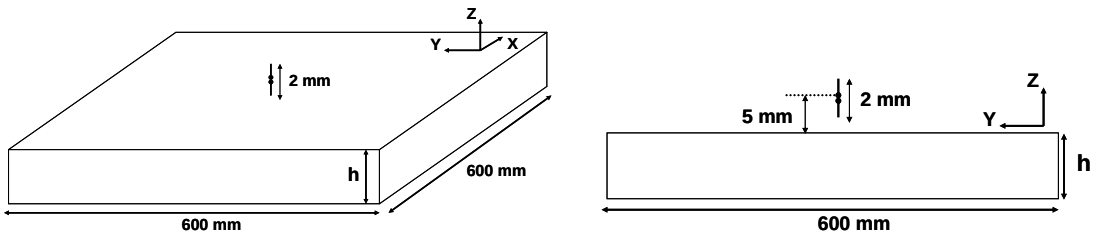

(a) (b)

Fig. 5.7 Small dipole mounted over flat phantom, h = 50 mm, (a) 3D view, (b) Side view

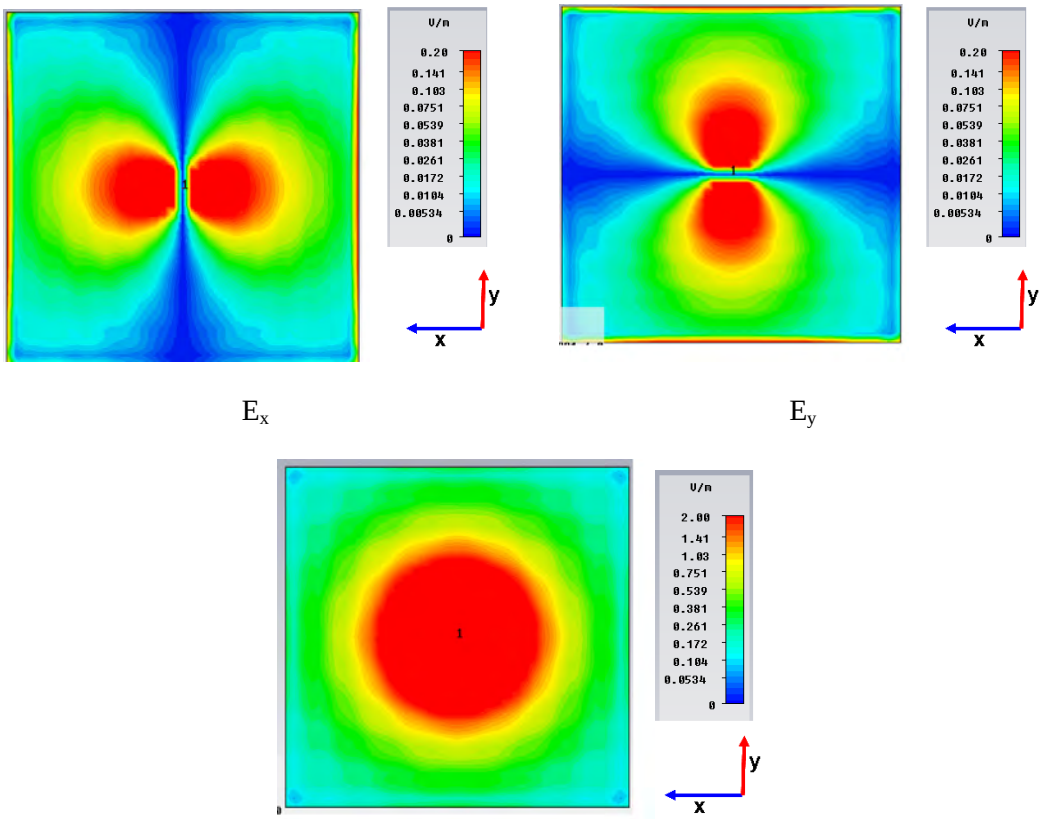

E_x E_y

E_z

Fig. 5.8 Simulated near field distribution of a vertical dipole antenna on a muscle phantom at 2.45 GHz (ε_r = 52.7, σ = 1.77 S/m)

5.5.2 Horizontal Dipole

A parallel dipole of 2 mm length, mounted 5 mm away from a muscle phantom was also simulated. As shown in Fig. 5.9, the far field radiation patterns in the θ=90° or XY plane is shown in Fig. 5.10. It can be seen from Fig. 5.11 that there is a strong E_z present for φ=0° and 180°, or the two opposite directions of the X axis, in the direction of the dipole. This component does not exist in the free space radiation pattern.

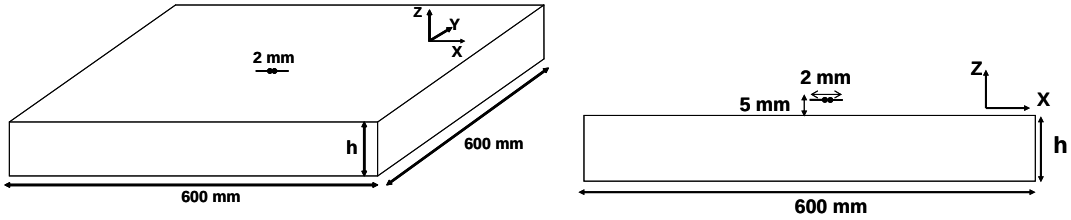

(a) (b)

Fig. 5.9 Small dipole mounted over phantom (ε_r = 52.7, σ = 1.77 S/m)., h = 50 mm, (a) 3D view, (b) Side view

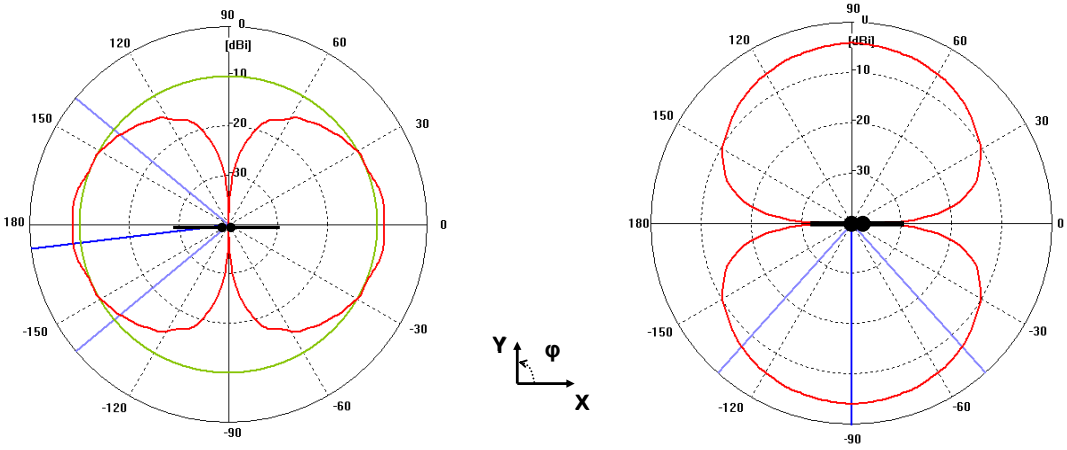

D_θ D_φ

Fig. 5.10 Far field directivity pattern of horizontal short dipole antenna on a muscle phantom at 2.45 GHz

(Cuts are in θ=90°, or XY plane, Details as Fig. 5.9)

E_z, the component normal to the surface, has nulls in the Y direction and E_y has nulls in both X and Y orientations. The E_x component is distributed in all directions. In the Y direction, E_x is transverse to the propagation direction. However in the X direction, E_x is in the direction of the propagation. Thus, in the direction of the antenna (X), propagation is in the form of a TM surface wave which is the same as the vertical dipole case. The propagation mode is both TEM and TE in the Y or φ=90˚ direction, because there is no electric field in the direction of propagation. This observation suggests that the antenna excites different

propagation modes in different directions which confirms the conclusions derived from the Norton wave equations.

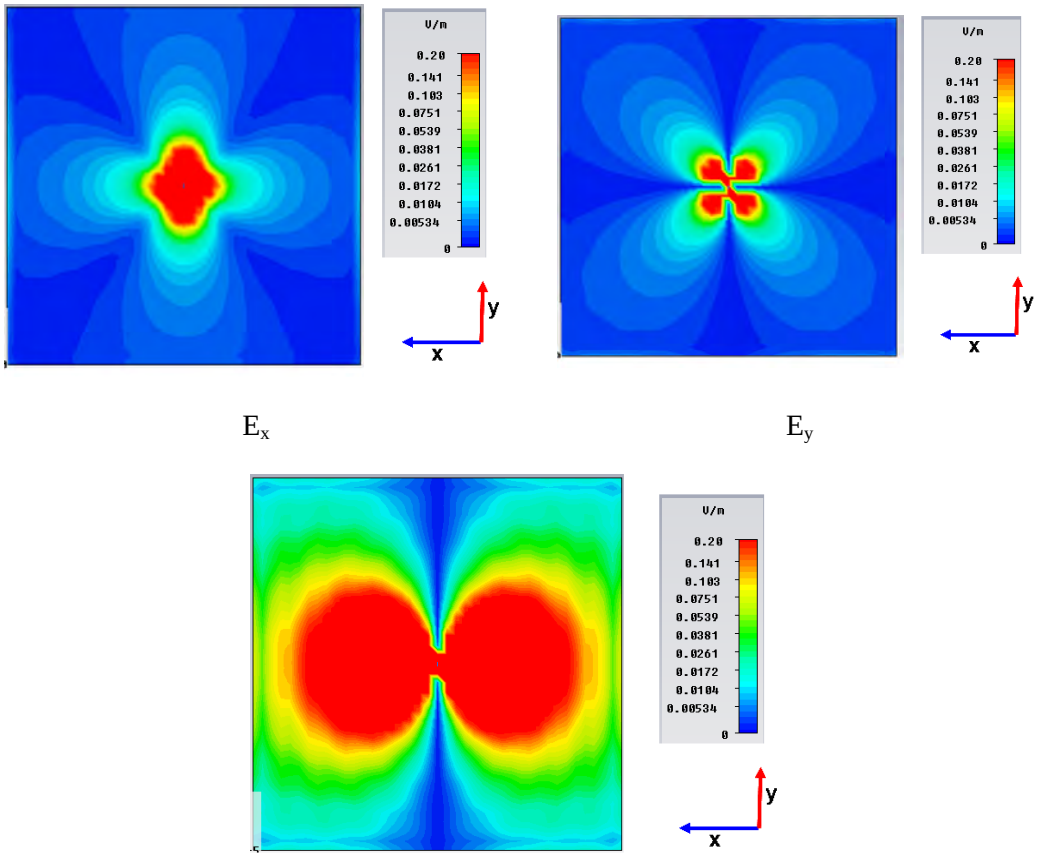

E_x E_y

E_z

Fig. 5.11 Near field distribution of the dipole antenna on a muscle phantom at 2.45 GHz (Details as Fig. 5.9)

5.6. TRANSMISSION CHANNEL ON A FLAT RECTANGULAR PHANTOM

5.6.1 Homogeneous Phantom

In order to investigate the radio channel between two short dipole antennas on a human torso a number of computer simulations with CST Microwave Studio have been performed, on a flat phantom of body tissue material. Phantoms with both muscle and fat tissue properties were simulated while antennas were mounted 5 mm above them.

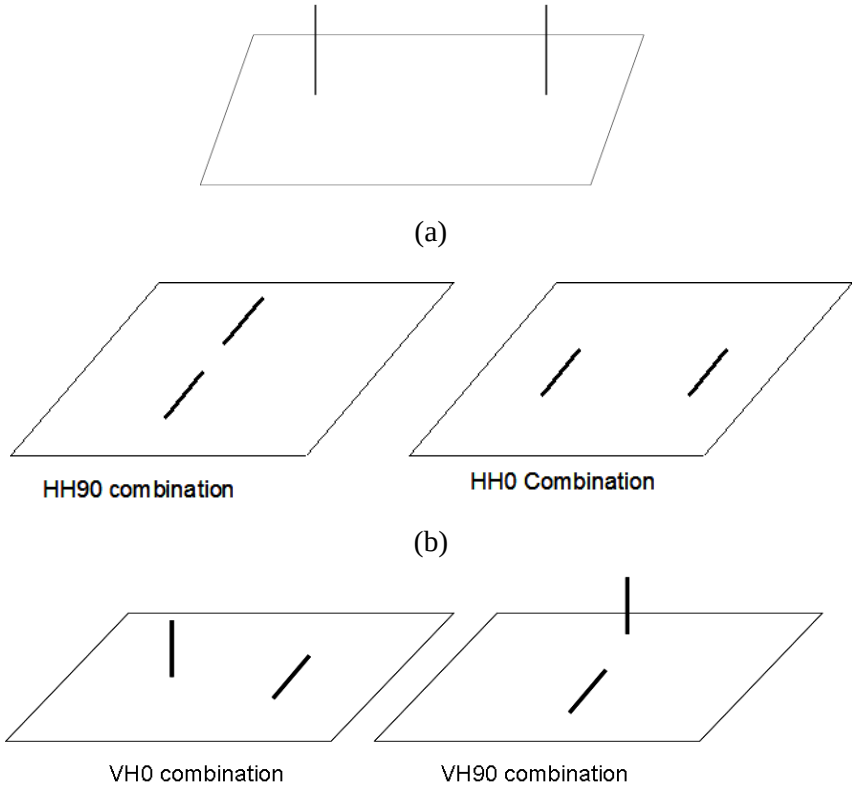

Fig. 5.12 Antenna combinations used in simulations, (a) VV combination (b) HH combination, (c) VH combination,
(V = Vertical, H = Horizontal)

The length and the width of the rectangular phantom were both 600 mm, and its thickness was 50 mm for the muscle tissue and 200 mm for fat, respectively. The distance between two antennas is increased from 10 cm to 60 cm and at each case the S_{21} parameter is extracted at 2.45 GHz. Fig. 5.12 shows different vertical and horizontal dipole arrangements which are considered in the simulation. Fig. 5.12(a) shows two dipoles vertical to the surface. In Fig. 5.12(b) dipoles horizontal to the surface aligned and facing each other indicated by HH90 and HH0, respectively. Fig. 5.12(c) shows combination of vertical and horizontal dipoles named as VH0 and VH90.

Fig. 5.13 shows the simulated S_{21} versus distance for the arrangements shown in Fig. 5.12. The S_{21} of all the configurations is normalised to free space S_{21} value for the VV combination at the distance of 10 cm. As expected, the pair of dipole antennas vertical to the surface provides the strongest link. The path gain of the VV combination is almost higher 10 dB on fat, and 20 dB on muscle, than the second strongest link, that is HH90. Also, placing the pair of vertical dipoles on the phantom made of fat and muscle reduces the path gain by 17 and 31 dB in comparison to the free space. The horizontal antennas which are aligned with each other (HH90 arrangement) provide a stronger link in comparison to the HH0 arrangement in which the antennas face to each other and is the conventional arrangement used in free space. The two combinations of vertical and horizontal dipoles, namely VH0 and VH90 yield very different path gains from each other. In the VH90 arrangement which the vertical dipole is placed in line with the horizontal dipole, the path gain and attenuation rate is very similar to the HH90 combination. However, VH0 path gain is much lower than all the combinations, which implies that the horizontal dipole provides a different mode from vertical dipole. Comparing the results on the fat and muscle provides good insight on the effect of the material property on the path gain variation versus distance. On fat the level of the path gain is higher compared to the muscle, but it does not support the wave as tight as the muscle and the path gain attenuates faster versus the distance.

Since, the horizontal dipole field is not symmetrically distributed around the antenna, the orientation of the transmitter and receiver position relative to each other at a fixed distance is very important and affects the path gain. In the previous section, just two orientations, $\varphi=0°$ and $\varphi=90°$, which excite distinctive modes, TE and TM, were examined. In the following, four directions are simulated. Fig. 5.14 shows the configuration. The antennas are spaced by 400 mm on a fat phantom. The results, shown in Fig.5.15 at 0 deg, suggest that when pure TE mode is excited, the level of the signal is very low for all the possible combinations, but by moving antenna to 30 deg, the received signal increases significantly, due to the excitation of

a TM mode. From 30 to 90 deg, the path gain improvement is within few dBs and the antenna position is not very crucial.

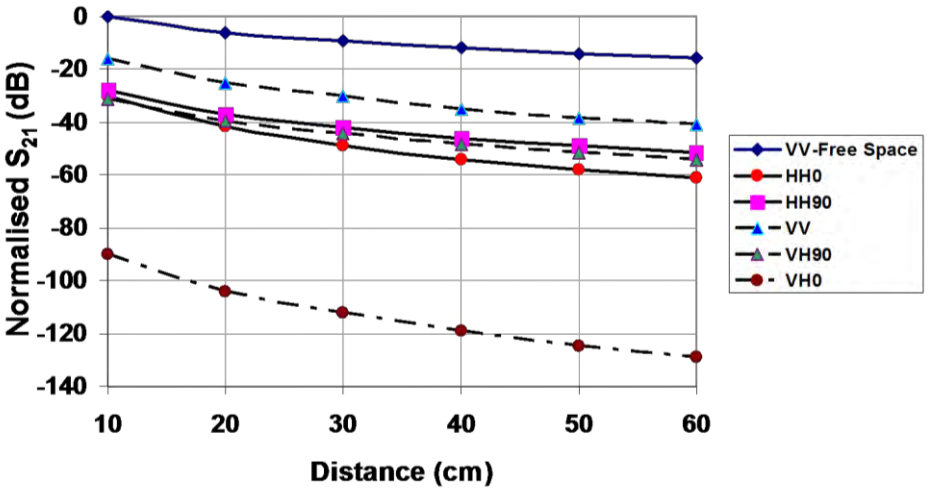

(a)

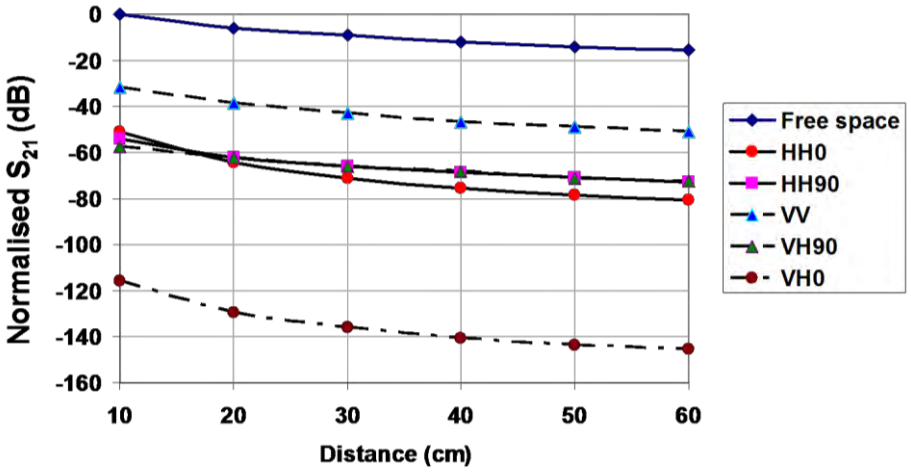

(b)

Fig. 5.13 Transmission channel gain (S_{21}) versus distance for the different antenna combinations of Fig. 5.12, (a) Fat phantom, (b) Muscle phantom
(S_{21} of all the configurations is normalised to value of free space S_{21} for VV combination at the distance of 10 cm)

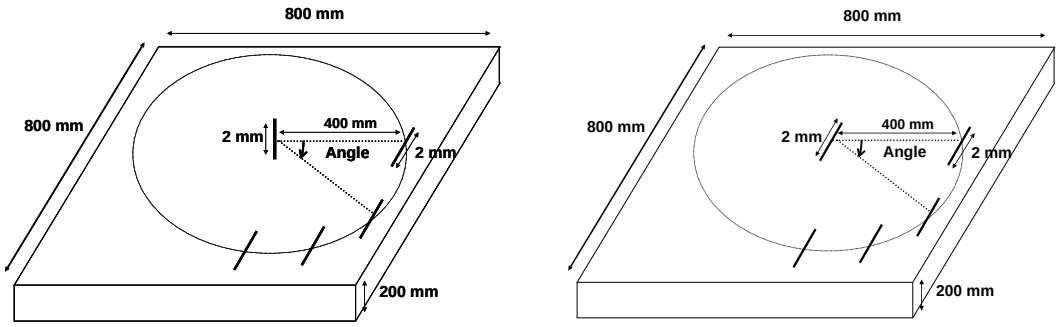

(a) (b)

Fig. 5.14 Vertical and horizontal dipole arrangements at different directions on fat phantom

(a) VH arrangement, (b) HH arrangement

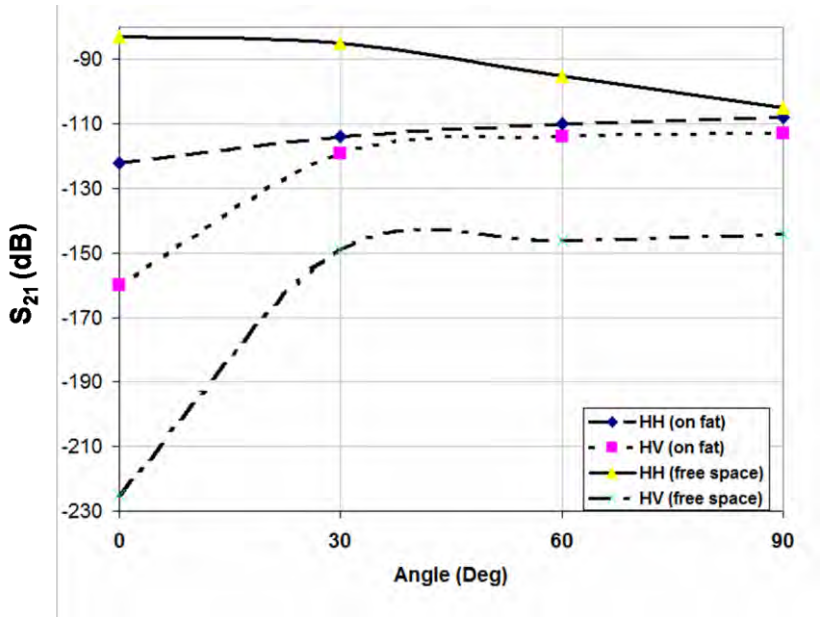

Fig. 5.15 Transmission channel gain versus angle orientations of Fig. 5.14

5.6.2 Multilayer Phantom

In order to compare the single and a multilayer phantom, simulations were made of two identical monopole antennas, resonating at 2.45 GHz, as transmitter and receiver, respectively, placed 5 mm away from a three layer phantom made of skin, fat and muscle as shown in Fig. 5.16. The monopole was modelled by a 25 mm wire placed above a circular ground plane with the radius of 20 mm. To feed the antenna a coaxial line was used which was fed with a

50 Ohms discrete port. The thickness of skin and muscle is fixed at 2 mm and 20 mm, but the fat layer is varied from 5 to 30 mm in 5mm steps. Fig. 5.17(a) shows the simulated S_{21} between the antennas. The increase in the thickness of the fat layer thickness from 5 to 25 mm increases the path gain by 5 dB at 80 cm distance. Further increase of the thickness, reduces the path gain by few dBs. Fig. 5.17(b) shows the Poyinting vector in the X direction. The penetrated power in the muscle layer is significantly reduced by increasing the thickness of the fat layer up to 25 mm. Some weakly trapped energy can be observed in the fat layer, but this progressively leaks out into free space as the distance from the antenna increases. However, it is not very clear what causes the decrease of the path gain when the fat layer thickness is changed from 25 mm to 30 mm, as the Poyinting vector distribution is very similar in the two cases. This may be explained from the transmission equivalent circuit theory of the layered lossy dielectric model. The variation of the fat layer thickness will change the surface impedance. This means that both the real and imaginary part of the surface impedance are increased or decreased and as explained in section 5.2, any change in these two parameters affects the attachment and attenuation rate of the surface wave on the surface.

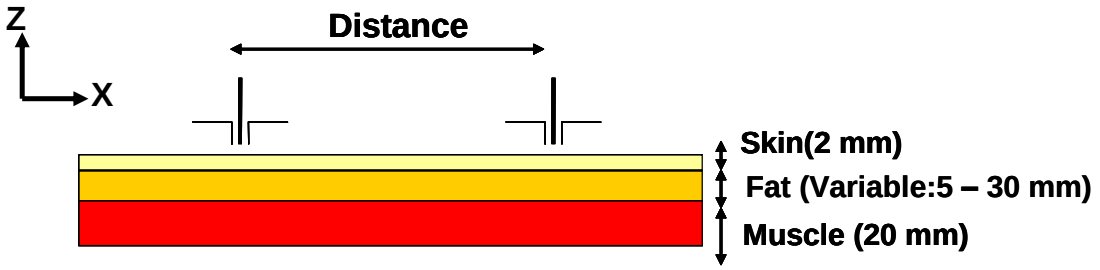

Fig. 5.16 Multilayer phantom schematic

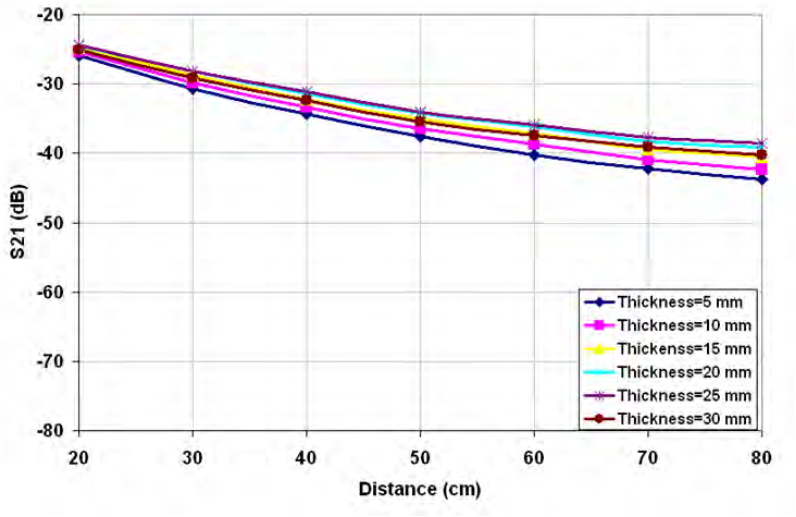

(a)

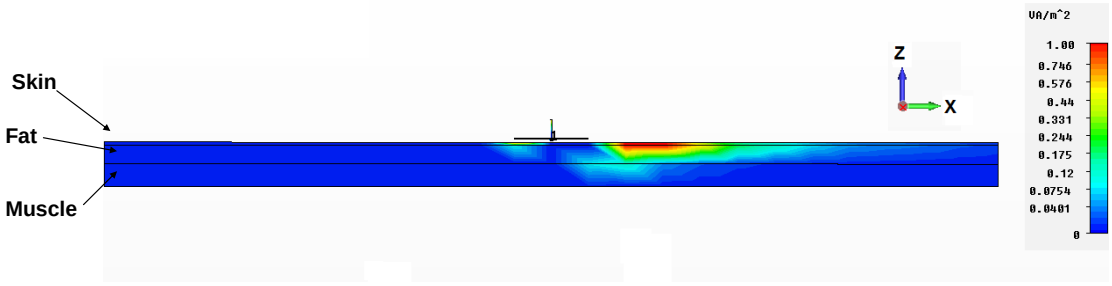

(b)

Fig. 5.17 (a) Path gain of monopole on the multilayer structure of Fig. 5.16, (b) Maximum value of the Poynting vector at every spatial point, within one period of time, on the multilayer phantom for the fat with a thickness of 25 mm in the ZX Plane

5.7. CREEPING WAVES ON A CYLINDER

The Norton wave analysis describes the surface wave excitation for sources on flat surfaces. This can be useful in helping to provide understanding for some parts of the body such as the chest or the back. However, insight into propagation on the limbs and around the trunk can be gained by examining creeping waves on a cylinder. Generally, the term of creeping waves is usually used to describe all type of azimuthally propagating waves on a cylinder. Many investigations have been done to understand the wave propagation around the cylinder [87-89]. Most of the work focused on metallic or coated cylinders, and different analytical methods were used to derive the solution of the wave propagation around them. The

waves are classified regarding their attenuation rate and phase velocity [88]. But less work has been done on exciting different waves around the cylinder by practical antenna.

In this section, an analytical method, derived from Maxwell equations, is used to solve the field distribution around the cylinder with electric properties representative of human tissues for a parallel point source. In order to find the total field of a point source close to an infinite cylinder, the easiest way is to solve the problem for an infinite line source and then convert it to a point source by performing an inverse Fourier transform on the source along the vertical spectral coordinate (k_z). This method is a well-known way to derive the small dipole field distribution in the presence of a metallic or dielectric cylinder. In the current work, it is used to confirm the simulation results done using CST Microwave Studio software. In addition, due to faster calculation time, it can be also used for further investigation of the effect of tissue properties and antenna distance from the cylinder.

5.7.1 Line Source Excitation

Suppose an infinite lossy dielectric cylinder of radius a is oriented along the Z axis, as shown in Fig. 5.18. An infinite source of constant electric current (I_e) is located at d distance from the surface of the cylinder. The total field in and outside of the cylinder can be calculated by superposing the incident field (E^i) and scattered field (E^s), that is,

$$E^t = E^i + E^s \tag{5-42}$$

The electric field generated in the whole space by the line source in the absence of the scatterer (cylinder) is given by [90]

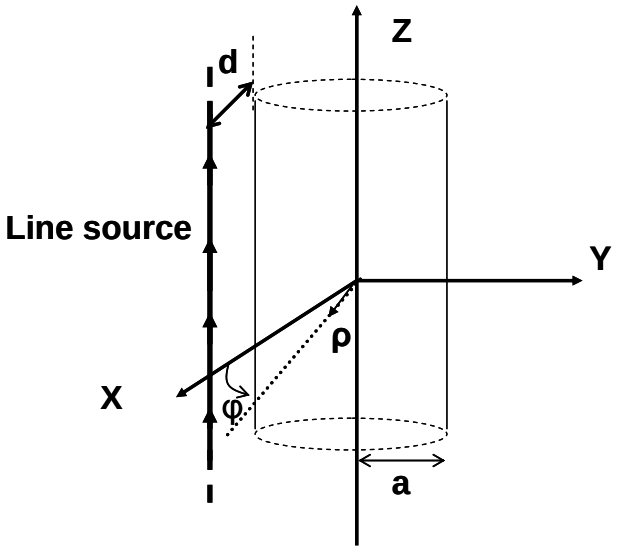

Fig. 5.18 Parallel line source in the Z direction placed at d distance in front of infinite cylinder with radius a

$$E_z^i = -\frac{\beta^2 I_e}{4\omega\varepsilon} H_0^{(2)}\left(k_\rho \left|\rho - \rho'\right|\right) \tag{5-43}$$

where ρ is the radial coordinate, ρ' is the line source position, ω is the angular frequency , ε is the free space permittivity, $H_o^{(2)}$ represents a Hankel function of the second kind with order 0 and k_ρ is the propagation constant given in (5-49).

By the addition theorem for Hankel functions, we can write (5-43) as [90]

$$E_z^i = \begin{cases} \sum_{n=-\infty}^{n=\infty} C_n J_n\left(k_\rho \rho\right) e^{jn(\varphi-\varphi')} e^{-jk_z z} & \rho \le \rho' \\ \sum_{n=-\infty}^{n=\infty} C_n{}' H_n^{(2)}\left(k_\rho \rho\right) e^{jn(\varphi-\varphi')} e^{-jk_z z} & \rho \ge \rho' \end{cases} \tag{5-44}$$

where $H_n^{(2)}$, J_n represent a Hankel function of the second kind with order n and a Bessel function with order of n, respectively and C_n and C_n' are the coefficients given in (5-45) and (5-46).

$$C_n = -\frac{k_\rho{}^2 I_e}{4\omega\varepsilon} H_n^{(2)}\left(k_\rho \rho'\right) \tag{5-45}$$

$$C_n{}' = -\frac{k_\rho{}^2 I_e}{4\omega\varepsilon} J_n\left(k_\rho \rho'\right) \tag{5-46}$$

The corresponding magnetic field can be found by using Maxwell's equation [90]

$$H^i = \frac{-1}{j\omega\mu}\left(\nabla \times E^i\right) = \frac{-1}{j\omega\mu}\left(\frac{1}{\rho}\frac{\partial E_z{}^i}{\partial \varphi}\hat{a}_\rho - \frac{\partial E_z{}^i}{\partial \rho}\hat{a}_\varphi\right) \tag{5-47}$$

Then,

$$H_\varphi^i = \frac{1}{j\omega\mu}\frac{\partial E_z^i}{\partial \rho}\hat{a}_\varphi = \begin{cases} \dfrac{1}{j\omega\mu} k_\rho \sum_{n=-\infty}^{n=\infty} C_n J_n{}'\left(k_\rho \rho\right) e^{jn(\varphi-\varphi')} e^{-jk_z z} & \rho \le \rho' \\ \dfrac{1}{j\omega\mu} k_\rho \sum_{n=-\infty}^{n=\infty} C_n{}' H_n{}'\left(k_\rho \rho\right) e^{jn(\varphi-\varphi')} e^{-jk_z z} & \rho \ge \rho' \end{cases} \tag{5-48}$$

k_ρ is the propagation constant at ρ direction and defined as:

$$k_\rho = \sqrt{k^2 - k_z^2} \tag{5-49}$$

where $k = \omega\sqrt{\mu\varepsilon}$ is the wavenumber and k_z is propagation constant at Z direction.

The scattered field which is produced by the current induced on the surface of the cylinder acts as a secondary radiator. The z component of the scattered field can be defined as:

$$E_z^s = \sum_{n=-\infty}^{n=\infty} A_n' H_n^{(2)}(k_\rho \rho) e^{jn(\varphi-\varphi')} e^{-jk_z z} \qquad a \le \rho \le \rho', \rho \ge \rho' \qquad (5\text{-}50)$$

where A_n' are coefficients yet to be found.

The total electric field inside the cylinder can be found from:

$$E_z^t = \sum_{n=-\infty}^{n=\infty} A_n J_n(k_{\rho d} \rho) e^{jn(\varphi-\varphi')} e^{-jk_z z} \qquad \rho \le a \qquad (5\text{-}51)$$

and the corresponding magnetic field can be obtained for the scattered and total field from equation (5-47)

$$H_z^s = \frac{k_\rho}{j\omega\mu} \sum_{n=-\infty}^{n=\infty} A_n' H_n^{(2)'}(k_\rho \rho) e^{jn(\varphi-\varphi')} e^{-jk_z z} \qquad a \le \rho \le \rho', \rho \ge \rho' \qquad (5\text{-}52)$$

$$H_z^t = \frac{k_{\rho d}}{j\omega\mu} \sum_{n=-\infty}^{n=\infty} A_n J_n'(k_{\rho_d} \rho) e^{jn(\varphi-\varphi')} e^{-jk_z z} \qquad \rho \le a \qquad (5\text{-}53)$$

The coefficient, A_n and A_n' can be found by applying the boundary condition at the surface of the cylinder. In this problem, the tangential component of electric and magnetic fields are equal inside and outside of the cylinder.

$$E^t\Big|_{\rho=a^-} = E^t\Big|_{\rho=a^+} \tag{5-54}$$

$$H^t\Big|_{\rho=a^-} = H^t\Big|_{\rho=a^+} \tag{5-55}$$

which by use of equation (5-42) can be expressed as:

$$E^t\Big|_{\rho=a^-} = \left(E^s + E^i\right)\Big|_{\rho=a^+} \tag{5-56}$$

$$H^t\Big|_{\rho=a^-} = \left(H^s + H^i\right)\Big|_{\rho=a^+} \tag{5-57}$$

for simplicity of equations, the summation and $e^{jn(\varphi-\varphi')}$ and $e^{jk_z z}$ terms will be implicit in the next few equation:

$$A_n J_n\left(k_{\rho d} a\right) = C_n J_n\left(k_\rho a\right) + A_n' H_n^{(2)}\left(k_\rho a\right) \tag{5-58}$$

$$A_n \frac{k_{\rho d}}{j\omega\mu} J_{nd}\left(k_{\rho d} a\right) = C_n \frac{k_\rho}{j\omega\mu} J_n'\left(k_\rho a\right) + A_n' \frac{k_\rho}{j\omega\mu} H_n^{(2)\prime}\left(k_\rho a\right) \tag{5-59}$$

where A_n and $A_{n'}$ are the unknown coefficients, which can be calculated by solving the matrix given in (5-60) which is derived by rearranging the equations (5-58) and (5-59).The matrix equation is

$$\begin{bmatrix} J_n(k_{\rho d}a) & -H_n^{(2)}(k_\rho a) \\ \frac{k_{\rho d}}{k_\rho} J_n'(k_{\rho d}a) & -H_n^{(2)'}(k_\rho a) \end{bmatrix} \begin{bmatrix} A_n \\ A_n' \end{bmatrix} = \begin{bmatrix} C_n J_n(k_\rho a) \\ C_n J_n'(k_\rho a) \end{bmatrix} \tag{5-60}$$

which is solved to give

$$A_n = \frac{\left(-C_n J_n(k_\rho a) H_n^{(2)'}(k_\rho a) + C_n J_n'(k_\rho a) H_n^{(2)}(k_\rho a)\right)}{\left(-J_n(k_{\rho d}a) H_n^{(2)'}(k_\rho a) + \frac{k_{\rho d}}{k_\rho} J_n'(k_{\rho d}a) H_n^{(2)}(k_\rho a)\right)} \tag{5-61}$$

$$A_n' = \frac{\left(C_n J_n'(k_\rho a) J_n(k_{\rho d}a) - \frac{k_{\rho d}}{k_\rho} C_n J_n(k_\rho a) J_n'(k_{\rho d}a)\right)}{\left(-J_n(k_{\rho d}a) H_n^{(2)'}(k_\rho a) + \frac{k_{\rho d}}{k_\rho} J_n'(k_{\rho d}a) H_n^{(2)}(k_\rho a)\right)} \tag{5-62}$$

The theory used for the other orientation of the source, is almost the same as the previous orientation, the only difference being the orientation of the current, which is now in the φ direction, instead of Z, as shown Fig. 5.19. Aligning the antenna in the φ direction can produce both magnetic and electric field in the Z direction.

Incident electric field can be described in a way similar to equation (5-44) and the incident magnetic field is defined as:

$$H_z^i = \begin{cases} \sum_{n=-\infty}^{n=\infty} D_n J_n(k_\rho \rho) e^{jn(\varphi-\varphi')} e^{-jk_z z} & \rho \le \rho' \\ \sum_{n=-\infty}^{n=\infty} D_n' H_n^{(2)}(k_\rho \rho) e^{jn(\varphi-\varphi')} e^{-jk_z z} & \rho \ge \rho' \end{cases} \tag{5-63}$$

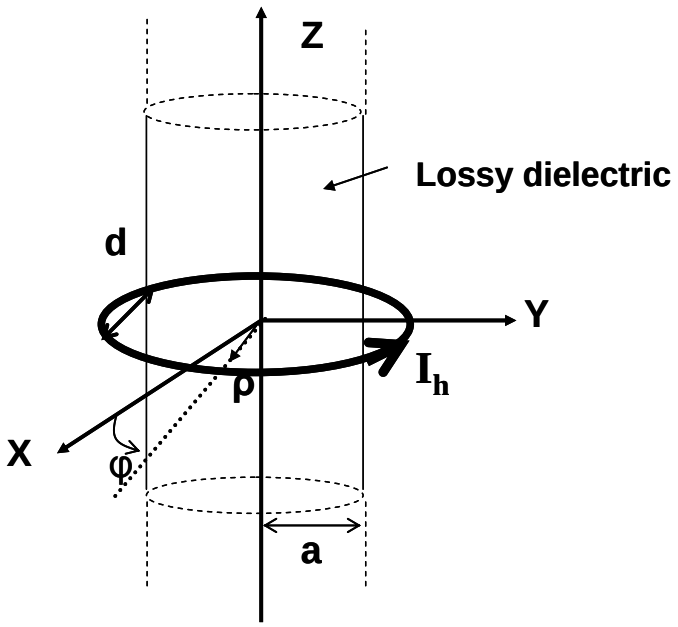

Fig. 5.19 Parallel line source in φ direction placed at d distance in front of infinite cylinder with radius a, and lossy dielectric properties

where C_n and C_n' and D_n and D_n' are, [91],

$$C_n = -I_h \frac{nk_z}{4\omega\varepsilon\rho'} H_n^{(2)}\left(k_\rho \rho'\right) \tag{5-64}$$

$$C_n' = -I_h \frac{nk_z}{4\omega\varepsilon\rho'} J_n\left(k_\rho \rho'\right) \tag{5-65}$$

$$D_n = -I_h k_\rho \frac{1}{4j} H_n^{(2)\prime}\left(k_\rho \rho'\right) \tag{5-66}$$

$$D_n' = -I_h k_\rho \frac{1}{4j} J_n'\left(k_\rho \rho'\right) \tag{5-67}$$

The other components of the electromagnetic field can be determined by using following equations:

$$E = \frac{1}{k_\rho^{\,2}}\left(-jk_z \nabla_s E_z + j\omega\mu \hat{z} \times \nabla_s H_z\right) \tag{5-68}$$

$$H = \frac{1}{k_\rho^{\,2}}\left(-jk_z \nabla_s H_z + j\omega\mu \hat{z} \times \nabla_s H_z\right) \tag{5-69}$$

where

$$E = E_\varphi \hat{\varphi} + E_\rho \hat{\rho} \tag{5-70}$$

$$H = H_\varphi \hat{\varphi} + H_\rho \hat{\rho} \tag{5-71}$$

$$\nabla_s = \hat{\rho}\frac{\partial}{\partial \rho} + \hat{\varphi}\frac{jn}{\rho} \tag{5-72}$$

$$\hat{z} \times \nabla_s = \hat{\varphi}\frac{\partial}{\partial \rho} - \hat{\rho}\frac{jn}{\rho} \tag{5-73}$$

Simplifying equation (5-68) and (5-69) by applying the operators given in (5-72) and (5-73) will result in φ components for the both electric and magnetic fields as follows:

$$E_\varphi^i = \begin{cases} \dfrac{1}{k_\rho^{\,2}}\left(C_n \dfrac{nk_z}{\rho} J_n(k_\rho \rho) + j\omega\mu k_\rho D_n J_n'(k_\rho \rho)\right) & \rho \le \rho' \\ \dfrac{1}{k_\rho^{\,2}}\left(C_n' \dfrac{nk_z}{\rho} H_n^{(2)}(k_\rho \rho) + j\omega\mu k_\rho D_n' H_n^{(2)'}(k_\rho \rho)\right) & \rho \ge \rho' \end{cases} \tag{5-74}$$

$$H_\varphi^i = \begin{cases} \dfrac{1}{k_\rho^{\,2}}\left(D_n \dfrac{nk_z}{\rho} J_n(k_\rho \rho) - j\omega\varepsilon_0 k_\rho C_n J_n'(k_\rho \rho)\right) & \rho \le \rho' \\ \dfrac{1}{k_\rho^{\,2}}\left(D_n' \dfrac{nk_z}{\rho} H_n^{(2)}(k_\rho \rho) - j\omega\varepsilon_0 k_\rho C_n' H_n^{(2)'}(k_\rho \rho)\right) & \rho \ge \rho' \end{cases} \tag{5-75}$$

The z component of the scattered and total magnetic field inside the cylinder can be described in a way similar to equation (5-44) and (5-63). The z component of the scattered field can be defined as:

$$H_z^s = \sum_{n=-\infty}^{n=\infty} B_n' H_n^{(2)}\left(k_\rho \rho\right) e^{jn(\varphi-\varphi')} e^{-jk_z z} \qquad a \le \rho \le \rho', \rho \ge \rho' \tag{5-76}$$

The total electric field inside the cylinder can be found from:

$$H_z^t = \sum_{n=-\infty}^{n=\infty} B_n J_n\left(k_{\rho d} \rho\right) e^{jn(\varphi-\varphi')} e^{-jk_z z} \qquad \rho \le a \tag{5-77}$$

The coefficients of A_n, A_n', B_n and B_n' can be found by applying the boundary condition given in equation (5-55) and (5-56) and solving the matrix given in (5-78)

$$\begin{bmatrix} J_n\left(k_{\rho d} a\right) & -H_n^{(2)}\left(k_\rho a\right) & 0 & 0 \\ -\frac{F_\varepsilon \varepsilon_r}{k_{\rho d}} J_n'\left(k_{\rho d} a\right) & -\frac{F_\varepsilon}{k_\rho^2} H_n^{(2)'}\left(k_\rho a\right) & \frac{F_m}{k_{\rho d}^2} J_n\left(k_{\rho d} a\right) & -\frac{F_m}{k_\rho^2} H_n^{(2)}\left(k_{\rho d} a\right) \\ \frac{F_m}{k_{\rho d}^2} J_n'\left(k_{\rho d} a\right) & -\frac{F_m}{k_\rho^2} H_n^{(2)'}\left(k_\rho a\right) & \frac{F_\mu \mu_r}{k_{\rho d}} J_n\left(k_{\rho d} a\right) & -\frac{F_\mu}{k_\rho} H_n^{(2)'}\left(k_\rho a\right) \\ 0 & 0 & J_n\left(k_{\rho d} a\right) & -H_n^{(2)}\left(k_\rho a\right) \end{bmatrix} \begin{bmatrix} A_n' \\ A_n \\ B_n' \\ B_n \end{bmatrix} = \begin{bmatrix} E_z^i \\ H_\varphi^i \\ E_\varphi^i \\ H_z^i \end{bmatrix} \tag{5-78}$$

where $F_m = mk_z/a$, $F_\mu = j\omega\mu$, $F_\varepsilon = j\omega\varepsilon_0$, E_z^i, H_φ^i, E_φ^i and H_z^i at r = a can be calculated from equation (5-74), (5-75) and (5-63) respectively.

5.7.2 Point Source Excitation

The point source solution can be derived by integrating the line source field for all values of k_z [91]

$$E_{point} = \frac{1}{2\pi}\int_{-\infty}^{\infty} E^{t}_{line}(k_z)dk_z \tag{5-79}$$

Because $k_\rho = \sqrt{k_0^{\,2} - k_z^{\,2}}$, the integrand has two poles at $k_z = \pm k_0$ which can cause singularity in the calculation of the integrals. Therefore, the integral should be performed in the complex plane with deformation of the contour in order to avoid the poles. The suggested contour given in [91-92] and depicted in Fig. 5.20, is used to do the numerical integration and can be defined as:

$$Im(k_z) = C\left(1 - \left(\frac{Re(k_z) - k_0}{k_0}\right)^2\right) \tag{5-80}$$

where C is a constant parameter and should be selected carefully.

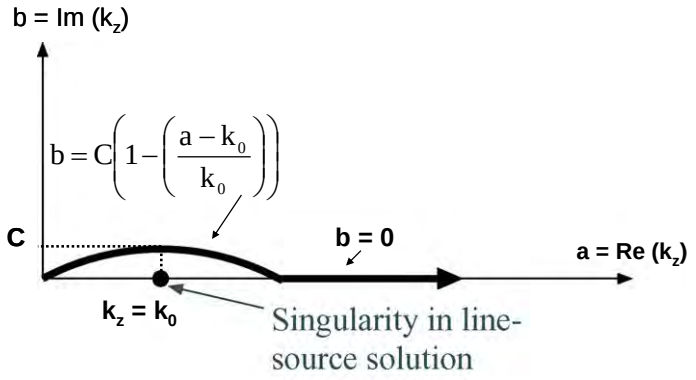

Fig. 5.20 A parabolic contour around the singularity at $k_z = k_0$

It is worth noting that k_ρ can be real or imaginary for k_z smaller or greater than k_0 respectively, but choosing the right sign for k_ρ in order to satisfy the far field condition is required. To choose the right sign, the far field radiation condition of the antenna is used. At large distances from the antenna, the Hankel function can be simplified to:

$$H_n^{(2)}(k_\rho \rho) = \sqrt{\frac{2}{\pi z}} e^{-jk_\rho \rho + j(2n+1)\pi/4} \tag{5-81}$$

In a physical situation, in the far field region, the integrand should be an outgoing wave and no wave should return from infinity, which is the so-called radiation condition. To satisfy this condition, k_ρ should be chosen in 4th quadrant of the complex plane, that is, $\mathrm{Re}(k_\rho) > 0$ and $\mathrm{Im}(k_\rho) < 0$. The real part shows the outgoing phase progression and imaginary part represent attenuation of the wave to the infinity [91-92].

Although the integration is supposed to be done over k_z from $-\infty$ to $+\infty$, the fields with a large value of k_z decay rapidly and their contribution to the total field is small. To decrease computational time, the integration can be done from 0 to $+\infty$ due to integrant symmetry property and then its value can be doubled. Typically, the integration can be done within $-2k_z$ to $2k_z$ for the current problem. The main problem with this method is the convergence of the summation. Generally this method suffers from slow convergence. On the other hand, the summation cannot be done over a large number of terms, since the Hankel function increases exponentially and leads to infinity for large number of n. To achieve the best result, it is necessary to modify values for C, n (number of terms) and the maximum value of k_z, accordingly. Convergence of the field for large k_z values requires increasing of the number of terms used in the summation. On the other hand, small k_z and large n value can cause

overflow in Hankel function calculation. To avoid these problems, small n must be used for small k_z and large n for large k_z.

Fig. 5.21 shows the transverse field at the azimuth plane of an infinitely long cylinder, when the point source is placed parallel to the cylinder surface and oriented along the φ direction. The source is placed at φ = 0˚, 2 mm away from the cylinder surface which has a 150 mm radius made of muscle tissue. Table 5.3 shows the number of terms, n, for different k_z values. The constant parameter in the contour expression, C, was fixed at 20. It is worth noting that numbers given in Table 5.3 were derived for C = 20. Any change in C may affect the convergence of the summation and new values should be derived for n and k_z. To verify the analytical results, a 2 mm dipole was placed on the cylinder with similar specification but with a truncated length (1000 mm) and simulated in CST. The simulated field is shown in the same figure. Since the behaviour of the two curves are different up to φ = 20°, they are normalised to their values at φ = 20° to aid comparison. Beyond φ = 20°, analysis and simulation results are in very good agreement. The difference of the field behaviour from φ= 0° to 20°, is due to use of a small dipole antenna instead of a point source in the simulation. The superposition of the rays creeping in both directions around the cylinder causes ripples in the field. As is expected, the analytical method is much faster than the CST simulations. The analytical method yields the field in less than a minute. However, the simulation for the similar problem in CST Microwave studio takes several hours to solve the problem.

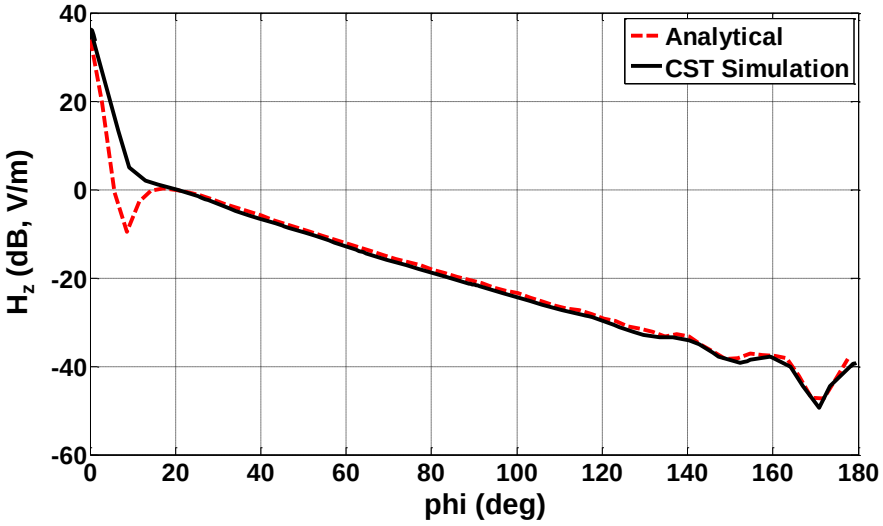

Fig. 5.21 H_z as a function of φ for a φ directed point source close to dielectric cylinder (Geometry as in Fig. 5.19, d = 2 mm, a =150 mm, Fields are normalised to their values at φ = 20˚)

Table 5.3 Number of terms (n) used in the summation for different k_z values for a point source parallel to the cylinder surface and pointed to the φ direction for, C=20

	$0 < k_z < 0.5$	$0.5 < k_z < 0.9$	$0.9 < k_z$
Number of terms, n	220	280	300

For the other antenna orientation, shown in Fig. 5.18, the transverse electric field in the azimuth plane of the cylinder is shown in Fig. 5.22. In this case, the point source is placed parallel to the cylinder surface and oriented along Z axis. Table 5.4 shows values for n. As is shown, the analytical results are in overall agreement with the simulation results. However, the analytical method showed more loss at the shadowing area (φ=120° to φ=180°). In the CST Microwave Studio simulation the cylinder is truncated and its length is 1000 mm. The truncation can produce some reflections, which interferes in the shadowed area. In this area, the signal is very weak and even very weak reflections can change the antennas results. The reasoning was investigated by changing the length of the cylinder. Significant differences were observed in the results.

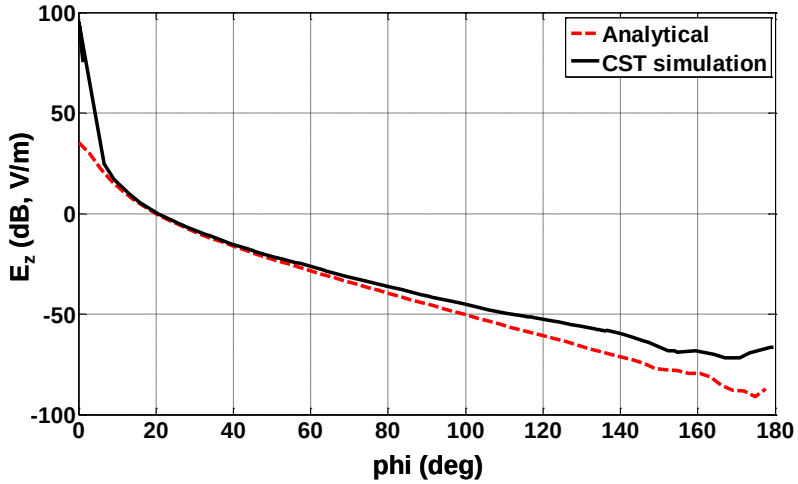

Fig. 5.22 E_z as a function of φ for a Z directed point source parallel to a dielectric cylinder, (Geometry as in Fig. 5.19, d = 2 mm, a =150 mm, Fields are normalised to their values at φ = 20˚)

Table 5.4 Number of terms (n) used in the summation for different k_z values for a point source parallel to the cylinder surface and pointed to the Z direction, C=20

	$0 < k_z < 0.9$	$0.9 < k_z < 1.1$	$1.1 < k_z < 2$
Number of terms, n	220	280	300

The attenuation of the field around the cylinder is exponential (see section 5.8) [P. S. Hall book]. The attenuation rate of the wave depends on the cylinder dielectric property and also its radius. The attenuation rate of the fields shown in Fig. 5.21 and 5.22 for the φ and Z directed sources are listed in Table 5.5. The φ directed source shows much less attenuation rate compared to the Z directed source. This reveals that that the antenna excites different modes at different directions, and the mode generated by φ directed source is well-supported by the cylinder phantom.

Table 5.5 Attenuation rate of the wave launched by Z and φ directed sources parallel to dielectric cylinder

	Z directed source	φ directed source
Attenuation rate	2.9	1.5

5.8. TRANSMISSION CHANNEL ON THE BODY

The results in the previous sections were flat and cylindrical phantoms. The human body can be very different from these canonical structures. In this section the importance of the actual body shape is investigated. Two arrangements of short parallel dipoles are simulated. On a body-shaped homogeneous fat phantom of a height of 170 cm, described in Chapter 4. One of the dipoles was placed on the left side of the abdomen, and the other in one of the following three positions, right ankle, right side of the chest, and right wrist. The antennas were placed almost 5 mm away from the body surface. Two different configurations of the dipoles were investigated namely, HH0 and HH90 explained in section 5.6. The distance between two antennas at two end of each channel is 77 cm, 37 cm and 33 cm in belt-ankle, belt-chest and belt-wrist, respectively. Fig. 5.23 shows the two arrangements for the three channels.

The simulated S_{21} values for the three different channels are shown in Fig. 5.24. As is evident from Fig. 5.24, the HH90 arrangement results in stronger S_{21} compared to the corresponding HH0 arrangement, for all the tested channels. For comparison, the results of two arrangements on the flat fat phantom at distances equal to the path length of each channel are shown in Fig. 5.24.

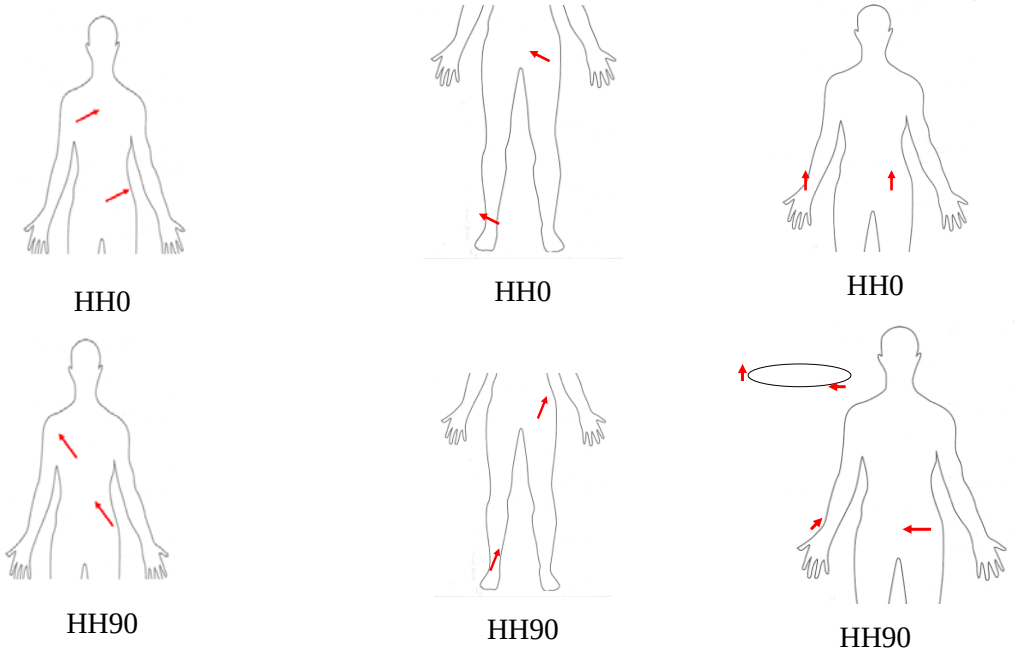

Fig. 5.23 Antenna arrangements on body phantom made of fat, (a) belt-chest (b) belt-ankle, (c) belt-wrist

The results suggest that, in the shadowed channels such as that to the wrist, the existence of surface and creeping wave which is excited by HH90 arrangement is more evident. In the belt-chest channel, the antenna is obstructed by the chest and similar to the wrist, HH90 provides higher path gain and the difference between two arrangements is more than the flat phantom. For the ankle link, the difference between the two arrangements is relatively smaller than the fat because the surface wave propagation is disrupted by the air gap between the two legs. Since the surface of the body between the two antennas is not flat but curvy, so that a number of transitions from surface wave to space wave (radiation) and vice versa may occur along the propagation path in spite of the flat phantom. However, even for the channels with fairly complicated geometry, such as the ankle and wrist channels, HH90 which excites TM surface wave mode shows better performance.

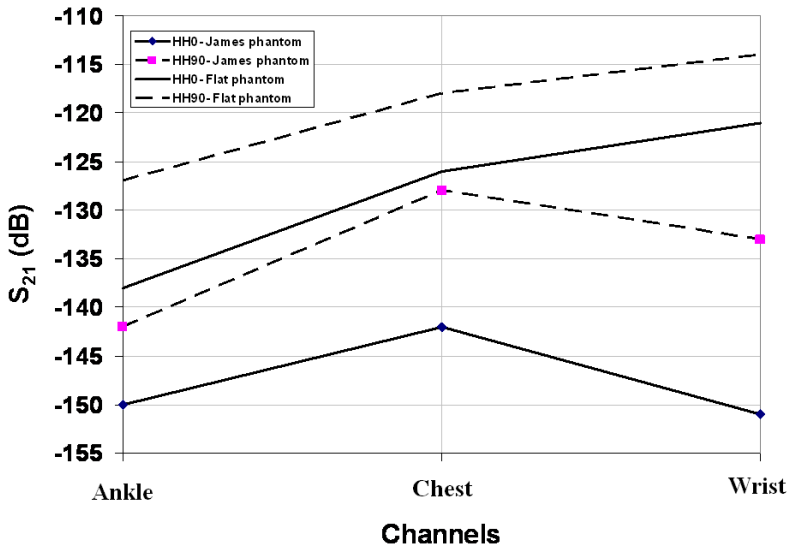

Fig. 5.24 Simulated S_{21} for the two horizontal dipole arrangements of Fig. 5. 23 at 2.45 GHz

(Electric properties of phantoms represent fat tissue: $\varepsilon_r = 5.3$, $\sigma = 0.11$ S/m)

5.8.1 Surface Wave Launching by On-Body Antennas

The analysis of the electric fields excited by a short dipole on the surface of a lossy dielectric, such as human tissue, demonstrate that these fields are due to two possible types of a surface wave, namely TM and TE. Each of these two modes attenuates with the distance according to a law independent of the type or parameters of the antenna or its orientation and is fully determined by the property of the surface. On the other hand, the relative amplitudes of the three components of the surface wave electric field (i.e. perpendicular to the surface, radial, and transverse) do depend on the orientation and type of the source. Therefore, an arbitrary antenna near the surface of the body, with an arbitrary current distribution, can be expected also to excite a mixture of the two surface wave modes, which attenuate with distance according to the same laws as the surface waves of the short dipoles.

For the purpose of comparing the surface wave launching ability of different antennas, the amplitudes of the three components of the surface wave field have to be obtained for each

antenna and compared. Since the TM mode is, in general, stronger on body tissues and therefore will contribute most significantly to the communication link, comparing only the components of the electric fields normal to the phantom surface (Z component) can be sufficient.

The field distributions on the surface of a human tissue phantom have been simulated in CST Microwave Studio for a number of practical small antennas shown in Fig. 5.25, namely planar inverted-F antenna (PIFA), printed inverted-F antenna (IFA), printed loop, patch antenna, and a half-wavelength dipole. They were placed 5 mm above a rectangular phantom made of either fat or muscle tissue with the surface dimension of 600 × 600 mm^2 and the height of 200 and 50 mm for the fat and muscle, respectively. Each antenna was excited with an S-parameter discrete port with 50 Ω internal impedance, providing 1 W input power. The antennas operate at 2.45 GHz and their dimensions are as follows:

Monopole:- *ground plane dia = 40 mm, top loading dia = 26 mm, height = 18 mm, wire dia = 5 mm.*

PIFA:- *ground plane (grey) = 30 mm × 30 mm with full metallisation on underside and feed strip (black) of width = 2mm, top plate (black) = 19 mm × 10 mm of height = 6mm, short 1mm from lower left hand corner of top plate, feed 2 mm from short*.

Patch: *substrate of 1.5 mm thick FR4, size = 80 mm × 80 mm, patch size= 35 mm × 27 mm, feed stip size=27 mm × 2.8 mm.*

Loop:- *substrate of 0.5 mm thick FR4, size = 40 mm × 40 mm, outer radius= 18 mm, inner radius= 16 mm, strip width = 2 mm.*

Dipole: *wire with a length of 50 mm and 1 mm radius, oriented parallel to the phantom surface.*

IFA: *substrate of 0.5 mm thick FR4, size = 40 mm × 30 mm, ground plane size = = 40 mm × 17 mm, feed strip= 17 mm × 2 m.*

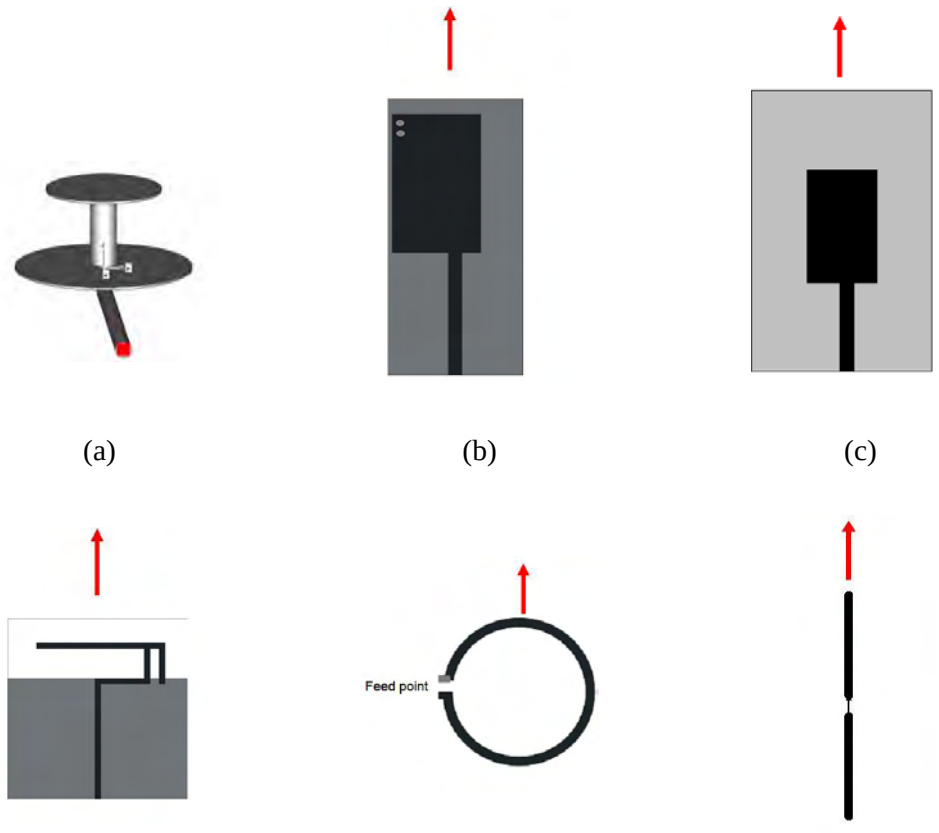

(a) (b) (c)

(d) (e) (f)

Fig. 5.25 Antenna structures used in surface wave coupling study,

(a) Monopole, (b) PIFA, (c) Patch, (d) IFA, (e) Loop, (f) Dipole

(arrow shows the assumed direction for field characterisation)

The electric field distribution, in the plane 5 mm above the phantom surface was obtained from the simulation, and the components of the field, E, were then fitted to the following expression:

$$E[dB] = E_1[dB] - \alpha \cdot 20\log_{10}(d/d_0) \tag{5-82}$$

where d_0 is a reference distance, and E_1 is the field value at this distance. In the rest of the chapter the reference distance will be chosen to be d_0 = 10 cm. The reference distance of 10 cm was chosen as it was empirically found to correspond to the lower bound of antenna separations over which field decayed experimentally.

The monopole antenna was found to launch only the TM mode of the surface wave, while the rest of the antennas launch a combination of TM and TE modes in different directions, much as the tangential short dipole discussed earlier. Fig. 5.26 shows the electric field (E_z) amplitude of a TM wave excited by the different antennas at different distances on the surface of the flat fat phantom in the direction indicated with an arrow in Fig. 5.25. Tables 5.5 and 5.6 give α and E_1 derived by fitting the model given by (5-79) to the simulated data.

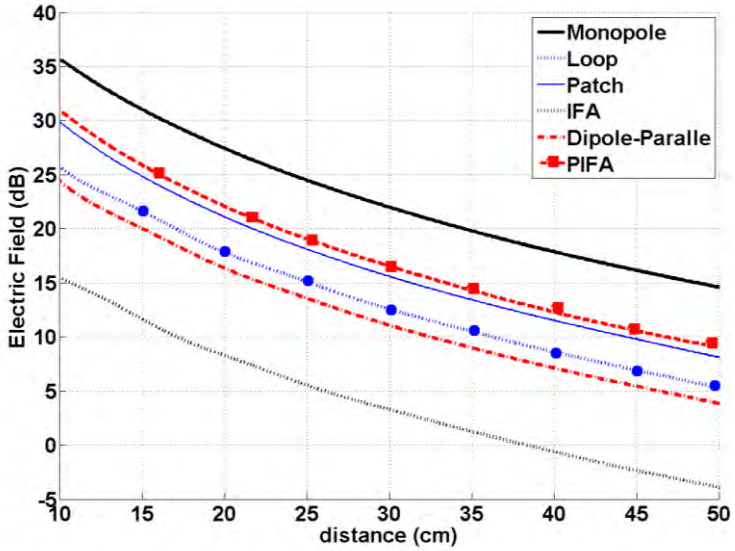

Fig. 5.26 Electric field variation versus distance for the antennas of Fig. 5.23 on the surface of the flat fat phantom

Table 5.6 Attenuation exponent of the surface wave, α, launched by antennas on the cylindrical surface of muscle and fat tissues at 2.45 GHz

	Monopole	Dipole	Loop	Patch	IFA	PIFA	Norton wave
Fat	1.7	1.6	1.6	1.6	1.5	1.7	1.6
Muscle	1.1	1.05	1.05	1.2	1.1	1.1	1.2

Table 5.7 Electric field amplitude, E_{1z} (dB), launched by antennas on the cylindrical surface of muscle and fat tissues at 2.45 GHz at the reference distance of 10 cm

	Monopole	Dipole	Loop	Patch	IFA	PIFA
Fat	36	26	27.5	31	16	31
Muscle	37	19.9	22	32.5	11	35

The small range of α variation, 1.5 to 1.7 on fat and 1.05 to 1.2 on muscle, suggests that all the antennas excite the TM mode of the surface wave similar to the Norton surface wave generated by a short dipole as described in section 5.3 which is given in Table 5.5. Simulation results are affected by the limited size of the phantom and cause small variation of the wave parameters, while the Norton results are on the infinite surface. Comparing the E_1 parameter

for different antennas, it can be seen that the monopole and IFA excite the strongest and the weakest surface waves, respectively, on both fat and muscle tissues. The antennas with a vertical polarization such as monopole, PIFA and patch are much more efficient than the horizontal polarised antenna such as loop, dipole and IFA and are less affected by the material type.

The angular patterns of E_{1z} on fat tissue, expressed in dB are shown in Fig. 5.27. The direction $\varphi = 0$ is indicated by an arrow for each of the antennas in Fig. 5.25. With the exception of the monopole, which excites the strongest surface waves in all the azimuth directions, the PIFA appears to be the best antenna for launching the TM surface wave in any direction, and the only one with an omni-directional pattern. All the other antennas have a figure-of-eight-shaped pattern, similar to the dipoles pattern. Among all the others, the half-wavelength dipole tangential to the surface appears to be the worst antenna for surface wave launching.

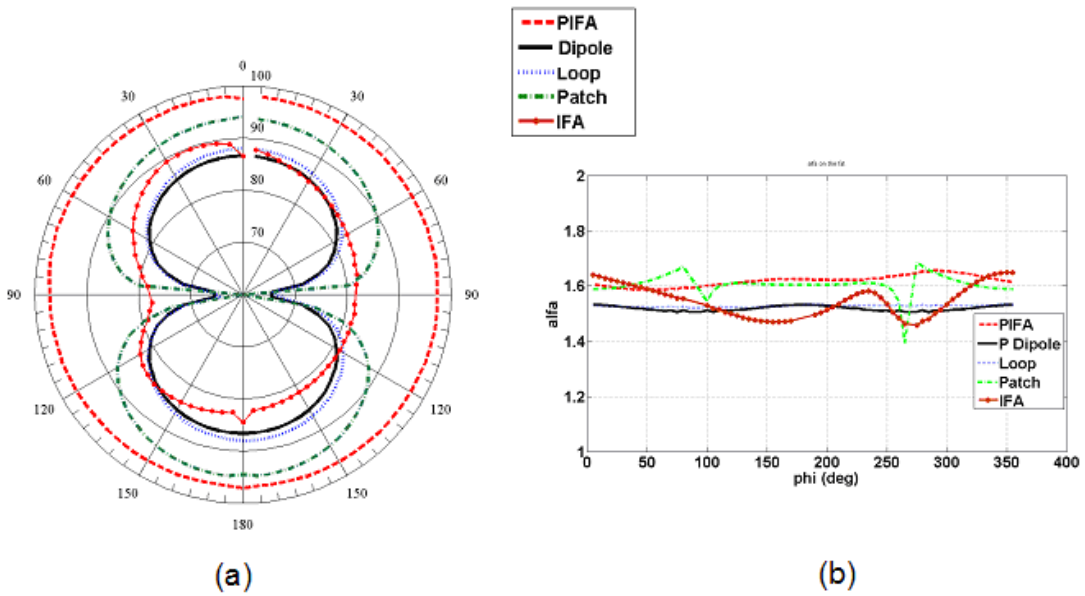

Fig. 5.27 Azimuthally variation of the parameters of the TM mode surface wave launched by body-mounted antennas of Fig.5.25 on fat tissue,
(a) E_{1z} (angle is φ, and radial scale is dB), (b) α.

In order to investigate how different antennas perform on a curved surface they were simulated on a half cylinder phantom shown in Fig. 5.28. The bottom and the sides of the structure were covered by a perfectly matched layer (PML) boundary to eliminate contributions from other rays and hence allowing only the wave propagating around the cylinder to be examined. The radius of the cylinder was 10 cm and the circumference of the path of the wave was almost 32 cm. The structure was assigned dielectric properties of muscle. Simulation on fat tissue are not reported here because, due to fat being rather transparent for radio waves (see the penetration depth in Table 5.1) and, therefore, the surface wave field is mixed with the field of the wave transmitted through the bulk of the tissue. The fields simulated on the cylindrical surface were fitted to the following model, representing exponential attenuation:

$$E[\mathrm{dB}] = E_0[\mathrm{dB}] - \beta d \tag{5-83}$$

where E_0 is the electric field at 0 cm from the antenna, and β is the attenuation rate of the field on the cylinder. The distance, d, from the antenna measured along the surface varied from 10 cm to 32 cm.

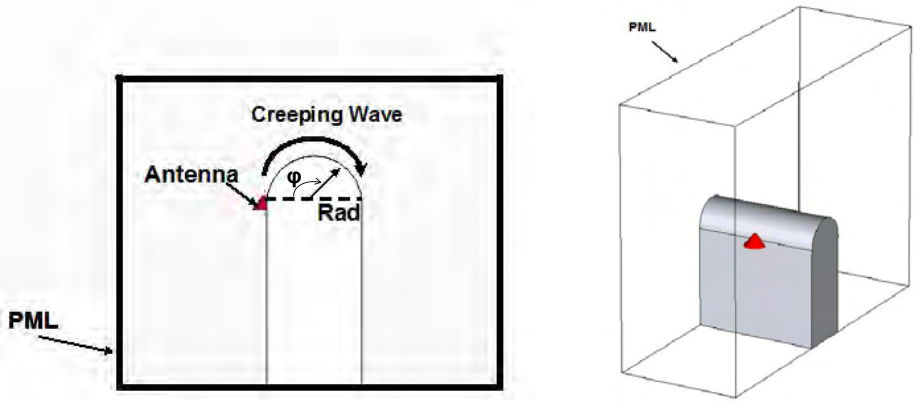

(a) (b)

Fig. 5.28 Antenna on half cylinder, (a) side view, (b) 3-D view

Fig. 5.29 shows the electric field variation around the cylinder in the plane perpendicular to the cylinder axis. The field data in CST is only available in the Cartesian coordinate system. This means, to plot the field around the cylinder, the coordinate system should be converted to a cylindrical one. However, there are a small number of points that are located on the desired radius and the rest of them are scattered around it. To tackle this problem, points within an interval of ± 1 mm of the radius were chosen. The points located within this criteria were assumed to be points located on the radius. This means that some of the adjacent points have slightly different distances from the cylindrical surface. This assumption adds some errors to the field values which appear as ripples in the curves in Fig. 5.29. Tables 5.8 shows the model parameters β and E_0 evaluated by fitting equation (5-83) to the electric field data plotted in Fig. 5.29. Values of β change only slightly for the different antennas, which indicates that they all excite the same wave mode. Also, similarly to the case of the flat surface, the vertically polarised antennas (i.e. monopole, PIFA and patch) couple energy into the creeping wave more efficiently than the horizontally polarised ones. The φ directed point source which excites a similar mode to the other antennas was analysed on the cylinder with a radius of 10 cm and β was derived. The value of β, 1.5, is almost in the same range with other antenna values, but it is slightly higher which can be due to the differences in the geometries of the phantoms.

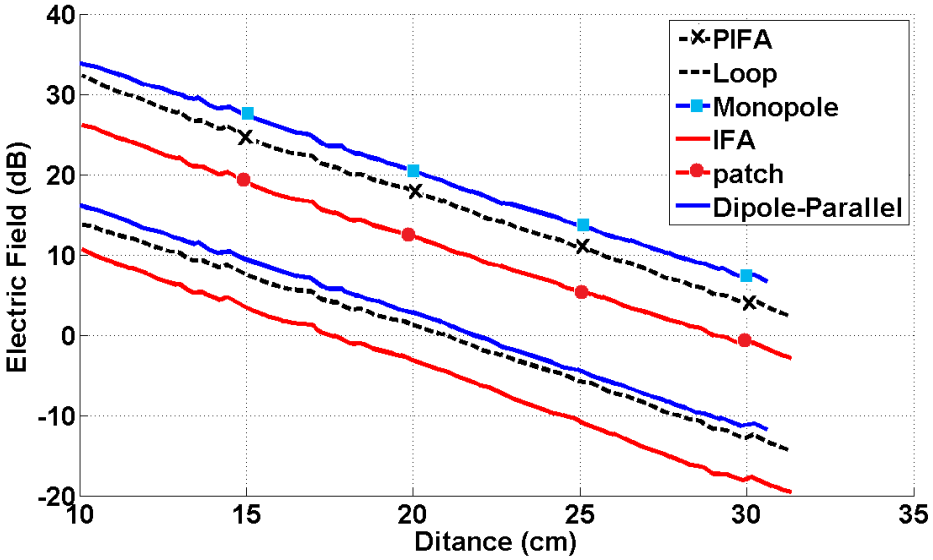

Fig. 5.29 Electric field variation versus distance for the antennas of Fig. 5.25 on the model of Fig. 5.28

Table 5.8 Parameters of the creeping wave launched by antennas on the cylindrical surface of muscle tissue at 2.45 GHz

	Monopole	Dipole	Loop	Patch	IFA	PIFA	Analysis, φ directed point source
E0 (dB)	47.4	30.1	28.0	39.6	25.3	45.4	-
β (dB/cm)	1.3	1.4	1.3	1.3	1.4	1.4	1.5

In order to investigate the effect of the cylinder radius on the creeping wave parameters, the half-wavelength dipole was simulated on the structure shown in Fig. 5.25 with different cylinder radii. The variation of the electric field around the cylinder is shown in Fig. 5.30, for three different radii. Obviously, the propagation path lengths are different on the cylinders with different radii, which is why the curves in Fig. 5.30(a) have different lengths. In spite of slow attenuation of the wave versus the distance on the cylinder with the larger radius, the signal weakens much more at the end of the path due to the longer distance. Fig. 5.30(b) shows the same electric field amplitudes versus the angle, φ, (Fig. 5.28) for three different radii. Obviously, the propagation path length on the cylinder at an arbitrary angle depends on

its radius. The larger radius results in a longer propagation path length on the cylinder. Hence, the field amplitude on the cylinder with a larger radius at an arbitrary angle is smaller.

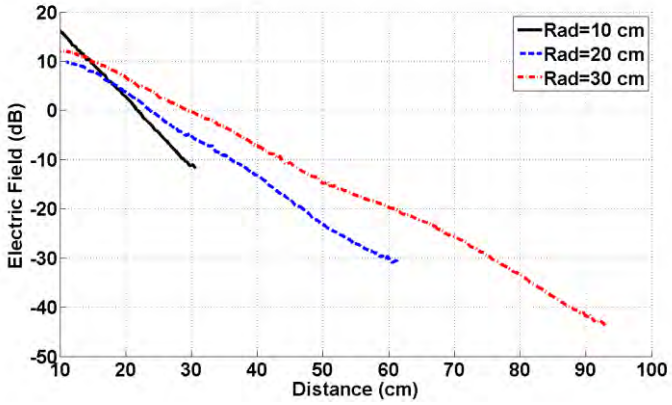

(a)

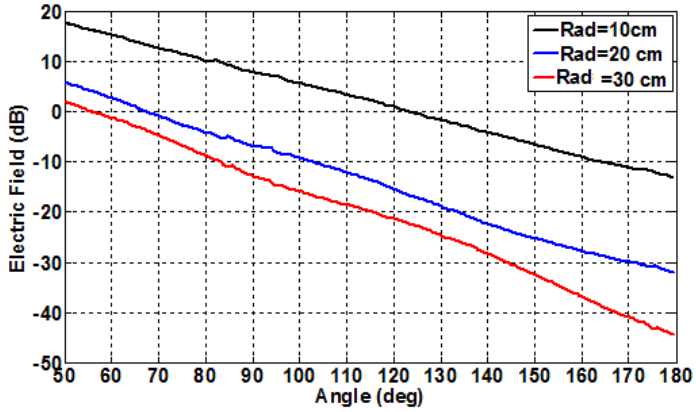

(b)

Fig. 5.30 Electric field variation of the dipole of Fig. 5.25 for different cylinder radii, (a) Versus distance, (b) Versus angle

The creeping wave parameters are given in Table 5.9. As mentioned above, increasing the radius of the cylinder reduces the attenuation rate, β. However, according to the results given in Table 5.9, the decrease of E_0 and β does not behave linearly by increase of the radius of the cylinder. In other words, the bigger the cylinder becomes, the change of the both parameters becomes smaller. To confirm the results of CST simulation, the β is calculated for the wave launched by φ directed point source. The solution was described earlier in

section 5.7. The results of the simulation and analysis are in a good agreement as can be seen in the example of Fig. 5.31, and the small differences can be due to the differences in the phantom geometry.

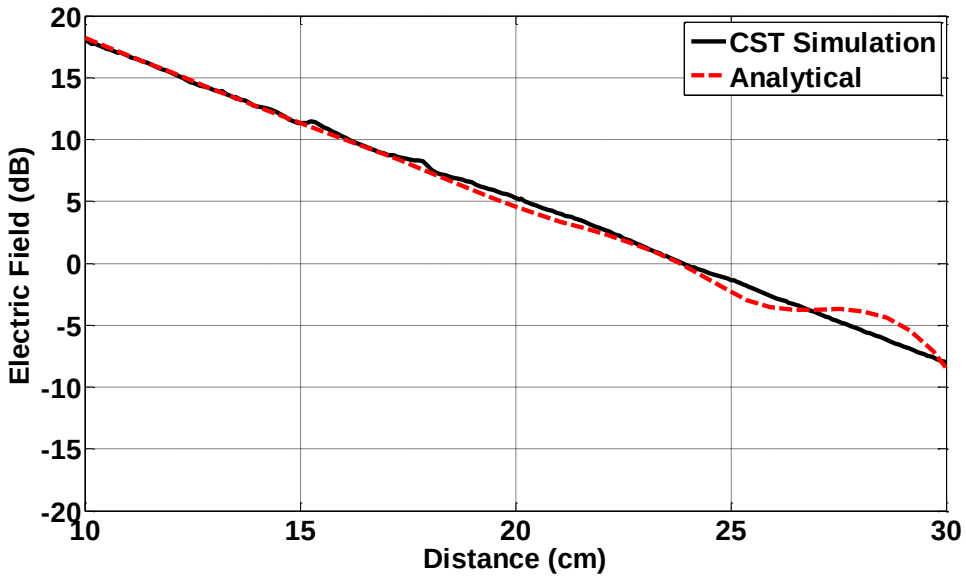

Fig. 5.31 Electric field variation of the dipole versus distance on the model of Fig. 5.28 and Fig. 5.19 cylindrical surfaces of muscle tissue with a radius of 10 cm for the CST simulation and Analytical method, respectively at 2.45 GHz

Table 5.9 Parameters of the creeping wave launched by a half-wavelength dipole on the cylindrical surfaces of muscle tissue with different radii at 2.45 GHz

Radious	10 cm	20 cm	30 cm
E_0 (dB)	30.1	20.5	20.0
β (dB/cm) simulation	1.4	0.86	0.65
β (dB/cm) Analysis	1.52	0.80	0.55

5.9. SUMMARY

The propagation of the surface wave on the flat and cylindrical phantom made of human tissues were investigated by use of the analytical method and also simulation through commercially available software. On the flat phantom, the possibility of the existence of the Zenenck and Norton surface waves in the form of TM and TE modes were studied. It was shown that, either on the flat or the cylindrical phantom, TM mode can be supported and its attenuation depends on the tissue electric property. However, exciting of the Zenneck wave with the practical antennas is not very possible and they can excite Norton type surface wave. Various practical antennas used for on-body communications, such as the monopole, tangential dipole, patch, IFA and PIFA performance on the flat and cylindrical phantoms were investigated. It was shown that the TM wave is excited by all the antennas regardless of their polarization and they show similar attenuation factors. However, the vertically polarised antenna acts much more efficiently than the horizontally polarised ones. Also, fields of the antennas on a cylinder were simulated, which is more representative of the human trunk. The attenuation was much faster than on a flat surface, and it decayed exponentially.

Chapter 6

Parasitic Array Antenna with Enhanced Surface Wave Launching

6.1. INTRODUCTION

As shown in the previous chapter, placing a small dipole antenna very close to the surface of a human tissue phantom changes its radiation pattern and a vertical electric field component appears along the direction of the dipole, which in turn excites a TM surface wave. Also, it was shown that maximum path gain of an on-body channel consisting of two dipoles parallel to the body surface can be obtained if two antennas are placed in line with each other. However, even this arrangement does not yield a path gain as high as an antenna polarised normal to the surface, such as monopole. In fact, a significant amount of energy of the parallel dipole is dissipated inside the tissue which also serves to reduce the surface wave strength. One way to tackle this problem is to enhance the directivity of the antenna parallel to the surface. To increase the directivity, parasitic elements can be added. In the following sections,

the dipole behaviour on the fat and muscle is investigated and then a novel directive surface wave antenna is described.

6.2. PARALLEL DIPOLE ANTENNA ON A PHANTOM

The performance of a dipole on a tissue phantom was investigated using CST Studio software. A 50 mm long centre fed dipole antenna fed by a 50 Ohms discrete port operating at 2.45 GHz was placed 5 mm above a square fat phantom size of 200 × 200 × 200 mm^3 parallel to the surface (XY plane) oriented in the X direction, as shown in Fig. 6.1.

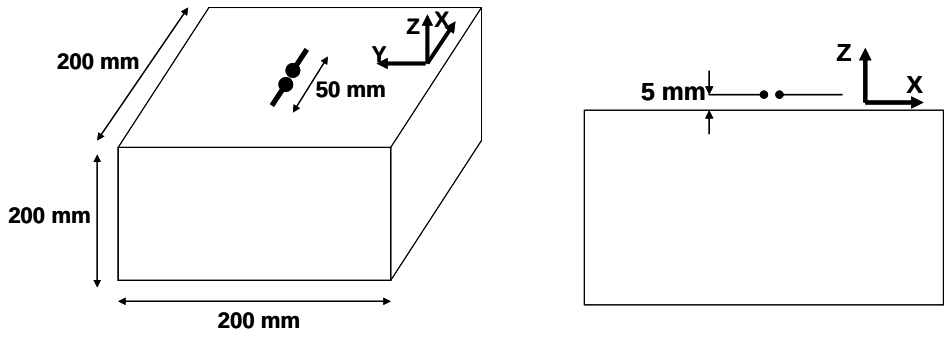

(a) (b)

Fig. 6.1 Parallel dipole on the tissue phantom,
phantom properties (ε_r = 5.3, δ = 0.11 S/m), (a) 3D view, (b) Side view

Far field directivity patterns of the antenna in the plane of the phantom surface are shown in Fig. 6.2(a). As it can be seen, the strongest component is polarised in the theta direction, that is normal to the surface, and is in the direction of the antenna, at φ = 0˚. This component does not exist in the free space radiation pattern. The level of the normal and parallel component depends on the dielectric constant property of the material underneath of the antenna, which will be explained later. Also, the size of the phantom can affect the far field characteristics of the antenna. It has been observed that, an increase in the phantom size can

reduce the phi oriented component, which is parallel to the surface. These results can be compared to those in Fig. 6.10(b), which are for a short dipole, and show strong similarities.

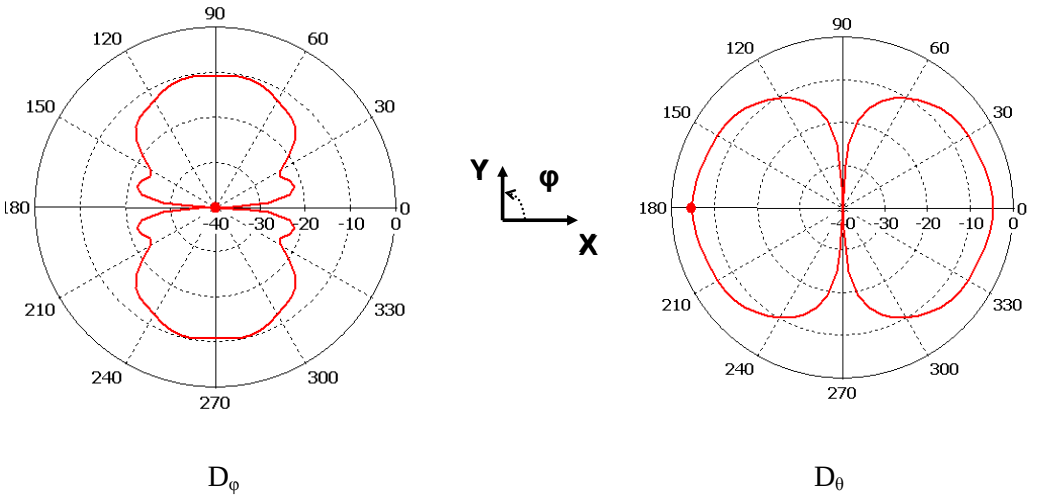

D_φ D_θ

(a)

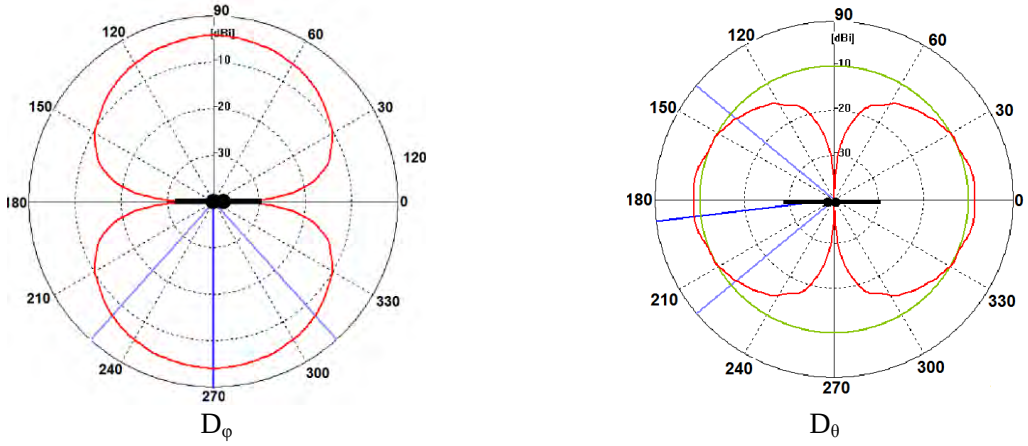

D_φ D_θ

(b)

Fig. 6.2 Far field directivity pattern of the dipole in XY plane on the configuration of Fig. 6.1 (a) Half wavelength dipole, (b) Short dipole

The electric field distribution, E_x, E_y and E_z, on the phantom surface is shown in Fig. 6.3. Two components, E_x and E_z are present in the direction of the antenna (φ=0˚) which indicates a TM surface wave is launched. However, in the Y direction (φ=90˚) there is just one component, E_x, which is transverse to the propagation wave direction. This implies the

propagation mode is TEM (space wave) and TE mode (surface wave). Therefore, the antenna excites different propagation modes in different directions.

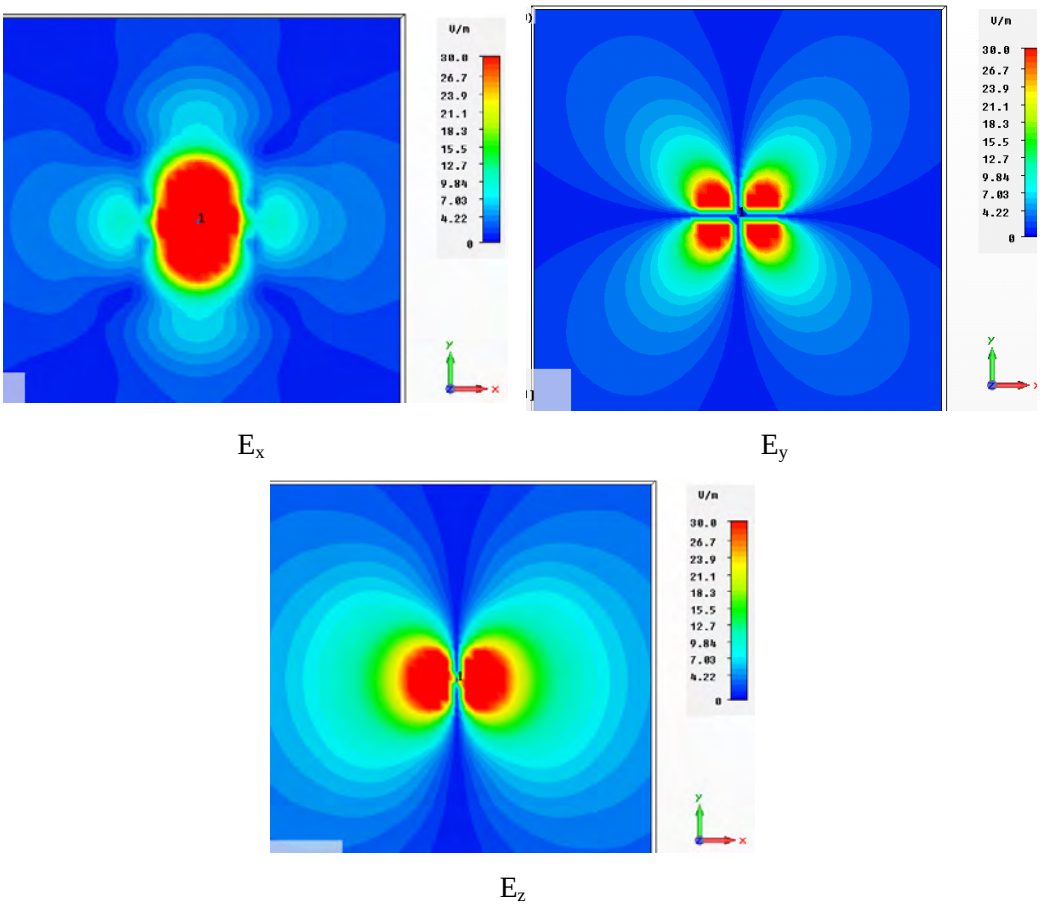

E_x E_y

E_z

Fig. 6.3 Electric field distribution 5 mm above phantom surface of configuration of Fig.6.1

To investigate the effect of the gap between the dipole and the surface on the field distributions, it is varied from 2 to 20 mm (0.016λ to 0.16 λ) at 2.45 GHz and the phi and theta components of the maximum directivity in the XY plane is shown for both fat and muscle tissues. The surface size of the phantom is three times the size used in the previous simulation (600 × 600 × 200 mm3) to reduce the edge effects. Fig. 6.4 shows that the theta and phi components do not change significantly for a gap of less than 5 mm (0.04λ), but at increasing distances, the directivity drops faster on the muscle in comparison to the fat. At 20 mm gap, the normal component of the dipole on the fat phantom surface shows -13 dBi directivity.

The phi component of directivity behaves differently on the fat and muscle with the gap size. On the muscle, the phi component is higher than the fat. On both tissues, increasing the gap lowers the directivity.

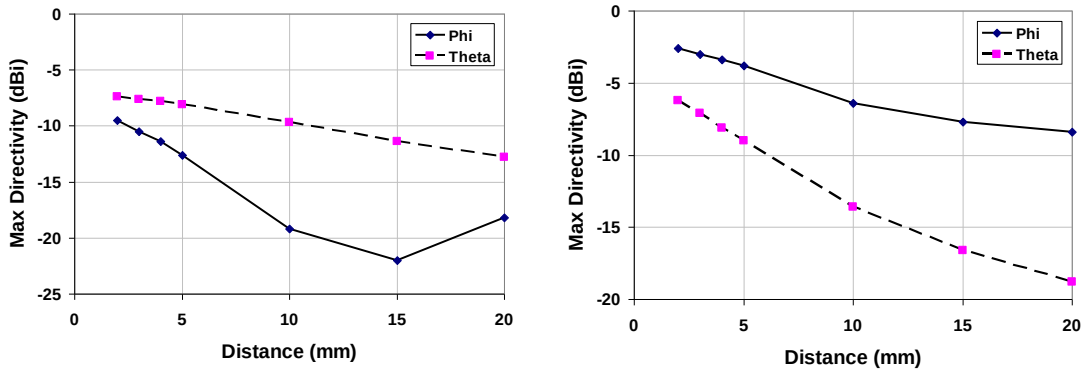

(a) (b)

Fig. 6.4 Maximum far field directivity of configuration of Fig. 6.1 versus distance between antenna and phantom, (a) Fat phantom, (b) Muscle phantom

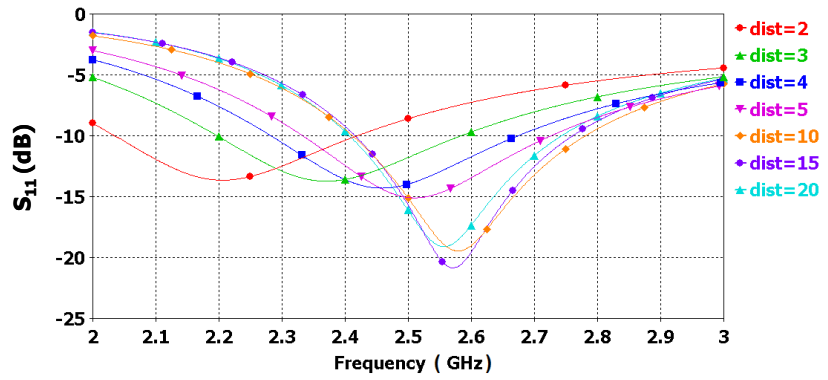

(a)

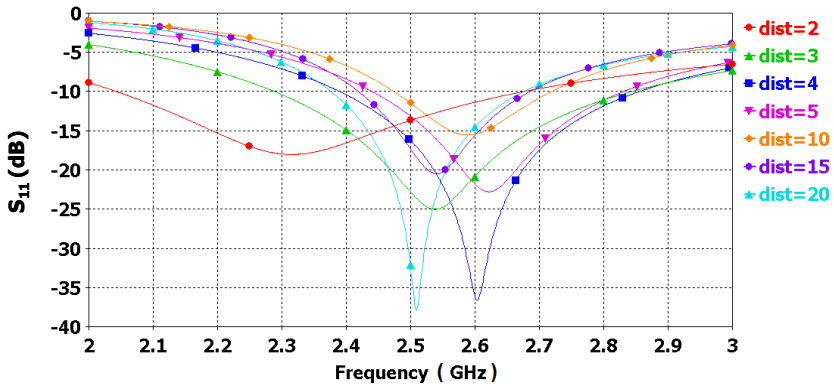

(b)

Fig. 6.5 Return loss of the dipole on the phantom for different gap sizes, (a) Fat phantom, (b) Muscle phantom

The S_{11} variation of the antenna above the fat and muscle for different gap size is shown in Fig. 6.5. The resonant frequency varies on both tissues from 2.3 GHz to 2.6 GHz. For smaller distances from the phantom, the antenna resonances at lower frequencies with a wider bandwidth. However, by increasing the distance the resonance frequency shifts to higher frequencies and the return loss bandwidth of the antenna decreases.

6.3. SURFACE WAVE PARASITIC ARRAY ANTENNA DESIGN

In general, as described in chapter 2, an array of metallic or dielectric rods with a high directivity along the surface are used to excite surface wave on the ground or sea. However, increasing the gain of the antenna along the surface does not necessarily excite stronger surface wave and energy can couple to the untrapped radiated wave. In principle, to be able to launch the surface wave, the phase velocity of the wave along the antenna must be matched to the surface wave phase velocity on the surface. This can be achieved by proper spacing between the antenna array elements [55]. In addition, to maximise the transition of the slow wave from the antenna to the surface, the antenna must be long enough ($l>\lambda$) and tapered properly [55].

In this section, parasitic elements are added to the fed dipole described in the previous section to increase its gain along the phantom surface. To increase the simulation speed, fat phantom is used in the antenna optimisation and the design procedure and optimised antenna performance is then examined on the muscle. As an initial step, just one parasitic element is placed in parallel to the driven element as shown in Fig. 6.6. The parasitic element is located in the same plane as the dipole, that is 5 mm above the phantom surface with a spacing of 2 mm from the driven element to achieve the strongest coupled current on the parasitic element. Three factors affect the gain enhancement, namely, the offset, parasite length and spacing. Fig. 6.7(a) shows the variation of the directivity versus offset and parasitic element length for

a spacing of 2 mm. 30 simulations were performed and in each case the maximum directivity of the antenna on the surface of the phantom was extracted. As is shown, placing a parasitic element in the wire direction can increase the directivity up to almost 6 dB in comparison to a dipole without any parasitic element. In general increasing the length of the parasitic element increases the maximum directivity, regardless of the offset value. Although, the offset parameter has a small effect on the maximum directivity (within 1 to 2 dBi) for the fixed length, it can change the back lobe level significantly. The maximum directivity of 1.4 dBi can be achieved by using one parasitic element along the antenna according to the parametric study. Also, a similar parametric study on the muscle phantom was performed and the dipole antenna with one director was placed above the muscle and the length and offset variations were investigated in terms of antenna maximum directivity at the surface of the phantom. The result is shown in Fig 6.7(b). The general behaviour of the maximum directivity versus length and offset parameters are approximately similar to the fat, but the level of the directivity is reduced by almost 2 dBs. Since the simulation time of the antenna on the muscle is almost 10 times more than that on the fat, at the next design stage the parametric study is done for the antenna above the fat and only the final design is simulated on the muscle phantom.

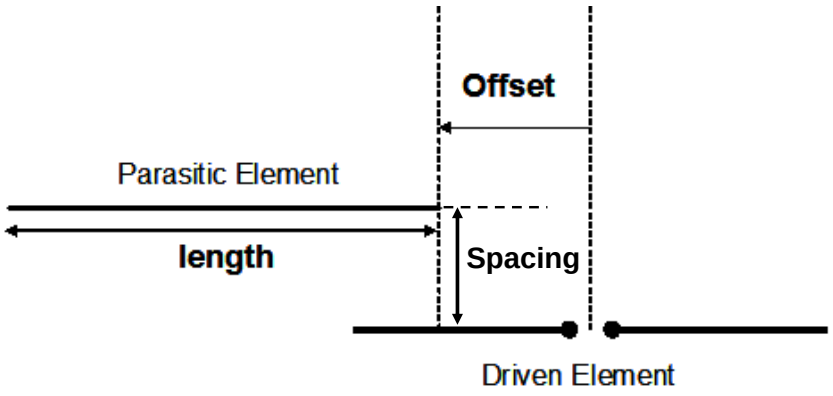

Fig. 6.6 Dipole antenna with one parasitic element

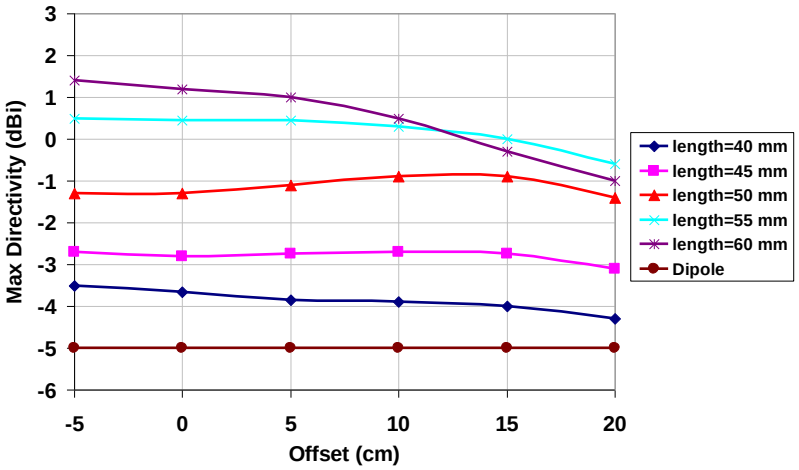

(a)

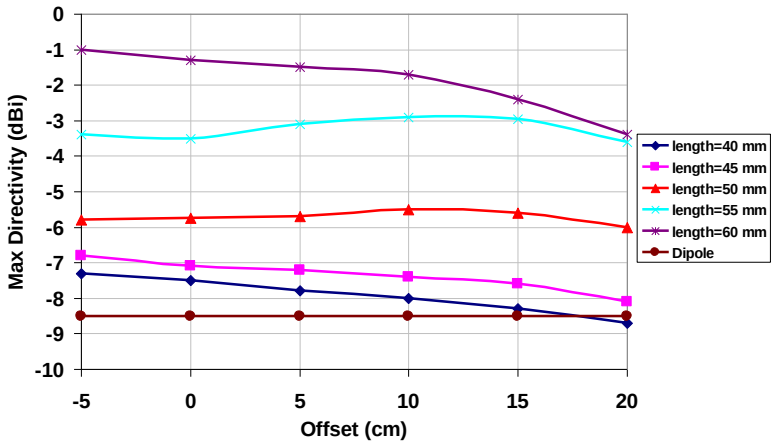

(b)

Fig. 6.7 Maximum directivity of the dipole with one parasitic element, (a) Fat phantom, (b) Muscle phantom (Muscle phantom: size = 600 × 600 × 50 mm^3, properties (ε_r = 52.7, δ=1.7 S/m)), (Fat phantom: size = 600 × 600 × 200 mm^3, Phantom properties (ε_r = 5.3, δ=0.11 S/m))

To further increase of the directivity, more parasitic elements were used. Fig. 6.8(a) shows the dipole with two parasitic elements. The second parasitic element is placed at the opposite side to the first parasitic element to improve the symmetry of the radiation pattern and placed at the same distance, 2 mm, from the dipole. While the length of the parasitic element is fixed at 60 mm and placed +5 mm offset from dipole feeding, the length and the position of the second parasitic is adjusted to achieve the maximum directivity in the XY

plane. Variation of the directivity versus the offset for the various length of the parasitic element is shown in 6.8(b). As it can be seen, the second parasitic element of a 55 mm length placed at 30 mm away from dipole feeding can increase the maximum directivity to 2~3 dBi. As in the case of the first parasitic element, the length of the parasitic element is more effective than its offset in increasing the directivity of the antenna. Adding other extra directors to the end of the structure does not change the directivity significantly, because of the reduction of the amplitudes of the coupled current on the parasitic element. The simulations showed that adding one more director increases the antenna directivity less than 1 dBi.

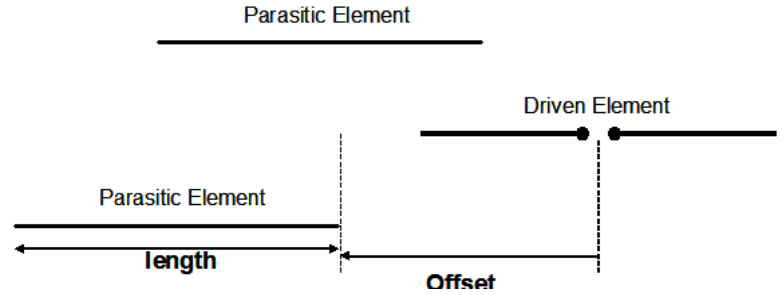

(a)

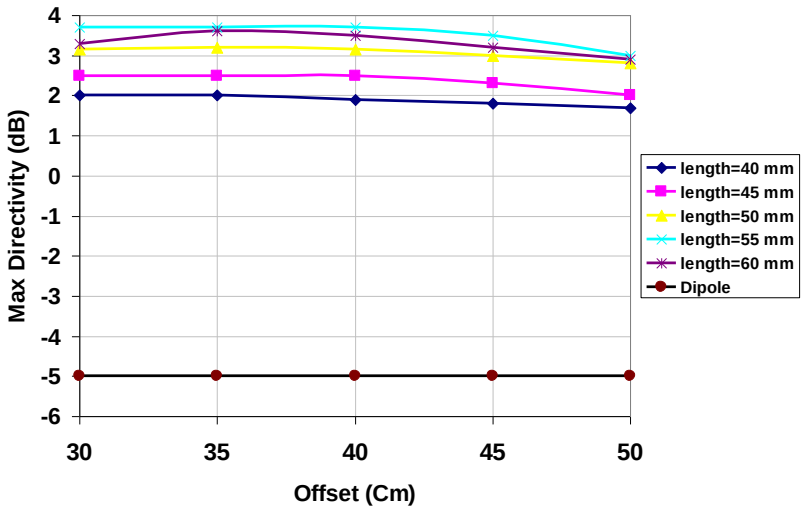

(b)

Fig. 6.8 Surface wave parasitic array with two directors on fat phantom, details as Fig.6.9,
(a) Antenna configuration, (b) Maximum directivity

In addition to the directors, a reflector is also used at the opposite end of the antenna as shown in Fig. 6.9. This reflector yields an extra 3 dBi of directivity. The length, position and the angle (θ) are the parameters which are considered in the optimisation process to obtain the maximum directivity in the XY plane. The antenna can provide 5 dBi directivity on a fat surface which is 10 dB more than a parallel dipole on the same phantom size. To test the antenna performance on muscle, the final antenna is placed on similar size of muscle phantom. The antenna performs similarly to on the fat. The only difference is the maximum directivity which drops by almost 2 dBi.

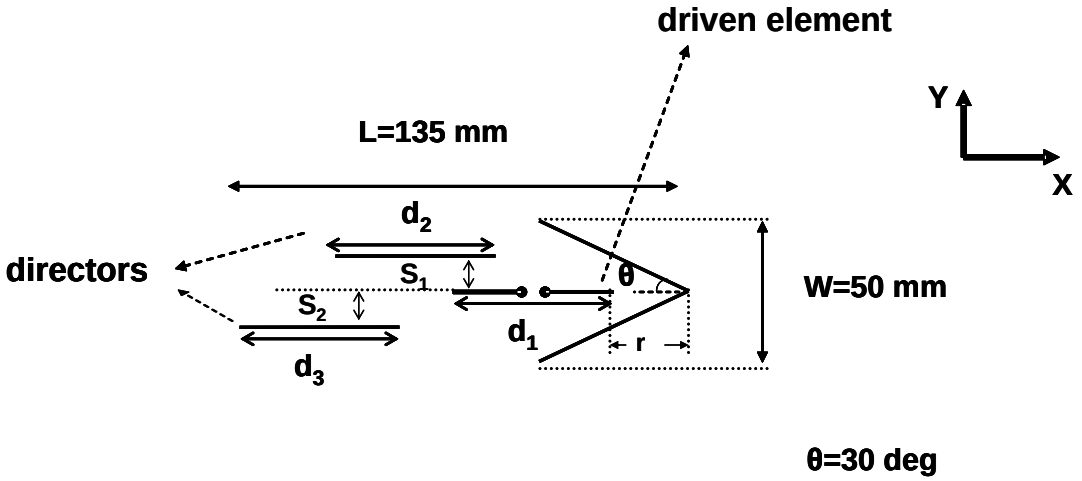

Fig. 6.9 Surface wave parasitic array antenna: d_1=50 mm, d_2= 60 mm, d_3=55 mm, S_1 = 2 mm , S_2 = 2 mm, r = 20 mm,

Fig. 6.10 shows the far field directivity pattern of the antenna in the plane of the surface of the phantom (XY plane), and perpendicular to the phantom surface, (XZ plane). In the XY plane, the antenna shows directive along the X axis, D_θ, and the front to back ratio is almost 25 dB. The phi component pattern, D_φ, in the same plane is almost similar to the dipole pattern shown in Fig. 6.2. The ripples and deformation in the D_φ pattern is due to the presence of the parasitic elements. In the XZ plane, which is the plane perpendicular to the surface of the phantom and is the cut along the driven element of the antenna, the theta component

pattern, D_θ, is tilted toward the surface by 60˚ from the normal axis and it provides almost 9.5 dBi directivity. In this plane, the D_φ is very small.

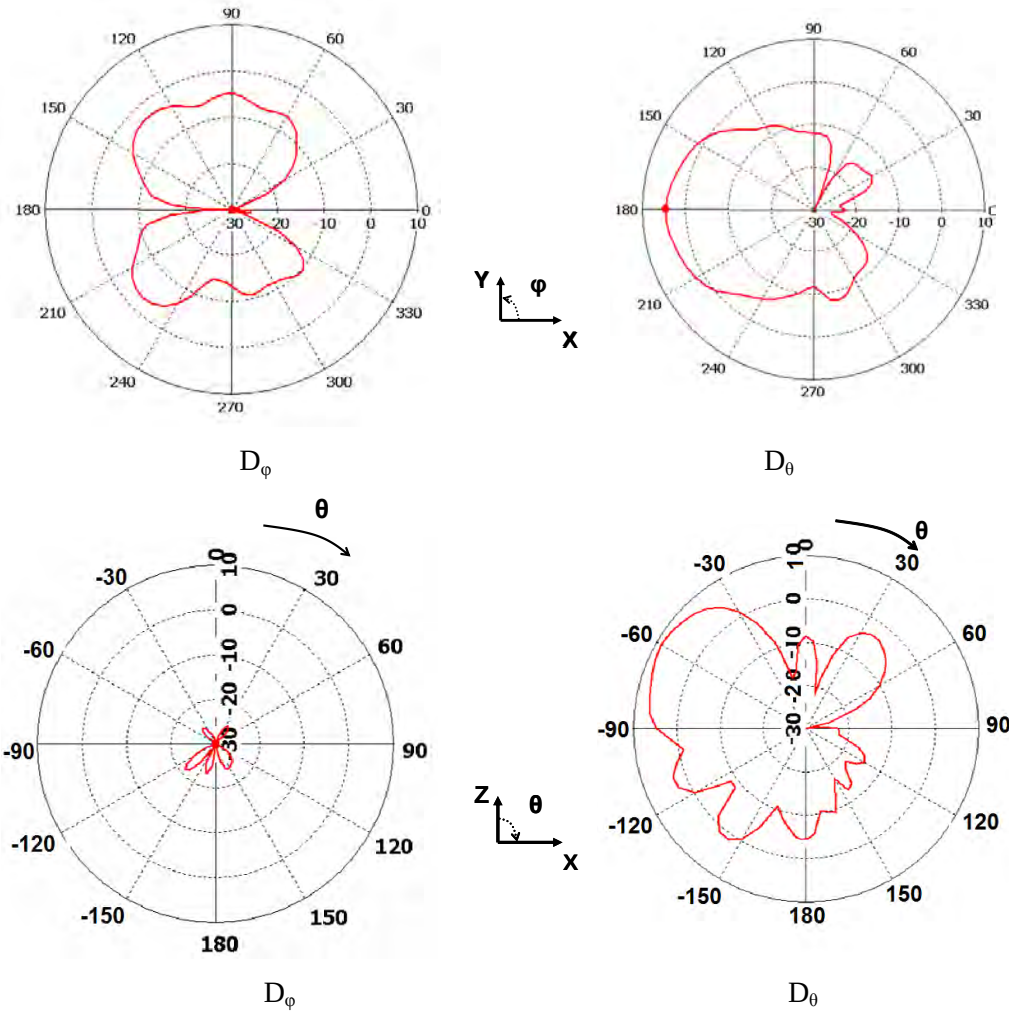

D_φ D_θ

D_φ D_θ

Fig. 6.10 Far field radiations pattern of a surface wave parasitic array antenna on fat phantom at 2.45 GHz,
(Phantom size = 200 × 200 × 200 mm^3, antenna 5 mm away from surface, antenna points in φ = 180° direction)

Achieving the maximum directivity in XY plane was the main goal of the optimisation. But it was observed that adding the parasitic element close to the dipole shifts the resonance frequency of the antenna to the higher frequencies as shown in Fig. 6.12. Hence, the resonance frequency and the frequency of maximum directivity are not similar. Placing a parasitic element very close to the dipole can add series capacitance (C_{ext}) to the antenna equivalent

circuit as shown in Fig. 6.13. C_{ext} reduces the total capacitance of the antenna and shifts the frequency toward the higher frequencies. In the following section, the effect of the gap between the dipole and the parasitic element on the return loss (S_{11}) and radiation pattern are investigated.

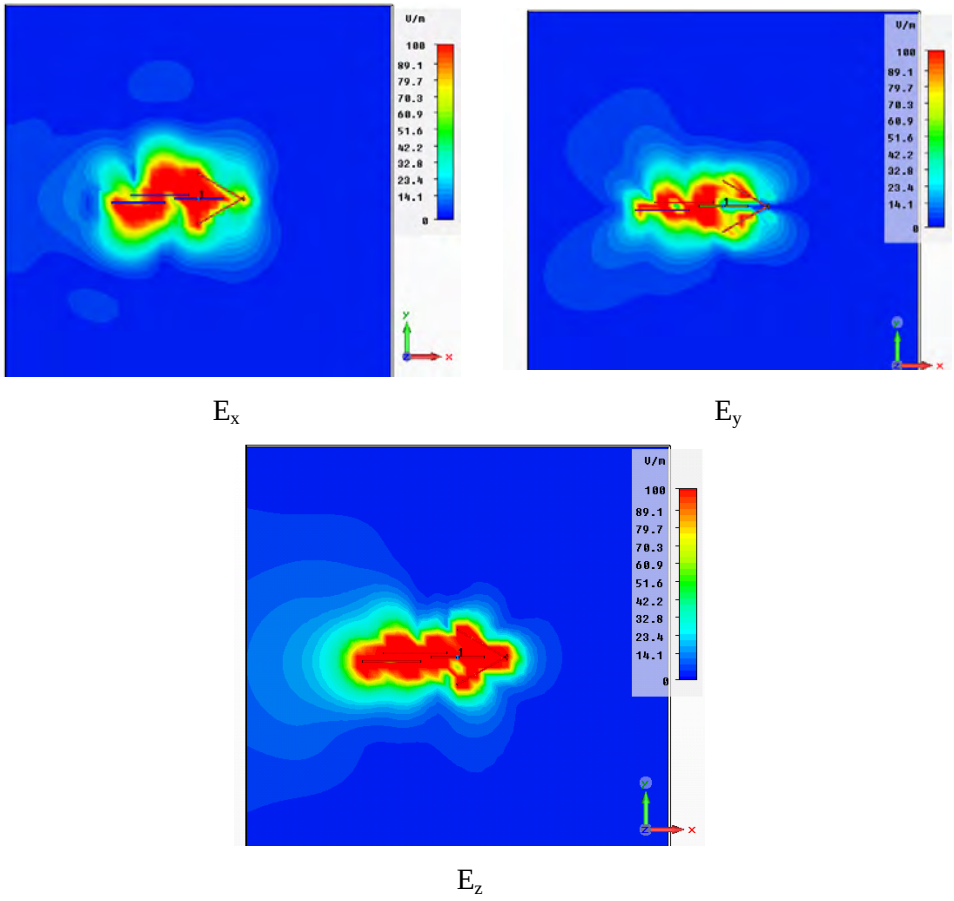

Fig. 6.11 Electric field distribution of surface wave parasitic array antenna, (Details as Fig.6.10)

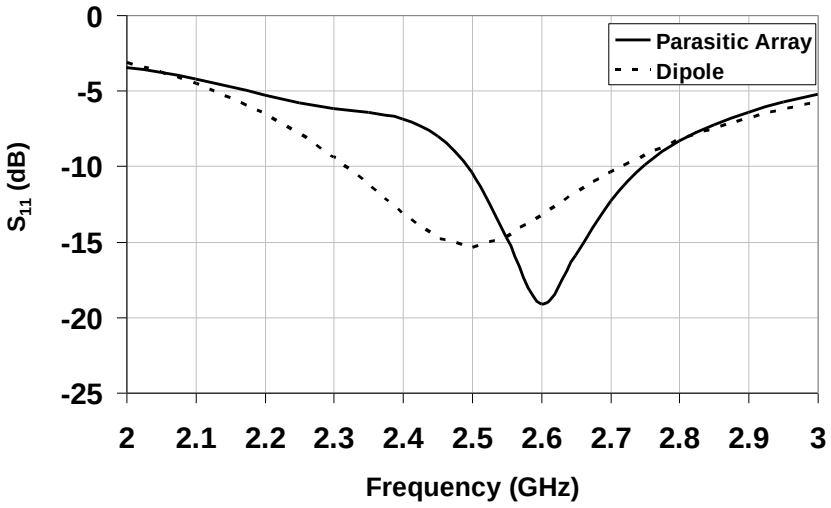

Fig. 6.12 Simulated return loss of surface wave parasitic array antenna and dipole, (Details as Fig.6.10)

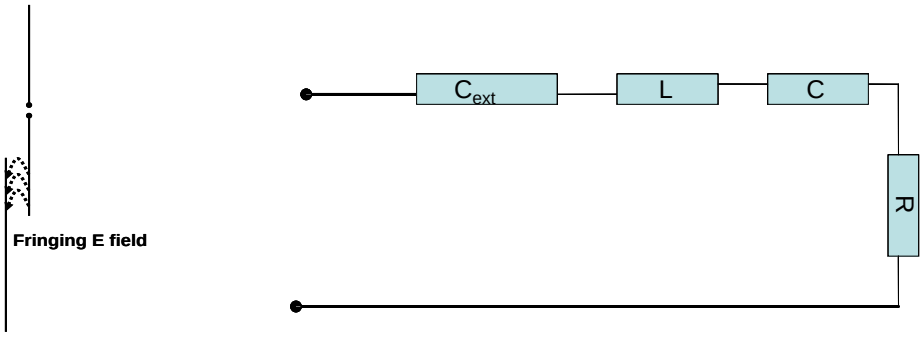

(a) (b)

Fig. 6.13 (a) Electric field coupling of dipole on the parasitic element in proximity of phantom, (b) External capacitance added in series with the dipole equivalent circuit

6.3.1 Effect of Parasitic Position

In the previous section, the parasitic element was placed very close to the antenna to give strong coupling of the currents on the fed and parasitic elements. This coupling is equivalent to an extra capacitance in series with the dipole capacitance, which increases the resonance frequency. In this section, the effect of the position of the parasitic is investigated. The gap size is changed from 4 mm to 12 mm in 2 mm increments. The S_{11} of the antenna from 2 to 3 GHz is shown for the various gaps in Fig. 6.14. The resonance frequency shifts from 2.6 to 2.5

GHz. However, further increase of the gap affects the resonance frequency only slightly. The theta component of the antenna directivity is shown in Fig. 6.15 in the XY and YZ planes. The maximum directivity in both planes occurs for the smallest gap size, 4 mm, and increasing the gap size lowers the maximum gain, distorts the radiation pattern and increases the back lobe.

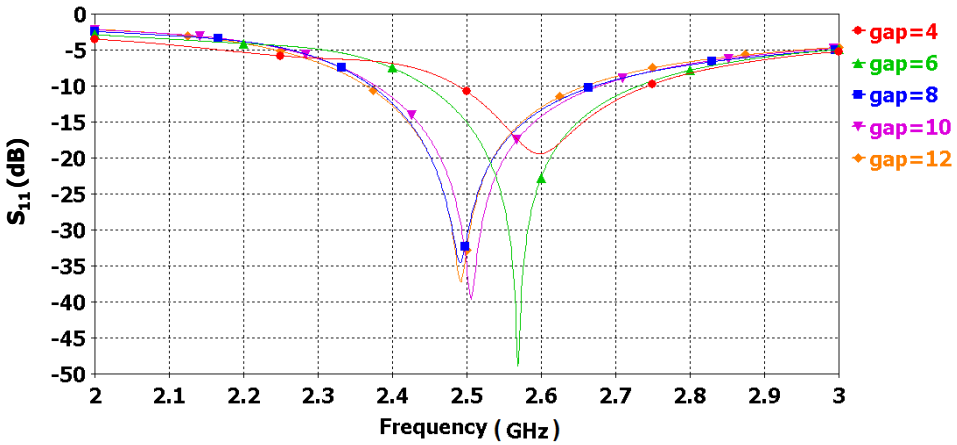

Fig. 6.14 Return loss of surface wave parasitic array antenna for different gap size between dipole and parasitic elements, (Details as Fig.6.10)

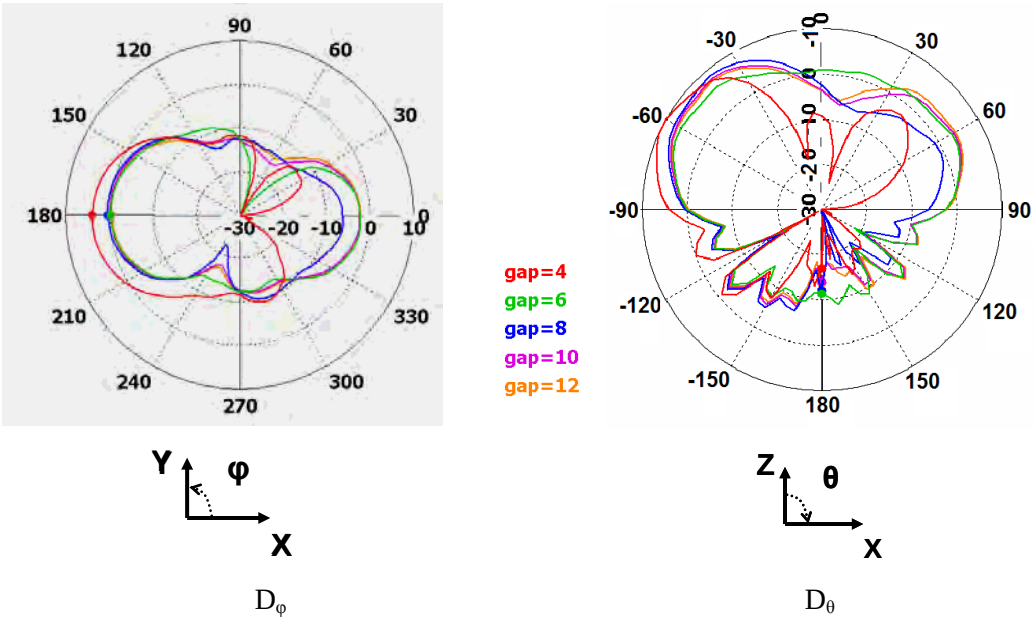

D_φ D_θ

Fig. 6.15 Far field directivity pattern of surface wave parasitic array antenna for different gap size between dipole and parasitic elements, (Details as Fig.6.10)

6.3.2 Axially Symmetry

The structure shown in Fig. 6.9 is sensitive to the length of the parasitic elements and their position related to each other, which makes the design of the antenna more demanding. The axially symmetric structure shown in Fig. 6.16 is less sensitive to the dimension of the parasitic because of the use of pairs of parasitic elements. In this structure, the antenna is symmetric about the X axis and consists of two series of cascaded parasitic elements parallel to the driven element. Each two adjacent elements are separated by a 2 mm gap. The simulated return loss of the new antenna is shown in Fig. 6.17. The resonant frequency is shifted to higher frequencies and the antenna matching is not as good as the previous one. In terms of the equivalent circuit, the two parallel parasitic elements at each side of the driven element provide two external capacitances in series with the dipole capacitance, and the total capacitance decreases and the resonance frequency moves upward. Also, this extra capacitance worsens the matching of the antenna. The far field directivity patterns, Fig. 6.18 are similar to the previous structure, but the patterns in the XY plane are symmetric and the back lobe in D_θ increases by almost 10 dB in the XY plane. The phi component in the both planes reduces slightly.

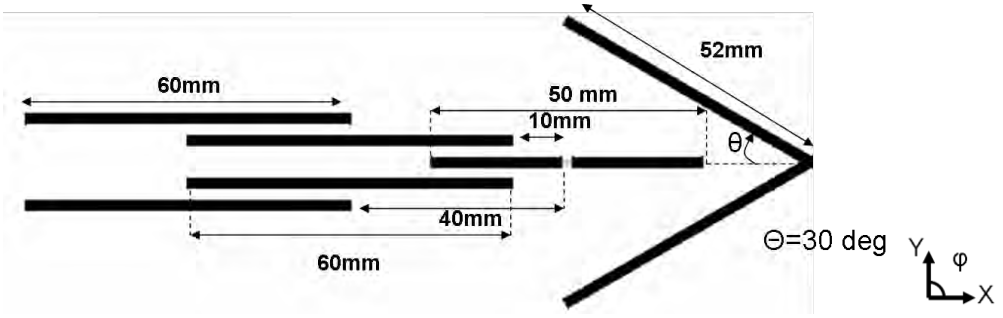

Fig. 6.16 Configuration of the axially symmetric surface wave parasitic array antenna

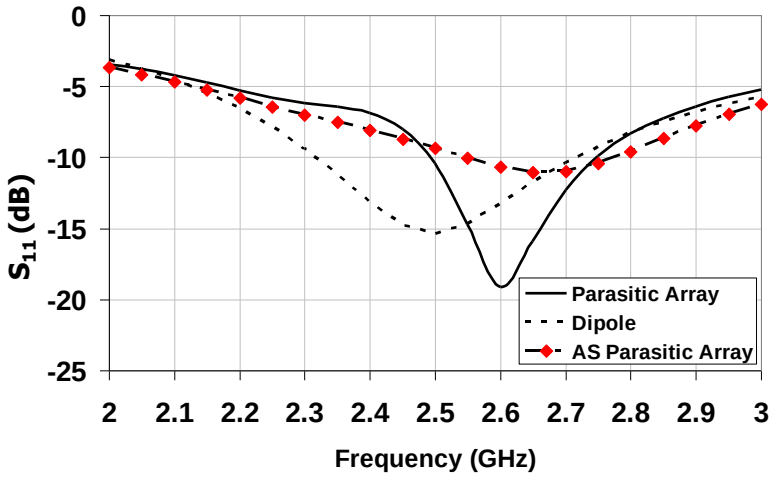

Fig. 6.17 Simulated return loss of axially symmetric surface wave parasitic array antenna on fat phantom (Details as Fig.6.10)

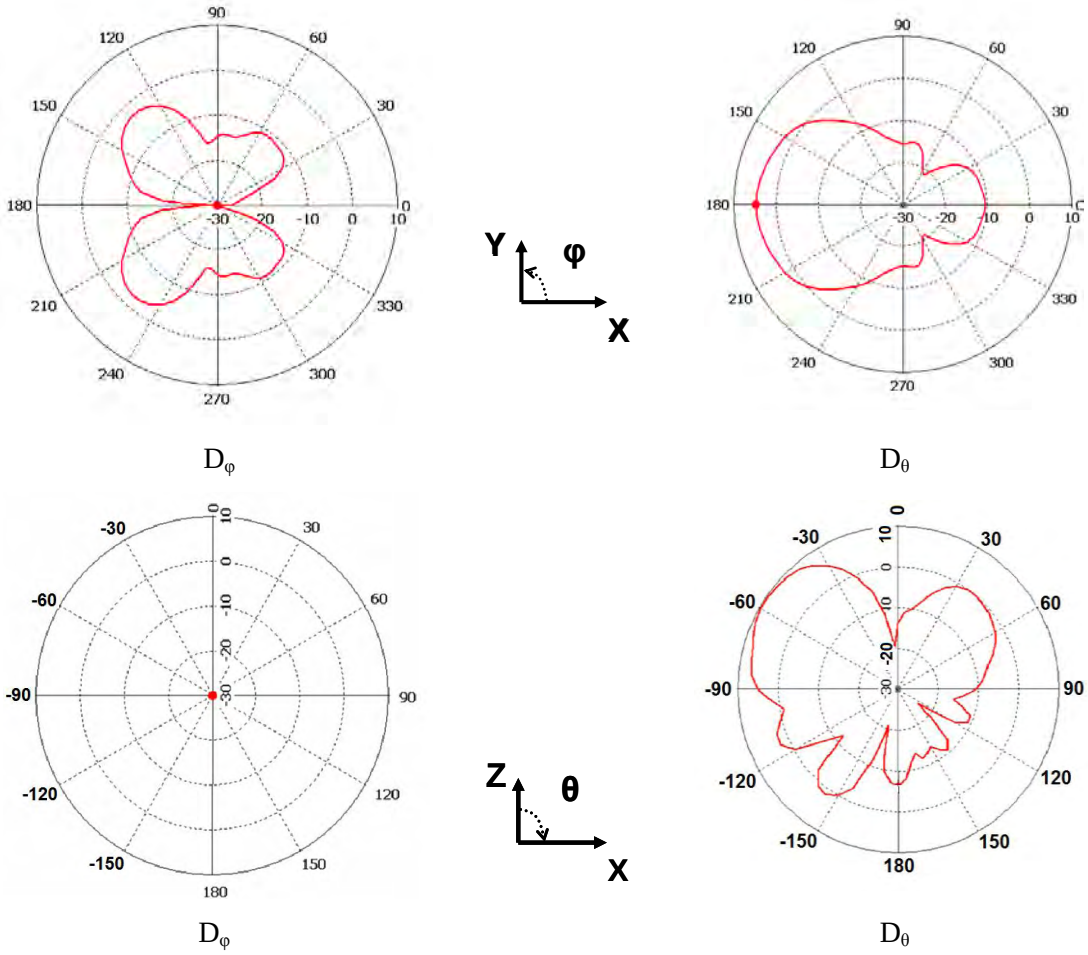

Fig. 6.18 Far field directivity pattern of axially symmetric surface wave parasitic array antenna for different gap size between dipole and parasitic elements on fat phantom, (Details as Fig.6.10)

6.3.3 Comparison of Parasitic Array with Other Antennas

The far field characteristics of other antennas such as a conventional Yagi array, a monopole and a dipole are compared to the parasitic array above a phantom made of fat and muscle. All the antennas are designed to operate at 2.45 GHz and they are placed 5 mm away from the box surface. The details of the conventional Yagi array are given in Fig. 6.19. The antenna has one reflector and two directors. In the conventional method of Yagi array design the first director is placed λ/4 at the resonance frequency of the antenna away from the driven element. However for the Yagi on a phantom, the first director is placed very close to the driven element namely ~λ/10. Placing the director far from the antenna on the phantom, reduces the coupling of the driven element on the director significantly, and the directivity of the antenna does not change compared to the dipole. To resolve the problem and increase the coupling, the first parasitic element is placed much closer to the antenna, though small spacing between these two elements affects the return loss of the antenna. The current design yields a peak directivity of 2 dBi in the phi component in the X direction.

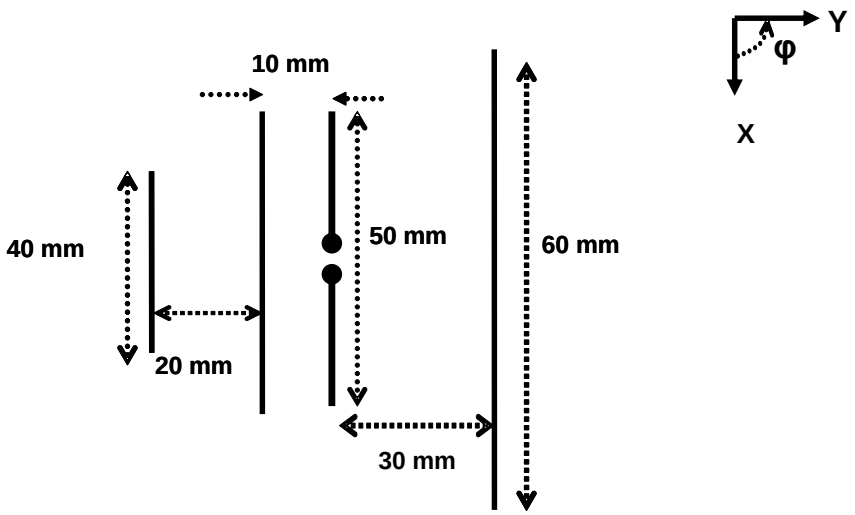

Fig. 6.19 Conventional planar Yagi array

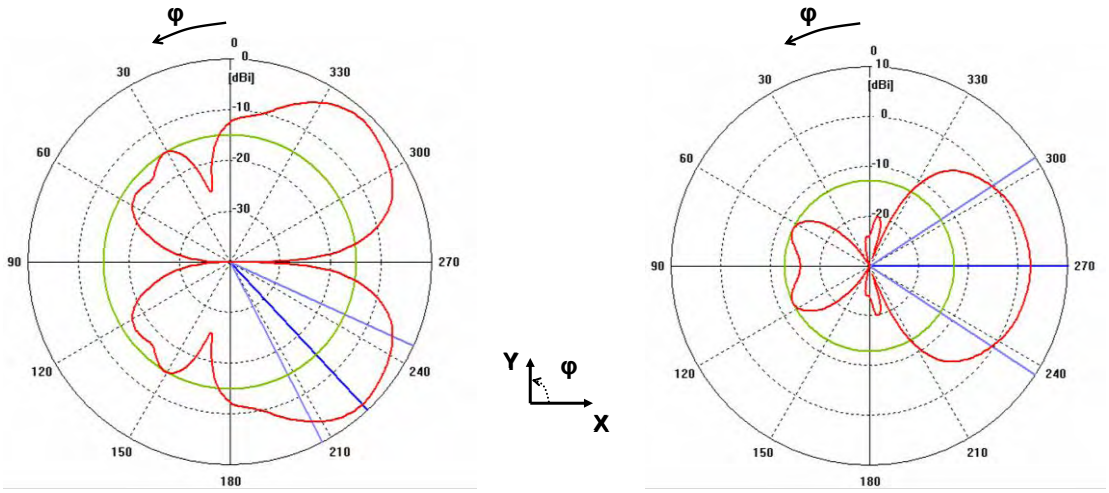

(a) (b)

Fig. 6.20 Far field directivity pattern of conventional Yagi array on fat phantom in XY Plane (Phantom size = 200 × 200 × 200 mm^3)
(a) Theta component (b) Phi component,

Tables 6.1 and 6.2 provide the total and radiation efficiency, S_{11} and the maximum directivity for the various antennas discussed, on the surface of the phantom of fat and muscle, respectively. As described earlier in this chapter, the dipole parallel to the phantom radiates normal and parallel field component in different directions. Because of that the antenna far field characteristic is considered in two directions known as H90 (along the wire), and H0 (perpendicular to the wire), respectively. The dipole with the length of 50 mm was fed with 50 Ohms discrete port. The monopole is modelled by a piece of wire length of 30 mm on a circular ground plane with a radius of 25 mm.

It worth mentioning that the numbers are given in the tables are based on the far field characteristics. Therefore, any change of the phantom size may affect the values of some parameters, such as directivity and efficiency. The energy dissipation in the phantom directly depends on its size and the radiation efficiency can vary considerably. However, the radiation efficiency of the monopole is not significantly affected by the phantom size. The presence of

the ground plane isolates the monopole from the dielectric effect and prevents efficiency reduction. But the dipole, conventional Yagi and parasitic array all are affected.

Comparing the radiation and total efficiency of the surface wave parasitic array to other antennas on each tissue indicates that the radiated energy of the antenna in the far field is the lowest. In the other words, most of energy of the antenna travels close to the surface of the box and dissipates into the material. Due to the similar reasoning, the conventional Yagi array efficiency is relatively low. The dipole radiates most of the energy outward from the phantom and its efficiency is higher than the two directive arrays. The parasitic array antenna provides high directivity in comparison to the other antennas on the fat tissue. However, using the muscle phantom reduces its gain by almost 4 dB.

Table 6.1 Far field characteristics of various antennas at 2.45 GHz on a fat phantom (Phantom size = 600 × 600 ×200 mm^3, Phantom properties (ε_r = 5.3, δ = 0.11 S/m))

	Field component	Directivity (dBi)	S_{11} (d B)	Total efficiency (dB)	Radiation efficiency (dB)
SW Parasitic Array	theta	2.6	-8	-15.1	-15.8
Dipole (H90)	theta	-8.8	-14	-8.6	-8.5
Dipole (H0)	phi	-6	-15	-8.6	-8.5
Monopole	theta	-3.8	-9	-3.7	-3.1
Conventional Yagi	phi	-0.3	-7	-15	-14

Table 6.2 Far field characteristics of various at 2.45 GHz on the muscle phantom (Phantom size = 600 × 600 × 50 mm3, Phantom properties (ε_r = 52.7, δ = 1.7 S/m))

	Field component	Directivity (dB)	S_{11} (d B)	Total efficiency (dB)	Radiation efficiency (dB)
SW Parasitic Array	theta	-1.7	-6.8	-14.9	-13.8
Dipole (H90)	theta	-9.8	-11.4	-10.2	-9.8
Dipole (H0)	phi	-3	-11.4	-10.2	-9.8
Monopole	theta	0	-8	-3.3	-2.5
Conventional Yagi	phi	0	-7	-13	-12

6.4. TRANSMISSION CHANNEL WITH SURFACE WAVE PARASITIC ARRAY

6.4.1 Flat Surfaces

To evaluate the path gain improvement of the SW parasitic array antenna, a number of different antennas were mounted 5 mm above a 1000 × 600 × 200 mm^3 phantom, as shown in Fig.6.21. The distance between two antennas was changed from 20 cm to 80 cm and the path gain was simulated for each case by CST Microwave Studio. The variation of the distance between the two antennas is chosen in the range of the human body propagation channel path length. When the separation distance between two antennas is small relative to the wavelength, the antennas might be still in the near field region. The feeding point at the middle of the dipole is assumed as the reference to measure the distance between the antennas. To reduce the diffraction from the phantom edges, the PML layers are placed as close as possible to the box, though when the muscle phantom is used the diffraction from the edges still affects the results.

The path gain of the antennas is simulated on both fat and muscle phantoms. The simulated path gain versus distance is shown in Fig 6.22 for different antenna pairs. The distance between the antennas is varied from 20 cm to 80 cm which is the range of distance seen in on-body channels.

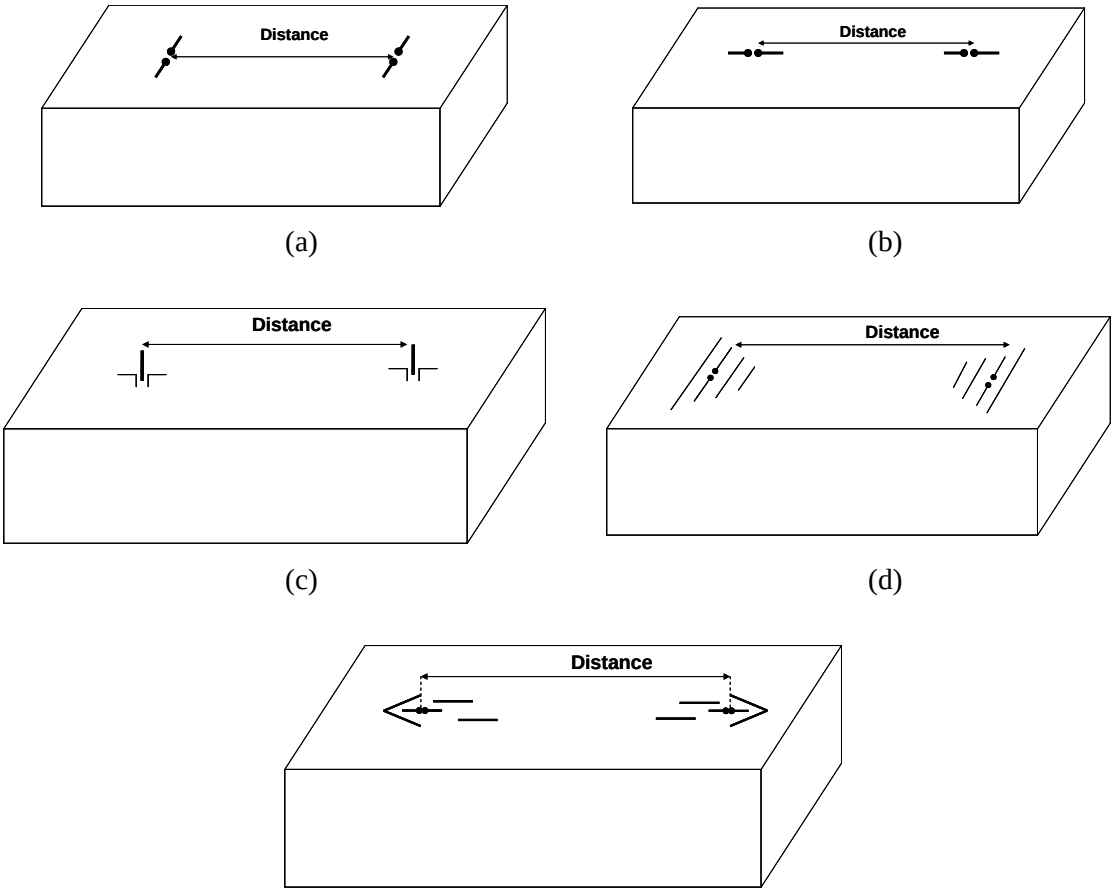

Fig. 6.21 (a) Parallel dipoles, (HH0), (b) Parallel dipoles, (HH90), (c) Monopole antennas, (MM) (d) Conventional Yagi antennas, (YY) (e) Surface wave parasitic arrays (SW)

(Muscle phantom: size = 600 × 600 × 50 mm^3, properties (ε_r = 52.7, δ = 1.7 S/m)),

(Fat phantom: size = 600 × 600 × 200 mm^3,Phantom properties (ε_r = 5.3, δ = 0.11 S/m))

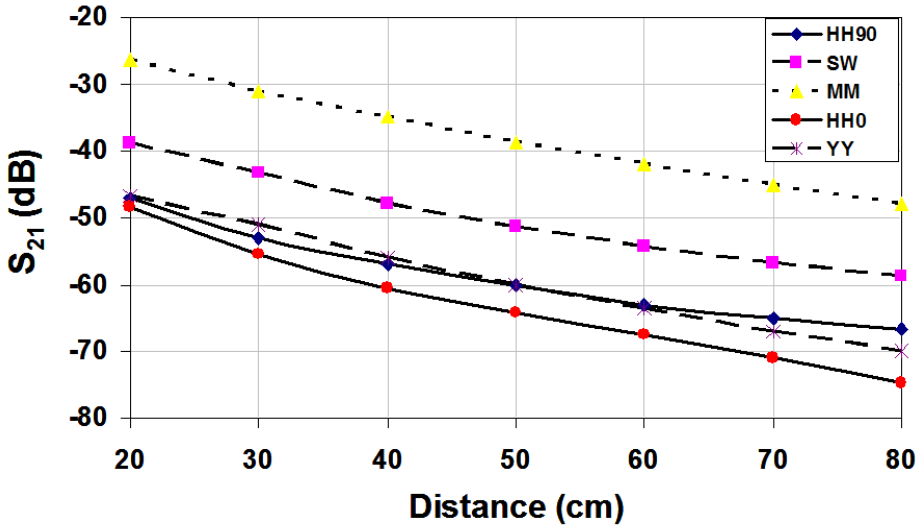

(a)

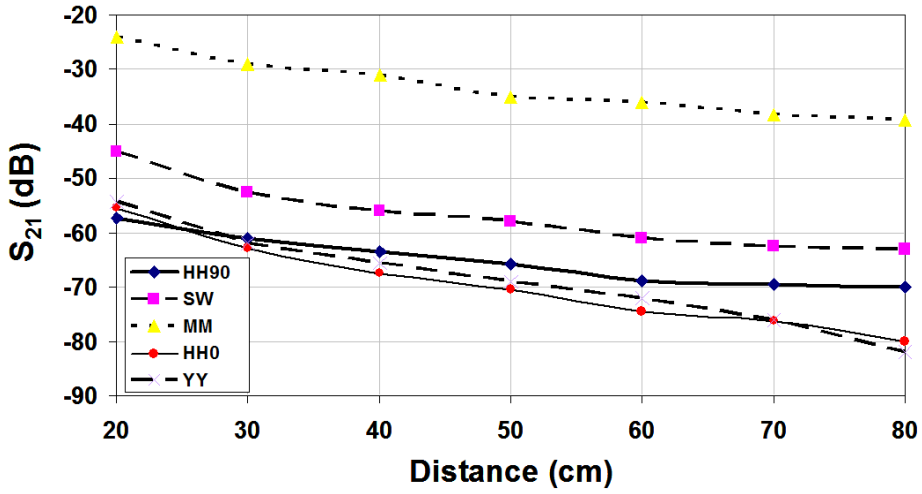

(b)

Fig. 6.22 Path gain of different antenna pairs versus distance between antennas for the configuration shown in Fig. 6.21,
(a) Fat phantom, (b) Muscle Phantom, (Details as Fig. 6.21)

The monopole pair provides the highest path gain on both phantoms, but it is not planar and not preferred for on-body applications. The surface wave parasitic array provides the best path gain of the planar types. The other antennas, including the dipole in both orientations and the conventional Yagi array, provide 10 to 15 dB lower path gain than the surface wave parasitic antenna. Comparing the trend of the curves on each tissue reveals that surface wave parasitic array, monopole and HH90 attenuates approximately at the same rate versus

distance. However, the conventional Yagi and HH0 path gain attenuate faster. The surface wave parasitic array excites the same mode (TM) as the monopole and HH90, which attenuates almost at the same rate. However, HH0 excites the TE mode as does the planar Yagi. Although the directivity of the Yagi is almost 13 dB higher than dipole (HH0), its smaller efficiency suggests that it is more affected by the phantom than the dipole. Hence, its path gain is not much higher than the dipole. There are some ripples in the muscle path gain results due to the diffraction from the phantom edges.

Comparing the path gains of the planar antennas on the fat with those on muscle indicate that although the results on fat at shorter distances is 5 to 10 dB is higher than muscle for all the antenna pairs, the surface wave parasitic array and the dipoles in the HH90 configuration decays slower on the muscle and at a distance of 80 cm the difference is almost 2 dB. However, the conventional Yagi and the dipole in the HH0 configuration path gain decay almost at the same rate on the fat and muscle and changing the tissue does not help to decrease the attenuate rate. The path gain of the monopole on both the fat and muscle phantoms at shorter distances is almost similar, and due to the lower attenuation on the muscle, the path gain on the muscle at the distance of 80 cm is almost 10 dB higher than fat.

6.4.2 Cylindrical Surface

Modelling the antenna on the flat phantom demonstrates its potential, but it is not a very useful approximation for the on-body model. Therefore, a cylindrical muscle phantom was modelled. A pair of surface wave parasitic array antennas, monopoles and dipoles were placed on two different side of the cylinder, 5 mm away from its surface as shown in Fig. 6.23. The radius and height of the phantom was 20 cm and 100 cm, respectively. The antennas were located at the middle of the cylinder and the top and the bottom of the cylinder was covered

with perfect matched layer (PML) boundary to reduce the diffraction from their edges. Table 6.3 shows the path gain for the antenna pairs.

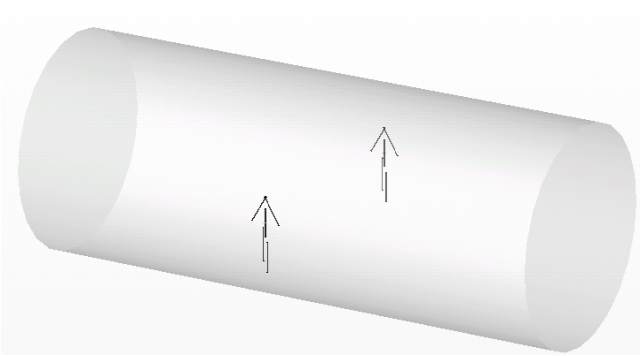

Fig. 6.23 Pair of surface wave parasitic array antennas on a muscle phantom cylinder (radius = 20 cm, height = 100 cm)

Table 6.3 Path gain of different antenna combinations on cylinder of Fig. 6. 23

	Dipoles (HH0)	Dipoles (HH90)	Surface wave parasitic array	Monopoles
S_{21} (dB)	-97	-104	-65	-65

The results show that the surface wave parasitic array antennas combination provides as strong a link as that of the monopoles. However, both of the dipole configurations do not show a good performance and the level of the received signal is very low.

6.5. ANTENNA REALISATION AND MEASUREMENT

In the simulation environment, the surface wave parasitic array is fed by a discrete port. However, this is difficult to feed in practice, and an alternative feeding was developed. The conventional method is to feed the antenna by a parallel line perpendicular to the antenna from side of the antenna as shown in Fig. 6.24. However simulation showed that this type of the feeding perturbs the radiation pattern in the plane of the antenna. In order to move the feeding

to the direction opposite to that of the maximum directivity, the antenna configuration is modified as shown in Fig. 6.25. The dipole antenna is transformed into a printed monopole antenna and a 50 ohms parallel transmission line of a 2 mm width is used to feed it, such that the antenna can be fed from the edge of the substrate behind the reflector. The reflector is located at the position of the gap in the original dipole and is perpendicular to the driven element. It thus acts as both reflector and ground of what is now effectively a monopole antenna. Because the structure is intended for construction on FR4 substrate, the dimensions of all the elements are changed from those used previously (see Fig. 6.25).

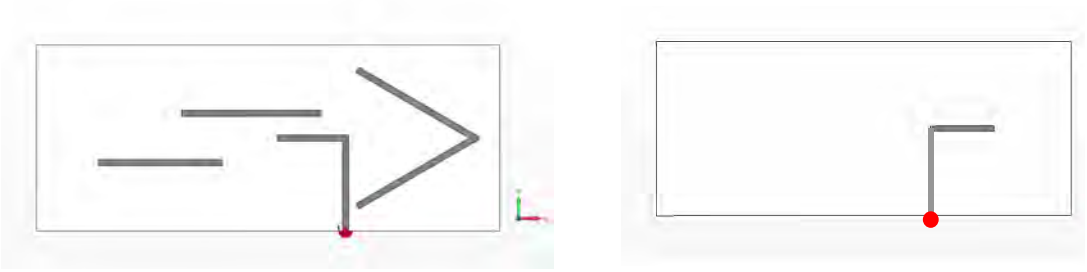

(a) (b)

Fig. 6.24 Configuration of surface wave parasitic array with side feed
(a) Top view, (b) Bottom view

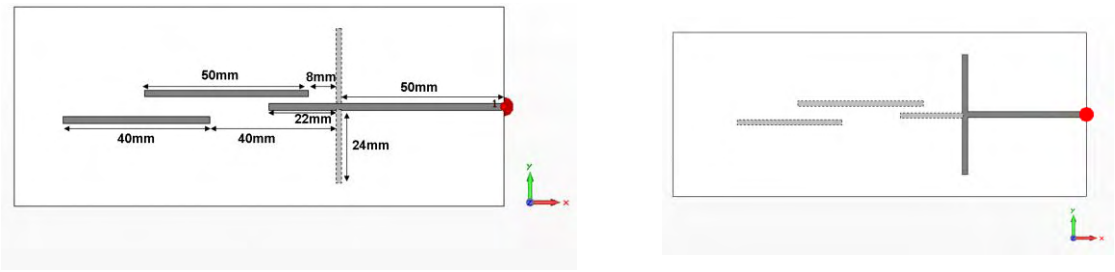

(a) (b)

Fig. 6.25 Printed surface wave parasitic array antenna
(a) Top view, (b) Bottom view

The simulated return loss is shown in Fig. 6.26. Comparing this to Fig. 6.12 shows that the both wire and printed antennas are resonating at 2.6 GHz. At 2.45 GHz, the return loss of the antenna is almost -10dB. The simulated radiation patterns of the antenna in both XY and XZ plane are shown in Fig. 6.27. The radiation pattern is also similar to the wire one.

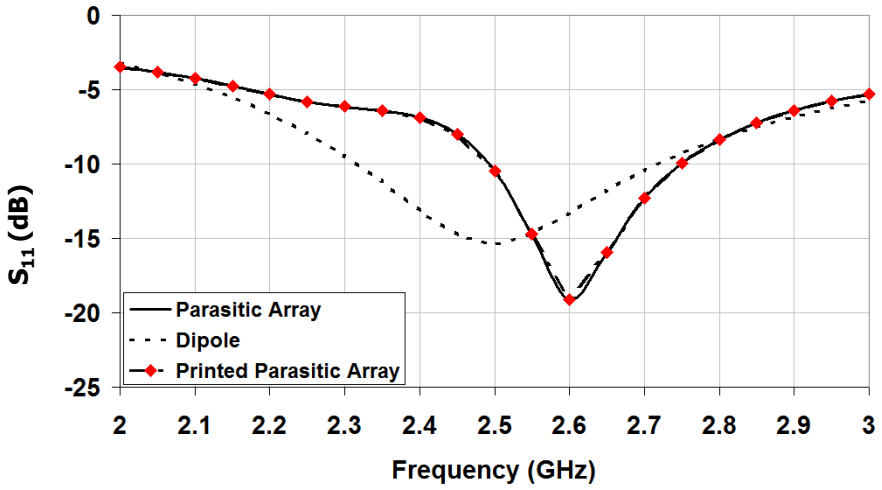

Fig. 6.26 Simulated return loss of printed surface wave parasitic array antenna on fat phantom (Details as Fig.6.10)

(Phantom size=200×200×200 mm^3, antenna 5 mm away from surface, antenna points in φ=180° direction)

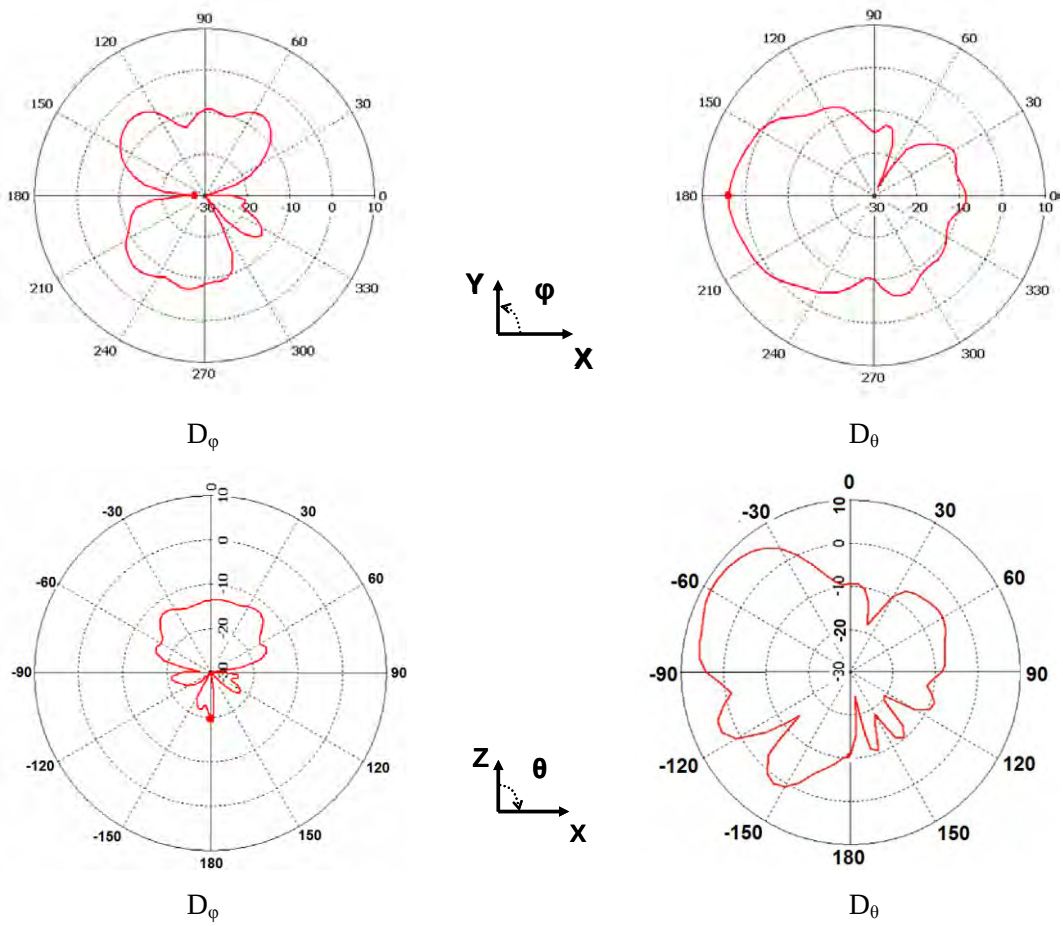

D_φ D_θ

D_φ D_θ

Fig. 6.27 Simulated far field directivity pattern of printed surface wave parasitic array antenna on fat phantom, (Details as Fig.6.26),

The printed surface wave parasitic array was built and measured. The antenna is shown in Fig. 6.28. To test its capability to launch a surface wave two antennas were placed on a bath of liquid with the dielectric properties of muscle tissue. The plastic container (740 × 350 × 142 mm^3) was filled with the liquid and the antennas were placed on a 3-mm thick plastic holder which was fixed almost 6 mm above the liquid phantom surface, as shown in Fig. 6.29. The measurements were done inside the anechoic chamber to exclude effects of the laboratory environment from the measured results. To improve the signal to noise ratio of the measurement set-up, an amplifier was used just after the VNA and the VNA was calibrated prior to the measurement, with the connected amplifier and long cables. The measured noise floor level after calibration was approximately –85 dBm.

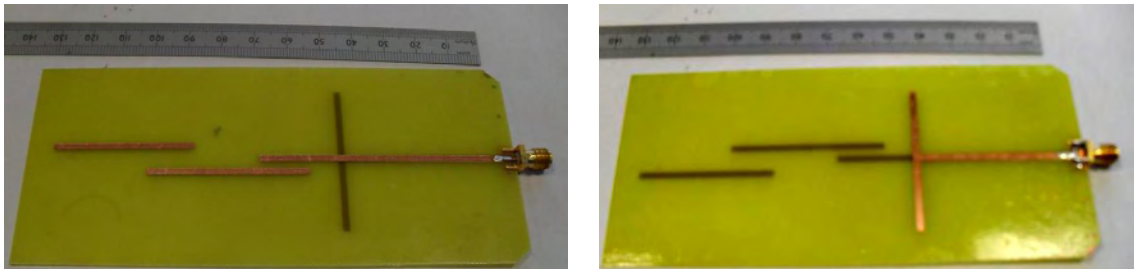

(a) (b)

Fig. 6.28 Fabricated surface wave parasitic array antenna, (a) Top view, (b) Bottom View

To measure the path gain versus the distance, the distance between the two antennas was varied between 22 cm and 56 cm with a 2 cm increment, and S_{21} was measured for each distance. The distance was measured from the reflector of one antenna to the reflector of the other antenna. Fig. 6.30 shows the measured and also simulated results. Comparing the results of the simulation and the actual measured data at 2.45 GHz reveals that the two curves are attenuating with the distance almost at the same rate. However, the measured path gain is higher by almost 8 dB. Performing the measurements inside an anechoic chamber decreases the level of scattering from the surrounding environment, but reflections from the absorbers and partially exposed metallic floor still exist. To eliminate the multipath effect from the

measured data, the time gating technique was used and the results are shown in Fig. 6.30. In time gating method, the response in frequency domain is transformed into the time domain and the strongest pulse is chosen as the direct ray and the rest is filtered out which are caused by the multi-path interferences [93]. The frequency bandwidth which determines the resolution of time gating was chosen to be 500 MHz. This bandwidth results in 60 cm resolution. This resolution is sufficient to isolate the reflections from the anechoic chamber's walls and floor, but the reflections from the plastic tub still remain. An increase of the bandwidth would increase the resolution. However, the antennas are narrowband and it is not possible to do a wideband measurement. As Fig. 6.30 shows, time gating reduces the signal level by almost 8 dB to approximately the level predicted by the simulations, however the time-gated path gain fluctuates somewhat, probably due to the reflections from the plastic tub.

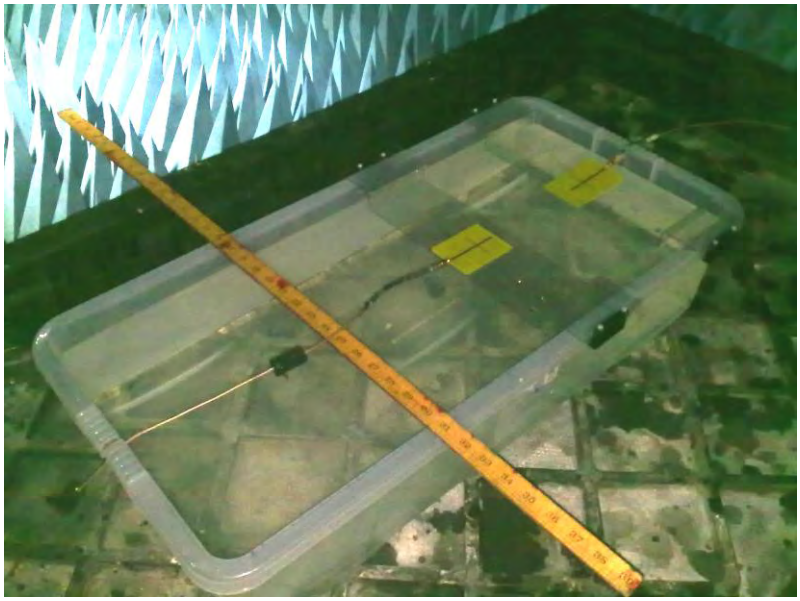

Fig. 6.29 Measurement set-up inside the anechoic chamber

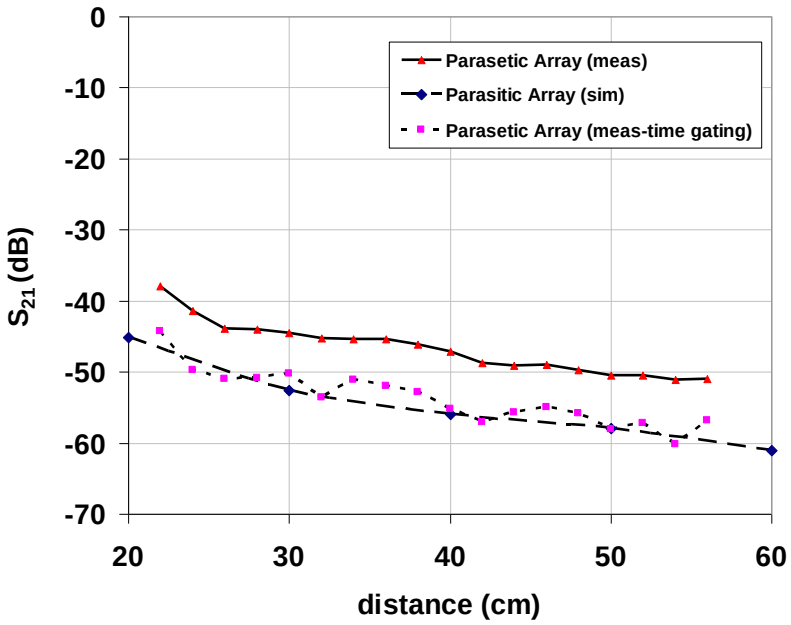

Fig. 6.30 Measured S_{21} of the parasitic array on the muscle phantom liquid

To evaluate the path gain improvement of the SW parasitic array antenna, three different types of antennas, including monopoles (Fig. 6.31(a)), planar monopoles (Fig. 6.31(b)), and planar dipoles (Fig. 6.31(c)), were placed on the liquid phantom in the set-up shown in Fig. 6.29, and the path gain measurements were repeated in the similar way. The antennas shown in Fig. 6.31 are all resonant at 2.45 GHz.

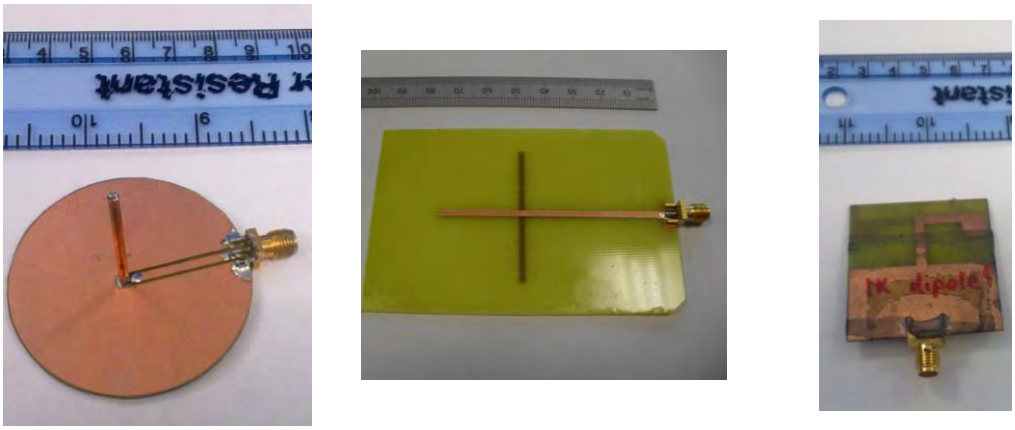

(a) (b) (c)

Fig. 6.31 (a) Monopole antenna, (b) Planar monopole antenna, (c) Planar dipole antenna

As shown in Fig. 6.32, SW parasitic array provides higher path gain compared to the planar dipole and planar monopole which are representative of HH0 and HH90 combination (see Fig. 6.21), by almost 12 and 14 dB at 50 cm distance. However, the path gain of the parasitic array is smaller by almost 18 dB than that of the monopole at the same distance. The path gains produced by the parasitic arrays, monopoles and planar monopoles all decrease with the distance at almost the same rate which suggests that they excite the same surface wave mode. The planar dipoles, which are placed as shown in Fig. 6.21(a), behave differently. The path gain decreases faster than that of the other antennas which is representative of the different mode of propagation.

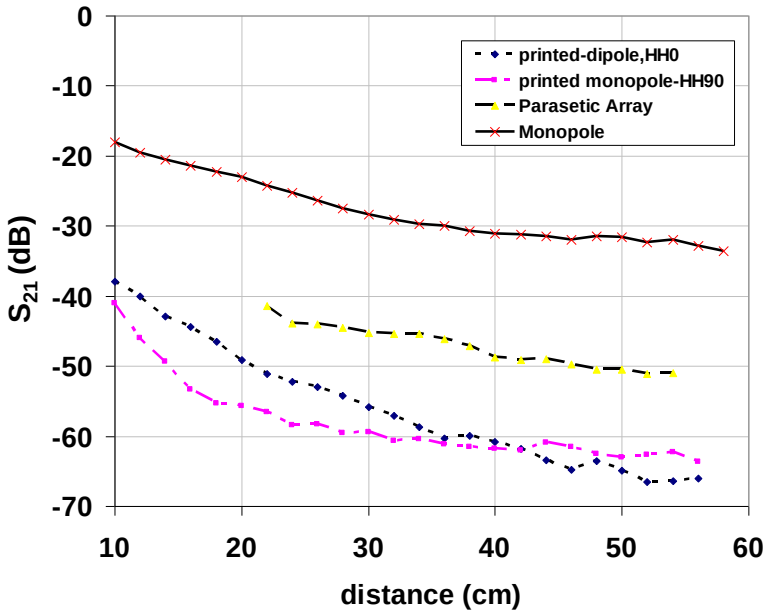

Fig. 6.32 Measured path gain of different antenna pairs on the muscle liquid phantom inside anechoic chamber

6.6. SUMMARY

A novel surface wave parasitic array antenna was presented and its performance on the body phantom was investigated. In fact, the change in the dipole antenna characteristics in proximity of the body phantom and providing the high path gain on the body phantom surface,

was the main motivation to design the new antenna with a higher directivity. To increase the directivity of the dipole, parasitic elements were used along the antenna and the antenna was optimised to yield the maximum directivity on the phantom surface. It was shown that use of this antenna can improve the path gain by almost 10 dB compared to the planar dipole on the muscle phantom. The measurements were also carried out on the bath of the muscle liquid phantom. The path gain results were in a good agreement with simulation and the parasitic array antenna showed higher path gain compared to the planar dipole.

Chapter 7

Body Centric Wireless Communications at Millimetre Wavelengths

7.1. INTRODUCTION

Recently, a great deal of work has been conducted by researchers to develop millimetre wavelength (MMW) communication systems for commercial application. The 60 GHz band has a great potential for many short range applications, including body area networks. Interference into and control of the radiated power out of on-body modules is one of the main problems at lower frequencies for example at 2.45 GHz, which can be improved at 60 GHz by use of directive antennas with very small sizes.

In this chapter, MM wave applications for short range wireless will be explained and then the advantage and disadvantage of its use will be addressed. Later, the design of a waveguide to microstrip transition will be described, which is used to feed some on-body antennas

designed in another PhD study and finally MM wave measurements performed on the body will be presented.

7.2. MM WAVES FOR SHORT RANGE APPLICATION

The 7 GHz of free spectrum at 60 GHz makes it very attractive proposition for high data rate applications, where 2 Gb/s or higher is possible at this range of frequency. However, working at such a high frequency introduces several challenges. The high propagation attenuation, the reduced multipath and diffraction effects which at low frequencies gives rise to reliable non-line-of-sigh (NLOS) communications and the high potential cost at front end devices, are some of the problems. Attenuation can be tackled to some extent by the use of high gain antennas. At this frequency, devices become small, and directive antennas can be integrated on MM wave chips.

Many studies have been done to characterise the channel at 60 GHz by doing extensive measurements in the indoor environment [61-69]. In fact, the wave propagation mechanism and the quality of the received signal depend on transmit and receive antenna characteristics such as polarization and antenna directivity, antenna position, the environment (furniture and materials) and also human activity [63, 67, 69, 94-95]. In many experiments, MM wave is considered for the line of sight (LOS) situation, where transmit and receive antennas are pointed at each other and just temporary signal blockage may happen due to human activity such as passing through the line of sight. It has been shown that the presence of the body can add an extra 20 dB loss to the received signal [94]. In these scenarios, directive antennas are preferred, due to their high gain which can overcome to the channel loss problem, but use of these antennas for NLOS is not suggested due to the reduction of the multipath effect contribution. Multipath plays an important role in NLOS situations, and use of the antennas with a moderate directivity (10 to 15 dBi) with fan beam shape can be helpful to collect

reflected waves from the walls, ceiling, floor and also from the furniture in the room for these scenarios [95]. In addition, other techniques such as diversity, beam switching and phased array antenna are suggested to overcome the shadowing effect [60].

7.3. MM WAVES FOR ON-BODY APPLICATIONS

One of the major problems in using low frequencies namely, 2.45 GHz or the UWB band, for on-body applications is the significant radiation off the body from the antennas mounted close to the body. This may cause interference with other users and also make it insecure for the application such as health and military. Use of MM waves can resolve the problem by using directive antennas. Furthermore, at this range of the frequencies, the signal attenuates very quickly with distance which increases the security levels, significantly. In addition, the small size of the RF devices is evident at this frequency. However, high data rate is less of an advantage in on-body application as data rates for many applications are rather low. The main challenge in the use of MM waves for on-body channels is the shadowing effect, which can be due to both body movement and also body curvature. Similar to the other short range applications, it seems that choice of the right antenna and appropriate on-body channel are crucial for the communication at this frequency range.

7.4. ANTENNA CONSIDERATIONS FOR MM WAVES

Using the Friss formula to do simple link budgets shows that channel loss at 60 GHz in free space is almost 28 dB higher compared that at 2.45 GHz for a given distance appropriate to body use. For example, at a distance of 50 cm, the ratio of the loss at 2.45 and 60 GHz is proportional to their wavelength which is $(125/5)^2$ or 28 dB. One way to compensate this increased loss at 60 GHz is to use directive antennas as the transmitter and receiver, each with at least 10 to 15 dBi gain. However, use of these narrow beam antennas is also challenging

due to the variable geometry giving rise to changes in beam direction and hence loss of signal. Use of the antennas with a wider beam or even omni-directional can tackle the problem to some extent, but received signal levels will reduce significantly. For on-body applications, other techniques, such as beam switching or diversity may provide better performance [96]. In addition to the beam width and gain of the antennas, other important needs are low profile, light weight, and shape conformal to the body surface. Printed antennas can fulfil these criteria, but many of printed antennas using planar feeding techniques such as microstrip lines. At MM wavelengths, use of waveguide to feed the antenna is preferred to coaxial line, due to the mechanical difficulty of connecting the coaxial probe to the microstrip line, for very thin substrates and line widths. In addition, the use of metallic waveguides are still very popular at this range of frequency because of their high performance in different MM wave modules, such as high Q-filters, high-Q oscillators and nonreciprocal components [97]. Hence, the waveguide to microstrip transition is required to feed the antennas through the waveguide. In the next section, the design and realization of the transition, which is then used to feed printed Yagi the antennas, will be described.

7.4.1 Stepped Waveguide Design

In millimetre-wave hybrid and monolithic integrated circuit applications, there are many requirements for evaluation of microstrip line circuits using waveguide measurement systems and the combination of integrated circuits with air filled or dielectric filled waveguide components. High performance transitions from microstrip to waveguides are essential. One of the most widely used transitions is shown in Fig. 7.1, which consists of a microstrip-to-ridge waveguide junction in which the ridge extends from the top of the microstrip line to the waveguide wall forming an impedance transformer [97]. The transition converts the dominant quasi TEM mode in the microstrip line to TE_{10} mode in the rectangular waveguide. The dominant mode field distribution in the first section of the ridge waveguide

(with deepest ridge) resembles that of the microstrip line, whilst the last ridge section has a mode structure similar to that in the waveguide.

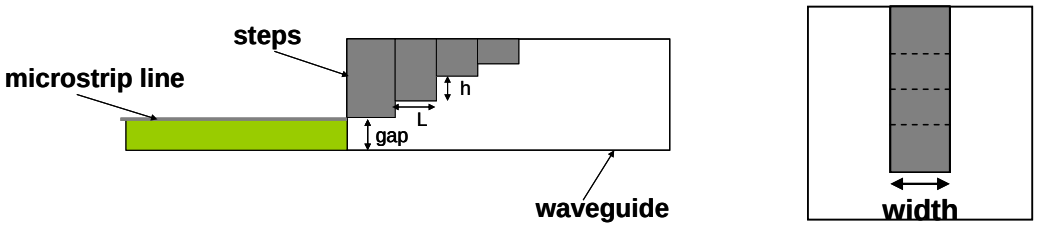

(a) (b)

Fig. 7.1 Step waveguide schematic, (a) side view, (b) front view

To design the transition, Chebyshev multisection matching theory is used. The equivalent circuit model of the transition for two steps is shown in Fig. 7.2. Z_L and Z_0, two known impedances, are the waveguide wave impedance and the microstrip line characteristic impedance, respectively. Z_1 and Z_2 are the wave impedance of the each step which needs to be calculated. Z_0 is usually 50 Ohms and Z_L is the wave impedance of the waveguide with WR15 standard aperture size which is 520 Ohms at 60 GHz. The number of sections in the transformer determines the bandwidth of the waveguide. More sections provide wider bandwidth. The last step gap from the bottom wall of the waveguide is determined by the thickness of the board used as the microstrip substrate. For this design, the substrate is Roger RT 5880 (ε_r = 2.2) with 0.13 mm thickness. Hence, the last section dimension is fixed, and its impedance is around 90 Ohms. The impedance of each section can be derived from the tables given in [98]. For the current design, two sections are used with Z_1 90 Ohms, and Z_2, 275 Ohms. To simulate the steps, CST Microwave Studio software was used and the gap between the steps and the bottom wall of the waveguide were changed in a way to yield the required impedances. The dimensions of the steps and waveguide aperture are shown in Fig. 7.3. Small variation of the height and the width of the steps, h_1, h_2, w_1, do not affect the

performance of the transition significantly and the insertion loss of the transformer can change within 0.5 dB by variation of their sizes.

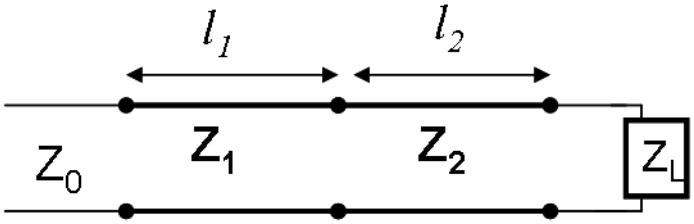

Fig. 7.2 Two section matching transformer

To demonstrate performance, a 50 Ohms microstrip line is connected to the waveguide as shown in Fig. 7.4(a) in CST studio and S_{21} between the two ports is simulated. As is shown in Fig. 7.4(b), the transition provides a satisfactory performance and its insertion loss is almost 0.6 dB at 60 GHz.

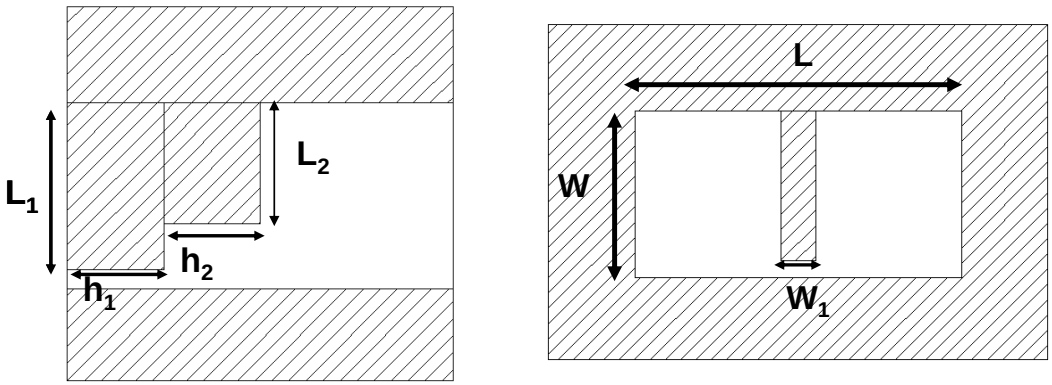

(a) (b)

Fig. 7.3 Waveguide to microstrip transition schematic (a) size view, (b) front view, L_1 = 1.7296mm, L_2 = 1.2496mm, h_1 = 1 mm, h_2 = 1mm, W_1 = 0.4mm, W = 1.8796 mm, L =3.7592 mm

7.5. ON-BODY MM WAVE MEASUREMENT

In this section, the measured received signal levels are reported for a chest-belt on-body channel at 60 GHz. Several attempts were made to perform on-body measurements in other channels, but due to the small dynamic range of the set-up described in section 7.5.1,

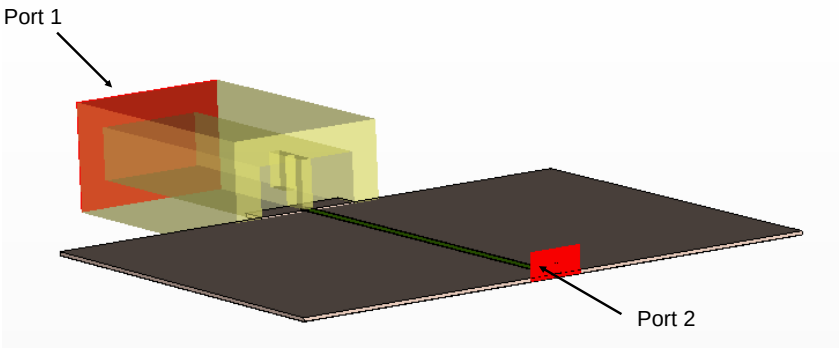

(a)

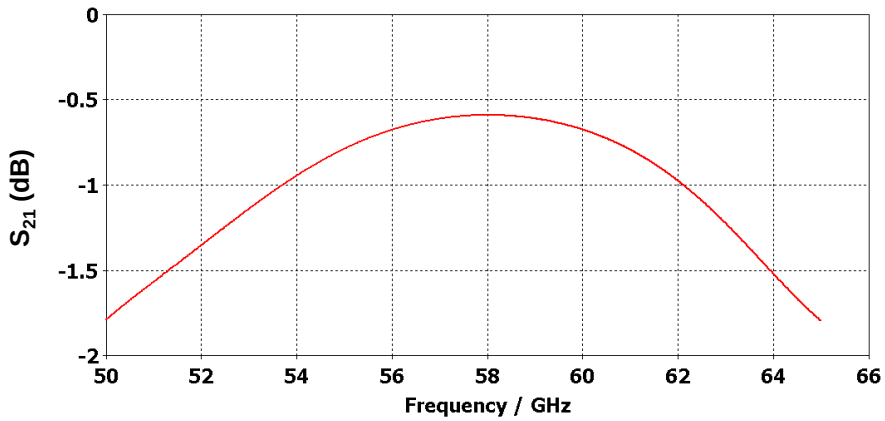

(b)

Fig. 7.4 Stepped waveguide transition to 50 microstrip line,
(a) Configuration, (b) Simulated S_{21}

these were unsatisfactory, since the received signal level often fell below the noise level. To tackle the problem, a power amplifier at the transmit antenna and a low noise amplifier at the receive antenna were used in the set-up to lower the noise level and improve the dynamic range of the set-up.

7.5.1 Measurement Set-Up

Channel measurements were done on a 166 cm height and 55 kg male in an indoor environment which was a 7.5 m × 9 m sized laboratory containing equipment, tables, chairs, and computers. Standard horn antennas with 20 dBi gain were placed on the right side of the belt and right side of the chest in a way that their apertures pointed toward each other. The distance between them was approximately 16 cm. Initially, a Gunn diode source operating at 60 GHz was used. But the frequency was extremely temperature sensitive. To resolve this problem, a vector network analyzer (VNA), HP/Agilent 8719/20/22, at 20 GHz, followed by a frequency multiplier, was used as the source. The level of the power in VNA was set to 5 dBm. The multiplier, V-3X, had 15 dB conversion loss. To compensate for this, a 28.7 dB gain Spacek medium power amplifier (SP604-13-12W) followed the multiplier. The transmitter configuration is shown in Fig. 7.5. To receive the signal, a Agilent/HP 8563E spectrum analyser with an external HP harmonic mixer with an insertion loss of 34 dB at 60 GHz (Model no. 11970V) mixer is used. To amplify the signal received by the antenna, a 18.4 dB gain Spacek low noise amplifier with 4.9 noise figure (SLV-20-4) was used just before the

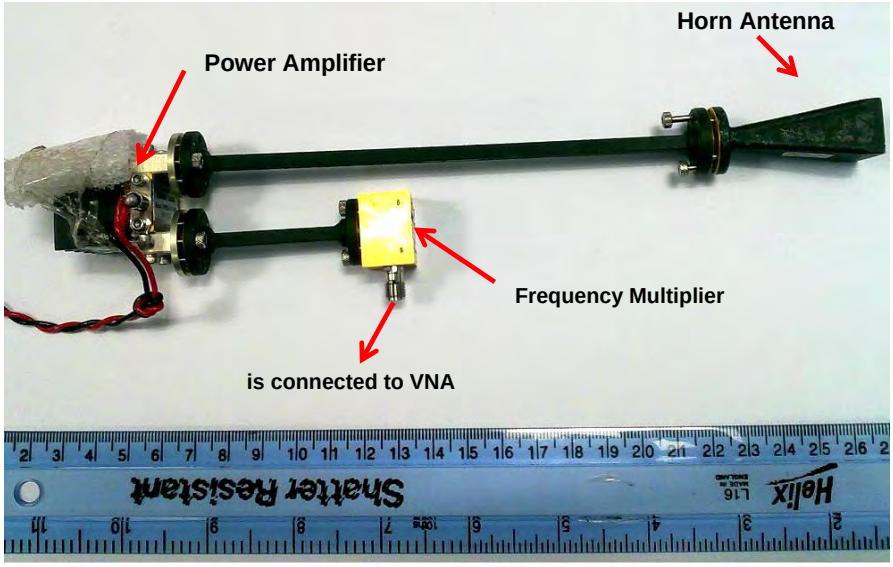

Fig. 7.5 Transmitter set-up used at 60 GHz on-body measurement

mixer. The receiver set-up is shown in Fig. 7.6. The noise level of this set-up was around -55 dBm. 601 data points were collected every 5 sec and during the measurement some movements performed to investigate the effect of the shadowing in the channel. The measurement set-up is shown in Fig. 7.7.

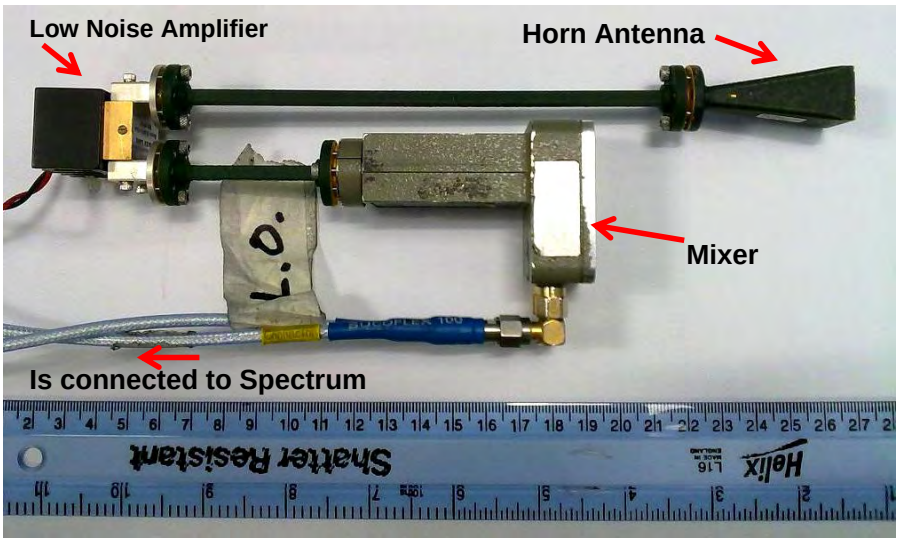

Fig. 7.6 Receiver set-up used at 60 GHz on-body measurement

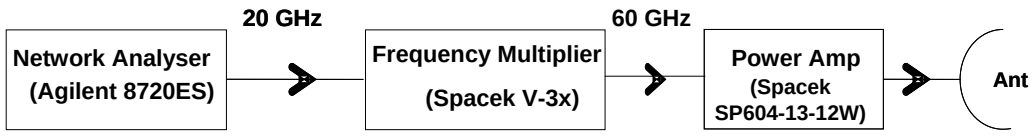

(a)

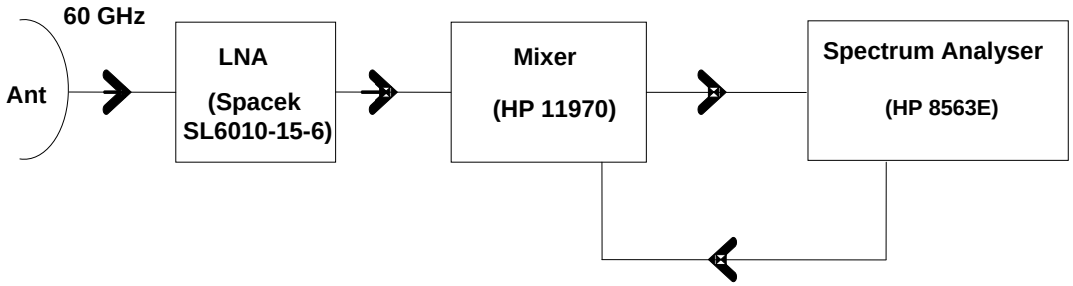

(b)

Fig. 7.7 MM wave measurement set-up,
(a) Transmitter, (b) Receiver,
(VNA- Vector Network Analyser, LNA: Low Noise Amplifier)

7.5.2 Measurement Experiments

The chest to belt is a LOS channel and the distance between the antennas is quite short compared to the other on-body channels. Several measurements were done to investigate the effect of the shadowing at 60 GHz in this channel. Also, the effect of the relative movement and changes of orientation of the antennas was studied. Fig. 7.8 shows the received signal in a 5 sec period while the posture was static. As it can bee seen, even though the posture was quite steady, the level of the signal varies by almost 5 dB. This measurement suggests that small movements, such as breathing, can significantly affect the signal level Fig. 7.9 to Fig. 7.11 show the effect of body movements on the received signal for various movements. The results suggest that movements which shadow the channel, such as hand movement in front of the body, can have severe effects and the signal can fall below the noise level very easily. Other movements, such as bending and turning the chest to the right and left do not shadow the channel as strongly as the hand movement but can change the orientation and hence the polarization of the transmit antenna which also lowers the level of the received signal and depending on the type of the movements the signal may results in loss of the signal.

Table 7.1 Movements description

Movement	Description	Corresponding Figure
Static	Standing upright and hands by sides	7.8
Bending over	Body rotates at hip, chest and head move forward	7.9
Moving hands in front	Standing upright and hands in front of the chest are moving periodically toward each other	7.10

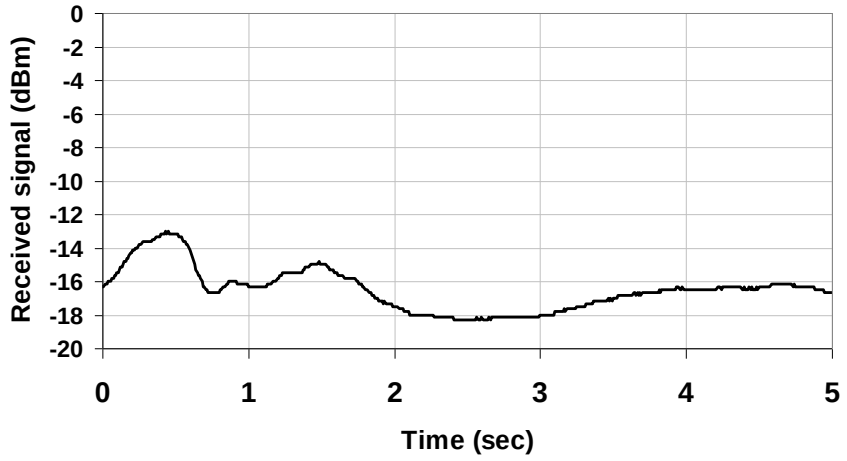

Fig. 7.8 Received signal variation on the static posture in chest to belt

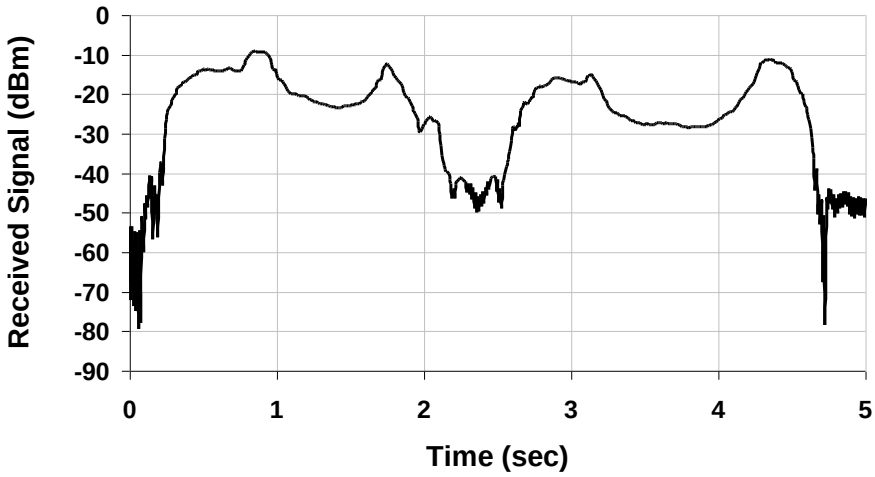

Fig. 7.9 Received signal variation in chest to belt while bending over

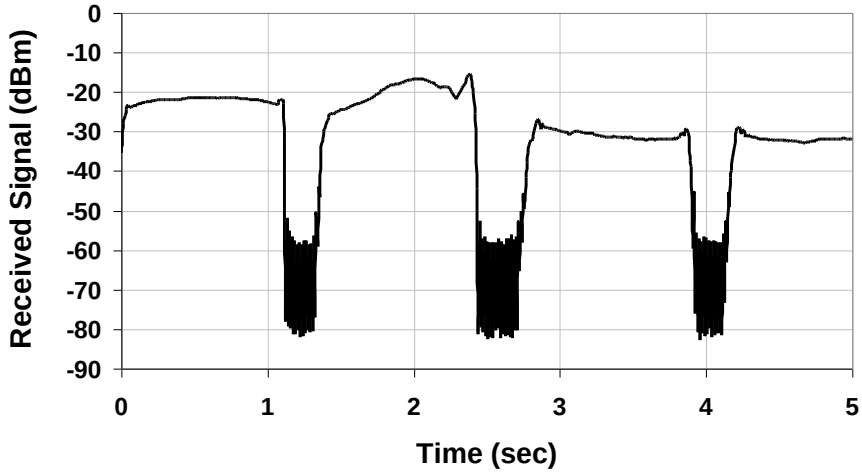

Fig. 7.10 Received signal variation in chest to belt while moving hands in front

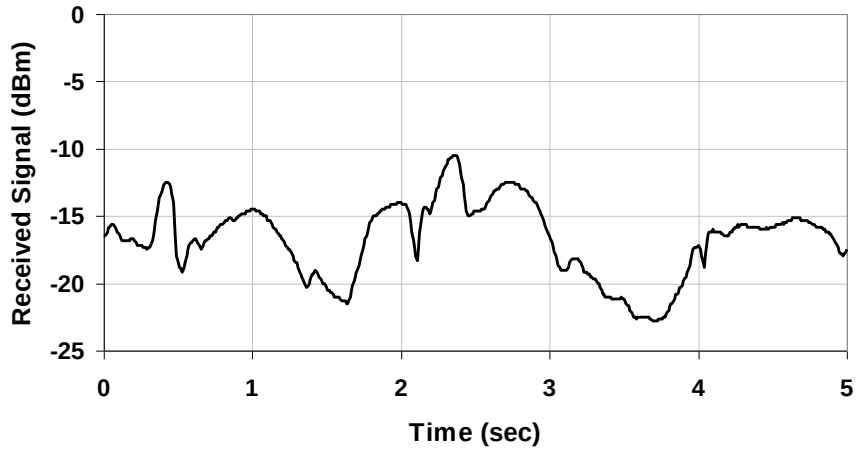

Fig. 7.11 Received signal variation in chest to belt while moving the chest right and left

Other experiments were carried out in which antenna aperture were put offset to each other by almost 1 cm. This caused drop in the received signal of almost 15 dB. With this antenna arrangement, similar movements were repeated and the results are shown in Fig. 7.12 to Fig. 7.14. Hand movements and bending over reduced the received the signal significantly, while bending to the right and the left resulted in less reduction.

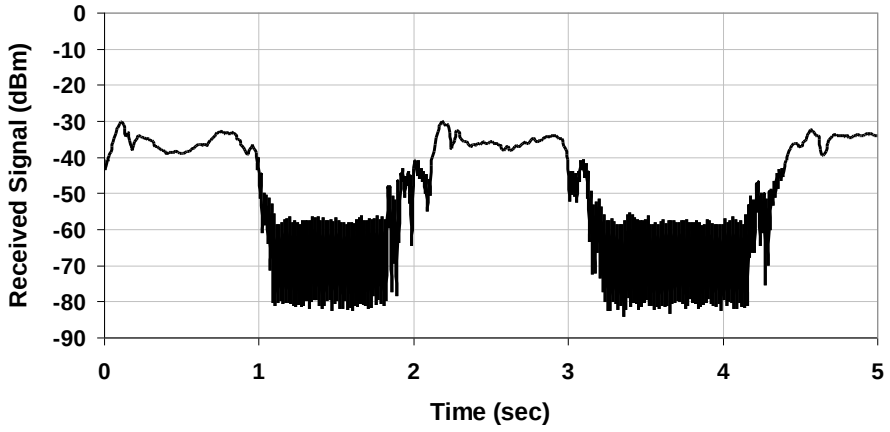

Fig. 7.12 Received signal variation for the displaced antennas while bending over

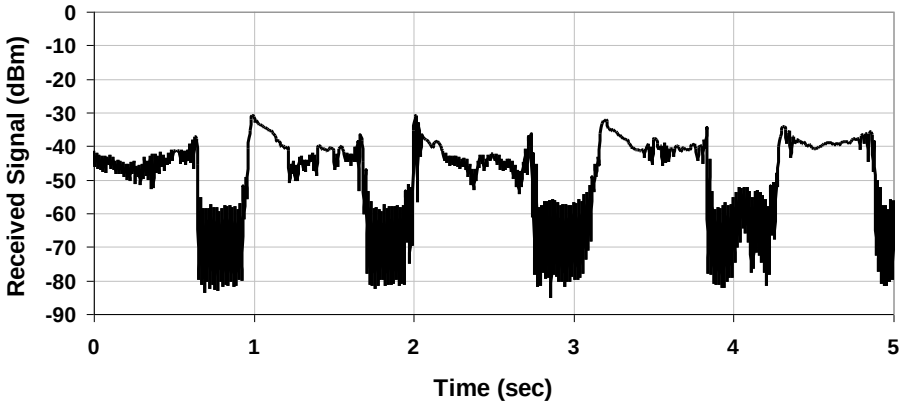

Fig. 7.13 Received signal variation for the displaced antennas while moving hands in front

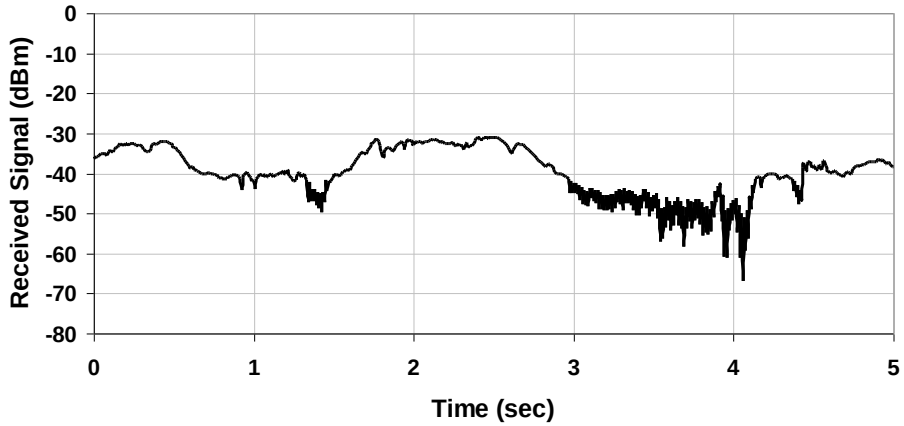

Fig. 7.14 Received signal variation for the displaced antennas in chest to belt while moving the chest right and left, and the antennas are displaced

Table 7.2 shows the percentage of time that signal falls below the noise level (fade probability) and also the average power of the received signal above the noise level. The most blockage of the signal with 37% occurs when the antennas are placed offset from each other in the body moving forward case. In the static body posture and moving the chest left and right cases the fade probability is 0% which shows the signal stay above the noise level. The average power above the noise level reveals that, the movements do not reduce the level of the signal significantly compared to the static body. However, the received signal drops almost by 20 dB by changing the position of the antenna on the chest in the antenna offset case.

Table 7.2 Fade probability and averaged received power above the fade level (-55 dBm) of the chest to belt channel at 60 GHz

Movements	Fade probability %	Average power above threshold level (dBm)
Static posture, Fig. 7.8	0	-16.3
Bending over, Fig. 7.9	1.7	-17.8
Moving hands in front, Fig. 7.10	14.33	-23.2
Moving chest right and left, Fig. 7.11	0	-15.9
Offset- Bending over Fig. 7.12	37	-36.1
Offset- Moving hands in front Fig. 7.13	26	-39.8
Offset- Moving chest right and left Fig. 7.14	1.8	-36.4

7.6. SUMMARY

In this chapter, MM wave for on-body application was investigated. The measurements results at 60 GHz in the chest-belt channel for both static and moving body were presented. It was shown that received signal is significantly affected by the body movement and also antenna orientation. The signal fell below noise floor when the channel was shadowed.

Chapter 8

Discussions, Conclusions and Future Work

8.1. DISCUSSIONS AND CONCLUSION

Many investigations have been done in the last decade with the aim to provide more reliable on-body communication links for the users of body area networks. Characterisation of on-body channels and the design of suitable antennas for electronic devices in on-body applications remain very challenging, due to the unique specification of the human body as the primary environment of the link. Due to the complexity of on-body channels, physical experiments have been the main methods to estimate the antenna behaviour and channel performance by performing measurement both inside the anechoic chamber or in indoor environments. However, effort has been made to understand the propagation mechanism on the body by studying surface and creeping waves which are believed to be main propagation mechanism for shadowed channels. This thesis is a continuation of that work and investigates on-body propagation from a wave polarization point of view. The achievements will help to move the topic forward both in understanding and in the production better optimises systems.

To investigate the channel polarization behaviour, practical antennas with polarization normal or parallel to the surface of the body were initially examined and four separate measurements with co- and cross- polarized at the both ends of the channels were performed. The inconsistency of the results suggested that the measurements with separate antennas were not reliable, due the change of the cable orientation, position of the antenna and even the posture. A new dual-polarised antenna was introduced to improve the measurements. Use of this antenna led to simultaneous measurements for all four possible polarization combinations which help to reduce the variations in the measurement scenarios. The measured data was processed by calculating the mean of received signal amplitude and the cross polarization discrimination for different polarization combinations. It was demonstrated that use of vertically polarised antennas (relative to the body surface) at the both ends of the channel provides 10 to 15 dB higher path gain compared to a pair of horizontally polarised antennas. The combination of vertically and horizontally polarised at each end of the each channel gave path gain between the all vertical and horizontal combinations. The cross polarization discrimination analysis suggested that static channels, such as belt-chest, are less likely to experience the depolarization of the wave. However, in the dynamic channels, such as the belt-wrist or belt-ankle, the depolarization effect is more evident. In general, use of vertically polarised antennas can significantly reduce depolarization. Also, fast fading analysis was performed. The results revealed that all the antenna combinations fit to Rician distribution and provide almost similar K factor, between 1 and 2, for different channels in the laboratory environment. The expectance to this is the belt-chest channel which due to the presence of strong line of sight for vertically polarised antennas yields a K factor of 4. In the chamber measurements, the scattering reduces and hence the K factor increases compared to the laboratory for all the polarization combination other than horizontal at both ends.

The polarization diversity technique has been investigated for on-body communication channels. A novel integrated dual-polarized antenna was used for the measurements. The

results suggest that polarization diversity can yield good diversity gain of around 7 dB for dynamic channels, such as the belt-ankle and belt-head. Channels such as the belt-chest and belt-wrist do not provide significant diversity gain due to the presence of strong LOS. In general, it was shown that the polarization diversity performance is not as good as other diversity techniques.

To understand the measurement results discussed above, the surface wave was studied on the flat phantoms of skin, fat and muscle tissue. Both Zenneck and Norton wave behaviour were discussed and the condition to support these waves on the phantom was presented. It was shown that to bind the surface wave to the tissue strongly, the reactive part of its surface impedance must be largely inductive. However, human tissue, which includes skin, fat and muscle, result in a surface impedance with a small inductance part, which means the surface waves may not be well supported on the body. In addition, the coupling of the small dipole and practical antennas to the surface wave on the flat phantom were investigated. The Norton wave and simulation results suggested that the parallel small dipole close to the phantom launches a surface wave mode along the antenna similar to the vertical dipole, but with smaller amplitude. To evaluate the antenna performance, the path gain between two dipoles in different orientations were simulated and it was shown that maximum path gain of an on-body channel consisting of two dipoles parallel to the body surface can be obtained if two antennas are placed in line with each other, though the level of the signal is lower than two vertical polarised antennas. The characterisation was repeated for the various practical antennas used for on-body communications, such as the monopole, tangential dipole, patch, IFA and PIFA. It was found that horizontal polarised antennas in proximity of the body surface launch strong surface wave in the direction which there is no free space radiation. Hence, the TM wave is excited by all of the antennas regardless of their polarization and they show similar attenuation factors. However, the vertically polarised antenna acts much more efficiently than the horizontally polarised ones.

In addition, fields of the antennas on a cylinder were simulated, which is more representative of the human trunk. The attenuation on the cylinder was much faster than a flat surface and it decayed exponentially. On the cylinder the polarization of the antenna does not affect on the attenuation factor but its influence is noticeable in the strength of the creeping wave excitation. The results were confirmed by an analytical method. The results are used to confirm the simulation results in CST Microwave Studio. It was shown that the attenuation was much faster than on a flat surface, and it decayed exponentially.

To launch a stronger surface wave on the body with a planar antenna, a new parasitic array antenna with relatively high directivity was introduced. The launching of a TM mode surface wave, by a dipole parallel to the phantom was the basis of this innovation. To increase the directivity and excite the maximum energy on the body, parasitic elements were used. The antenna provides almost 5 dBi directivity on the surface of the flat fat phantom. The perpendicular cuts of the radiation pattern also show that the pattern is tilted down toward the surface of the phantom by almost 60°. It was noticed that a change of the phantom type to muscle lowered the directivity by almost 2 dBs. Comparing the far field characteristics of this antenna with a monopole, dipole and planar Yagi antenna showed that the parasitic array provides the highest directivity. However, the radiation efficiency of the antenna is the lowest due to radiating more energy into the phantom. To evaluate the performance of this antenna, its path gain on the flat and cylinder phantom were simulated and compared with the other antennas. It was shown that this antenna provides almost 10 dB more path gain on the muscle tissue when compare to the dipole. Also, on the muscle cylindrical phantom it provides satisfactory performance and the path gain results are very close to the monopole antenna. The simulation results on the flat phantom were confirmed by performing the path gain measurement on the liquid muscle phantom. The results suggest almost 10 dB improvement to the planar monopole and dipole.

On-body MM wave measurements were conducted in the chest to belt channel on a static and moving human at 60 GHz. Two identical horn antennas with the gain of 20 dBi were used in the two ends of the channel. They were oriented toward each other in their maximum directivity direction. It was shown that movements, such as moving hands in front of the body, block the signal for 30% of the measurement period. The other movement such as moving the trunk or bending over, was found to block the signal much less. Also, it was shown that changing the position of one the antennas by 1 cm reduces the level of the received signal by 20 dB.

8.2. FUTURE WORK

Following research aspects are suggested as the continuous of the works accomplished in this work:

A simplified model was described in this thesis for the de-embedding purposes. The formulas can be extended to include the surface wave propagation which was neglected in the proposed models. Also, it seems that de-embedding at lower frequencies is more challenging than higher due to the problems in the control of the radiated energy from the antennas on the body. Hence, de-embedding of the antenna from the transmission channel is suggested at 60 GHz by use of well-defined antennas.

In this thesis, canonical structures were used to investigate the surface wave behaviour. However, the propagation in the actual body is more complicated since the space wave, surface wave and scattering collaborate in the communication. More investigations are

required to understand the nature of the surface wave on the body and determine the rate of the each wave contribution in the received signal level.

The analytical methods to solve the Maxwell equation around the lossy cylinder can be expanded for a normal point source.

The performance of the parasitic array antenna at higher frequencies such as 10 GHz can be tested and on-body to off- body measurements is suggested to determine the leakage of the energy off the body.

The parasitic array antenna size need to be reduces to be able to integrate in the electronic devices. To reduce the size of the antenna the meander lines can be used instead of straight parasitic elements.

References

[1] H.-B. Li, *et al.*, "Wireless body area network combined with satellite communication for remote medical and healthcare applications," *Wireless Personal Communications*, vol. 51, pp. 697-709, 2009.

[2] Ch. Baber, *et al.*, "Ergonomics of wearable computers," *Mobile Networks and Applications*, vol. 4, pp. 15-21, 1999.

[3] P. S. Hall and Y. Hao, *Antennas and propagation for body-centric wireless communications*. London: Artech House, 2006.

[4] *Bluetooth watch MBW-200* Available: http://www.sonyericsson.com/cws/products/accessories/overview/mbw-200sparklingallure?cc=gb&lc=en#view=overview [20/4/2011].

[5] *Apple Nile+iPod Sport Kit*. Available: http://www.apple.com/uk/ipod/nike/

[6] *IEEE 802.11 Standard Working Group*. Available: http://standards.ieee.org/about/get/802/802.11.html [20/4/2011].

[7] *IEEE 802.15 Standard Working Group*. Available: http://standards.ieee.org/about/get/802/802.15.html [20/4/2011].

[8] A. Alomainy, "Antennas and Radio Propagation for Body-centric Wireless Networks," PhD, Queens Mary University, London, 2007.

[9] A. Alomainy, *et al.*, "Comparison between two different antennas for UWB on-body propagation measurements," *IEEE Antennas and Wireless Propagation Letters*, vol. 4, pp. 31-34, 2005.

[10] M. R. Kamarudin, *et al.*, "Performance of antennas in the on-body environment," in *IEEE Antennas and Propagation Society International Symposium*, Washington, DC, United states, 2005, pp. 475-478.

[11] K. I. Ziri-Castro, *et al.*, "Characterisation of body-shadowing effects in the indoor environment at 5.2 GHz," in *High Frequency Postgraduate Student Colloquium*, Piscataway, NJ, USA, 2003, pp. 2-5.

[12] S. L. Cotton and W. G. Scanlon, "Characterization and modeling of on-body spatial diversity within indoor environments at 868 MHz," *IEEE Transactions on Wireless Communications*, vol. 8, pp. 176-185, 2009.

[13] W. G. Scanlon and S. L. Cotton, "Understanding on-body fading channels at 2.45 GHz using measurements based on user state and environment," in *Antennas and Propagation Conference (LAPC 2008)*, Loughborough, United kingdom, 2008, pp. 10-13.

[14] A. Alomainy, *et al.*, "UWB on-body radio propagation and system modelling for wireless body-centric networks," *IEE Proceedings: Communications*, vol. 153, pp. 107-114, 2006.

[15] A. Alomainy, *et al.*, "Statistical analysis and performance evaluation for on-body radio propagation with microstrip patch antennas," *IEEE Transactions on Antennas and Propagation*, vol. 55, pp. 245-248, 2007.

[16] S. L. Cotton and W. G. Scanlon, "Characterization of the on-body channel in an outdoor environment at 2.45 GHz," in *3rd European Conference on Antennas and Propagation (EuCAP)*, Berlin, Germany, 2009, pp. 722-725.

[17] K. Sulonen and P. Vainikainen, "Performance of Mobile Phone Antennas Including Effect of Environment Using Two Methods," *IEEE Transactions on Instrumentation and Measurement,* vol. 52, pp. 1859-1864, 2003.

[18] W. C.-Y. Lee, "Polarization diversity system for mobile radio," *IEEE Trans. Commun.,* vol. 20, pp. 912–923, 1972.

[19] K. T. Wong, *et al.*, "Fast-Polarization-Hopping Transmission Diversity to Mitigate Prolonged Deep Fades in Indoor Wireless Communications," *IEEE Antennas and Propagation Magazine,* vol. 48, pp. 20 - 27, 2006.

[20] T. Pratt, *et al.*, " System Performance of Dual Polarization Satellite Communication Links Affected by Attenuation and Depolarization " in *IEEE Military Communications Conference (MILCOM)*, 1983, pp. 135-139.

[21] P. Kyritsi and D. C. Cox, "Propagation characteristics of horizontally and vertically polarized electric fields in an indoor environment: simple model and results," in *IEEE Vehicular Technology Conference*, 2001, pp. 1422–1426.

[22] K. Yazdandoost and K. Hamaguchi, "Antenna Polarization Mismatch in Body Area Network Communications," in *Fourth European Conference on Antennas and Propagation (EuCAP)*, Barcelona, Spain, 2010, pp. 1-4.

[23] A. Khaleghi and I. Balasingham, "Non-Line-of-Sight On-Body Ultra Wideband (1-6-GHz) Channel Characterisation Using Different Antenna Polarisations," *IET Microwaves, Antennas & Propagation,* vol. 3, pp. 1019-27, 2009.

[24] P. S. Hall, "Antennas and propagation for body centric communications," in *Institution of Engineering and Technology Seminar on Antennas and Propagation for Body-Centric Wireless Communications*, London, United kingdom, 2007, pp. 1-4.

[25] P. S. Hall, "Antennas Challenges for Body Centric Communications," in *International Workshop on Antenna Technology: Small and Smart Antennas Metamaterials and Applications (IWAT '07)*, Cambridge, 2007, pp. 41-44.

[26] M. R. Kamarudin, *et al.*, "Antennas for On-Body Communication Systems," in *IEEE International Workshop on Antenna Technology: Small Antennas and Novel Metamaterials (IWAT 2005)*, Singapore, 2005, pp. 17-20.

[27] Y. Hao and P. S. Hall, "On-body antennas and propagation: Recent development," *IEICE Transactions on Communications,* vol. E91-B, pp. 1682-1688, 2008.

[28] V. Y. Vu, *et al.*, "Simplified Propagation Channel Characterization Considering the Disturbance of Antennas in the Case of a Multipath Cluster," *Microwave and Optical Technology Letters,* vol. 50, pp. 2604–2608, 2008.

[29] H. Friis, "A Note on a Simple Transmission Formula," *Proceedings of the IRE,* vol. 34, pp. 254-256, 1946.

[30] C. A. Balanis, *Antenna Theory: Analysis and Design*, Second ed. New York: Jhon Wiley & Sons, 1997.

[31] M. Benedetto, *et al., UWB Communication Systems: A Comprehensive Overview (EURASIP Book Series on Signal Processing and Communications)*: Hindawi Publishing Corporation, 2006.

[32] J. Parson, *The Mobile Radio Propagation Channel*. New york: John Wiley & Sons 2008.

[33] M. Hata, "Empirical Formula for Propagation Loss in Land Mobile Radio Services," *IEEE Transactions on Vehicular Technology,* vol. VT. 29, pp. 317-325, 1980.

[34] T. Taga, "Analysis of Mean Effective Gain of Mobile Antennas in Land Mobile Radio Environments," *IEEE Transactions on Vehicular Technology,* vol. 39, pp. 117-131, 1990.

[35] M. Landmann, "Limitations of experimnetal channel characteristics," PhD, TU Ilmenau, Germany, 2008.

[36] M. I. V. Anreddy, "Capacity of measured Ricean and Rayleigh indoor MIMO channels at 2.4 GHz with polarization and spatial diversity," in *Wireless Communications and Networking Conference*, 2006, pp. 946-951.

[37] J. Kermoal, *et al.*, "Polarization diversity in MIMO radio channels: Experimental validation of a stochastic model and performance assessment," in *IEEE Vehicular Technology Conference*, 2001, pp. 22-26.

[38] R. Vaughan, "Polarization diversity in mobile communications," *IEEE Transactions on Vehicular Technology,* vol. 39, pp. 177-186, 1990.

[39] M. Jensen and J. Wallace, "A review of antennas and propagation for MIMO wireless communications," *IEEE Transactions on Antennas and Propagation,* vol. 52, pp. 2810 - 2824, 2004.

[40] Y. I. Nechayev, *et al.*, "Characterisation of Narrowband Communication Channels on the Human Body at 2.45 GHz," *IET Microwaves, Antennas & Propagation,* vol. 4, pp. 722-732, 2010.

[41] S. Ullah, *et al.*, "Evaluation of Implant Communication with Polarisation and Unslotted CSMA/CA Protocol inWireless Body Area Networks," *EURASIP Journal onWireless Communications and Networking,* vol. 2010, pp. 1-4, 2010.

[42] L. Liu, *et al.*, "An Analytical Modeling of Polarized Time-Variant On-Body Propagation Channels with Dynamic Body Scattering," *EURASIP Journal on Wireless Communications and Networking,* vol. 2011, pp. 1-12, 2011.

[43] S. Ali and R. Amineh, "User effect analysis on polarisation in multi-input multi-output systems," *IET Microwaves, Antennas & Propagation*, vol. 4, pp. 2265–2272, 2010.

[44] A. Lea, *et al.*, "Propagation Between On-Body Antennas," *IEEE Transactions on Antennas and Propagation,* vol. 57, pp. 3619-3627, 2009.

[45] J. R. Wait, "The ancient and modern history of EM ground-wave propagation," *IEEE Antennas and Propagation Magazine,* vol. 40, pp. 7-24, 1998.

[46] K. A. Norton, "The physical reality of space and surface waves in the radiation field of radio antennas," *Proceedings of the IRE,* vol. 25, pp. 1192-1202, 1937.

[47] R. M. Edwards and M. I. Khattak, "Understanding Body-Centric Antennas," in *Loughborough Antennas & Propagation Conference (LAPC)*, Loughborough, UK, 2010, pp. 629-632.

[48] U. Rehman, *et al.*, "On-Body Bluetooth Link Budget: Effects of Surrounding Objects and Role of Surface Waves," in *Loughborough Antennas & Propagation Conference*, Loughborough, UK, 2008, pp. 97-100.

[49] J. Wang, *et al.*, "Analysis of On-Body Transmission Mechanism and Characteristic Based on an Electromagnetic Field Approach," *IEEE Transactions on Microwave Theory and Techniques*, vol. 57, pp. 2464-2470, 2009.

[50] M. Grimm and D. Manteuffel, "Electromagnetic Wave Propagation on Human Trunk Models excited by Half-Wavelength Dipoles," presented at the Loughborough Antennas & Propagation Conference (LAPC), Loughborough, UK, 2010.

[51] J. Ryckaert, *et al.*, "Channel Model For Wireless Communication Around Human Body," *Electronics Letters*, vol. 40, pp. 543-544, 2004.

[52] L. Petrillo, *et al.*, "Towards a Better Excitation of the Surface Wave," *Progress In Electromagnetics Research M*, vol. 13, pp. 17-28, 2010.

[53] A. V. Kukushkin, "On the existence and physical meaning of the Zenneck wave," *Physics-Uspekhi*, vol. 52, pp. 755-756, 2009.

[54] V. N. Datsko and A. A. Kopylov, "On Surface Electromagnetic Waves," *Physics-Uspekhi*, vol. 51, pp. 101-102, 2008.

[55] F. J. Zucker, "Surface-Wave Antennas," in *Antenna Engineering Handbook*, J. L. Volakis, Ed., ed: McGraw-Hill Companies, 2007.

[56] G. A. Conway and W. G. Scanlon, "Antennas for Over-Body-Surface Communication at 2.45 GHz," *IEEE Transactions on Antennas and Propagation*, vol. 57, pp. 844-855, 2009.

[57] N. Haga, *et al.*, "A Cavity-Backed Slot Antenna for On-Body BAN Devices," in *International Workshop on Antenna Technology: Small Antennas and Novel Metamaterials (IWAT 2008)*, 2008, pp. 510-513.

[58] R. Khouri, *et al.*, "A Thin Surface-Wave Antenna using a Via-Less EBG structure for 2.45 GHz ON-Body Communication Systems," in *Fourth European Conference on Antennas and Propagation (EuCAP)*, 2010, pp. 1-4.

[59] R. Fisher, "60 GHz WPAN Standardization within IEEE 802.15.3c," in *International Symposium on Signals, Systems and Electronics, ISSSE '07*, 2007, pp. 103-105.

[60] P. Smulders, "Exploiting the 60 GHz Band for Local Wireless Multimedia Access: Prospects and Future Directions," *IEEE Communications Magazine*, vol. 40, pp. 140-147, 2002.

[61] X. Hao, *et al.*, "Spatial and Temporal Characteristics of 60-GHz Indoor Channels," *IEEE Journal on Selected Areas in Communications*, vol. 20, pp. 620-630, 2002.

[62] D. M. Matic, *et al.*, "Indoor and Outdoor Frequency Measurements for MM-Waves in the Range of 60 GHz," in *48th IEEE Vehicular Technology Conference (VTC 98)*, 1998, pp. 567-571.

[63] P. F. M. Smulders and G. J. A. P. Vervuurt, "Influence of Antenna Radiation Patterns on MM-wave Indoor Radio Channels," in *2nd International Conference on Universal Personal Communications*, 1993, pp. 631-635.

[64] P. F. M. Smulders and A. G. Wagemans, "Wide-Band Measurements of MM-Wave Indoor Radio Channels," in *Third IEEE International Symposium on Personal, Indoor and Mobile Radio Communications (PIMRC '92)*, 1992, pp. 329-333.

[65] S. A. Mohamed, *et al.*, "Indoor Channel Sounding Measurements at Millimetre Wave Frequencies," in *IEE Colloquium on High Bit Rate UHF/SHF Channel Sounders - Technology and Measurement*, 1993, pp. 7/1-7/6.

[66] H. Tran Ngoc, *et al.*, "Measurement of Indoor Multipath Propagation Characteristics at 60 GHz With High Delay Time Resolution," in *International Conference on Advanced Technologies for Communications (ATC)*, 2008, pp. 250-253.

[67] F. Yildirim, *et al.*, "Polarization Effects for Indoor Wireless Communications at 60 GHz," *IEEE Communications Letters*, vol. 12, pp. 660-662, 2008.

[68] G. Suiyan and P. Vainikainen, "Millimeter-Wave Propagation in Indoor Corridors," *IEEE Antennas and Wireless Propagation Letters*, vol. 8, pp. 1242-1245, 2009.

[69] T. Manabe, *et al.*, "Effects of Antenna Directivity and Polarization on Indoor Multipath Propagation Characteristics at 60 GHz," *IEEE Journal on Selected Areas in Communications*, vol. 14, pp. 441-448, 1996.

[70] S. Alipour, *et al.*, "Propagation characteristics for a 60 GHz Wireless body area network (WBAN)," in *Military Communications Conference*, 2010, pp. 719-723.

[71] P. Salonen and Y. Rahmat-Samii, "Textile Antennas: Effects of Antenna Bending on Input Matching and Impedance Bandwidth," *IEEE Aerospace and Electronic Systems Magazine*, vol. 22, pp. 18-22, 2007.

[72] A. Alomainy, "Antennas and Radio Propagation for Body-centric Wireless Networks," PhD, Queen Mary University, London, May 2007.

[73] Y. I. Nechayev, *et al.*, "Short-Term and Long-Term Fading of On-Body Transmission Channels at 2.45 GHz," in *Loughborough Antennas Propagation Conference (LAPC)*, Piscataway, USA, 2009, pp. 657-60.

[74] R. G. Vaughan and J. B. Andersen, "Antenna Diversity in Mobile Communications," *IEEE Transaction on Vehicular Technology*, vol. 36, pp. 149-172, 1987.

[75] R Agostino and M A Stephens, *Goodness-of-Fit Techniques*. ,ew York,: Marcel Dekker, Inc., 1986.

[76] A. A. Serra, *et al.*, "Diversity Measurements for On-Body Communication Systems," *IEEE Antennas and Wireless Propagation Letters*, vol. 6, pp. 361-3, 2007.

[77] I. Khan and P. S. Hall, "Multiple Antenna Reception at 5.8 and 10 GHz for Body-Centric Wireless Communication Channels," *IEEE Transactions on Antennas and Propagation*, vol. 57, pp. 248-255, 2009.

[78] I. Khan, *et al.*, "Diversity Performance Analysis for On-Body Communication Channels at 2.45 GHz," *IEEE Transactions on Antennas and Propagation*, vol. 57, pp. 956-963, 2009.

[79] A. M. D. Turkmani, *et al.*, "An Experimental Evaluation of the Performance of Two-Branch Space and Polarization Diversity Schemes at 1800 MHz," *IEEE Transactions on Vehicular Technology*, vol. 44, pp. 318 - 326, 1995.

[80] N. L. Scott and R. G. Vaughn, "The Effect of Demeaning on Signal Envelope Correlation Analysis," in *the 4th Intl. Symposium on Personal, Indoor and Mobile Radio Communications (PIMRC'93)* Yokohama, Japan, 1993, pp. 583–587.

[81] Y.-T. Hsiao, *et al.*, "Channel Modeling and Signaling of Medical Implanted Communication Systems and a Step to Medical ICT," in *IEEE Antennas and Propagation Society International Symposium*, Budapest, Hungary, 2003, pp. 794 - 797.

[82] K. Tai, *et al.*, "Channel modeling and signaling of medical implanted communication systems and a step to medical ICT," in *16th Mobile and Wireless Communications Summit (IST)*, Budapest, Hungary, 2007, pp. 1-5.

[83] R. E. Collin, *Field Theory of Guided Waves*. New York: McGraw Hill, 1960.

[84] H. Barlow and A. Cullen, "Surface Waves," *Proceedings of the IRE* vol. 46, pp. 1413-1417, 1958.

[85] K. A. Norton, "The Propagation of Radio Waves Over the Surface of the Earth and in the Upper Atmosphere: Part I," *Proceedings of the IRE*, vol. 24, pp. 1367-1387, 1936.

[86] B. G. Pressey, *et al.*, "The Measurement of the Phase Velocity of Ground-Wave Propagation at Low Frequencies over a Land Path," *Proceedings of the IEE - Part III: Radio and Communication Engineering*, vol. 100, pp. 73-84, 1953.

[87] R. Paknys, "Uniform Asymptotic Formulas for the Creeping Wave field On or Off a Cylinder," *IEEE Transactions on Antennas and Propagation,* vol. 41, pp. 1099-1104, 1993.

[88] R. Paknys and D. R. Jackson, "The Relation Between Creeping Waves, Leaky waves, and Surface Waves," *IEEE Transactions on Antennas and Propagation,* vol. 53, pp. 898-907, 2005.

[89] R. Paknys and N. Wang, "Creeping Wave Propagation Constants and Modal Impedance for a Dielectric Coated Cylinder," *IEEE Transactions on Antennas and Propagation,* vol. 34, pp. 674-680, 1986.

[90] C. A. Balanis, *Advanced Engineering Electromagnetics*: John Wiley & Sons, 1989.

[91] A. Fort, *et al.*, "A Body Area Propagation Model Derived From Fundamental Principles: Analytical Analysis and Comparison With Measurements," *IEEE Transactions on Antennas and Propagation,* vol. 58, pp. 503-514, 2010.

[92] A. Ishimaru, *Electromagnetic Wave Propagation, Radiation, and Scattering*. New Jersey, : Prentice Hall, 1991.

[93] e. a. Y. Hsiao, "Applications of time-gating method to improve the measurement accuracy of antenna radiation inside an anechoic chamber," in *IEEE Antennas and Propagation Society International Symposium*, 2003, pp. 794-797.

[94] S. Collonge, *et al.*, "Influence of the Human Activity on Wide-Band Characteristics of the 60 GHz Indoor Radio Channel," *IEEE Transactions on Wireless Communications,* vol. 3, pp. 2396-2406, 2004.

[95] Y. Haibing, *et al.*, "Impact of Antenna Pattern and Reflective Environment on 60 GHz Indoor Radio Channel Characteristics," *IEEE Antennas and Wireless Propagation Letters,* vol. 4, pp. 300-303, 2005.

[96] R. C. Daniels and R. W. Heath, "60 GHz Wireless Communications: Emerging Requirements and Design Recommendations," *IEEE Vehicular Technology Magazine,* vol. 2, pp. 41 - 50, 2007.

[97] Y. Hui-Wen, *et al.*, "Analysis and Design of Microstrip-to-Waveguide Transitions," *IEEE Transactions on Microwave Theory and Techniques,* vol. 42, pp. 2371-2380, 1994.

[98] D. Pozar, *Microwave Engineering*, 3rd ed. New York: Jhon Wiley & Sons, 2004.